Enhancement of Lateral Stability for a Multi-Wheeled Combat Vehicle Using Various Control Strategies

by

Mohamed Omar

A thesis submitted to the
School of Graduate and Postdoctoral Studies in partial
fulfillment of the requirements for the degree of

Master of Applied Science in Automotive Engineering

Faculty of Engineering and Applied Science
University of Ontario Institute of Technology (Ontario Tech University)
Oshawa, Ontario, Canada
August 2021

THESIS EXAMINATION INFORMATION

Submitted by: **Mohamed Omar**

Mater of Applied Science in **Automotive Engineering**

Thesis title: Enhancement of Lateral Stability for a Multi-Wheeled Combat Vehicle Using Various Control Strategies

An oral defense of this thesis took place on June 15th, 2021, in front of the following examining committee:

Examining Committee:

Chair of Examining Committee	Dr. Martin Agelin-Chaab
Research Supervisor	Dr. Moustafa El-Gindy
Examining Committee Member	Dr. Jing Ren
Thesis Examiner	Dr. Yuping He, FEAS - AME

The above committee determined that the thesis is acceptable in form and content and that a satisfactory knowledge of the field covered by the thesis was demonstrated by the candidate during an oral examination. A signed copy of the Certificate of Approval is available from the School of Graduate and Postdoctoral Studies.

ABSTRACT

This thesis investigates various active chassis control strategies for multi-wheeled combat vehicle to enhance its lateral stability at limit handling. The proposed control strategies are Active All-Wheel Steering (AWS), Torque Vectoring (TV) and Differential Braking (DB).

At high-speed cornering maneuvers, the vehicle experiences higher load transfer which can lead to a loss of the grip between the tires and the ground. Consequently, deterioration of vehicle handling capability can occur. Hence, integration of Semi-Active Suspension (SAS) is introduced to each control strategy to enhance the vehicle's lateral stability at high-speed cornering maneuvers.

The evaluation method is conducted by executing the simulations utilizing a validated TRUCKSIM vehicle model in co-simulation with the proposed controllers in MATLAB SIMULINK. Based on the results obtained, it was concluded that the integration of SAS has a significant enhancement on the vehicle lateral stability at a high coefficient of friction, unlike at a low coefficient of friction.

Keywords: Active All-Wheel Steering; Torque Vectoring; Differential Braking; Semi-Active Suspension; Linear Quadratic Regulator.

AUTHOR’S DECLARATION

I hereby declare that this thesis consists of original work of which I have authored. This is a true copy of the thesis, including any required final revisions, as accepted by my examiners.

I authorize the University of Ontario Institute of Technology (Ontario Tech University) to lend this thesis to other institutions or individuals for the purpose of scholarly research. I further authorize University of Ontario Institute of Technology (Ontario Tech University) to reproduce this thesis by photocopying or by other means, in total or in part, at the request of other institutions or individuals for the purpose of scholarly research. I understand that my thesis will be made electronically available to the public.

Mohamed Omar

STATEMENT OF CONTRIBUTIONS

Part of the work described in chapters 2, 3 and 4 have been published as:

Omar, M. and El-Gindy, M., "Direct Yaw Control Based on Optimal Longitudinal Tire Forces for 8×8 Combat Vehicle," SAE Technical Paper 2021-01-0261, 2021, https://doi.org/10.4271/2021-01-0261.

Omar, M., El-Gindy, M., “Vehicle Yaw Stability Control: Literature Review”, *International Journal of Vehicle System Modelling and Testing (IJVSMT)*, 2020. (In press)

ACKNOWLEDGMENTS

First and foremost, I would like to show my endless love and gratitude to my mother for giving me the unconditional support, motivation, and strength through out not only in my academic journey but in my life.

I would like to show my utmost gratitude to my supervisor, Professor Moustafa El-Gindy and Moataz Ahmed for their support and motivation throughout my research and MASc. Their continuous advice, support and motivation have been invaluable throughout the two years I have been at Ontario Tech University.

I would also like to express my appreciation to NSERC Discovery Grant and GDLS-C for their funding of this research work and allowing me to contribute to the state-of-art.

À mon père

– Comme je te l'avais promis avant de quitter ce monde,

je dédie cette thèse à ton âme *mon cher Papa*

Table of Contents

LIST OF FIGURES

LIST OF TABLES

NOMENCLATURE

A	System parameters matrix
a	Distance between the center of the wheel of the first axle to vehicle center of gravity, m
$a_{x-\text{desired}}$	Desired longitudinal acceleration, m/s^2
a_y	Lateral acceleration, g's
B	System input matrix
b	Distance between the center of the wheel of the second axle to vehicle center of gravity, m
$C_{d_{ij}}$	Damping coefficient, Ns/m
$C_{\alpha_{ij}}$	Tire cornering stiffness, N/rad
c	Distance between the center of the wheel of the third axle to vehicle center of gravity, m
D	Feedforward matrix
d	Distance between the center of the wheel of the fourth axle to vehicle center of gravity, m
d_1	Vector of disturbance variables
E	System input matrix for disturbance
$F_{d_{ij}}$	Damper force, N
$F_{s_{ij}}$	Spring force, N
$F_{x_{ij}}$	Tire longitudinal force, N
F_{Xdes}	Total desired longitudinal force, N
$F_{y_{ij}}$	Tire latera force, N
$F_{t_{ij}}$	Tire spring force, N
$F_{z_{ij}}$	Tire normal force, N
$F_{(zij)_c}$	LQR corrective damper force control input, N
$F_{(z)c}$	LQR corrective heave motion control input, N
f	Rolling resistance coefficient, $(-)$
g	Acceleration due to gravity, m/s^2
I_{xx}	Vehicle roll mass of inertia, Kg. m^2
I_{yy}	Vehicle pitch mass of inertia, Kg. m^2
I_{zz}	Vehicle yaw mass of inertia, Kg. m^2
I_w	Wheel mass of inertia, Kg. m^2
K	Controller gain
K_s	Spring stiffness, N/m
K_{2-1}	The average steering angle of the second axle expressed as a ratio of the average steering angle of the average steering of the first axle
l	Vehicle wheelbase, m
M_z	LQR corrective yaw moment control input, Nm
M_ϕ	LQR corrective roll moment control input, Nm
M_θ	LQR corrective pitch moment control input, Nm
m	Vehicle mass (Sprung + Unsprung), Kg

m_s	Sprung mass, Kg
$m_{u_{ij}}$	Unsprung mass, Kg
Q	States weighting matrix
R	Control input weighting matrix
r	Vehicle yaw rate, rad/s
r_{des}	Desired yaw rate, rad/s
r_{eff}	Effective rolling radius of the tire, m
r_{ss}	Yaw rate in steady state, rad/s
$T_{b_{ij}}$	Braking torque, Nm
$T_{d_{ij}}$	Driving torque, Nm
t	Vehicle track width, m
U	Control input
u	Vehicle longitudinal speed, m/s
V	Vehicle lateral speed, m/s
v	Longitudinal speed of wheel center, m/s
W	Weighting factor
w	Angular speed of the wheel, rad/s
X	State variables vector
$Z_{r_{ij}}$	Road displacement, m
Z_s	Sprung mass displacement, m
$Z_{u_{ij}}$	Unsprung mass displacement, m

Greek Letters

α_{ij}	Tire slip angle, rad
β	Vehicle sideslip angle, rad
δ_i	Average steering angle of ith, rad
$\delta_i c$	Average controlled steering angle of ith axles, rad
θ	Vehicle pitch angle, rad
λ_{ij}	Slip ratio of the tire, (-)
μ	Coefficient of friction
τ_{delay}	Time delay, s
ϕ	Vehicle roll angle, rad
i, j	Used as a subscript to specify the number of the axle and right or left wheel respectively

List of ABBREVIATIONS AND SYMBOLS

ABS	Anti-lock braking system
ACC	Active chassis control
AFS	Active front steering
ARS	Active rear steering
ASC	Active steering control
AVTP	Allied vehicle testing publications
AWD	All wheel drive
AWS	All wheel steering
DB	Differential braking
DLC	Double lane change
DOF	Degrees of freedom
DYC	Direct yaw control
ESC	Electronic stability control
FMVSS	Federal motors vehicle stability standards
FWD	Front wheel drive
LAV	Light armoured Vehicle
LPV	Linear parameter varying
LQG	Linear quadratic gaussian
LQR	Linear quadratic regulator
MIMO	Multi-input multi-output
MPC	Model predictive control
NATO	North Atlantic treaty organization
RMSE	Root Mean Square Error
RWD	Rear wheel drive
SAS	Semi-active suspension
SMC	Sliding mode control
TV	Torque vectoring
VDC	Vehicle dynamics control
ZSS	Zero sideslip
4WS	Four-wheel steering
4WS/8WD	Four-wheel steering/Eight-wheel drive
8WS/8WD	Eight-wheel steering/Eight-wheel drive

Chapter 1 INTRODUCTION

1.1 MOTIVATION

Light Armored Vehicles (LAVs) are widely employed in many armed services and military domain to accomplish multi tasks. One of these tasks are intended to serve as infantry and weapons carriers, also as command, control, and reconnaissance vehicle and providing logistics support [1]. The merit of utilizing multi-wheeled combat vehicles over traditional four-wheeled vehicles is improving the steering capability in tight maneuvers, providing better in/off-road traction capabilities. Furthermore, the loads are distributed on multiple axles, which enhances vehicle's stability.

Regardless the various advantages of LAV, there are disadvantages associated with the operation of this vehicle. The main disadvantages are that it has higher center of gravity and limited payload carrying capacity. This can lead the vehicle to rollover easily at a given lateral acceleration, exposing the cabin crew into fatalities [2]. Moreover, the vehicle is designed to be operated in severe conditions and subjected to uncertainties, such as different road coefficient of frictions and vehicle varying parameters in terms of weight and inertia, which can affect inadequately the vehicle lateral stability and maneuverability, resulting in loss of vehicle's directional stability.

The past three decades many automotive companies have been working on developing Active Chassis Control Systems, to improve vehicle lateral stability at high-speed cornering conditions and ensure the ride comfort. Nowadays, several control systems have been implemented and became a norm for automotive industry, such as Anti-lock Brake System (ABS), Traction Control System (TCS), Active Wheel Steering (AWS), Torque Vectoring (TV), Active/Semi-Suspension and Electronic Stability Control (ESC). There is a study that has been carried out to assess the effect of ESC in reducing accidents, the study showed that ESC prevented rollover to be occurred by 50 %, run-off-road by 40% and single vehicle crashes by 25% [3].

1.2 SCOPE AND OBJECTIVES

1.2.1 Scope

This thesis is intended to compare various control strategies on a multi-wheeled combat vehicle. Specifically, Active All-Wheel Steering, Torque Vectoring, Differential Braking, and their integration with Semi-Active Suspension. This comparison is aimed to investigate the effect of each control strategy on the given vehicle at limit handling state. Furthermore, the assessment is conducted in this research based on the enhancements acquired on the vehicle's stability at various coefficient of friction, maneuver and speed using each control strategy.

1.2.2 Objectives

The objective of this research work is to present an insight on the benefits of implementing each control strategy and their integration on the multi-wheeled combat vehicle. Moreover, all the simulations in this research are performed using a full vehicle model that was validated in previous research work. The TRUCKSIM vehicle model is 22 degrees of freedom and in co-simulation with the designed controllers in MATLAB/SIMULINK.

Objectives comprise:

- Design a Linear Quadratic Regulator (LQR) controller for Active All-Wheel Steering as a lower control allocation for 8WS/8WD combat vehicle.
- Design an LQR controller for Torque Vectoring as a lower control allocation for 4WS/8WD combat vehicle considering optimal tire driving forces distribution.
- Design an LQR controller for Differential Braking as a lower control allocation for 4WS/8WD combat vehicle considering optimal tire braking forces distribution.
- Design an LQR controller for Semi-Active Suspension as a lower control allocation and integrated with all aforementioned controllers.
- Perform an assessment for each control strategy with and without integration of Semi-Active Suspension at high and low road friction surface.

- Conduct the simulations at various maneuvers at several road coefficient of friction, to assess the performance and the effectiveness of each controller at limit handling speed at high and low coefficient of friction.
- Suggest a recommendation for future work, based on the performance of each proposed control strategy and the possibilities of integrating more than two control strategies for further enhancements in terms of vehicle lateral stability.

1.3 THESIS OUTLINE

This thesis will be introduced in 7 chapters which are as follows.

Chapter 1: This chapter covers the background, scope, and objectives of this thesis.

Chapter 2: This chapter presents a literature review on various active control systems and control allocation strategies including active all wheel steering, torque vectoring and differential braking.

Chapter 3: This chapter introduces the validated TRUCKSIM vehicle model, various vehicle's mathematical models developed for LQR control design purpose and the reference yaw rate model.

Chapter 4: This chapter provides in detail the theory behind LQR controller design. Also, introduces the implementation of the hierarchical control structure for active all wheel steering, torque vectoring, differential braking, and semi-active suspension.

Chapter 5: This chapter introduces an assessment of each proposed control strategy through a comparison between them with and without integration of semi-active suspension to assess their performance at high and low friction surface during sever maneuver at limit handling.

Chapter 6: This chapter presents the simulation results and discussions at various test events.

Chapter 7: The conclusions and future work are summarized in this chapter.

Chapter 2 LITERATURE REVIEW

The literature review emphasises on lateral dynamics control (yaw stability control) utilizing active steering, torque vectoring and differential braking as a control allocation strategy. Whereas the survey on vehicle vertical dynamics investigates only the benefits of integrating semi-active suspension with all mentioned above to enhance vehicle lateral stability. The study of ride comfort is not in the scope of this thesis.

The literature survey is organized as follows: section 2.1 presents an introduction on vehicle dynamics control, afterwards section 2.2 describes several vehicle mathematical models, followed by control objectives in section 2.3. Active chassis control systems are discussed in section 2.4, while control allocation strategies are introduced in section 2.5, respectively.

2.1 Introduction

Numerous research studies have been conducted in the past years in vehicle dynamics control (VDC). Vehicle lateral motion is significantly important as it determines the vehicle stability and safety in different operating and road conditions. Controlling the yaw motion is considered to be one of the most important techniques in vehicle lateral dynamics control, therefore implementing an effective control strategy can be achieved through multiple phases. In this literature, the main phases of yaw motion control are determining vehicle models, control objective, active chassis control and control allocation strategies [4], as shown in Figure 2-1.

The vehicle lateral dynamics motion behaviour that can be represented by either linear (bicycle or single-track) or nonlinear vehicle dynamics model is described for the purpose of designing and evaluating the controller. The control objective is to maintain the vehicle's stability and keep it on its desired trajectory at different driving scenarios. This can be achieved through controlling two variables - yaw rate and vehicle sideslip angle. Therefore, the actual vehicle yaw rate and sideslip angle should rapidly track the desired vehicle yaw rate and sideslip angle response. The vehicle can be unstable due to the following reasons: bad road conditions, sudden manoeuvres to avoid any obstacles and undesired driver's command. This may cause the vehicle to become unstable and results in severe accidents. It is essential to control the yaw motion of the vehicle by implementing an Active Chassis Control [3] to maintain the vehicle stable at any improper driving conditions to keep it on the desired trajectory and follow the driver's command.

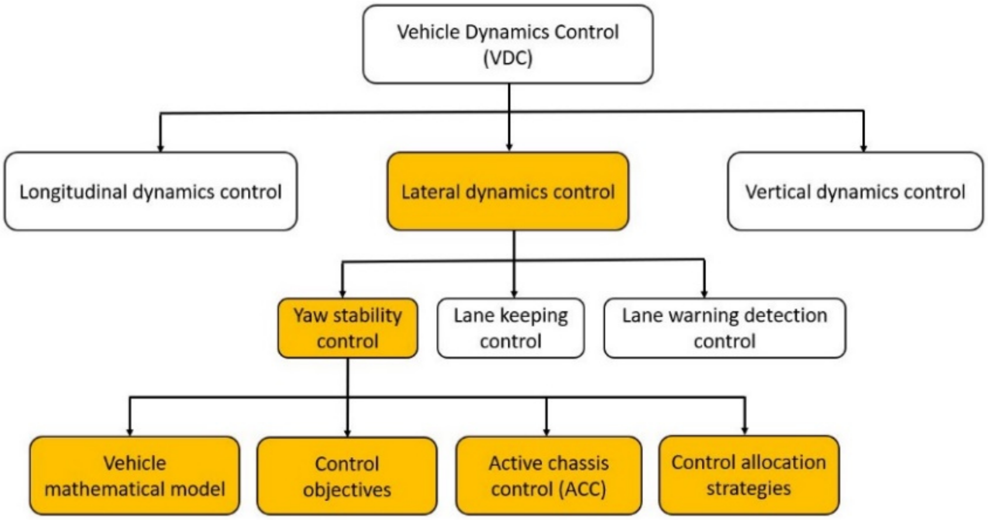

Figure 2-1 Yaw stability control for lateral dynamics control [4]

Whereas vertical dynamics control can be classified into two categories Semi-Active Suspension (SAS) and Active suspension system (ASS) as shown in Figure 2-2. Normally, the main duty of the suspension is to provide ride comfort by isolating the vehicle's sprung mass from the transmission of the uncomfortable frequencies generated from road irregularities. Also, to provide adequate cornering characteristics by preventing tires from losing contact with ground at high lateral acceleration. However, a conflict arises between the first and second requirements, since ride comfort needs soft suspension, while good cornering characteristics need stiff suspension to overcome the load variations caused by longitudinal and lateral load transfer.

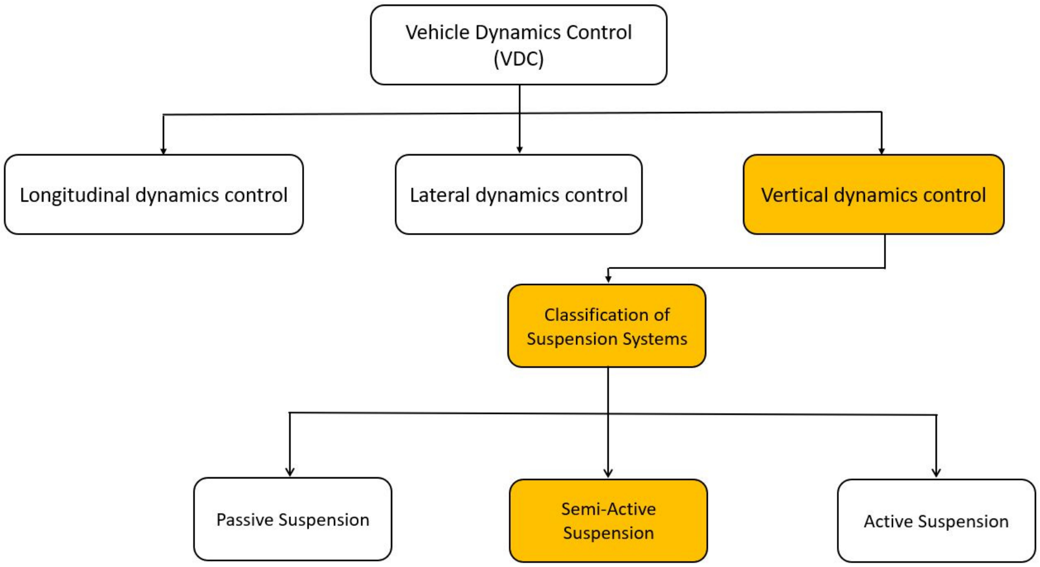

Figure 2-2 Classification of suspension systems

The traditional suspension is known as passive suspension, where it consists of a spring and damper that are mounted in parallel at each wheel of the vehicle. The spring functions to store and absorb energy, while the damper utilized to dissipate the vibration energy stored in the spring and both have fixed coefficients. Also, hold and connect the sprung and unsprung masses together.

The SAS is relatively the same as traditional suspension, except it incorporates a controlled damper where the damping force in the shock absorber can be regulated according to the driving conditions. Figure 2-3 illustrates a schematic view of a semi-active suspension system. The regulated damping force can be attained by controlling the orifice area in the shock absorber, hence varying the resistance to fluid flow [5].

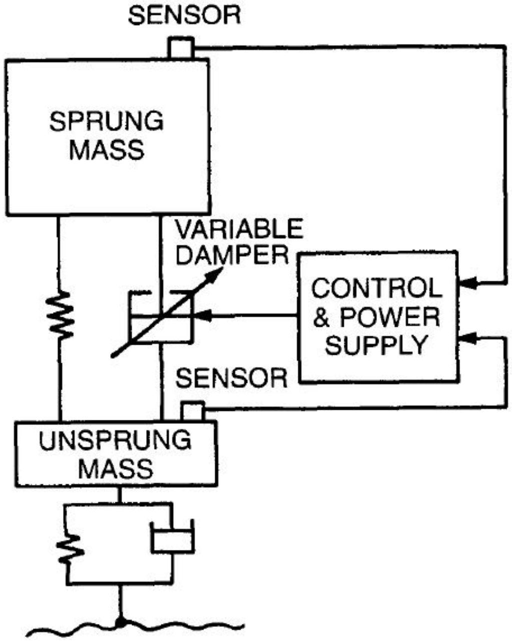

Figure 2-3 Concept of Semi-Active Suspension System [5]

While the concept of operation of an ASS is shown in Figure 2-4. The ASS is utilized to adjust and control the vehicle heave, pitch, and roll motions according to the driving conditions. The spring and shock absorber in a traditional system is replaced or assisted in parallel by a hydraulic or electromagnetic force actuator. Moreover, the actuator generates the force when required based on the operating conditions and performs independently regardless of the suspension condition. The vehicle is consistently monitored by sensors during its driving conditions. Furthermore, based on the signals received from the sensors, the force in the actuator is regulated to achieve better ride and handling performance. Thus, the conflict between offering ride comfort, suspension travel and wheel load variations can be compromised and resolved [5].

However, active suspension design is more complex, high weight to power ratio and significant external power needed. Unlike semi-active suspension that is simple in design, low energy use, easy to be implemented, simple control design and low cost [6-8].

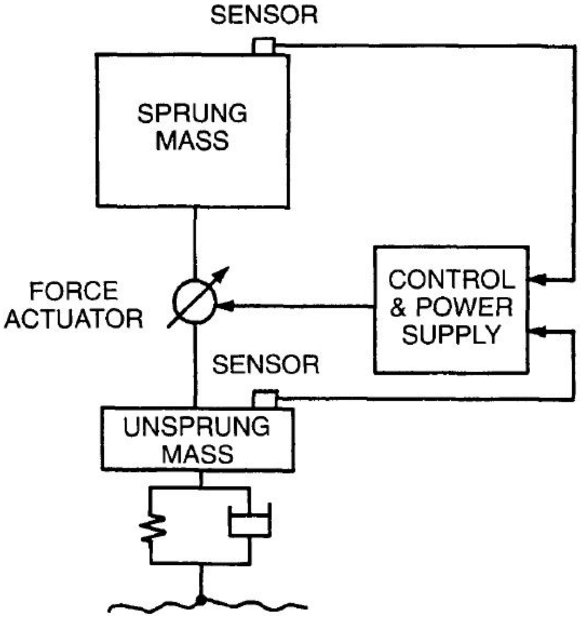

Figure 2-4 Concept of Active Suspension System [5]

2.2 Vehicle Mathematical Models

To achieve a controller that controls the yaw motion of any given vehicle, it must begin by describing all the forces and moments that act on the vehicle and represent its motion dynamics based on Newton-Euler's second law. Normally the mathematical vehicle model classifies into two models, which are the nonlinear and linearized vehicle models. These two models will be discussed in detail in the following subsections.

2.2.1 Linear model (Bicycle or single-track model)

The linear vehicle model has been used in many research studies as in [9-16] for controller purposes design to realize the yaw stability control. Generally, the linear mathematical model is simplified from the non-linear model based on some assumptions as follows:

- Roll and pitch motion are ignored.
- Longitudinal vehicle dynamics are neglected.
- Vehicle tires behave linearly (in the linear region).
- Aerodynamic and rolling resistance are neglected.

- Longitudinal speed of vehicle is constant.
- Lateral and longitudinal load transfer are neglected.
- The steering angle of any axle is considered to be the average steering angle of the right and left wheels.
- A small angle approximation is considered in the derivation of the vehicle model
- In steady state the rate of change of vehicle side slip angle and yaw rate assumed to be equal zero, $\dot{\beta} = \dot{r} = 0$.

The linear model has two degrees of freedoms (DOF) which are the rate of change of yaw motion and lateral velocity as shown in Figure 2-5.

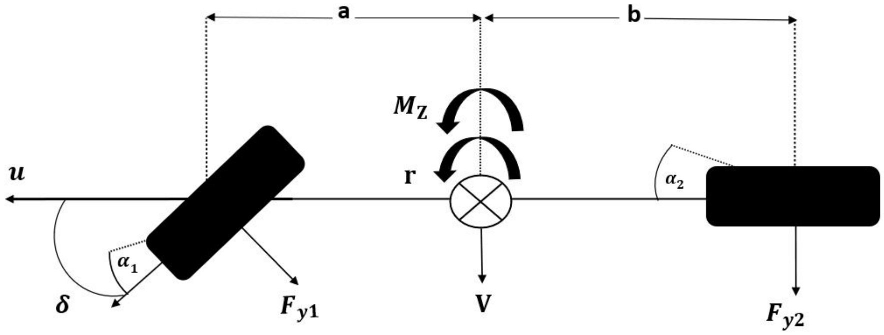

Figure 2-5 Bicycle model (single-track model)

Where the governing Equations of vehicle in lateral and yaw motions are listed below as follows in equations (2-1) and (2-2).

$$\sum \mathrm{F_y} = \mathrm{m}\left(\dot{\mathrm{V}} + \mathrm{ru}\right) \tag{2-1}$$

$$\mathrm{F_{y1}} + \mathrm{F_{y2}} = \mathrm{m}\left(\dot{\mathrm{V}} + \mathrm{ru}\right)$$

$$\sum \mathrm{M_Z} = \mathrm{I_{ZZ}}\dot{\mathrm{r}} \tag{2-2}$$

$$\mathrm{aF_{y1}} + \mathrm{bF_{y2}} + \mathrm{M_Z} = \mathrm{I_{ZZ}}\dot{\mathrm{r}}$$

Where $\mathrm{F_{y1}}$ and $\mathrm{F_{y2}}$ are the lateral forces at the front and rear tires, respectively, generated between the tires contact patch and the ground, $\dot{\mathrm{V}}$ and r are the rate of change of lateral velocity and the yaw motion respectively, m is the vehicle sprung mass, $\mathrm{I_{ZZ}}$ is the mass moment of inertia around z-axis, u is the longitudinal speed and finally a and b are the distance between the front and rear axles to the vehicle centre of gravity (CG).

Assuming linear tire characteristics, the cornering stiffness of the tires at the front and rear are described as follows in equation (2-3).

$$C_{\alpha i} = \frac{F_{yi}}{\alpha_i} \tag{2-3}$$

And the slip angles of the front and rear tires are described as follows in equations (2-4) and (2-5).

$$\alpha_1 = \delta_1 - \left(\frac{V - ra}{u}\right) \tag{2-4}$$

$$\alpha_2 = -\left(\frac{V - rb}{u}\right) \tag{2-5}$$

After an algebraic manipulation will yield the rate of change of vehicle side slip angle and yaw rate in state-space form as follows in equations (2-6),(2-7) and (2-8).

$$\dot{X} = AX + BU \tag{2-6}$$

$$Y = CX + DU \tag{2-7}$$

$$\begin{bmatrix} \dot{\beta} \\ \dot{r} \end{bmatrix} = \begin{bmatrix} -\dfrac{C_{\alpha 1} + C_{\alpha 2}}{mu} & \dfrac{-aC_{\alpha 1} + bC_{\alpha 2} - mu^2}{mu^2} \\ \dfrac{bC_{\alpha 2} - aC_{\alpha 1}}{I_{zz}} & \dfrac{-a^2C_{\alpha 1} - b^2C_{\alpha 2}}{I_{zz}\,u} \end{bmatrix} \begin{bmatrix} \beta \\ r \end{bmatrix} + \begin{bmatrix} \dfrac{C_{\alpha 1}}{mu} \\ \dfrac{aC_{\alpha 1}}{I_{zz}} \end{bmatrix} \delta \tag{2-8}$$

Where β and r are the state variables. Furthermore, the reference model or the desired vehicle side slip angle and yaw rate responses are normally generated using the linear model at steady state condition where $\dot{\beta} = \dot{r} = 0$.

In case of multi-axles vehicles, the mathematical model and dynamic equations will be changed, hence [17] introduced a generalized multi-axle technique to develop the dynamic equations in state-space form for any given arbitrarily number of steered and un-steered multi-axle vehicle as shown in equation (2-9).

$$\begin{bmatrix} \dot{\beta} \\ \dot{r} \end{bmatrix} = \begin{bmatrix} -\dfrac{\sum_1^n C_n}{mu} & \dfrac{-\sum_1^n x_n C_n}{mu^2} - 1 \\ -\dfrac{\sum_1^n x_n C_n}{I_{zz}} & \dfrac{-\sum_1^n x_n C_n}{I_{zz}\,u} \end{bmatrix} \begin{bmatrix} \beta \\ r \end{bmatrix} + \begin{bmatrix} \dfrac{C_1}{mu} & \cdots & \dfrac{C_n}{mu} \\ \dfrac{x_1 C_n}{I_{zz}} & \cdots & \dfrac{x_n C_n}{I_{zz}} \end{bmatrix} \begin{bmatrix} \delta_1 \\ \vdots \\ \delta_n \end{bmatrix} \tag{2-9}$$

2.2.2 Non-linear mathematical model

The aim of using a nonlinear mathematical model is to represent the actual vehicle dynamics behaviour. Many research studies [18-20] have introduced a nonlinear mathematical model for purpose of designing and evaluating a controller to improve the vehicle's lateral stability. An ordinary vehicle double-track nonlinear model in cornering manoeuvre is shown as follows in Figure 2-6.

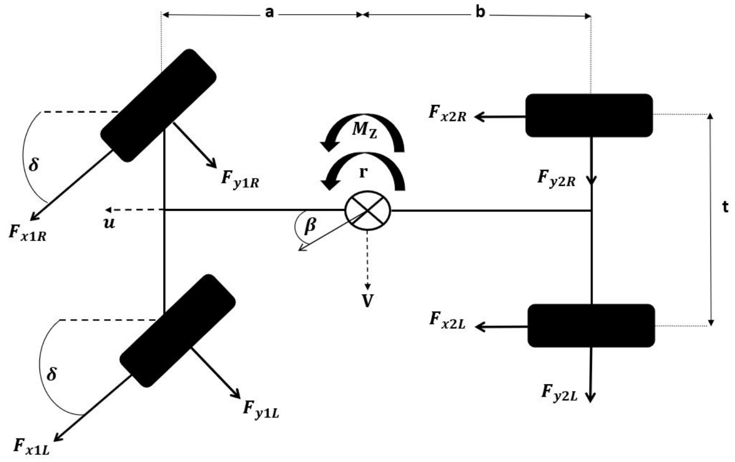

Figure 2-6 Double-track vehicle model

The vehicle parameters are vehicle track width t, a and b are the distance between the front and rear axle to the vehicle centre of gravity respectively, the longitudinal speed is u, the lateral velocity is V, the yaw rate is r, the vehicle side slip angle is β, the front steering angle is δ, F_X and F_y are the longitudinal and lateral forces respectively, while subscripts 1R,1L,2R,2L denote front axle right tire, front axle left tire, rear axle right tire, rear axle left tire respectively.

At very low speed the tire behaves linearly which means that the lateral force increases linearly with increasing of tire slip angle at a given small angle, while the longitudinal force increases linearly at a given small slip ratio. When the tire slip angle and slip ratio increase, the tire exhibits nonlinear behaviour resulting in nonlinear lateral and longitudinal forces that can affect the vehicle dynamic motion, therefore, a nonlinear tire model has to be used to describe the nonlinear tire forces, a DUGOFF nonlinear tire model was introduced in [11, 21, 22] and in [9, 19, 23] PACEIKA tire model was utilized, while both nonlinear tire models were implemented in [24].

The complexity of the nonlinear mathematical vehicle model is strongly dependent on the number of DOF utilized to describe the vehicle's dynamic motion. A 7-DOF nonlinear model was investigated in [18, 25-27] to express the dynamic motion of the given vehicle model, which are longitudinal acceleration, lateral acceleration, yaw rate and the rotational motions of the four wheels. The governing equations of the 7-DOF nonlinear model are presented as follows in equations (2-10), (2-11), (2-12) and (2-13).

Longitudinal motion

$$\sum \mathrm{F_X} = \mathrm{m}\left(\dot{U} - \mathrm{rv}\right)$$
$$\left(\mathrm{F_{X1R}} + \mathrm{F_{X1L}}\right)\cos\delta + \mathrm{F_{X2R}} + \mathrm{F_{X2L}} - \left(\mathrm{F_{Y1R}} + \mathrm{F_{Y1L}}\right)\sin\delta = \mathrm{m}\left(\dot{U} - \mathrm{rv}\right) \tag{2-10}$$

Lateral motion

$$\sum \mathrm{F_Y} = \mathrm{m}\left(\dot{\mathrm{V}} + \mathrm{ru}\right)$$
$$\left(\mathrm{F_{X1R}} + \mathrm{F_{X1L}}\right)\sin\delta + \left(\mathrm{F_{Y1R}} + \mathrm{F_{Y1L}}\right)\cos\delta + \mathrm{F_{Y2R}} + \mathrm{F_{Y2L}} = \mathrm{m}\left(\dot{\mathrm{V}} + \mathrm{ru}\right) \tag{2-11}$$

Yaw motion

$$\sum \mathrm{M_Z} = \mathrm{I_{ZZ}}\dot{\mathrm{r}} \tag{2-12}$$
$$\begin{aligned}\frac{\mathrm{t}}{2}&\left[\left(\mathrm{F_{X1R}} - \mathrm{F_{X1L}}\right)\cos\delta + \left(\mathrm{F_{Y1L}} - \mathrm{F_{Y1R}}\right)\sin\delta\right] + \mathrm{a}\left[\left(\mathrm{F_{Y1R}} + \mathrm{F_{Y1L}}\right)\cos\delta + \left(\mathrm{F_{X1R}}\right.\right. \\ &\left.\left.+ \mathrm{F_{X1L}}\right)\sin\delta\right] + \frac{\mathrm{t}}{2}\left(\mathrm{F_{X2R}} - \mathrm{F_{X2L}}\right) - \mathrm{b}\left(\mathrm{F_{Y2R}} + \mathrm{F_{Y2L}}\right) + \mathrm{M_Z} = \mathrm{I_{ZZ}}\dot{\mathrm{r}}\end{aligned}$$

The rotational motion of four wheels 4 DOF

$$\mathrm{I_{wij}}\alpha_{\mathrm{Wij}} = \mathrm{T_{dij}} - \mathrm{T_{bij}} - \mathrm{F_{xij}}\mathrm{r_{eff}} \tag{2-13}$$

Each wheel represents 1-DOF, where the mass moment of inertia of wheel is $\mathrm{I_w}$, the angular acceleration of wheel is α_W, wheel driving torque is $\mathrm{T_d}$ and braking torque is $\mathrm{T_b}$. longitudinal tractive or braking force is $\mathrm{F_x}$, while the effective rolling radius is $\mathrm{r_{eff}}$. The subscripts i and j represent either front or rear axle and left or right wheel, respectively.

It is notable that increasing the number of degrees of freedom that represent the vehicle's dynamic motion can enhance the accuracy of the simulations. In these research studies [19-22, 24, 28-31] an 8-DOF was utilized, including roll motion of the sprung mass, while in [9, 32, 33] adopted full vehicle model 14-DOF which are 6-DOF of sprung mass and 8-DOF of unsprung mass.

Furthermore, different commercial software packages that utilize the full vehicle model (nonlinear model) as CARSIM or TRUCKSIM were used by [12, 34-38].

2.3 Control Objectives

In vehicle lateral stability control, two important variables are used to determine vehicle yaw stability which is the vehicle sideslip angle β and yaw rate r. The control objective can be categorized into three control objectives as referred in [39] which are, controlling vehicle sideslip angle, yaw rate or controlling both together as shown in Figure 2-7, to follow the desired sideslip and yaw signals.

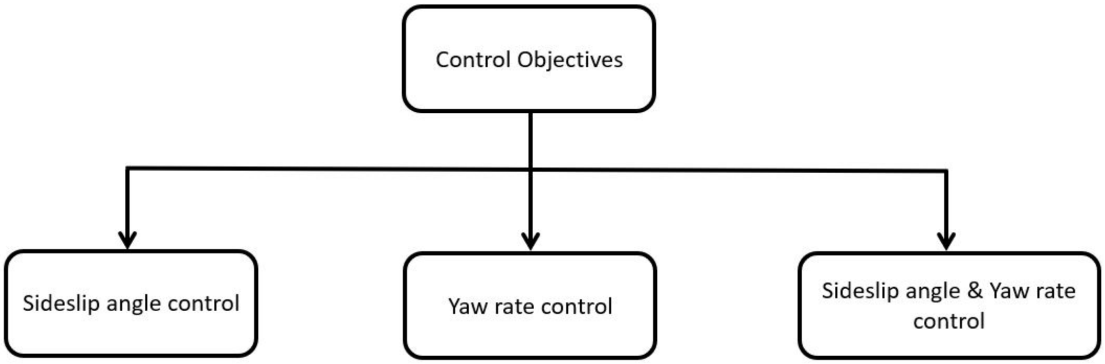

Figure 2-7 Control objectives of vehicle yaw stability control [4]

The vehicle sideslip angle is simply defined as the angle between where the vehicle pointing and heading motion or in other words the tangent angle of vehicle lateral velocity divided by the longitudinal velocity. For sideslip angle control in a steady-state condition, the desired sideslip slip angle may be equal to zero as stated in [9, 12, 21, 24, 30, 40, 41], accordingly, achieving this condition or close enough to be equal to zero means enhancing vehicle's lateral stability. An empirical formula was developed by [42], to compute the maximum allowable or maximum sideslip angle based on the road coefficient of adhesion as shown in equation (2-14) as follows.

$$\beta_{\max} = \tan^{-1}(0.02\mu g) \tag{2-14}$$

The second control objective in yaw stability control is controlling the vehicle yaw rate. The main goal of the yaw rate control is to be capable to maintain the actual vehicle yaw rate follow or to be imminent enough to the desired yaw rate reference model which will augment and enhance the vehicle's manoeuvrability as referred in [13, 18, 19, 26, 28, 31, 43, 44]. Moreover, the desired yaw rate reference model is normally generated at the steady-state condition as mentioned in section (2.2.1). The desired yaw rate can be computed for two axles vehicle as follows in equation (2-15).

$$\mathrm{r_d} = \frac{\mathrm{U}}{(\mathrm{a}+\mathrm{b}) + \mathrm{K_{us}}\,\mathrm{U}^2}\cdot\delta \tag{2-15}$$

Where $\mathrm{K_{us}}$ stands for understeer coefficient and it is dependent on vehicle parameters as vehicle's mass, front, and rear tires cornering stiffnesses, distances from the front and rear axles to vehicle's CG and vehicle wheelbase and can be obtained using the following equation (2-16).

$$\mathrm{K_{us}} = \frac{\mathrm{m}\,(\mathrm{bC_r} - \mathrm{aC_f})}{(\mathrm{a}+\mathrm{b})\,\mathrm{C_r C_f}} \tag{2-16}$$

In addition, [42] proposed an empirical formula to compute the maximum yaw rate based on the longitudinal speed and the road coefficient of adhesion as shown as follows in equation (2-17).

$$\mathrm{r_{max}} = 0.85\frac{\mu\mathrm{g}}{\mathrm{u}} \tag{2-17}$$

In order to realize the control objective, it is crucial to control both the vehicle sideslip angle and yaw rate and be able to track the desired yaw rate reference model.

2.4 Active Chassis Control Systems

Active chassis control can be applied to the vehicle's longitudinal or lateral or vertical motion [3]. This study focuses on vehicle handling and lateral stability control. Various ACC strategies have been proposed to improve vehicle lateral dynamics in terms of controlling the yaw rate and vehicle sideslip angle. It is classified into three control strategies, which are Direct Yaw Moment Control (DYC), Active Steering Control (ASC) or an integration between both control systems [45] as shown in Figure 2-8.

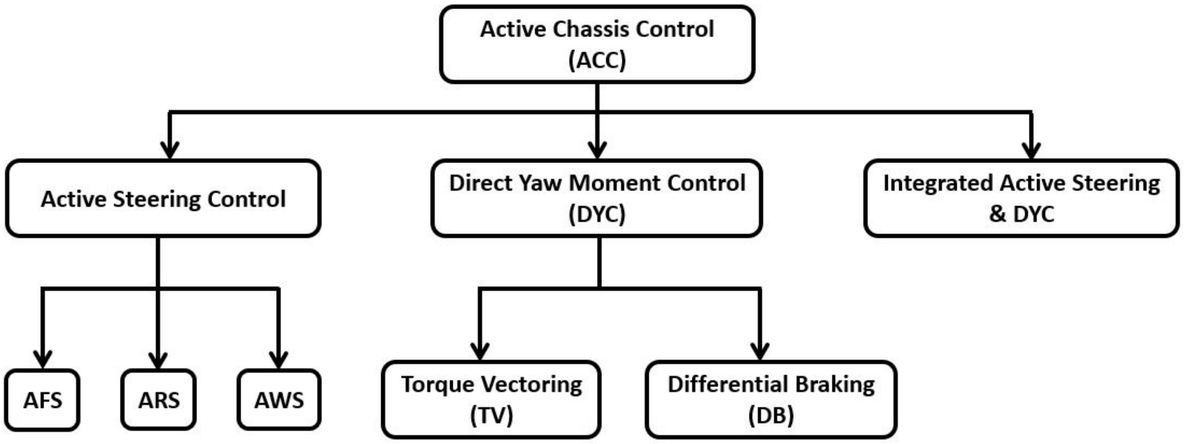

Figure 2-8 Active chassis control [4]

2.4.1 Active Steering Control (ASC)

Active steering control is considered as one of the ACC techniques to ensure vehicle yaw stability and enhance its handling and manoeuvrability behaviour at steady-state and transient condition. Extensive research studies have been conducted in this field as stated in [23, 26, 46-49]. Normally the active steering control is classified into three control allocation strategies, the first control strategy is, AFS where the designed controller interferes adding a corrective steer angle to the driver steer angle input, where this corrective steer angle computed by the controller based on the errors between the desired and actual vehicle sideslip angle and yaw rate as referred in [40, 50-53]. The second control strategy is, ARS where the designed controller steers only the rear axle wheels within limits. Generally, this limit does not exceed as far much as the front axle steer angle. while the last control strategy is AWS, where all the wheels are steerable based on the designed controller intervention as proposed in [37, 45, 54]. The difference between the three control strategies AFS, ARS and AWS are illustrated in Figure 2-9, Figure 2-10 and Figure 2-11 respectively as follows.

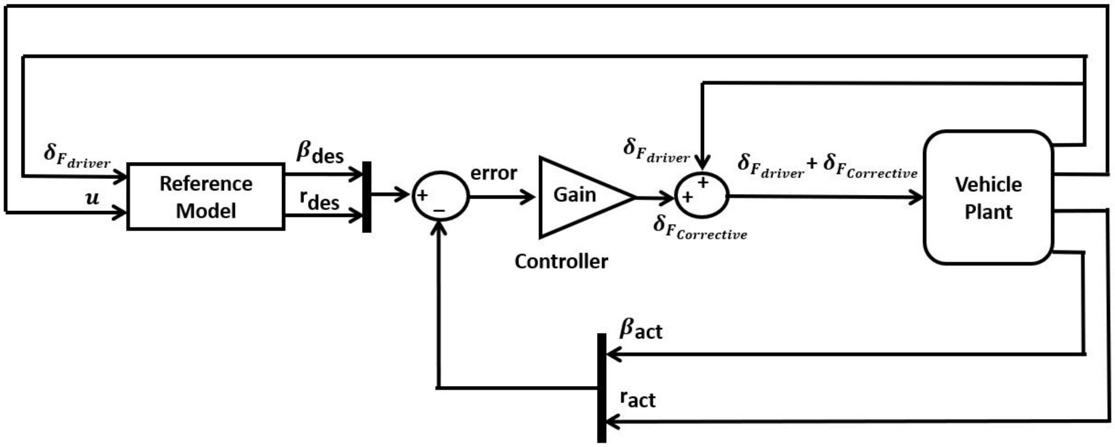

Figure 2-9 Active front steering control (AFS)

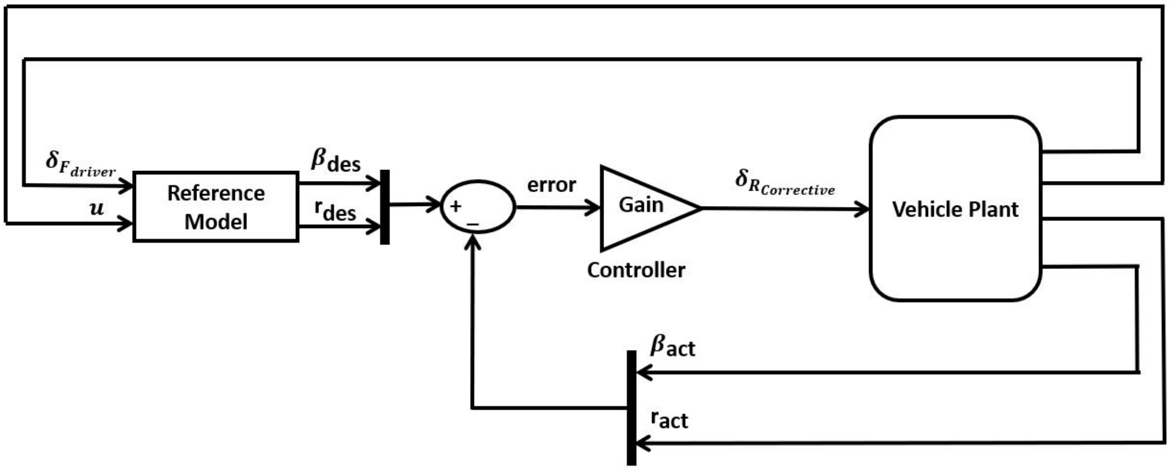

Figure 2-10 Active rear steering control (ARS)

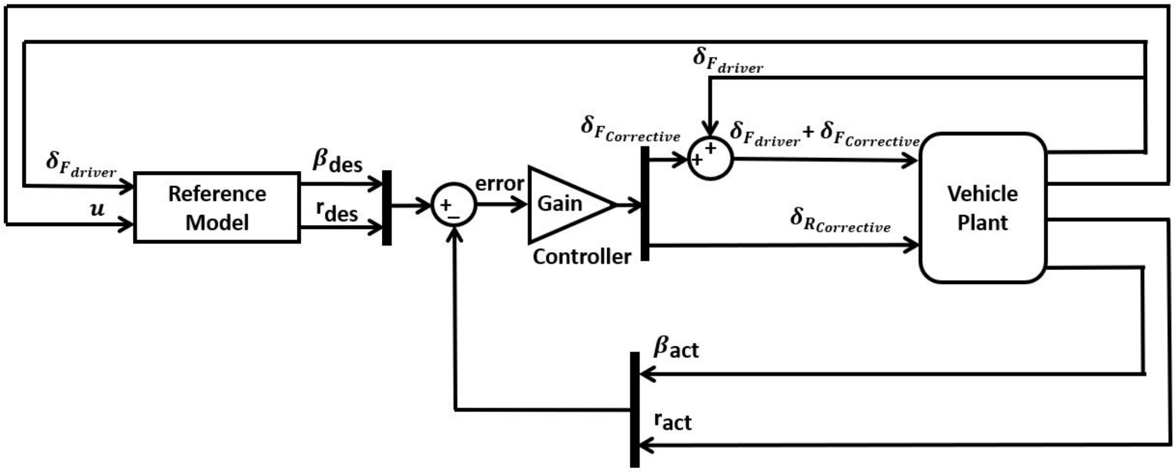

Figure 2-11 Active all wheel steering control (AWS)

In the case of AFS, the corrective front steer angle is considered to be the control input as it is added to the driver's steering input, while in the case of ARS the control input is the corrective rear steer angle. Furthermore, in the AWS control strategy the corrective front and rear steer angle are the control input. Accordingly, the state-space matrix form for all these three control strategies can be expressed simultaneously as in the following equations (2-18), (2-19) and (2-20).

$$\begin{bmatrix} \dot{\beta} \\ \dot{r} \end{bmatrix} = \begin{bmatrix} -\frac{C_{\alpha1}+C_{\alpha2}}{mu} & \frac{-aC_{\alpha1}+bC_{\alpha2}-mu^2}{mu^2} \\ \frac{bC_{\alpha2}-aC_{\alpha1}}{I_{zz}} & \frac{-a^2C_{\alpha1}-b^2C_{\alpha2}}{I_{zz}\,u} \end{bmatrix} \begin{bmatrix} \beta \\ r \end{bmatrix} + \begin{bmatrix} \frac{C_{\alpha1}}{mu} \\ \frac{aC_{\alpha1}}{I_{zz}} \end{bmatrix} (\delta_{F_{driver}} + \delta_{F_{Corrective}}) \tag{2-18}$$

$$\begin{bmatrix} \dot{\beta} \\ \dot{r} \end{bmatrix} = \begin{bmatrix} -\frac{C_{\alpha1}+C_{\alpha2}}{mu} & \frac{-aC_{\alpha1}+bC_{\alpha2}-mu^2}{mu^2} \\ \frac{bC_{\alpha2}-aC_{\alpha1}}{I_{zz}} & \frac{-a^2C_{\alpha1}-b^2C_{\alpha2}}{I_{zz}\,u} \end{bmatrix} \begin{bmatrix} \beta \\ r \end{bmatrix} + \begin{bmatrix} \frac{C_{\alpha1}}{mu} & \frac{C_{\alpha2}}{mu} \\ \frac{aC_{\alpha1}}{I_{zz}} & \frac{bC_{\alpha2}}{I_{zz}} \end{bmatrix} \begin{bmatrix} \delta_{F_{driver}} \\ \delta_{R_{Corrective}} \end{bmatrix} \tag{2-19}$$

$$\begin{bmatrix} \dot{\beta} \\ \dot{r} \end{bmatrix} = \begin{bmatrix} -\frac{C_{\alpha1}+C_{\alpha2}}{mu} & \frac{-aC_{\alpha1}+bC_{\alpha2}-mu^2}{mu^2} \\ \frac{bC_{\alpha2}-aC_{\alpha1}}{I_{zz}} & \frac{-a^2C_{\alpha1}-b^2C_{\alpha2}}{I_{zz}\,u} \end{bmatrix} \begin{bmatrix} \beta \\ r \end{bmatrix} + \begin{bmatrix} \frac{C_{\alpha1}}{mu} & \frac{C_{\alpha2}}{mu} \\ \frac{aC_{\alpha1}}{I_{zz}} & \frac{bC_{\alpha2}}{I_{zz}} \end{bmatrix} \begin{bmatrix} \delta_{F_{driver}} + \delta_{F_{Corrective}} \\ \delta_{R_{Corrective}} \end{bmatrix} \tag{2-20}$$

Generally, the AFS, ARS and AWS are dependent on tire lateral force, which behaves linearly at a small slip angle only in the linear region. at a low-speed cornering manoeuvre, the lateral acceleration is not high resulting in a small vehicle sideslip angle, therefore the active steering control can attain an adequate result in terms of vehicle handling and stability performance. However, near limit handling at high speed, the vehicle experiences higher lateral acceleration leading to a large vehicle sideslip angle, accordingly the tire exhibits nonlinear characteristics thus, the desired performance can not only be achieved by active steering control [55, 56].

2.4.2 Direct Yaw Moment Control

Various research studies have been conducted in yaw stability control utilizing direct yaw moment control with several allocation strategies techniques as stated in [9-12, 20, 21, 28-31, 38, 57]. The desired corrective moment needed to be generated by the controller is based on the difference between the desired vehicle sideslip angle and yaw rate from the reference model and the actual vehicle sideslip angle and yaw rate as shown in Figure 2-12. Based on the error, a desired corrective yaw moment is produced by coordination of selective wheel braking. Torque vectoring or active differential is a different control allocation strategy where the desired corrective yaw moment is produced by side-to-side torque distribution difference as implemented in [32, 33, 58, 59]. Moreover, a slip controller needs to be designed for each tire to prevent it from exceeding the slip peak ratio and maintain it to work at the maximum limit.

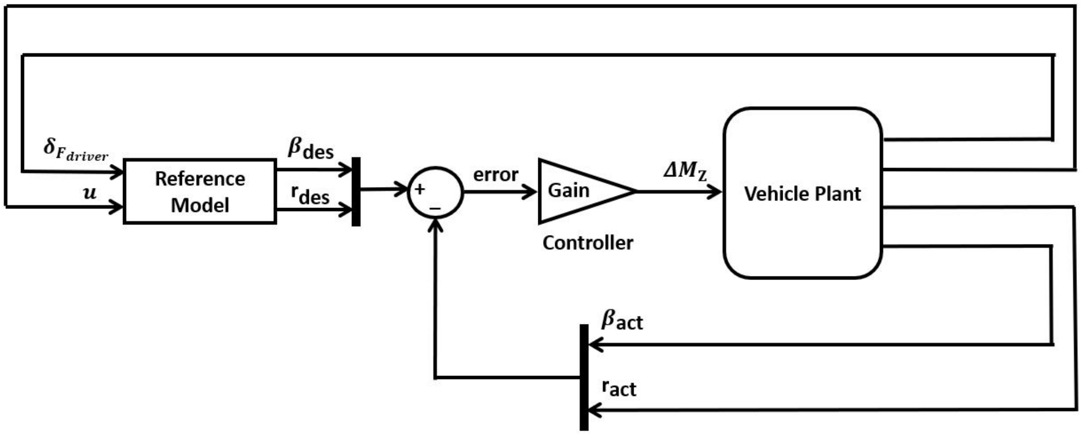

Figure 2-12 Direct yaw moment control (DYC)

The state-space matrix form for DYC is introduced as follows in equation (2-21), whereas M_Z represents the corrective yaw moment as an input to the lower control level.

$$\begin{bmatrix}\dot{\beta}\\ \dot{r}\end{bmatrix} = \begin{bmatrix} -\frac{C_{\alpha1}+C_{\alpha2}}{mu} & \frac{-aC_{\alpha1}+bC_{\alpha2}-mu^2}{mu^2} \\ \frac{bC_{\alpha2}-aC_{\alpha1}}{I_{zz}} & \frac{-a^2C_{\alpha1}-b^2C_{\alpha2}}{I_{zz}\,u}\end{bmatrix}\begin{bmatrix}\beta\\ r\end{bmatrix} + \begin{bmatrix}\frac{C_{\alpha1}}{mu}\\ \frac{aC_{\alpha1}}{I_{zz}}\end{bmatrix}\delta + \begin{bmatrix}0\\ \frac{1}{I_{zz}}\end{bmatrix}\Delta M_Z \qquad (2\text{-}21)$$

2.4.3 Integrated Active Chassis Control

In recent years active chassis control [3] has gradually become implemented on most vehicles in the market due to its great effect on improving vehicle handling performance as stated in [55].

The integration can be implemented by various chassis control strategies as active steering with DYC (active braking) or with active/semi-active suspension which improves vehicle handling performance or an integration of all these control strategies together as performed in [25, 36, 56, 60, 61]. In order to achieve the control objectives, sideslip motion can be controlled by generating sufficient lateral forces while yaw motion can be controlled by generating the desired yaw moment.

Hence the integration of active steering and DYC can realize this objective as implemented in [13, 14, 18, 22, 24, 56, 62-68]. This integration technique relies on providing a desired corrective yaw moment and steer angles as a control input to the vehicle based on the errors of the desired and actual sideslip and yaw rate motion as illustrated in Figure 2-13).

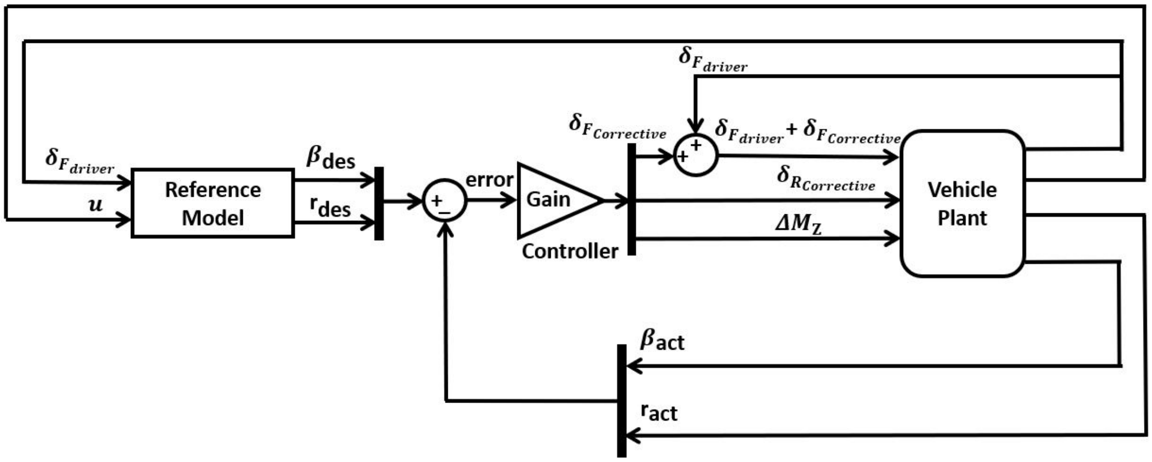

Figure 2-13 Integrated AWS-DYC

The state-space matrix form for the integrated AWS-DYC is expressed as follows in equation (2-22), while the control input for a lower controller level is the corrective front and rear steer angle and the corrective yaw moment.

$$\begin{bmatrix} \dot{\beta} \\ \dot{r} \end{bmatrix} = \begin{bmatrix} -\dfrac{C_{\alpha 1} + C_{\alpha 2}}{mu} & \dfrac{-aC_{\alpha 1} + bC_{\alpha 2} - mu^2}{mu^2} \\ \dfrac{bC_{\alpha 2} - aC_{\alpha 1}}{I_{zz}} & \dfrac{-a^2 C_{\alpha 1} - b^2 C_{\alpha 2}}{I_{zz}\, u} \end{bmatrix} \begin{bmatrix} \beta \\ r \end{bmatrix} + \begin{bmatrix} \dfrac{C_{\alpha 1}}{mu} & \dfrac{C_{\alpha 2}}{mu} & 0 \\ \dfrac{aC_{\alpha 1}}{I_{zz}} & \dfrac{bC_{\alpha 2}}{I_{zz}} & \dfrac{1}{I_{zz}} \end{bmatrix} \begin{bmatrix} \delta_{F_{driver}} + \delta_{F_{Corrective}} \\ \delta_{R_{Corrective}} \\ \Delta M_Z \end{bmatrix} \tag{2-22}$$

2.5 Control Allocation Strategies

This section will be discussing the numerous control allocation strategies that have been proposed in the past three decades based on each ACC system as described in section (2.4).

2.5.1 Active steering control (ASC) allocation strategy

As explained previously in section (2.4.1), ASC has been taken into attention by researchers in the past three decades. the evolution of ASC has started in 1986, by [69] introducing a control strategy to steer the rear wheels beside the front wheels. The objective of this study was to keep the sideslip angle at the vehicle centre of gravity to be zero known as vehicle zero side slip (ZSS). At low speed, the rear wheels exhibit counter phase while at the high-speed same phase (Parallel), which allows higher manoeuvrability at low speed and enhanced stability at high speed. However. it is not recommended that the steering control is activated over the whole speed range, because this will lead the vehicle to have a great tendency to understeer. Accordingly, designing two individual steering control systems for low and high speed is recommended to solve such a problem. Or different control technique should be adopted to steer all the front and rear wheels simultaneously in the meantime.

Later, [70] has proposed a robust control approach of AFS to enhance vehicle stability and prevent it from spinning by introducing the bifurcation concept, the study indicates that the vehicle behaves in instability manner due to reaching the saddle-node bifurcation which is strongly dependent on the rear tire lateral force saturation. $H\infty$ controller is designed to control the front wheel steer angle considering the uncertainties. Another robust AFS control technique has been introduced by [71] considering two linear models with 2-DOF (bicycle model) and 3-DOF to describe vehicle dynamics which are lateral, yaw and roll motion. $H\infty$ controller and μ-synthesis have been used considering the uncertainties, the simulation results in this study show the advantages and the improvements in vehicle performance when considering the roll motion especially when the vehicle suspensions are soft, which are fewer tracking errors, good ride quality, smaller gains obtained using 3DOF model and fewer oscillations compared to 2DOF model.

An AFS strategy using a feedforward and feedback H∞ controller conducted by [26]. A linear vehicle model has been used for synthesis analysis considering uncertainties due to the variations of road conditions and speed. [72] presented AFS control strategy based on a mixed H_2 norm and H_∞ norm controller (H_2/H_∞) to improve the vehicle handling performance. While [73] proposed a different control approach, where the proposed control technique seems to be more applicable, stated that in order to achieve controller more robustness under any driving condition, the designed controller has to be under any unstable conditions be able to transform the control information to an appropriate value range to tune the control output by a dependent degree. Consequently, a combination between $H_\infty/\text{extension}$ controller has been introduced. A comparison has been carried out between the proposed $(H_\infty/\text{extension})$ and (H_2/H_∞) controls, the results show that the proposed strategy can reduce the vehicle sideslip at a low coefficient of adhesion and the response time about 30 percent as a result, enhancement in vehicle handling performance can be achieved.

Even though AFS control has an advantage in preventing the vehicle from undesired yaw motion caused by uncertainties either due to driving or road conditions, the intervention of the AFS system can cause an unpleased impact on the driver's intentions. Accordingly, a trade-off between the control performance and the robustness needs to be compromised. as well as due to nonlinear tire characteristics, AFS becomes less effective when the lateral tire forces reach the limits of adhesion due to the variation of cornering stiffens especially at high speeds. Thus, ARS is introduced to compensate for saturation of the front tire lateral forces.

In 1986, Sano et al.[74] has introduced an ARS system as a function of front steering wheel angle and vehicle's speed, where at high speed the rear wheels steer were steered in the same direction as the front wheels and at low speeds they were steered in opposite direction as in [69]. Later, [75] conducted a robust feedback μ-synthesis ARS system. Another research study has been investigated in ARS by [76] using the H∞-μ synthesis technique to control sideslip angle. The proposed approach utilized the 2-DOF model, the controller is activated based on the sum of feedforward and feedback control variables. while a comparison has been carried out by [32] between two different chassis control actuators, which are active rear differential (ARD) and Active rear-wheel steering (ARS). In this study, a robust non-parametric approach has been used based on the internal model control technique based on H∞. The results show that the RWS achieved better performance than ARD in terms of preventing the vehicle from oversteer.

Multi-axle vehicles have been utilized in various fields, as in military domain and heavy commercial trucks. Because of many advantages that are possessed by these configurations, such as improving handling performance in terms of high steering capability in tight manoeuvres and also providing smoother ride over road irregularities. Furthermore, the loads are distributed on multiple axles which leads to enhancement in vehicle stability. Various studies have been conducted on multi-axle vehicle configurations as presented by [77] on a vehicle 6WS-6WD, where a 6WS control allocation strategy was implemented and compared to 2WS and 4WS modes. A 2-DOF linear model was used to describe the vehicle motion dynamics and for frequency analysis. The results show that a less lateral acceleration and sideslip angle were achieved by 6WS compared to 2WS and 4WS. [78] proposed an ARS control strategy for a 8 × 8 combat vehicle 6WS-8WD, where only the fourth axle wheels are actively steerable. A 2-DOF single track model was introduced in this study to express vehicle dynamics and also used for a comparison between using LQR and ZSS controller. The results show that the ZSS technique is only effective at low speed. Accordingly, the author recommended using both controllers separately where ZSS is activated at low speed while LQR at high speed. while later [79] performed a different control strategy for the same 8 × 8 combat vehicle model where all the rear wheels are actively steerable 8WS-8WD. The control structure of ARS is based on combining ZSS and LQR (ZSS-LQR) controllers to steer the third and fourth axle wheels independently to reduce the vehicle sideslip angle. The effectiveness of the proposed controller was evaluated based on standard test manoeuvres to investigate the vehicle handling performance at a steady and transient state. A comparison has been performed against vehicles without the controller and only active fourth axle wheel steering controller, where the results show an improvement achieved by the proposed controller with regard to minimizing the sideslip angle.

2.5.2 Direct yaw moment control allocation strategies

As discussed in section (2.4.2), all the implemented control allocation strategies rely on ACC. this section will be introducing the research studies in the past years that carried out utilizing direct yaw moment control (DYC) either by active differential or active braking.

In 1993, Huh et al. has introduced a new control strategy called "$\beta - \mathrm{Method}$", the proposed method aimed to control the yaw moment in proportion to vehicle longitudinal and lateral acceleration by means of controlling the tractive and braking forces [80]. A full range of motions has been established to describe vehicle characteristics in the nonlinear region and transient states in schematic representation based on vehicle sideslip angle β at its center of gravity and front-wheel steering angle as illustrated in Figure 2-14. The results show that the used technique can be greatly effective in improving vehicle performance at limit handling. Also controlling the distribution of tractive and braking force by using this method can lead to maximizing the tire lateral forces. Later, [81] studied generating corrective yaw moment by transversely torque distribution method on a vehicle 4WD equipped with continuously variable transmission (CVT) mechanism. The control allocation algorithm was implemented using proportional and integral control (PI) based on the yaw rate feedback reference model. Based on the simulation results improvements were achieved in terms of vehicle handling and manoeuvrability performance at high lateral acceleration and in energy loss compared to other differential torque transfer mechanisms. A different torque distribution control technique was introduced by [82] based on front to rear axles and left to right axle torque ratio. The front to rear distribution ratio is based on the actual and desired yaw rate (yaw error), while the left to right torque ratio is based on the desired and actual lateral acceleration (a_y error) using a PI controller. Although, [83] investigated a torque vectoring control strategy for active rear axle that is implemented on vehicle model equipped with a transfer case to control the front to rear torque distribution ratio. A sliding mode controller has been proposed to achieve the desired performance.

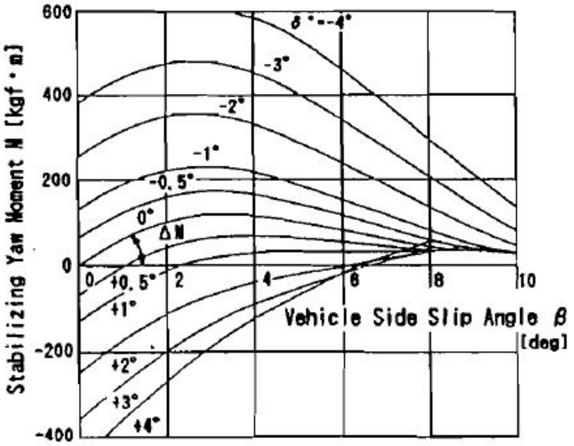

Figure 2-14 β-yaw moment diagram [80]

In 1999, Abe et al. introduced DYC obtained by sliding mode control (SMC), a non-linear tire model was developed to predict the sideslip angle β and to compute the corrective yaw moment generated by the controller [84]. The author mentioned that it is better to consider a sideslip response as a reference model than to adopt a yaw rate response as the reference model for the controller, due to the large side slip angle that can be induced when the rear tire lateral forces deteriorated. A hierarchical control strategy has been conducted by [85] for an electric vehicle in-wheel motor, where the upper-level controller is a PID controller to maintain the vehicle speed constant, while the lower level controller is adaptive sliding mode control (ASMC) to generate the corrective moment also s slip ratio controller is designed based on fuzzy logic control. A 7-DOF model and non-linear tire model have been used in this study. Based on the obtained results the vehicle sideslip angle has been reduced explicitly hence, a good vehicle handling performance was achieved.

An active braking control strategy was conducted to enhance vehicle performance in critical limit cornering by [86]. The author represented the effective range for each ACC system in form of vehicle friction circles for each system as illustrated in Figure 2-15 and based on that active braking was chosen to be control input in this study. The focus of the study was to investigate which wheel should be selected for braking in order to generate maximum corrective yaw moment. it was found that when a vehicle exhibits an extreme increase of sideslip angle at its centre of gravity, hence the rear wheels skid (oversteer). Consequently, the front outer wheel brake torque should be activated, in other words, an outward yaw moment is useful in such a case. However, the inward yaw moment is useful when front tires lateral forces reach the saturation limit (understeer) as demonstrated in Figure 2-16. Later, [87] proved which wheel should be selected to braking torque, to generate maximum corrective yaw moment needed based on various simulation tests on different road coefficients of adhesion. The results show that in case if the vehicle tends to spin (oversteer), thus the brake torque should be applied at the front outer wheel, where the maximum corrective yaw moment can be obtained. while in case if the vehicle tends to drift out (understeer) the torque brake should be applied at the rear inner wheel. One of the obtained results at dry and slippery road surface is shown in Figure 2-17 and Figure 2-18, demonstrate at which wheels the maximum corrective moment is obtained. The controller was used in this study to generate the corrective moment is H_∞.

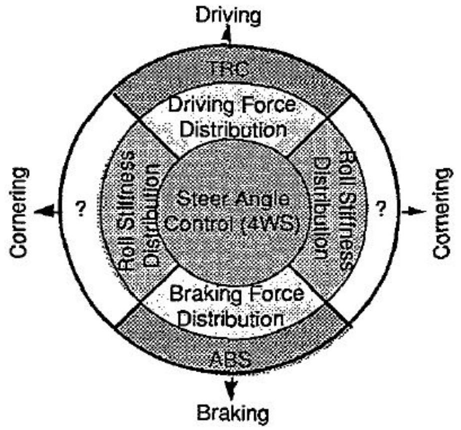

Figure 2-15 Effective range of each sub-control system in ACC [86]

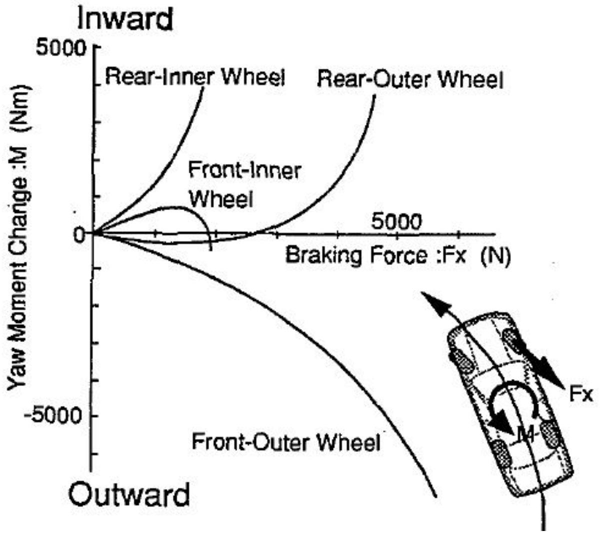

Figure 2-16 Change of corrective yaw moment by braking force for each wheel [86]

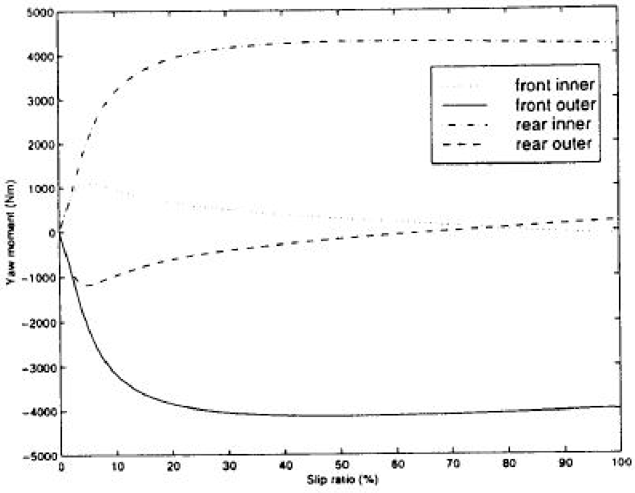

Figure 2-17 Corrective yaw moment versus slip ratio based on where brake torque is applied on a dry road [87]

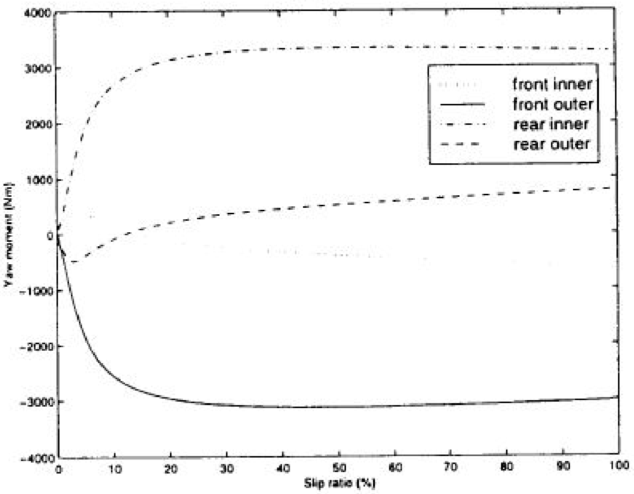

Figure 2-18 Corrective yaw moment versus slip ratio based on where brake torque is applied on a slippery road [87]

Another study has been conducted by [38] using gain schedule H_∞ control to obtain an optimal braking force needed to improve the vehicle's lateral stability. A supervisory of disturbance estimation is implemented based on driver steering input to guarantee the exact feed-forward yaw moment. While [88] proposed an electronic stability control (ESC) algorithm for 4 in-wheel electric vehicle. Three driving/braking torque distribution control strategies, the first strategy is equally distributed torque for each wheel in the same axle, the second strategy is, torque distributed on each axle based on the dynamic load on each tire, the third strategy is by using an optimization technique. An upper controller is designed to generate corrective yaw moment and Fuzzy logic PID controller is designed to control wheels' slip.

In 2005, Hancock et al. performed a comparison between two allocation strategies which are active differential and differential braking via a single design approach using Linear Quadratic Regulator Control (LQR) [89]. It was concluded that the control method prevented the tires from reaching the saturation limit and as a result, it can generate greater corrective yaw moment. As well as there would not be benefits of combining both systems, however, the coordination between the selection of braking wheels in active braking control strategy is easy to be implemented and could enhance the vehicle behaviour in critical driving scenarios if the coordination between the wheels is employed than only single wheel braking.

In general, there are several types of vehicle drivetrains such as front-wheel drive (FWD), rear-wheel drive (RWD) and all-wheel drive (AWD). It was recommended by [90] to apply right to left torque vectoring control to both front and rear wheels in case of AWD. However, to avoid complexity it's preferred to be applied to rear wheels. Figure 2-19 illustrates the vehicle dynamics limit for employing torque vectoring with front TV, rear TV and with front and rear TV.

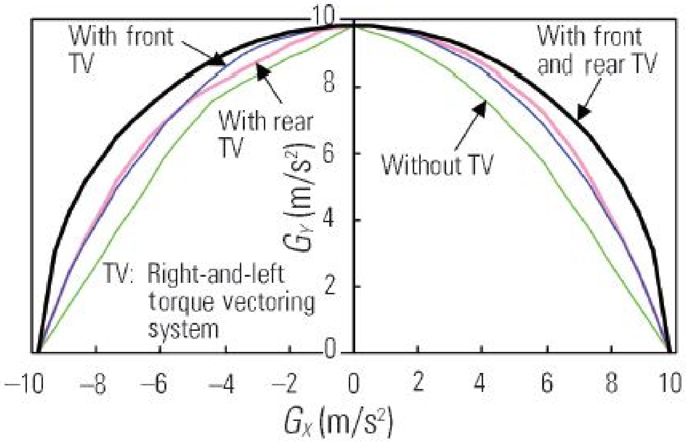

Figure 2-19 Vehicle dynamics limit with AWD [90]

Optimization methods have been used in many industry sectors, one of these sectors is the automotive industry. Many researchers have incorporated various optimization techniques (classical or metaheuristic) in order to obtain optimized tire forces that can enhance vehicle performance and save energy. One of these studies has been conducted by [91] by introducing a torque vectoring using a genetic fuzzy controller to distribute the desired torque left to right for each axle based on the normal load on each tire and PI controller has been designed for the desired front to rear torque distribution for an electric vehicle with in-wheel motors.

Also, one of the commonly used optimization-based controllers in the industry field is the Model Predictive Control (MPC) due to its simplicity to be designed and incorporate constraints on the control input and the given state variables, accordingly, [92] introduced a comparison between constrained MPC and un-constrained LQR control approach for an electric vehicle, applying torque vectoring only on the rear axle. The design of the controller is mainly based on the slip ratios of the rear axle tires, according to these ratios, the controller determines the needed torque to each wheel that maintain them below the slip ratio threshold. As well as a reference model at steady state is designed using a non-liner mathematical and tire vehicle model. the simulations results show that the MPC controller stabilized the vehicles faster than the LQR controller near limit of lateral acceleration, also [93] performed a comparison between using MPC and LQR in controlling yaw motion of four-wheel-drive vehicle (4WD) based on physical tire dynamics constraints, such as lateral and longitudinal tire forces limitations, tire nonlinearity behaviour and output torque limitations. The MPC controller results show better performance than LQR. The simulations have been carried out on different test manoeuvres such as DLC and step steering.

In 2015, Siampis et al. compared two different control strategies, the first proposed control strategy applied the torque vectoring on the rear wheels, while the second strategy was conducted by controlling the slip ratio for rear wheels [94]. The two control strategies were designed utilizing (MPC) and a nonlinear vehicle and tire model have been utilized to generate a reference model. The results showed that no notable difference between the two strategies except for much computational time for the first control strategy. As well as the results showed that constraining wheels' torque and combining both strategies give better results and enhance the vehicle limit handling. [95] introduced a torque vectoring control allocation using (MPC) for electric vehicle independent wheel drive. The proposed approach used a linear bicycle model for the selected vehicle, where a quadratic optimization problem is generated in each time step of the simulation to achieve the desired optimal torque distribution for each driving wheel to enhance the vehicle's handling behaviour. the results showed that the vehicle handling dynamics have been improved compared to uncontrolled vehicle especially, at low coefficient of friction.

For multi-axle vehicles DYC allocation strategies. [96] introduced an optimal torque vectoring allocation strategy for a vehicle 8WD/4WS to enhance vehicle handling behaviour. A hierarchical control structure has been designed, consists of upper-level control, to generate the desired corrective moment and optimal lower-level control to generates the optimal tire forces that satisfy tire friction ellipse. The wheels' torque distribution is based on the yaw rate and vehicle sideslip angle errors. Whereas [97] proposed an ESC control strategy for 8 electric driving motors in wheels. A hierarchical order incorporated a sliding mode control as an upper-level control, while an optimal lower-level control has been designed to generate an optimal driving and braking torque for 8 in-wheel electric motors. A multi-axle 8WD/4WS combat vehicle model has been investigated by [98], a PID controller was implemented to generate a corrective yaw moment by torque vectoring only on the rear two axles based on a 2-DOF linear model, later active braking integrated with ABS were employed on the same vehicle model to improve the vehicle handling and stability performance by [99].

2.5.3 Integrated chassis control allocation strategies

This section discusses the numerous control approaches in ICC that have been proposed in the past years. The reason behind the integration of multiple sub-system control is that each sub-system has its own effective range, for example, 4WS has been addressed by many research studies, however, at higher lateral acceleration and due to the non-linear tire characteristics, improvements of vehicle handling performance cannot be achieved due to the deterioration of cornering stiffness of the tire due to the saturation of tire lateral forces. Therefore the desired enhancements are limited at linear tire range, consequently integration of another sub-system as DYC can compensate this limitation in non-linear range. [86, 100] represented the effective ranges for each sub-system based on the tire fiction circle concept as demonstrated in Figure 2-20.

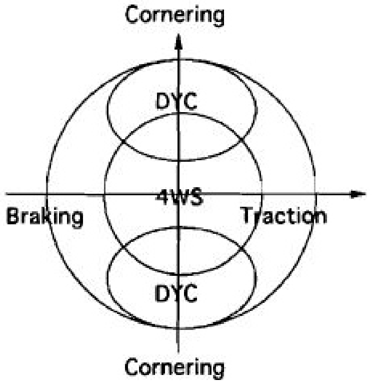

Figure 2-20 Effective areas of AWS and DYC [100]

Integration of multiple sub-systems as active steering, torque vectoring, differential braking and active suspension has evolved recently at different levels and each of these sub-systems has a different influence on enhancing vehicle performance in terms of handling, ride comfort and safety. However, intervention between these integrated sub-systems together considered to be a big challenge for the reason that it could lead to impair the vehicle performance. Accordingly, interventions and overlapping between these sub-systems should be avoided since they have different control actions in order to improve overall vehicle performance.

In general, ICC allocation strategy classified into two approaches, the first approach is centralized control structure (top-down) where the central or higher controller is in charge to make all control decision as illustrated in Figure 2-21, while the second approach is decentralized control structure (bottom-up) where each sub-system is controlled independently without communication to the other controllers. However, the coordination or the interaction with the other sub-systems could be realized by adding bus system between the controllers to perform the specific task [55] as shown in Figure 2-22.

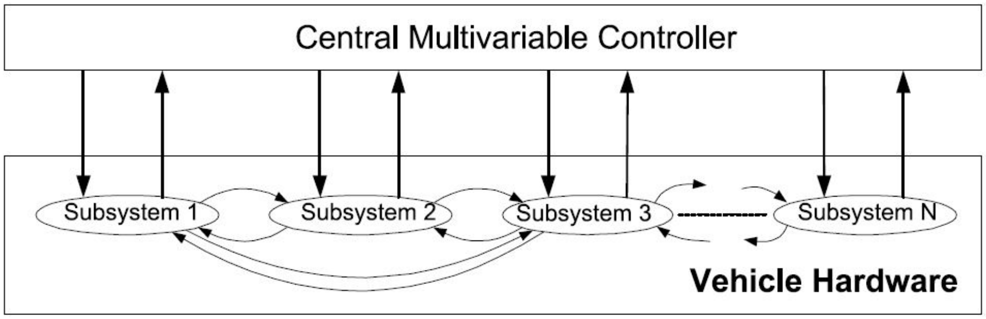

Figure 2-21 Centralized control structure (top-down) [101]

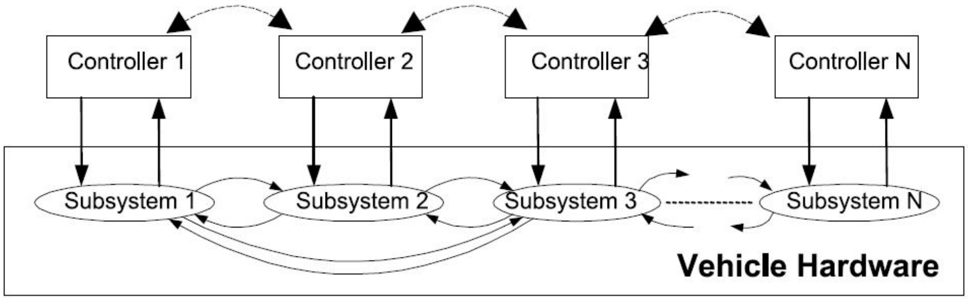

Figure 2-22 Decentralized control structure (bottom-up) [101]

The following sub-sections will be describing both approaches centralized and decentralized control allocation structures.

2.5.3.1 Centralized control allocation strategy

Most of the research studies that have been carried out on integrating active steering/ active braking adopt centralized control approach, the reason for that is, the implementation of both sub-systems can achieve the desired performance. However, the centralized control approach requires a powerful hardware controller due to the high computational effort needed to satisfy the control approach obligations [55].

One of the earliest studies that have investigated an integration between active steering and active braking was done by [102], where coordination between ARS and 4-wheel independently braking. A linear model is used to represent the vehicle dynamics and the coordination between ARS and active braking were achieved using a robust servomechanism controller to track the yaw rate, later, an AFS is integrated with braking force distribution were presented by [103] using model-matching control technique comprising a reference model is obtained based on ZSS rule based on ARS and a feedforward and feedback controllers. The results shows a great improvement in reducing vehicle sideslip angle, while, [104] integrated AFS and font braking forces distribution using fuzzy logic control (FLC) based on a 3-DOF vehicle model.

In 2013, Doumiati et al. proposed different control allocation by coordinating AFS with active rear braking [105]. The coordination was performed through gain scheduled linear parametric varying (LPV), the upper controller is designed to generate the corrective moment and corrective steering angle is H_∞, where AFS is only activated during normal driving condition while both actuators are implied near limit handling. Though, [14, 106] investigated a control allocation strategy via AFS/DB based on MPC, while, [62] used SMC.

However, [56] introduced a comparison between three different combinations of ICC which are DYC+AFS, DYC+ARS and DYC+AFS+ARS. The results show the superiority of combining the three sub-systems over DYC+AFS and DYC+ARS in terms of expanding the vehicle stability limit.

Integrating active roll control (ARC) in ICC can have an indirect effect in enhancing vehicle lateral stability especially at higher lateral acceleration, handling limit and rollover prevention. ARC can be integrated with coordination with ASC and DYC systems as introduced by [107, 108], 3-DOF model was used to describe vehicle dynamics which are lateral, yaw and roll motion, while the control structure consists of four sub-systems which are active steering, active differential, active braking and active roll control and a slip ratio controller is designed as lower control level. The coordination strategy between all these sub-systems is accomplished based on an FLC while the activation of all sub-control systems is based on multivariable vehicle states.

An optimal technique has been developed by [109] to compute and distribute tire tractive/ braking and cornering forces by optimization considering the road coefficient of adhesion limits, assuming all wheels can be driving, braking and steering. Based on vehicle yaw rate and sideslip angle feedback, equalities and un-equalities constraints have been established to provide the desired tire forces based on tire friction circle limit and corrective moment by dividing the controller into two control loops main and servo loop. However, [110] utilized quadratic programming optimization technique to obtain the desired forces using SMC as in the main loop while actuators action are considered by servo-loop.

For multi-axles vehicles, [111] introduced active middle axle wheel steering integrated with DYC for 6WS-6WD combat vehicles. The control structure based on SMC to generate the desired driving forces and corrective moment and a PI-speed controller, as well as a feed-forward controller is designed to compute the corrective middle steer wheel angle. The distribution of driving/braking forces is optimally determined based on the tire friction circle. The results show an improvement has been achieved in terms of vehicle handling performance, while [112] performed a TV integrated with ARS only for the fourth axle for a 6WS-8WD combat vehicle equipped with an electric powertrain. The upper controller is designed to generate the corrective yaw moment is $\mathrm{LPV}-\mathrm{H}_{\infty}$, while a feed-forward controller is implemented to determine the fourth axle corrective steering wheels angle. The coordination between both sub-control systems has been carried out utilizing a Gaussian distribution switching curve at different speed range to warrant a smooth collaboration.

2.5.3.2 Decentralized control allocation strategy

An integration of sub-control systems has been compared to the other two control allocation strategies without integration by [113] to assess the merits of each control system. the proposed three control strategies are ARS, DYC brake-based and AFS+ARS+DYC respectively using nonlinear predictive control. The results show that ARS is not effective during braking scenarios in cornering, DYC is capable to track the yaw rate reference model. However, it is not convenient to zero-side slip control while the integrated sub-systems control has achieved better performance than the other systems. [114] proposed coordination between AFS+DYC driving/braking based using two independent controllers SMC and phase plane method. AFS is activated in low to mid-range lateral acceleration while DYC at limit handling.

Multi sub-control systems have been implemented combining active aerodynamics (AAC), ARS, TV and semi-active suspension by [115], where the objective is to improve the vehicle's overall performance. LQR controller is designed to generate a corrective yaw moment and corrective rear steer angle, while the coordination between the sub-control systems is conducted utilizing a rule-based method. [116] integrated AFS, DYC and ARC using FLC and PID**,** while in [15, 36] utilized SMC.

Chapter 3 Multi-Wheeled Combat Vehicle Validation and Mathematical Modeling

This chapter introduces the validated TRUCKSIM vehicle model and all the vehicle's mathematical models developed for control design purposes, furthermore the reference yaw rate model.

3.1 TRUCKSIM Full Vehicle Model

A full vehicle model of 22 degrees of freedom (DOF) and non-linear measured tire manufacturer data is used for dynamic simulation. The vehicle's sprung mass has three rotational motions, roll, pitch, and yaw and three linear motion, surging, lurching, and bouncing, for a total of 6 DOF. The unsprung masses' motion, each wheel has two DOF spin and vertical motion, for a total of 16 DOF for 8 wheels. The TRUCKSIM vehicle model is developed based on the actual multi-wheeled combat vehicle as illustrated in Figure 3-1.


(a)

(b)

Figure 3-1 (a) actual combat vehicle model [1] and (b) TRUCKSIM vehicle mode [98]

The TRUCKSIM vehicle model was comprehensively validated and modeled by [117, 118] on various standard maneuver tests at different speeds. Moreover, the results obtained from software-in-loop simulation were compared against the actual combat vehicle experimental results in real life scenarios [119]. Hence, all the designed controllers on MATLAB & SIMULINK will be in co-simulation with this validated TRUCKSIM vehicle model to evaluate the controllers' effectiveness with respect to this full vehicle model.

Note: The relevant vehicle data and parameters can not be disclosed in this thesis as they are considered to be confidential.

3.2 Linear Mathematical Model for Active All Wheel Steering

A traditional bicycle vehicle model (single-track model) of 2-DOF is introduced to describe the lateral and yaw motion of the vehicle for LQR control design as shown in Figure 3-2. Several assumptions have been made to simplify the complexity of vehicle motion dynamics; the assumptions are as follows.

- Roll and pitch motion are ignored.
- Longitudinal vehicle dynamics are neglected.
- Vehicle tires behave linearly (in linear region).
- Aerodynamic and rolling resistance are neglected.
- Longitudinal speed of vehicle is constant.
- Lateral and longitudinal load transfer are neglected.
- The steering angle of the first, second, third and fourth axle is considered to be the average steering angle of the right and left wheels.
- A small angle approximation is considered in the derivation of the vehicle model.

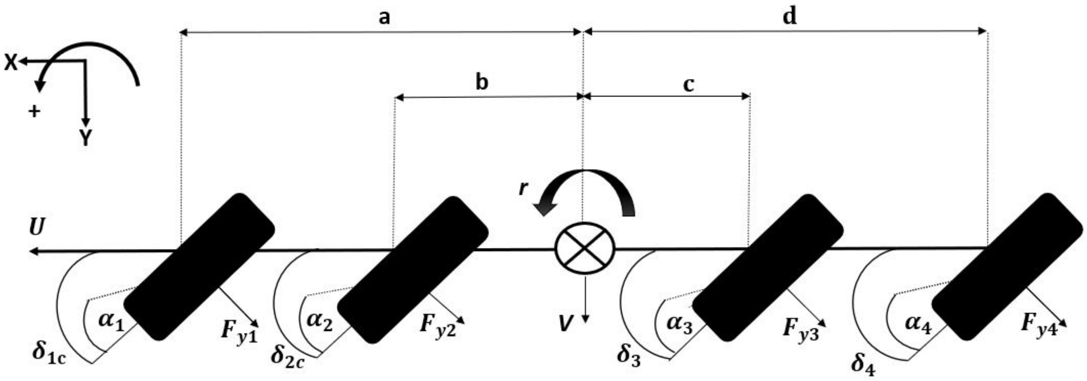

Figure 3-2 Bicycle model for multi-wheeled combat vehicle with Active-AWS

Equation of motion of two DOF bicycle model

$$\sum \mathrm{F_{yi}} = \mathrm{m}\left(\dot{\mathrm{V}} + \mathrm{ru}\right) \tag{3-1}$$

$$\mathrm{F_{y1}} + \mathrm{F_{y2}} + \mathrm{F_{y3}} + \mathrm{F_{y4}} = \mathrm{m}\left(\dot{\mathrm{V}} + \mathrm{ru}\right)$$

$$\sum M_Z = \mathrm{I_{ZZ}}\dot{\mathrm{r}} \tag{3-2}$$

$$\mathrm{aF_{y1}} + \mathrm{bF_{y2}} + \mathrm{cF_{y3}} + \mathrm{dF_{y4}} = \mathrm{I_{ZZ}}\dot{\mathrm{r}}$$

Where the lateral forces and slip angles of the linear mathematical model are calculated for each axle as follows.

$$\mathrm{F_{yi}} = \mathrm{C_{\alpha i}}\, \alpha_\mathrm{i} \tag{3-3}$$

$$\alpha_1 = \delta_{1c} - \left(\frac{\mathrm{V} + \mathrm{ra}}{\mathrm{u}}\right) \tag{3-4}$$

$$\alpha_2 = \delta_{2c} - \left(\frac{\mathrm{V} + \mathrm{rb}}{\mathrm{u}}\right) \tag{3-5}$$

$$\alpha_3 = \delta_3 - \left(\frac{\mathrm{V} - \mathrm{rc}}{\mathrm{u}}\right) \tag{3-6}$$

$$\alpha_4 = \delta_4 - \left(\frac{\mathrm{V} - \mathrm{rd}}{\mathrm{u}}\right) \tag{3-7}$$

Solving for Vehicle Lateral Motion Equation

By substituting and re-arranging equations (3-3) to (3-7) into equation (3-1) yields as follows.

$$\begin{aligned} &2\mathrm{C_{\alpha1}}\,\delta_{1c} + 2\mathrm{C_{\alpha2}}\,\delta_{2c} + 2\mathrm{C_{\alpha3}}\,\delta_3 + 2\mathrm{C_{\alpha4}}\,\delta_4 + \left[-2\mathrm{C_{\alpha1}} - 2\mathrm{C_{\alpha2}} - 2\mathrm{C_{\alpha3}} - 2\mathrm{C_{\alpha4}}\right]\frac{\mathrm{V}}{\mathrm{u}} \\ &+ \left[\frac{-2\mathrm{aC_{\alpha1}} - 2\mathrm{bC_{\alpha2}} + 2\mathrm{cC_{\alpha3}} + 2\mathrm{dC_{\alpha4}}}{\mathrm{U}}\right] r = \mathrm{m}\left(\dot{\mathrm{V}} + \mathrm{rU}\right) \end{aligned} \tag{3-8}$$

Now divide both sides by m yields as follows

$$\begin{aligned} &\frac{2\mathrm{C_{\alpha1}}}{\mathrm{m}}\,\delta_{1c} + \frac{2\mathrm{C_{\alpha2}}}{\mathrm{m}}\,\delta_{2c} + \frac{2\mathrm{C_{\alpha3}}}{\mathrm{m}}\,\delta_3 + \frac{2\mathrm{C_{\alpha4}}}{\mathrm{m}}\,\delta_4 + \left[\frac{-2\mathrm{C_{\alpha1}} - 2\mathrm{C_{\alpha2}} - 2\mathrm{C_{\alpha3}} - 2\mathrm{C_{\alpha4}}}{\mathrm{m}}\right]\frac{\mathrm{V}}{\mathrm{u}} \\ &+ \left[\frac{-2\mathrm{aC_{\alpha1}} - 2\mathrm{bC_{\alpha2}} + 2\mathrm{cC_{\alpha3}} + 2\mathrm{dC_{\alpha4}}}{\mathrm{m\,u}}\right]\mathrm{r} = \left(\dot{\mathrm{V}} + \mathrm{ru}\right) \end{aligned} \tag{3-9}$$

Then isolating for $\dot{\mathrm{V}}$ yields as follows

$$\begin{aligned} &\frac{2\mathrm{C_{\alpha1}}}{\mathrm{m}}\,\delta_{1c} + \frac{2\mathrm{C_{\alpha2}}}{\mathrm{m}}\,\delta_{2c} + \frac{2\mathrm{C_{\alpha3}}}{\mathrm{m}}\,\delta_3 + \frac{2\mathrm{C_{\alpha4}}}{\mathrm{m}}\,\delta_4 + \left[\frac{-2\mathrm{C_{\alpha1}} - 2\mathrm{C_{\alpha2}} - 2\mathrm{C_{\alpha3}} - 2\mathrm{C_{\alpha4}}}{\mathrm{m}}\right]\frac{\mathrm{V}}{\mathrm{u}} \\ &+ \left[\frac{-2\mathrm{aC_{\alpha1}} - 2\mathrm{bC_{\alpha2}} + 2\mathrm{cC_{\alpha3}} + 2\mathrm{dC_{\alpha4}} - \mathrm{mU^2}}{\mathrm{m\,u}}\right]\mathrm{r} = \dot{\mathrm{V}} \end{aligned} \tag{3-10}$$

By dividing both sides by U, will yield the final equation for vehicle lateral motion as follows.

$$\begin{aligned}\left(\frac{2C_{\alpha1}}{mu}\right)\delta_{1c} + \left(\frac{2C_{\alpha2}}{mu}\right)\delta_{2c} + \left(\frac{2C_{\alpha3}}{mu}\right)\delta_3 + \left(\frac{2C_{\alpha4}}{mu}\right)\delta_4 & \\ + \left[\frac{-2C_{\alpha1} - 2C_{\alpha2} - 2C_{\alpha3} - 2C_{\alpha4}}{mU}\right]\frac{V}{u} & \\ + \left[\frac{-2aC_{\alpha1} - 2bC_{\alpha2} + 2cC_{\alpha3} + 2dC_{\alpha4} - mU^2}{mu^2}\right]r = \frac{\dot{V}}{u} &\end{aligned} \tag{3-11}$$

Solving for Vehicle Yaw Motion Equation

By substituting and re-arranging equations (3-3) to (3-7) into equation (3-2) yields as follows.

$$\begin{aligned}2aC_{\alpha1}\delta_{1c} + 2bC_{\alpha2}\delta_{2c} - 2c\,C_{\alpha3}\delta_3 - 2dC_{\alpha4}\delta_4 & \\ + [-2aC_{\alpha1} - 2bC_{\alpha2} + 2cC_{\alpha3} + 2dC_{\alpha4}]\frac{V}{u} & \\ + \left[\frac{-2a^2C_{\alpha1} - 2\,b^2\,C_{\alpha2} - 2c^2C_{\alpha3} - 2d^2C_{\alpha4}}{u}\right]r = I_{ZZ}\dot{r} &\end{aligned} \tag{3-12}$$

By dividing both sides by I_{ZZ}, will yield the final equation for vehicle yaw motion as follows.

$$\begin{aligned}\left(\frac{2aC_{\alpha1}}{I_{ZZ}}\right)\delta_{1c} + \left(\frac{2bC_{\alpha2}}{I_{ZZ}}\right)\delta_{2c} - \left(\frac{2c\,C_{\alpha3}}{I_{ZZ}}\right)\delta_3 - \left(\frac{2dC_{\alpha4}}{I_{ZZ}}\right)\delta_4 & \\ + \left[\frac{-2aC_{\alpha1} - 2bC_{\alpha2} + 2cC_{\alpha3} + 2dC_{\alpha4}}{I_{ZZ}}\right]\frac{V}{U} & \\ + \left[\frac{-2a^2C_{\alpha1} - 2\,b^2\,C_{\alpha2} - 2c^2C_{\alpha3} - 2d^2C_{\alpha4}}{I_{ZZ}u}\right]r = \dot{r} &\end{aligned} \tag{3-13}$$

By re-arranging equations (3-11) and (3-13) into state-space equations form((3-14) and (3-15)), the LQR vehicle plant model yielded as follows in equations (3-16) and (3-17).

$$\dot{X} = AX + BU \tag{3-14}$$

$$Y = CX + DU \tag{3-15}$$

$$\dot{X} = \begin{bmatrix}\dot{\beta}\\ \dot{r}\end{bmatrix} = \begin{bmatrix} \left[\dfrac{-2C_{\alpha1} - 2C_{\alpha2} - 2C_{\alpha3} - 2C_{\alpha4}}{mu}\right] & \left[\dfrac{-2aC_{\alpha1} - 2bC_{\alpha2} + 2cC_{\alpha3} + 2dC_{\alpha4} - mu^2}{mu^2}\right] \\ \left[\dfrac{-2aC_{\alpha1} - 2bC_{\alpha2} + 2cC_{\alpha3} + 2dC_{\alpha4}}{I_{ZZ}}\right] & \left[\dfrac{-2a^2C_{\alpha1} - 2\,b^2\,C_{\alpha2} - 2c^2C_{\alpha3} - 2d^2C_{\alpha4}}{I_{ZZ}U}\right] \end{bmatrix} \begin{bmatrix}\beta\\ r\end{bmatrix} + \begin{bmatrix} \left(\dfrac{2C_{\alpha1}}{mu}\right) & \left(\dfrac{2C_{\alpha2}}{mu}\right) & \left(\dfrac{2C_{\alpha3}}{mu}\right) & \left(\dfrac{2C_{\alpha4}}{mu}\right) \\ \left(\dfrac{2aC_{\alpha1}}{I_{ZZ}}\right) & \left(\dfrac{2bC_{\alpha2}}{I_{ZZ}}\right) & -\left(\dfrac{2c\,C_{\alpha3}}{I_{ZZ}}\right) & -\left(\dfrac{2dC_{\alpha4}}{I_{ZZ}}\right) \end{bmatrix} \begin{bmatrix}\delta_{1c}\\ \delta_{2c}\\ \delta_3\\ \delta_4\end{bmatrix} \tag{3-16}$$

$$Y = \begin{bmatrix}1 & 0\\ 0 & 1\end{bmatrix}\begin{bmatrix}\beta\\ r\end{bmatrix} + \begin{bmatrix}0 & 0 & 0 & 0\\ 0 & 0 & 0 & 0\end{bmatrix}\begin{bmatrix}\delta_{1c}\\ \delta_{2c}\\ \delta_3\\ \delta_4\end{bmatrix} \tag{3-17}$$

3.3 Linear Mathematical Model for Direct Yaw Moment Control

A 2-DOF linear mathematical vehicle model is derived to represent the vehicle's lateral and yaw motion for LQR control design as shown in Figure 3-3. Some assumptions have been assumed to simplify the vehicle's dynamics complexity; the assumptions are as follows.

- Roll and pitch motion are ignored.
- Longitudinal vehicle dynamics are neglected.
- Vehicle tires behave linearly (in linear region).
- Aerodynamic and rolling resistance are neglected.
- Longitudinal speed of vehicle is constant.
- Lateral and longitudinal load transfer are neglected.
- The steering angle of the first axle is considered to be the average steering angle of the right and left wheels.
- The steering angle of the second axle is represented by ratio function of first axle steering angle $\delta_2 = K_{2-1}\,\delta_1$.
- A small angle approximation is considered in the derivation of the vehicle model.

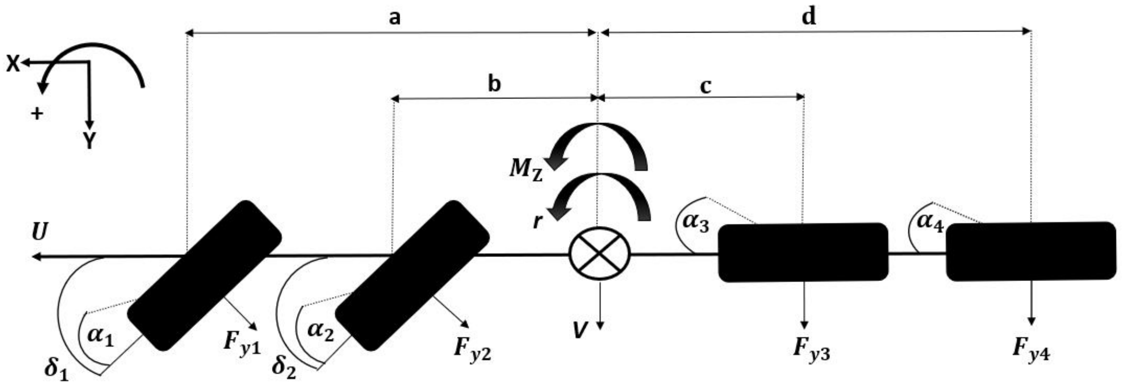

Figure 3-3 Bicycle model for multi-wheeled combat vehicle with DYC

Equation of motion of two DOF bicycle model for DYC

$$\sum F_{yi} = m\left(\dot{V} + ru\right) \tag{3-18}$$

$$F_{y1} + F_{y2} + F_{y3} + F_{y4} = m\left(\dot{V} + ru\right)$$

$$\sum M_Z = I_{ZZ}\dot{r} \tag{3-19}$$

$$aF_{y1} + bF_{y2} + cF_{y3} + dF_{y4} + M_Z = I_{ZZ}\dot{r}$$

Where the lateral forces and slip angles of the bicycle model are computed for each axle as follows.

$$F_{yi} = C_{\alpha i}\,\alpha_i \tag{3-20}$$

$$\alpha_1 = \delta_1 - \left(\frac{V + ra}{u}\right) \tag{3-21}$$

$$\alpha_2 = \delta_2 - \left(\frac{V + rb}{u}\right) \tag{3-22}$$

$$\alpha_3 = -\left(\frac{V - rc}{u}\right) \tag{3-23}$$

$$\alpha_4 = -\left(\frac{V - rd}{u}\right) \tag{3-24}$$

The average steering angle of the second axle can be expressed as a ratio of the average steering angle of the first axle according to Ackerman steering geometry [78, 112, 120] as follows.

$$\delta_2 = K_{2-1}\,\delta_1 \tag{3-25}$$

Solving for Vehicle Lateral Motion Equation

By substituting and re-arranging equations (3-20) to (3-25) into equation (3-18) yields as follows.

$$\begin{aligned}(2C_{\alpha1} + K_{2-1}2C_{\alpha2})\delta_1 + [-2C_{\alpha1} - 2C_{\alpha2} - 2C_{\alpha3} - 2C_{\alpha4}]\frac{V}{u} \\ + \left[\frac{-2aC_{\alpha1} - 2bC_{\alpha2} + 2cC_{\alpha3} + 2dC_{\alpha4}}{u}\right] r = m\left(\dot{V} + ru\right)\end{aligned} \tag{3-26}$$

Divide both sides by m.

$$\begin{aligned}\left(\frac{2C_{\alpha1} + 2\,K_{2-1}C_{\alpha2}}{m}\right)\delta_1 + \left[\frac{-2C_{\alpha1} - 2C_{\alpha2} - 2C_{\alpha3} - 2C_{\alpha4}}{m}\right]\frac{V}{u} \\ + \left[\frac{-2aC_{\alpha1} - 2bC_{\alpha2} + 2cC_{\alpha3} + 2dC_{\alpha4}}{mu}\right] r = \left(\dot{V} + ru\right)\end{aligned} \tag{3-27}$$

Now, isolate for $\dot{V}$

$$\begin{aligned}\left(\frac{2C_{\alpha1} + 2\,K_{2-1}C_{\alpha2}}{m}\right)\delta_1 + \left[\frac{-2C_{\alpha1} - 2C_{\alpha2} - 2C_{\alpha3} - 2C_{\alpha4}}{m}\right]\frac{V}{u} \\ + \left[\frac{-2aC_{\alpha1} - 2bC_{\alpha2} + 2cC_{\alpha3} + 2dC_{\alpha4} - mU^2}{mu}\right] r = \dot{V}\end{aligned} \tag{3-28}$$

By dividing both sides by u, will yield the final equation for vehicle lateral motion as follows.

$$\begin{aligned}\left(\frac{2C_{\alpha1} + 2\,K_{2-1}C_{\alpha2}}{mu}\right)\delta_1 + \left[\frac{-2C_{\alpha1} - 2C_{\alpha2} - 2C_{\alpha3} - 2C_{\alpha4}}{mu}\right]\frac{V}{u} \\ + \left[\frac{-2aC_{\alpha1} - 2bC_{\alpha2} + 2cC_{\alpha3} + 2dC_{\alpha4} - mU^2}{mu^2}\right] r = \frac{\dot{V}}{u}\end{aligned} \tag{3-29}$$

Solving for Vehicle Yaw Motion Equation

By substituting and re-arranging equations (3-20) to (3-25) into equations (3-19) yields as follows.

$$\begin{aligned}(2aC_{\alpha1} + 2b\,K_{2-1}C_{\alpha2})\delta_1 + [-2aC_{\alpha1} - 2bC_{\alpha2} + 2cC_{\alpha3} + 2dC_{\alpha4}]\frac{V}{u} \\ + \left[\frac{-2a^2C_{\alpha1} - 2b^2C_{\alpha2} - 2c^2C_{\alpha3} - 2d^2C_{\alpha4}}{u}\right] r + M_Z = I_{ZZ}\dot{r}\end{aligned} \tag{3-30}$$

By dividing both sides by I_{ZZ}, will yield the final equation for vehicle yaw motion as follows.

$$\left(\frac{2aC_{\alpha1} + 2b\,K_{2-1}C_{\alpha2}}{I_{ZZ}}\right)\delta_1 + \left[\frac{-2aC_{\alpha1} - 2bC_{\alpha2} + 2cC_{\alpha3} + 2dC_{\alpha4}}{I_{ZZ}}\right]\frac{V}{u} + \left[\frac{-2a^2C_{\alpha1} - 2b^2C_{\alpha2} - 2c^2C_{\alpha3} - 2d^2C_{\alpha4}}{I_{ZZ}u}\right]r + \frac{1}{I_{ZZ}}M_Z = \dot{r} \tag{3-31}$$

By re-arranging equations (3-29) and (3-31) into state-space equations form ((3-14) and (3-15)), the LQR vehicle plant model yielded as follows in equations (3-32) and (3-33).

$$\dot{X} = \begin{bmatrix}\dot{\beta}\\ \dot{r}\end{bmatrix} = \begin{bmatrix} \left[\frac{-2C_{\alpha1} - 2C_{\alpha2} - 2C_{\alpha3} - 2C_{\alpha4}}{mu}\right] & \left[\frac{-2aC_{\alpha1} - 2bC_{\alpha2} + 2cC_{\alpha3} + 2dC_{\alpha4} - mu^2}{mu^2}\right] \\ \left[\frac{-2aC_{\alpha1} - 2bC_{\alpha2} + 2cC_{\alpha3} + 2dC_{\alpha4}}{I_{ZZ}}\right] & \left[\frac{-2a^2C_{\alpha1} - 2\,b^2\,C_{\alpha2} - 2c^2C_{\alpha3} - 2d^2C_{\alpha4}}{I_{ZZ}u}\right] \end{bmatrix} \begin{bmatrix}\beta\\ r\end{bmatrix} + \begin{bmatrix} \left(\frac{2C_{\alpha1} + 2\,K_{2-1}C_{\alpha2}}{mu}\right) & 0 \\ \left(\frac{2aC_{\alpha1} + 2b\,K_{2-1}C_{\alpha2}}{I_{ZZ}}\right) & \frac{1}{I_{ZZ}} \end{bmatrix} \begin{bmatrix}\delta_1\\ M_Z\end{bmatrix} \tag{3-32}$$

$$Y = \begin{bmatrix}1 & 0\\ 0 & 1\end{bmatrix}\begin{bmatrix}\beta\\ r\end{bmatrix} + \begin{bmatrix}0 & 0\\ 0 & 0\end{bmatrix}\begin{bmatrix}\delta_1\\ M_Z\end{bmatrix} \tag{3-33}$$

3.4 Reference Yaw Rate Model

To enhance the vehicle's stability and maneuverability, the controlled vehicle's yaw rate and sideslip angle should follow the desired values. Therefore, the bicycle model is adopted to generate the reference model at steady state, where $\dot{\beta} = \dot{r} = 0$ as follows.

$$0 = \begin{bmatrix}A_{11} & A_{12}\\ A_{21} & A_{22}\end{bmatrix}\begin{bmatrix}\beta\\ r\end{bmatrix} + \begin{bmatrix}B_{11}\\ B_{21}\end{bmatrix}\delta_1 \tag{3-34}$$

Where, $A_{11} = \left[\frac{-2C_{\alpha1}-2C_{\alpha2}-2C_{\alpha3}-2C_{\alpha4}}{mu}\right]$, $A_{12} = \left[\frac{-2aC_{\alpha1}- 2bC_{\alpha2}+ 2cC_{\alpha3}+ 2dC_{\alpha4}-mu^2}{mu^2}\right]$

$A_{21} = \left[\frac{-2aC_{\alpha1}-2bC_{\alpha2}+2cC_{\alpha3}+2dC_{\alpha4}}{I_{ZZ}}\right]$, $A_{22} = \left[\frac{-2a^2C_{\alpha1}- 2\,b^2\,C_{\alpha2}-2c^2C_{\alpha3}- 2d^2C_{\alpha4}}{I_{ZZ}u}\right]$

$B_{11} = \left(\frac{2C_{\alpha1}+2\,K_{2-1}C_{\alpha2}}{mu}\right)$ and $B_{21} = \left(\frac{2aC_{\alpha1}+2b\,K_{2-1}C_{\alpha2}}{I_{ZZ}}\right)$

Isolate for $\begin{bmatrix}\beta\\ \mathrm{r}\end{bmatrix}$ as follows.

$$\begin{bmatrix}\beta\\ \mathrm{r}\end{bmatrix}=\begin{bmatrix}\mathrm{A}_{11} & \mathrm{A}_{12}\\ \mathrm{A}_{21} & \mathrm{A}_{22}\end{bmatrix}^{-1}\begin{bmatrix}-\mathrm{B}_{11}\\ -\mathrm{B}_{21}\end{bmatrix}\delta_1 \tag{3-35}$$

After algebraic manipulation will yield at steady state the desired vehicle side slip angle and desired yaw response as follows.

$$\begin{bmatrix}\beta_{\mathrm{ss}}\\ \mathrm{r}_{\mathrm{ss}}\end{bmatrix}=\begin{bmatrix}\dfrac{(\mathrm{A}_{12}\mathrm{B}_{21})-(\mathrm{A}_{22}\mathrm{B}_{11})}{(\mathrm{A}_{11}\mathrm{A}_{22})-(\mathrm{A}_{12}\mathrm{A}_{21})}\\ \dfrac{(\mathrm{A}_{21}\mathrm{B}_{11})-(\mathrm{A}_{11}\mathrm{B}_{21})}{(\mathrm{A}_{11}\mathrm{A}_{22})-(\mathrm{A}_{12}\mathrm{A}_{21})}\end{bmatrix}\delta_1 \tag{3-36}$$

By isolating for β_{ss} and r_{ss} the final equations are as follows.

$$\beta_{\mathrm{ss}}=\left[\frac{(\mathrm{A}_{12}\mathrm{B}_{21})-(\mathrm{A}_{22}\mathrm{B}_{11})}{(\mathrm{A}_{11}\mathrm{A}_{22})-(\mathrm{A}_{12}\mathrm{A}_{21})}\right]\delta_1 \tag{3-37}$$

$$\mathrm{r}_{\mathrm{ss}}=\left[\frac{(\mathrm{A}_{21}\mathrm{B}_{11})-(\mathrm{A}_{11}\mathrm{B}_{21})}{(\mathrm{A}_{11}\mathrm{A}_{22})-(\mathrm{A}_{12}\mathrm{A}_{21})}\right]\delta_1 \tag{3-38}$$

Although, the reference model generates the vehicle's yaw rate and sideslip angle at steady state based on the steering input and longitudinal speed. These values need to be constrained based on the driving condition. Hence, [42] developed an empirical relationship to compute the desired vehicle's yaw rate and sideslip. Therefore, the desired yaw rate response and desired vehicle sideslip angle are limited and bounded (Max and Min) by these empirical formulas as presented in equations (3-39) and (3-40).

$$\mathrm{r}_{\mathrm{ss,constrained}}=0.85\frac{\mu\mathrm{g}}{\mathrm{u}} \tag{3-39}$$

$$\beta_{\mathrm{ss,constrained}}=\tan^{-1}(0.02\mu\mathrm{g}) \tag{3-40}$$

The $\mathrm{r}_{\mathrm{ss,constrained}}$ and $\beta_{\mathrm{ss,constrained}}$ prohibit the yaw rate and sideslip angle obtained at steady state from exceeding the desired limit based on the driving condition such as coefficient of friction and speed.

However, the desired vehicle sideslip is set to be equal zero for both control strategies Active-AWS and DYC in all simulations as its recommended based on the literature review.

Note: a time delay of first order has been incorporated to only the reference model of Active-AWS control strategy. This time delay (τ_{delay}) is set to be equal 0.3 seconds. The time delay permits the yaw rate response at steady state to be retarded as follows.

$$\mathrm{r}_{\mathrm{des,constrained}} = \frac{1}{\tau_{\mathrm{delay}}\mathrm{S} + 1}\mathrm{r}_{\mathrm{ss}} \qquad (3\text{-}41)$$

3.5 Linear Mathematical Model for Semi-Active Suspension

An 11-DOF linear mathematical model is presented to describe the motion of the multi-wheeled combat vehicle's sprung and unsprung masses for the LQR control design's purpose. The vehicle's sprung mass has 3-DOF which are heave, pitch, and roll motions, while the unsprung masses each have 1-DOF, the vertical translational motion (bounce) with respect to sprung mass for a total 8-DOF as shown in Figure 3-4.

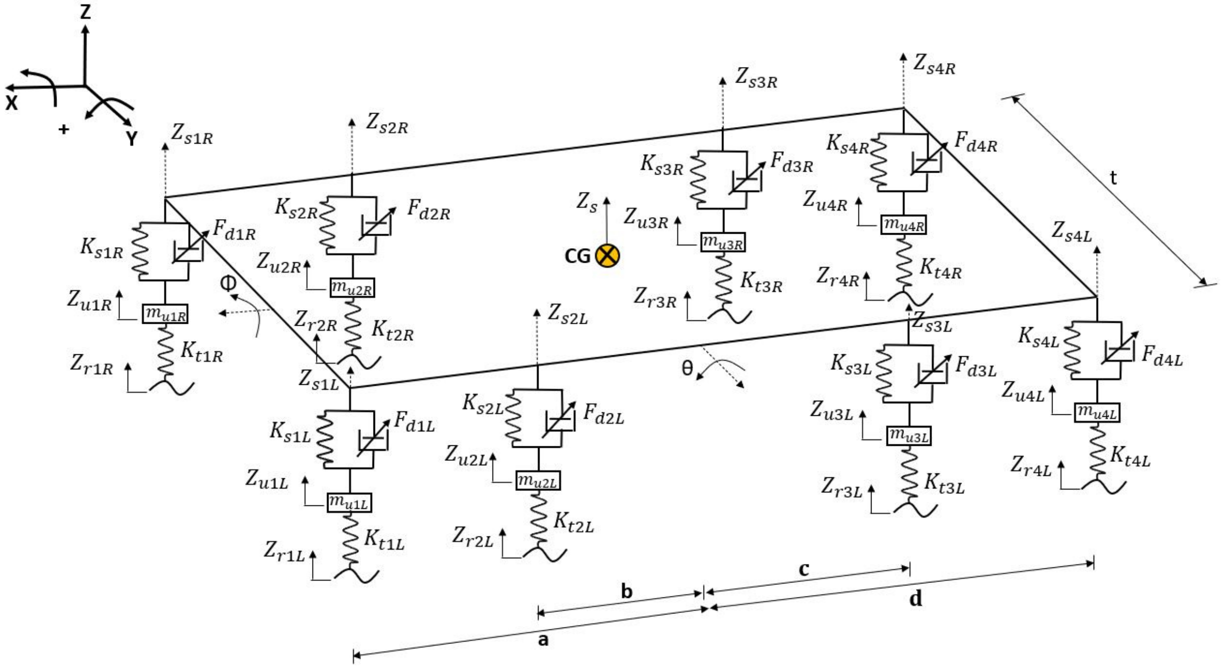

Figure 3-4 Multi-wheeled combat vehicle of 11-DOF with semi-active suspension

Some assumptions have been assumed to simplify the complexity of the derivation of the vehicle model; these assumptions are as follows.

- The vehicle's longitudinal speed is constant.
- Each wheel has only 1-DOF in the vertical direction (bounce).

- Road roughness (irregularities) are not considered (neglected).
- Pitch center is assumed coincident with the vehicle's center of gravity.
- The modelling of the suspension between the sprung and un-sprung masses are viscous passive dampers and spring, while each tire is modelled as linear spring without damping.
- A small angle approximation is considered in the derivation of the vehicle model.

Equations of motion of 11-DOF for multi-wheeled combat vehicle with semi-active suspension

Sprung mass heave motion

$$\sum \mathrm{F_{zi}} = \mathrm{m}_s \ddot{Z}_s \tag{3-42}$$

$$\mathrm{F_{s1R}} + \mathrm{F_{s1L}} + \mathrm{F_{s2R}} + \mathrm{F_{s2L}} + \mathrm{F_{s3R}} + \mathrm{F_{s3L}} + \mathrm{F_{s4R}} + \mathrm{F_{s4L}} + \mathrm{F_{d1R}} + \mathrm{F_{d1L}} + \mathrm{F_{d2R}} + \mathrm{F_{d2L}} + \mathrm{F_{d3R}} + \mathrm{F_{d3L}} + \mathrm{F_{d4R}} + \mathrm{F_{d4L}} + \mathrm{F_{(z)c}} = \mathrm{m}_s \ddot{Z}_s$$

Sprung mass pitch motion

The vehicle's pitch motion can be graphically analyzed based on a half car model as illustrated in Figure 3-5.

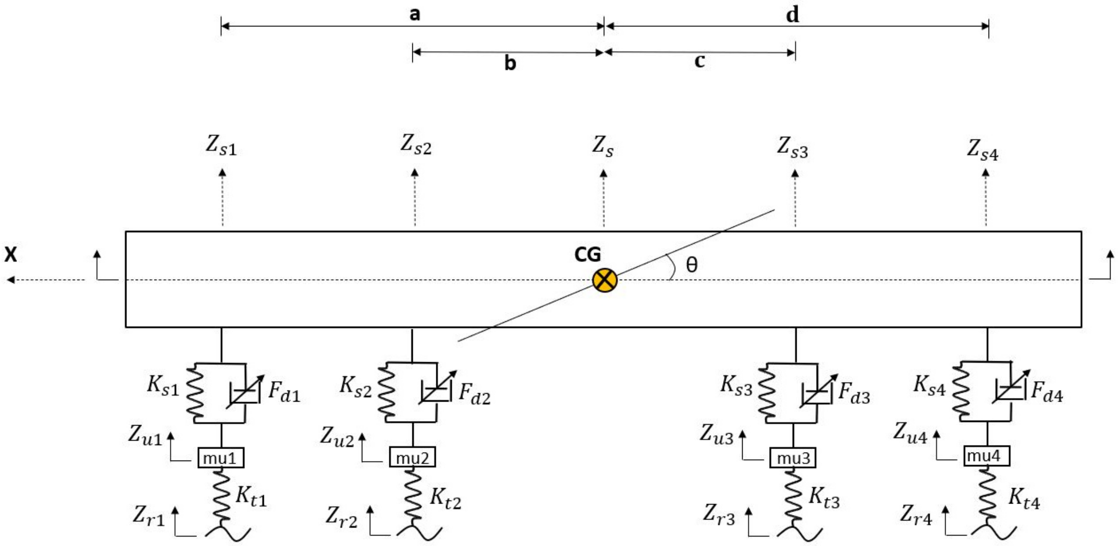

Figure 3-5 Multi-wheeled combat vehicle half car model

$$\sum \mathrm{M}_Y = \mathrm{I}_{YY}\ddot{\theta} \tag{3-43}$$

$$(\mathrm{F_{s4R}} + \mathrm{F_{s4L}} + \mathrm{F_{d4R}} + \mathrm{F_{d4L}})\mathrm{d} + (\mathrm{F_{s3R}} + \mathrm{F_{s3L}} + \mathrm{F_{d3R}} + \mathrm{F_{d3L}})\mathrm{c} - (\mathrm{F_{s1R}} + \mathrm{F_{s1L}} + +\mathrm{F_{d1R}} + \mathrm{F_{d1L}})\mathrm{a} - (\mathrm{F_{s2R}} + \mathrm{F_{s2L}} + \mathrm{F_{d2R}} + \mathrm{F_{d2L}})\mathrm{b} + \mathrm{M_\theta} = \mathrm{I_{yy}}\ddot{\theta}$$

Sprung mass roll motion

The vehicle’s roll motion can be graphically represented based as depicted in Figure 3-6.

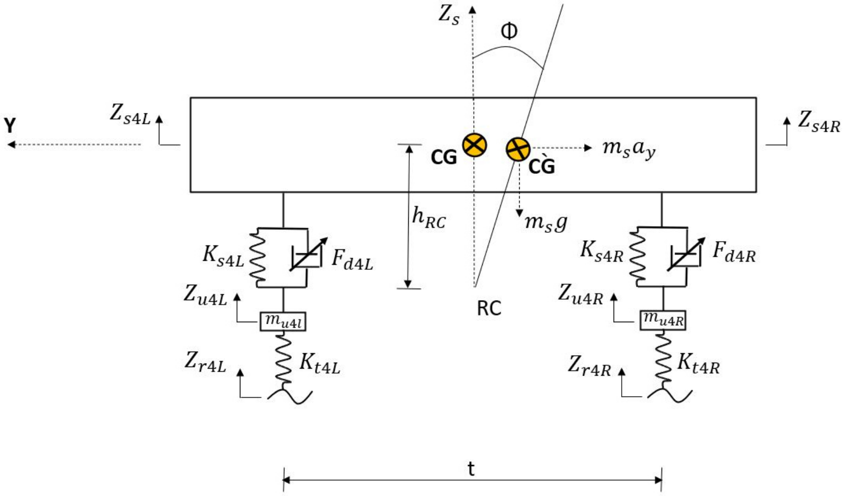

Figure 3-6 Multi-wheeled combat vehicle’s roll motion representation

$$\sum \mathrm{M}_X = \mathrm{I}_{XX}\ddot{\phi} \tag{3-44}$$

$$\mathrm{m_s g h_r \sin\phi} + \mathrm{m_s a_y h_r \cos\phi} + (\mathrm{F_{s1L}} + \mathrm{F_{s2L}} + \mathrm{F_{s3L}} + \mathrm{F_{s4L}} + \mathrm{F_{d1L}} + \mathrm{F_{d2L}} + \mathrm{F_{d3L}} + \mathrm{F_{d4L}})\frac{\mathrm{t}}{2} - (\mathrm{F_{s1R}} + \mathrm{F_{s2R}} + \mathrm{F_{s3R}} + \mathrm{F_{s4R}} + \mathrm{F_{d1R}} + \mathrm{F_{d2R}} + \mathrm{F_{d3R}} + \mathrm{F_{d4R}})\frac{\mathrm{t}}{2} + \mathrm{M_\phi} = \mathrm{I}_{XX}\ddot{\phi}$$

Where

$\mathrm{F_{s1R}}$: the spring force on the right-hand side of the first axle = $-\mathrm{K_{s1R}}(\mathrm{Z_{s1R}} - \mathrm{Z_{u1R}})$

$\mathrm{F_{s1L}}$: the spring force on the left-hand side of the first axle = $-\mathrm{K_{s1L}}(\mathrm{Z_{s1L}} - \mathrm{Z_{u1L}})$

$\mathrm{F_{s2R}}$: the spring force on the right-hand side of the second axle = $-\mathrm{K_{s2R}}(\mathrm{Z_{s2R}} - \mathrm{Z_{u2R}})$

$\mathrm{F_{s2L}}$: the spring force on the left-hand side of the second axle = $-\mathrm{K_{s2L}}(\mathrm{Z_{s2L}} - \mathrm{Z_{u2L}})$

$\mathrm{F_{s3R}}$: the spring force on the right-hand side of the third axle = $-\mathrm{K_{s3R}}(\mathrm{Z_{s3R}} - \mathrm{Z_{u3R}})$

$\mathrm{F_{s3L}}$: the spring force on the left-hand side of the third axle = $-\mathrm{K_{s3L}}(\mathrm{Z_{s3L}} - \mathrm{Z_{u3L}})$

$\mathrm{F_{s4R}}$: the spring force on the right-hand side of the fourth axle = $-\mathrm{K_{s4R}}(\mathrm{Z_{s4R}} - \mathrm{Z_{u4R}})$

$\mathrm{F_{s4L}}$: the spring force on the left-hand side of the fourth axle = $-\mathrm{K_{s4L}}(\mathrm{Z_{s4L}} - \mathrm{Z_{u4L}})$

F_{d1R}: the damper actuator force on the right-hand side of the first axle = $-C_{d1R}(\dot{Z}_{s1R} - \dot{Z}_{u1R})$

F_{d1L}: the damper actuator force on the left-hand side of the first axle = $-C_{d1L}(\dot{Z}_{s1L} - \dot{Z}_{u1L})$

F_{d2R}: the damper actuator force on the right-hand side of the second axle = $-C_{d2R}(\dot{Z}_{s2R} - \dot{Z}_{u2R})$

F_{d2L}: the damper actuator force on the left-hand side of the second axle = $-C_{d2L}(\dot{Z}_{s2L} - \dot{Z}_{u2L})$

F_{d3R}: the damper actuator force on the right-hand side of the third axle = $-C_{d3R}(\dot{Z}_{s3R} - \dot{Z}_{u3R})$

F_{d3L}: the damper actuator force on the left-hand side of the third axle = $-C_{d3L}(\dot{Z}_{s3L} - \dot{Z}_{u3L})$

F_{d4R}: the damper actuator force on the right-hand side of the fourth axle = $-C_{d4R}(\dot{Z}_{s4R} - \dot{Z}_{u4R})$

F_{d4L}: the damper actuator force on the left-hand side of the fourth axle = $-C_{d4L}(\dot{Z}_{s4L} - \dot{Z}_{u4L})$

$F_{(z)_c}$: the LQR corrective heave damper force.

M_θ: the LQR corrective pitch moment.

M_ϕ: the LQR corrective roll moment.

Un-sprung masses vertical motion

$$\sum F_{zi} = m_{uij}\,\ddot{Z}_{uij} \tag{3-45}$$

$$F_{s1R} + F_{d1R} + F_{t1R} + F_{(z1R)c} = m_{u1R}\,\ddot{Z}_{u1R}$$

$$F_{s1L} + F_{d1L} + F_{t1L} + F_{(z1L)c} = m_{u1L}\,\ddot{Z}_{u1L}$$

$$F_{s2R} + F_{d2R} + F_{t2R} + F_{(z2R)c} = m_{u2R}\,\ddot{Z}_{u2R}$$

$$F_{s2L} + F_{d2L} + F_{t2L} + F_{(z2L)c} = m_{u2L}\,\ddot{Z}_{u2L}$$

$$F_{s3R} + F_{d3R} + F_{t3R} + F_{(z3R)c} = m_{u3R}\,\ddot{Z}_{u3R}$$

$$F_{s3L} + F_{d3L} + F_{t3L} + F_{(z3L)c} = m_{u3L}\,\ddot{Z}_{u3L}$$

$$F_{s4R} + F_{d4R} + F_{t4R} + F_{(z4R)c} = m_{u4R}\,\ddot{Z}_{u4R}$$

$$F_{s4L} + F_{d4L} + F_{t4L} + F_{(z4L)c} = m_{u4L}\,\ddot{Z}_{u4L}$$

Where

F_{s1R}: the spring force on the right-hand side of the first axle = $-K_{s1R}(Z_{u1R} - Z_{s1R})$

F_{s1L}: the spring force on the left-hand side of the first axle = $-K_{s1L}(Z_{u1L} - Z_{s1L})$

F_{s2R}: the spring force on the right-hand side of the second axle = $-K_{s2R}(Z_{u2R} - Z_{s2R})$

F_{s2L}: the spring force on the left-hand side of the second axle = $-K_{s2L}(Z_{u2L} - Z_{s2L})$

F_{s3R}: the spring force on the right-hand side of the third axle = $-K_{s3R}(Z_{u3R} - Z_{s3R})$

F_{s3L}: the spring force on the left-hand side of the third axle = $-K_{s3L}(Z_{u3L} - Z_{s3L})$

F_{s4R}: the spring force on the right-hand side of the fourth axle = $-K_{s4R}(Z_{u4R} - Z_{s4R})$

F_{s4L}: the spring force on the left-hand side of the fourth axle = $-K_{s4L}(Z_{u4L} - Z_{s4L})$

F_{d1R}: the damper actuator force on the right-hand side of the first axle = $-C_{d1R}(\dot{Z}_{u1R} - \dot{Z}_{s1R})$

F_{d1L}: the damper actuator force on the left-hand side of the first axle = $-C_{d1L}(\dot{Z}_{u1L} - \dot{Z}_{s1L})$

F_{d2R}: the damper actuator force on the right-hand side of the second axle = $-C_{d2R}(\dot{Z}_{u2R} - \dot{Z}_{s2R})$

F_{d2L}: the damper actuator force on the left-hand side of the second axle = $-C_{d2L}(\dot{Z}_{u2L} - \dot{Z}_{s2L})$

F_{d3R}: the damper actuator force on the right-hand side of the third axle = $-C_{d3R}(\dot{Z}_{u3R} - \dot{Z}_{s3R})$

F_{d3L}: the damper actuator force on the left-hand side of the third axle = $-C_{d3L}(\dot{Z}_{u3L} - \dot{Z}_{s3L})$

F_{d4R}: the damper actuator force on the right-hand side of the fourth axle = $-C_{d4R}(\dot{Z}_{u4R} - \dot{Z}_{s4R})$

F_{d4L}: the damper actuator force on the left-hand side of the fourth axle = $-C_{d4L}(\dot{Z}_{u4L} - \dot{Z}_{s4L})$

F_{t1R}: the tire spring force on the right-hand side of the first axle = $-K_{t1R}(Z_{u1R} - Z_{r1R})$

F_{t1L}: the tire spring force on the left-hand side of the first axle = $-K_{t1L}(Z_{u1L} - Z_{r1L})$

F_{t2R}: the tire spring force on the right-hand side of the second axle = $-K_{t2R}(Z_{u2R} - Z_{r2R})$

F_{t2L}: the tire spring force on the left-hand side of the second axle = $-K_{t2L}(Z_{u2L} - Z_{r2L})$

F_{t3R}: the tire spring force on the right-hand side of the third axle = $-K_{t3R}(Z_{u3R} - Z_{r3R})$

F_{t3L}: the tire spring force on the left-hand side of the third axle = $-K_{t3L}(Z_{u3L} - Z_{r3L})$

F_{t4R}: the tire spring force on the right-hand side of the fourth axle = $-K_{t4R}(Z_{u4R} - Z_{r4R})$

F_{t4L}: the tire spring force on the left-hand side of the fourth axle = $-K_{t4L}(Z_{u4L} - Z_{r4L})$

$F_{(zij)c}$: the LQR corrective vertical damper force for each wheel.

Note: The displacement of each corner of the sprung mass is dependent on the pitch (θ) and roll (ϕ) motion and displacement (Z_s) at center of gravity of the spung mass. Therefore, a relationship has been introduced to relate each corner of the sprung mass to the sprung mass's center of gravity motion as follows.

$$\mathrm{Z_{s1L} = Z_s - a\sin\theta + \frac{t}{2}\sin\phi \approx Z_s - a\theta + \frac{t}{2}\phi} \tag{3-46}$$

$$\mathrm{Z_{s1R} = Z_s - a\sin\theta - \frac{t}{2}\sin\phi \approx Z_s - a\theta - \frac{t}{2}\phi} \tag{3-47}$$

$$\mathrm{Z_{s2L} = Z_s - b\sin\theta + \frac{t}{2}\sin\phi \approx Z_s - b\theta + \frac{t}{2}\phi} \tag{3-48}$$

$$\mathrm{Z_{s2R} = Z_s - b\sin\theta - \frac{t}{2}\sin\phi \approx Z_s - b\theta - \frac{t}{2}\phi} \tag{3-49}$$

$$\mathrm{Z_{s3L} = Z_s + c\sin\theta + \frac{t}{2}\sin\phi \approx Z_s + c\theta + \frac{t}{2}\phi} \tag{3-50}$$

$$\mathrm{Z_{s3R} = Z_s + c\sin\theta - \frac{t}{2}\sin\phi \approx Z_s + c\theta - \frac{t}{2}\phi} \tag{3-51}$$

$$\mathrm{Z_{s4L} = Z_s + d\sin\theta + \frac{t}{2}\sin\phi \approx Z_s + d\theta + \frac{t}{2}\phi} \tag{3-52}$$

$$\mathrm{Z_{s4R} = Z_s + d\sin\theta - \frac{t}{2}\sin\phi \approx Z_s + d\theta - \frac{t}{2}\phi} \tag{3-53}$$

Moreover, by differentiate the displacement, the velocity of each corner of the sprung mass can be obtained as follows.

$$\mathrm{\dot{Z}_{s1L} = \dot{Z}_s - a\dot{\theta} + \frac{t}{2}\dot{\phi}} \tag{3-54}$$

$$\mathrm{\dot{Z}_{s1R} = \dot{Z}_s - a\dot{\theta} - \frac{t}{2}\dot{\phi}} \tag{3-55}$$

$$\mathrm{\dot{Z}_{s2L} = \dot{Z}_s - b\dot{\theta} + \frac{t}{2}\dot{\phi}} \tag{3-56}$$

$$\mathrm{\dot{Z}_{s2R} = \dot{Z}_s - b\dot{\theta} - \frac{t}{2}\dot{\phi}} \tag{3-57}$$

$$\mathrm{\dot{Z}_{s3L} = \dot{Z}_s + c\dot{\theta} + \frac{t}{2}\dot{\phi}} \tag{3-58}$$

$$\mathrm{\dot{Z}_{s3R} = \dot{Z}_s + c\dot{\theta} - \frac{t}{2}\dot{\phi}} \tag{3-59}$$

$$\mathrm{\dot{Z}_{s4L} = \dot{Z}_s + d\dot{\theta} + \frac{t}{2}\dot{\phi}} \tag{3-60}$$

$$\mathrm{\dot{Z}_{s4R} = \dot{Z}_s + d\dot{\theta} - \frac{t}{2}\dot{\phi}} \tag{3-61}$$

After plug-in equations(3-46)to(3-61) into equations(3-42),(3-43),(3-44) and(3-45) and re-arranging and isolating for $\ddot{Z}_s$, $\ddot{\theta}$, $\ddot{\phi}$, $\mathrm{\ddot{Z}_{u1R}}$, $\mathrm{\ddot{Z}_{u1L}}$, $\mathrm{\ddot{Z}_{u2R}}$, $\mathrm{\ddot{Z}_{u2L}}$, $\mathrm{\ddot{Z}_{u3R}}$, $\mathrm{\ddot{Z}_{u3L}}$, $\mathrm{\ddot{Z}_{u4R}}$ and $\mathrm{\ddot{Z}_{u4L}}$ the final equations for sprung mass's heave, pitch and roll motions and un-sprung masses' vertical motions are obtained as follows.

$$\begin{aligned} & S_{1_1}\dot{Z}_s + S_{1_2}\dot{\theta} + S_{1_3}\dot{\phi} + S_{1_4}\dot{Z}_{u1R} + S_{1_5}\dot{Z}_{u1L} + S_{1_6}\dot{Z}_{u2R} + S_{1_7}\dot{Z}_{u2L} + S_{1_8}\dot{Z}_{u3R} \\ & \quad + S_{1_9}\dot{Z}_{u3L} + S_{1_{10}}\dot{Z}_{u4R} + S_{1_{11}}\dot{Z}_{u4L} + S_{1_{12}}Z_s + S_{1_{13}}\theta + S_{1_{14}}\phi \\ & \quad + S_{1_{15}}Z_{u1R} + S_{1_{16}}Z_{u1L} + S_{1_{17}}Z_{u2R} + S_{1_{18}}Z_{u2L} + S_{1_{19}}Z_{u3R} + S_{1_{20}}Z_{u3L} \\ & \quad + S_{1_{21}}Z_{u4R} + S_{1_{22}}Z_{u4L} + \frac{1}{m_s}F_{(z)c} = \ddot{Z}_s \end{aligned} \qquad (3\text{-}62)$$

Where

$$S_{1\_1} = \frac{[-C_{d1R}-C_{d1L}-C_{d2R}-C_{d2L}-C_{d3R}-C_{d3L}-C_{d4R}-C_{d4L}]}{m_s}$$

$$S_{1\_2} = \frac{[(C_{d1R}+C_{d1L})a + (C_{d2R}+C_{d2L})b - (C_{d3R}+C_{d3L})c - (C_{d4R}+C_{d4L})d]}{m_s}$$

$$S_{1\_3} = \frac{\left[(C_{d1R} + C_{d2R} + C_{d3R} + C_{d4R} - C_{d1L} - C_{d2L} - C_{d3L} - C_{d4L})\frac{t}{2}\right]}{m_s}$$

$$S_{1\_4} = \left(\frac{C_{d1R}}{m_s}\right), S_{1\_5} = \left(\frac{C_{d1L}}{m_s}\right), S_{1\_6} = \left(\frac{C_{d2R}}{m_s}\right), S_{1\_7} = \left(\frac{C_{d2L}}{m_s}\right), S_{1\_8} = \left(\frac{C_{d3R}}{m_s}\right), S_{1\_9} = \left(\frac{C_{d3L}}{m_s}\right)$$

$$S_{1\_10} = \left(\frac{C_{d4R}}{m_s}\right), S_{1\_11} = \left(\frac{C_{d4L}}{m_s}\right)$$

$$S_{1\_12} = \frac{[-K_{s1R}-K_{s1L}-K_{s2R}-K_{s2L}-K_{s3R}-K_{s3L}-K_{s4R}-K_{s4L}]}{m_s}$$

$$S_{1\_13} = \frac{[(K_{s1R}+K_{s1L})a + (K_{s2R}+K_{s2L})b - (K_{s3R}+K_{s3L})c - (K_{s4R}+K_{s4L})d]}{m_s}$$

$$S_{1\_14} = \frac{\left[(K_{s1R} + K_{s2R} + K_{s3R} + K_{s4R} - K_{s1L} - K_{s2L} - K_{s3L} - K_{s4L})\frac{t}{2}\right]}{m_s}$$

$$\begin{aligned} S_{1\_15} &= \left(\frac{K_{s1R}}{m_s}\right), S_{1\_16} = \left(\frac{K_{s1L}}{m_s}\right), S_{1\_17} = \left(\frac{K_{s2R}}{m_s}\right), S_{1\_18} = \left(\frac{K_{s2L}}{m_s}\right), S_{1\_19} = \left(\frac{K_{s3R}}{m_s}\right), S_{1\_20} \\ &= \left(\frac{K_{s3L}}{m_s}\right) \end{aligned}$$

$$S_{1\_21} = \left(\frac{K_{s4R}}{m_s}\right), S_{1\_22} = \left(\frac{K_{s4L}}{m_s}\right)$$

$$\begin{aligned} S_{2\_1}\dot{Z}_s + S_{2\_2}\dot{\theta} + S_{2\_3}\dot{\phi} + S_{2\_4}\dot{Z}_{u1R} + S_{2\_5}\dot{Z}_{u1L} + S_{2\_6}\dot{Z}_{u2R} + S_{2\_7}\dot{Z}_{u2L} + S_{2\_8}\dot{Z}_{u3R} \\ + S_{2\_9}\dot{Z}_{u3L} + S_{2\_10}\dot{Z}_{u4R} + S_{2\_11}\dot{Z}_{u4L} + S_{2\_12}Z_s + S_{2\_13}\theta + S_{2\_14}\phi \\ + S_{2\_15}Z_{u1R} + S_{2\_16}Z_{u1L} + S_{2\_17}Z_{u2R} + S_{2\_18}Z_{u2L} + S_{2\_19}Z_{u3R} \\ + S_{2\_20}Z_{u3L} + S_{2\_21}Z_{u4R} + S_{2\_22}Z_{u4L} + \frac{1}{I_{YY}}M_\theta = \ddot{\theta} \end{aligned} \tag{3-63}$$

Where

$$S_{2\_1} = \frac{[(C_{d1R}+C_{d1L})a+(C_{d2R}+C_{d2L})b-(C_{d3R}+C_{d3L})c-(C_{d4R}+C_{d4L})d]}{I_{YY}}$$

$$S_{2\_2} = \frac{[-(C_{d1R}+C_{d1L})a^2 - (C_{d2R}+C_{d2L})b^2 - (C_{d3R}+C_{d3L})c^2 - (C_{d4R}+C_{d4L})d^2]}{I_{YY}}$$

$$S_{2\_3} = \frac{\left[(C_{d1L} - C_{d1R})\frac{at}{2} + (C_{d2L} - C_{d2R})\frac{bt}{2} + (C_{d3R}-C_{d3L})\frac{ct}{2} + (C_{d4R}-C_{d4L})\frac{dt}{2}\right]}{I_{YY}}$$

$$S_{2\_4} = \left(\frac{-aC_{d1R}}{I_{YY}}\right), S_{2_5} = \left(\frac{-aC_{d1L}}{I_{YY}}\right), S_{2_6} = \left(\frac{-bC_{d2R}}{I_{YY}}\right), S_{2_7} = \left(\frac{-bC_{d2L}}{I_{YY}}\right), S_{2_8} = \left(\frac{cC_{d3R}}{I_{YY}}\right)$$

$$S_{2\_9} = \left(\frac{cC_{d3L}}{I_{YY}}\right), S_{2\_10} = \left(\frac{dC_{d4R}}{I_{YY}}\right), S_{2\_11} = \left(\frac{dC_{d4L}}{I_{YY}}\right)$$

$$S_{2\_12} = \frac{[(K_{s1R}+K_{s1L})a+(K_{s2R}+K_{s2L})b-(K_{s3R}+K_{s3L})c-(K_{s4R}+K_{s4L})d]}{I_{YY}}$$

$$S_{2\_13} = \frac{[-(K_{s1R}+K_{s1L})a^2 - (K_{s2R}+K_{s2L})b^2 - (K_{s3R}+K_{s3L})c^2 - (K_{s4R}+K_{s4L})d^2]}{I_{YY}}$$

$$S_{2\_14} = \frac{\left[(K_{s1L} - K_{s1R})\frac{at}{2} + (K_{s2L} - K_{s2R})\frac{bt}{2} + (K_{s3R}-K_{s3L})\frac{ct}{2} + (K_{s4R}-k_{s4L})\frac{dt}{2}\right]}{I_{YY}}$$

$$\begin{aligned} S_{2\_15} = \left(\frac{-aK_{s1R}}{I_{YY}}\right), S_{2\_16} = \left(\frac{-aK_{s1L}}{I_{YY}}\right), S_{2\_17} = \left(\frac{-bK_{s2R}}{I_{YY}}\right), S_{2\_18} = \left(\frac{-bK_{s2L}}{I_{YY}}\right), S_{2\_19} \\ = \left(\frac{cK_{s3R}}{I_{YY}}\right) \end{aligned}$$

$$S_{2\_20} = \left(\frac{cK_{s3L}}{I_{YY}}\right), S_{2\_21} = \left(\frac{dK_{s4R}}{I_{YY}}\right), S_{2\_22} = \left(\frac{dK_{s4L}}{I_{YY}}\right)$$

$$\begin{aligned} S_{3\_1}\dot{Z}_s + S_{3\_2}\dot{\theta} + S_{3\_3}\dot{\phi} + S_{3\_4}\dot{Z}_{u1R} + S_{3\_5}\dot{Z}_{u1L} + S_{3\_6}\dot{Z}_{u2R} + S_{3\_7}\dot{Z}_{u2L} + S_{3\_8}\dot{Z}_{u3R} \\ + S_{3\_9}\dot{Z}_{u3L} + S_{3\_10}\dot{Z}_{u4R} + S_{3\_11}\dot{Z}_{u4L} + S_{3\_12}Z_s + S_{3\_13}\theta + S_{3\_14}\phi \\ + S_{3\_15}Z_{u1R} + S_{3\_16}Z_{u1L} + S_{3\_17}Z_{u2R} + S_{3\_18}Z_{u2L} + S_{3\_19}Z_{u3R} \\ + S_{3\_20}Z_{u3L} + S_{3\_21}Z_{u4R} + S_{3\_22}Z_{u4L} + \frac{m_s h_{RC}}{I_{XX}} a_y + \frac{1}{I_{XX}} M_{\phi} = \ddot{\phi} \end{aligned} \tag{3-64}$$

Where

$$S_{3\_1} = \frac{\left[(C_{d1R} + C_{d2R} + C_{d3R} + C_{d4R} - C_{d1L} - C_{d2L} - C_{d3L} - C_{d4L})\frac{t}{2}\right]}{I_{XX}}$$

$$S_{3\_2} = \frac{\left[(C_{d1L} - C_{d1R})\frac{at}{2} + (C_{d2L} - C_{d2R})\frac{bt}{2} + (C_{d3R} - C_{d3L})\frac{ct}{2} + (C_{d4R} - C_{d4L})\frac{dt}{2}\right]}{I_{XX}}$$

$$S_{3\_3} = \frac{\left[(C_{d1R} + C_{d2R} + C_{d3R} + C_{d4R} + C_{d1L} + C_{d2L} + C_{d3L} + C_{d4L})\frac{-t^2}{4}\right]}{I_{XX}}$$

$$S_{3\_4} = \left(\frac{-tC_{d1R}}{2I_{XX}}\right), S_{3\_5} = \left(\frac{tC_{d1L}}{2I_{XX}}\right), S_{3\_6} = \left(\frac{-tC_{d2R}}{2I_{XX}}\right), S_{3\_7} = \left(\frac{tC_{d2L}}{2I_{XX}}\right), S_{3\_8} = \left(\frac{-tC_{d3R}}{2I_{XX}}\right)$$

$$S_{3\_9} = \left(\frac{tC_{d3L}}{2I_{XX}}\right), S_{3\_10} = \left(\frac{-tC_{d4R}}{2I_{XX}}\right), S_{3\_11} = \left(\frac{tC_{d4L}}{2I_{XX}}\right)$$

$$S_{3\_12} = \frac{\left[(K_{s1R} + K_{s2R} + K_{s3R} + K_{s4R} - K_{s1L} - K_{s2L} - K_{s3L} - K_{s4L})\frac{t}{2}\right]}{I_{XX}}$$

$$S_{3\_13} = \frac{\left[(K_{s1L} - K_{s1R})\frac{at}{2} + (K_{s2L} - K_{s2R})\frac{bt}{2} + (K_{s3R} - K_{s3L})\frac{ct}{2} + (K_{s4R} - K_{s4L})\frac{dt}{2}\right]}{I_{XX}}$$

$$S_{3\_14} = \frac{\left[m_s g h_{RC} + (K_{s1R} + K_{s2R} + k_{s3R} + K_{s4R} + K_{s1L} + k_{s2L} + K_{s3L} + K_{s4L})\frac{-t^2}{4}\right]}{I_{XX}}$$

$$S_{3\_15} = \left(\frac{-tK_{s1R}}{2I_{XX}}\right), S_{3\_16} = \left(\frac{tK_{s1L}}{2I_{XX}}\right), S_{3\_17} = \left(\frac{-tK_{s2R}}{2I_{XX}}\right), S_{3\_18} = \left(\frac{tK_{s2L}}{2I_{XX}}\right), S_{3\_19} = \left(\frac{-tK_{s3R}}{2I_{XX}}\right)$$

$$S_{3\_20} = \left(\frac{tK_{s3L}}{2I_{XX}}\right), S_{3\_21} = \left(\frac{-tK_{s4R}}{2I_{XX}}\right), S_{3\_22} = \left(\frac{tK_{s4L}}{2I_{XX}}\right)$$

$$\begin{aligned} S_{4_1}\dot{Z}_s + S_{4_2}\dot{\theta} + S_{4_3}\dot{\phi} + S_{4_4}\dot{Z}_{u1R} + S_{4_5}\dot{Z}_{u1L} + S_{4_6}\dot{Z}_{u2R} + S_{4_7}\dot{Z}_{u2L} + S_{4_8}\dot{Z}_{u3R} \\ + S_{4_9}\dot{Z}_{u3L} + S_{4_{10}}\dot{Z}_{u4R} + S_{4_{11}}\dot{Z}_{u4L} + S_{4_{12}}Z_s + S_{4_{13}}\theta + S_{4_{14}}\phi \\ + S_{4_{15}}Z_{u1R} + S_{4_{16}}Z_{u1L} + S_{4_{17}}Z_{u2R} + S_{4_{18}}Z_{u2L} + S_{4_{19}}Z_{u3R} + S_{4_{20}}Z_{u3L} \\ + S_{4_{21}}Z_{u4R} + S_{4_{22}}Z_{u4L} + \frac{1}{m_{u1R}}F_{(z1R)c} = \ddot{Z}_{u1R} \end{aligned} \tag{3-65}$$

Where

$$S_{4\_1} = \left(\frac{C_{d1R}}{m_{u1R}}\right), S_{4\_2} = \left(\frac{-aC_{d1R}}{m_{u1R}}\right), S_{4\_3} = \left(\frac{-tC_{d1R}}{2m_{u1R}}\right), S_{4\_4} = \left(\frac{-C_{d1R}}{m_{u1R}}\right)$$

$$S_{4\_5} = S_{4\_6} = S_{4\_7} = S_{4\_8} = S_{4\_9} = S_{4\_10} = S_{4\_11} = 0$$

$$S_{4\_12} = \left(\frac{K_{s1R}}{m_{u1R}}\right), S_{4\_13} = \left(\frac{-aK_{s1R}}{m_{u1R}}\right), S_{4\_14} = \left(\frac{-tK_{s1R}}{2m_{u1R}}\right), S_{4\_15} = \left(\frac{-K_{s1R} - K_{t1R}}{m_{u1R}}\right)$$

$$S_{4\_16} = S_{4\_17} = S_{4\_18} = S_{4\_19} = S_{4\_20} = S_{4\_21} = S_{4\_22} = 0$$

$$\begin{aligned} S_{5\_1}\dot{Z}_s + S_{5\_2}\dot{\theta} + S_{5\_3}\dot{\phi} + S_{5\_4}\dot{Z}_{u1R} + S_{5\_5}\dot{Z}_{u1L} + S_{5\_6}\dot{Z}_{u2R} + S_{5\_7}\dot{Z}_{u2L} + S_{5\_8}\dot{Z}_{u3R} \\ + S_{5\_9}\dot{Z}_{u3L} + S_{5\_10}\dot{Z}_{u4R} + S_{5\_11}\dot{Z}_{u4L} + S_{5\_12}Z_s + S_{5\_13}\theta + S_{5\_14}\phi \\ + S_{5\_15}Z_{u1R} + S_{5\_16}Z_{u1L} + S_{5\_17}Z_{u2R} + S_{5\_18}Z_{u2L} + S_{5\_19}Z_{u3R} \\ + S_{5\_20}Z_{u3L} + S_{5\_21}Z_{u4R} + S_{5\_22}Z_{u4L} + \frac{1}{m_{u1L}}F_{(z1L)c} = \ddot{Z}_{u1L} \end{aligned} \tag{3-66}$$

Where

$$S_{5\_1} = \left(\frac{C_{d1L}}{m_{u1L}}\right), S_{5\_2} = \left(\frac{-aC_{d1L}}{m_{u1L}}\right), S_{5\_3} = \left(\frac{tC_{d1L}}{2m_{u1L}}\right), S_{5\_4} = 0, S_{5\_5} = \left(\frac{-C_{d1L}}{m_{u1L}}\right)$$

$$S_{5\_6} = S_{5\_7} = S_{5\_8} = S_{5\_9} = S_{5\_10} = S_{5\_11} = 0$$

$$S_{5\_12} = \left(\frac{K_{s1L}}{m_{u1L}}\right), S_{5\_13} = \left(\frac{-aK_{s1L}}{m_{u1L}}\right), S_{5\_14} = \left(\frac{tK_{s1L}}{2m_{u1L}}\right), S_{5\_15} = 0, S_{5\_16} = \left(\frac{-K_{s1L} - K_{t1L}}{m_{u1L}}\right)$$

$$S_{5\_17} = S_{5\_18} = S_{5\_19} = S_{5\_20} = S_{5\_21} = S_{5\_22} = 0$$

$$\begin{aligned} S_{6\_1}\dot{Z}_s + S_{6\_2}\dot{\theta} + S_{6\_3}\dot{\phi} + S_{6\_4}\dot{Z}_{u1R} + S_{6\_5}\dot{Z}_{u1L} + S_{6\_6}\dot{Z}_{u2R} + S_{6\_7}\dot{Z}_{u2L} + S_{6\_8}\dot{Z}_{u3R} \\ + S_{6\_9}\dot{Z}_{u3L} + S_{6\_10}\dot{Z}_{u4R} + S_{6\_11}\dot{Z}_{u4L} + S_{6\_12}Z_s + S_{6\_13}\theta + S_{6\_14}\phi \\ + S_{6\_15}Z_{u1R} + S_{6\_16}Z_{u1L} + S_{6\_17}Z_{u2R} + S_{6\_18}Z_{u2L} + S_{6\_19}Z_{u3R} \\ + S_{6\_20}Z_{u3L} + S_{6\_21}Z_{u4R} + S_{6\_22}Z_{u4L} + \frac{1}{m_{u2R}}F_{(z2R)c} = \ddot{Z}_{u2R} \end{aligned} \tag{3-67}$$

Where

$$S_{6\_1}=\left(\frac{\mathrm{C_{d2R}}}{\mathrm{m_{u2R}}}\right),S_{6\_2}=\left(\frac{-b\mathrm{C_{d2R}}}{\mathrm{m_{u2R}}}\right),S_{6\_3}=\left(\frac{-t\mathrm{C_{d2R}}}{2\mathrm{m_{u2R}}}\right),S_{6\_4}=S_{6\_5}=0$$

$$S_{6\_6}=\left(\frac{-\mathrm{C_{d2R}}}{\mathrm{m_{u2R}}}\right),S_{6\_7}=S_{6\_8}=S_{6\_9}=S_{6\_10}=S_{6\_11}=0,S_{6\_12}=\left(\frac{\mathrm{K_{s2R}}}{\mathrm{m_{u2R}}}\right),S_{6\_13}=\left(\frac{-b\mathrm{K_{s2R}}}{\mathrm{m_{u2R}}}\right)$$

$$S_{6\_14}=\left(\frac{-t\mathrm{K_{s2R}}}{2\mathrm{m_{u2R}}}\right),S_{6\_15}=S_{6\_16}=0,S_{6\_17}=\left(\frac{-\mathrm{K_{s2R}}-\mathrm{K_{t2R}}}{\mathrm{m_{u2R}}}\right)$$

$$S_{6\_18}=S_{6\_19}=S_{6\_20}=S_{6\_21}=S_{6\_22}=0$$

$$\begin{aligned}S_{7\_1}\dot{Z}_s+S_{7\_2}\dot{\theta}+S_{7\_3}\dot{\phi}+S_{7\_4}\dot{Z}_{u1R}+S_{7\_5}\dot{Z}_{u1L}+S_{7\_6}\dot{Z}_{u2R}+S_{7\_7}\dot{Z}_{u2L}+S_{7\_8}\dot{Z}_{u3R}\\+S_{7\_9}\dot{Z}_{u3L}+S_{7\_10}\dot{Z}_{u4R}+S_{7\_11}\dot{Z}_{u4L}+S_{7\_12}Z_s+S_{7\_13}\theta+S_{7\_14}\phi\\+S_{7\_15}Z_{u1R}+S_{7\_16}Z_{u1L}+S_{7\_17}Z_{u2R}+S_{7\_18}Z_{u2L}+S_{7\_19}Z_{u3R}\\+S_{7\_20}Z_{u3L}+S_{7\_21}Z_{u4R}+S_{7\_22}Z_{u4L}+\frac{1}{\mathrm{m_{u2L}}}F_{(z2L)c}=\ddot{Z}_{u2L}\end{aligned} \tag{3-68}$$

Where

$$S_{7\_1}=\left(\frac{\mathrm{C_{d2L}}}{\mathrm{m_{u2L}}}\right),S_{7\_2}=\left(\frac{-b\mathrm{C_{d2L}}}{\mathrm{m_{u2L}}}\right),S_{7\_3}=\left(\frac{t\mathrm{C_{d2L}}}{2\mathrm{m_{u2L}}}\right),S_{7\_4}=S_{7\_5}=S_{7\_6}=0$$

$$S_{7\_7}=\left(\frac{-\mathrm{C_{d2L}}}{\mathrm{m_{u2L}}}\right),S_{7\_8}=S_{7\_9}=S_{7\_10}=S_{7\_11}=0,S_{7\_12}=\left(\frac{\mathrm{K_{s2L}}}{\mathrm{m_{u2L}}}\right),S_{7\_13}=\left(\frac{-b\mathrm{K_{s2L}}}{\mathrm{m_{u2L}}}\right)$$

$$S_{7\_14}=\left(\frac{t\mathrm{K_{s2L}}}{2\mathrm{m_{u2L}}}\right),S_{7\_15}=S_{7\_16}=S_{7\_17}=0,S_{7\_18}=\left(\frac{-\mathrm{K_{s2L}}-\mathrm{K_{t2L}}}{\mathrm{m_{u2L}}}\right)$$

$$S_{7\_19}=S_{7\_20}=S_{7\_21}=S_{7\_22}=0$$

$$\begin{aligned}S_{8\_1}\dot{Z}_s+S_{8\_2}\dot{\theta}+S_{8\_3}\dot{\phi}+S_{8\_4}\dot{Z}_{u1R}+S_{8\_5}\dot{Z}_{u1L}+S_{8\_6}\dot{Z}_{u2R}+S_{8\_7}\dot{Z}_{u2L}+S_{8\_8}\dot{Z}_{u3R}\\+S_{8\_9}\dot{Z}_{u3L}+S_{8\_10}\dot{Z}_{u4R}+S_{8\_11}\dot{Z}_{u4L}+S_{8\_12}Z_s+S_{8\_13}\theta+S_{8\_14}\phi\\+S_{8\_15}Z_{u1R}+S_{8\_16}Z_{u1L}+S_{8\_17}Z_{u2R}+S_{8\_18}Z_{u2L}+S_{8\_19}Z_{u3R}\\+S_{8\_20}Z_{u3L}+S_{8\_21}Z_{u4R}+S_{8\_22}Z_{u4L}+\frac{1}{\mathrm{m_{u3R}}}F_{(z3R)c}=\ddot{Z}_{u3R}\end{aligned} \tag{3-69}$$

Where

$$S_{8\_1}=\left(\frac{\mathrm{C_{d3R}}}{\mathrm{m_{u3R}}}\right),S_{8\_2}=\left(\frac{c\mathrm{C_{d3R}}}{\mathrm{m_{u3R}}}\right),S_{8\_3}=\left(\frac{-t\mathrm{C_{d3R}}}{2\mathrm{m_{u3R}}}\right),S_{8\_4}=S_{8\_5}=S_{8\_6}=S_{8\_7}=0$$

$$S_{8\_8} = \left(\frac{-C_{d3R}}{m_{u3R}}\right), S_{8\_9} = S_{8\_10} = S_{8\_11} = 0, S_{8\_12} = \left(\frac{K_{s3R}}{m_{u3R}}\right), S_{8\_13} = \left(\frac{cK_{s3R}}{m_{u3R}}\right), S_{8\_14} = \left(\frac{-tK_{s3R}}{2m_{u3R}}\right)$$

$$S_{8\_15} = S_{8\_16} = S_{8\_17} = S_{8\_18} = 0, S_{8\_19} = \left(\frac{-K_{s3R} - K_{t3R}}{m_{u3R}}\right), S_{8\_20} = S_{8\_21} = S_{8\_22} = 0$$

$$\begin{aligned} S_{9\_1}\dot{Z}_s + S_{9\_2}\dot{\theta} + S_{9\_3}\dot{\phi} + S_{9\_4}\dot{Z}_{u1R} + S_{9\_5}\dot{Z}_{u1L} + S_{9\_6}\dot{Z}_{u2R} + S_{9\_7}\dot{Z}_{u2L} + S_{9\_8}\dot{Z}_{u3R} \\ + S_{9\_9}\dot{Z}_{u3L} + S_{9\_10}\dot{Z}_{u4R} + S_{9\_11}\dot{Z}_{u4L} + S_{9\_12}Z_s + S_{9\_13}\theta + S_{9\_14}\phi \\ + S_{9\_15}Z_{u1R} + S_{9\_16}Z_{u1L} + S_{9\_17}Z_{u2R} + S_{9\_18}Z_{u2L} + S_{9\_19}Z_{u3R} \\ + S_{9\_20}Z_{u3L} + S_{9\_21}Z_{u4R} + S_{9\_22}Z_{u4L} + \frac{1}{m_{u3L}}F_{(z3L)c} = \ddot{Z}_{u3L} \end{aligned} \tag{3-70}$$

Where

$$S_{9\_1} = \left(\frac{C_{d3L}}{m_{u3L}}\right), S_{9\_2} = \left(\frac{cC_{d3L}}{m_{u3L}}\right), S_{9\_3} = \left(\frac{tC_{d3L}}{2m_{u3L}}\right), S_{9\_4} = S_{9\_5} = S_{9\_6} = S_{9\_7} = S_{9\_8} = 0$$

$$S_{9\_9} = \left(\frac{-C_{d3L}}{m_{u3L}}\right), S_{9\_10} = S_{9\_11} = 0, S_{9\_12} = \left(\frac{K_{s3L}}{m_{u3L}}\right), S_{9\_13} = \left(\frac{cK_{s3L}}{m_{u3L}}\right), S_{8\_14} = \left(\frac{tK_{s3L}}{2m_{u3L}}\right)$$

$$S_{9\_15} = S_{9\_16} = S_{9\_17} = S_{9\_18} = S_{9\_19} = 0, S_{9\_20} = \left(\frac{-K_{s3L} - K_{t3L}}{m_{u3L}}\right), S_{9\_21} = S_{9\_22} = 0$$

$$\begin{aligned} S_{10\_1}\dot{Z}_s + S_{10\_2}\dot{\theta} + S_{10\_3}\dot{\phi} + S_{10\_4}\dot{Z}_{u1R} + S_{10\_5}\dot{Z}_{u1L} + S_{10\_6}\dot{Z}_{u2R} + S_{10\_7}\dot{Z}_{u2L} \\ + S_{10\_8}\dot{Z}_{u3R} + S_{10\_9}\dot{Z}_{u3L} + S_{10\_10}\dot{Z}_{u4R} + S_{10\_11}\dot{Z}_{u4L} + S_{10\_12}Z_s \\ + S_{10\_13}\theta + S_{10\_14}\phi + S_{10\_15}Z_{u1R} + S_{10\_16}Z_{u1L} + S_{10\_17}Z_{u2R} \\ + S_{10\_18}Z_{u2L} + S_{10\_19}Z_{u3R} + S_{10\_20}Z_{u3L} + S_{10\_21}Z_{u4R} + S_{10\_22}Z_{u4L} \\ + \frac{1}{m_{u4R}}F_{(z4R)c} = \ddot{Z}_{u4R} \end{aligned} \tag{3-71}$$

Where

$$S_{10\_1} = \left(\frac{C_{d4R}}{m_{u4R}}\right), S_{10\_2} = \left(\frac{dC_{d4R}}{m_{u4R}}\right), S_{10\_3} = \left(\frac{-tC_{d4R}}{2m_{u4R}}\right), S_{10\_4} = S_{10\_5} = S_{10\_6} = S_{10\_7} = 0$$

$$S_{10\_8} = S_{10\_9} = 0, S_{10\_10} = \left(\frac{-C_{d4R}}{m_{u4R}}\right), S_{10\_11} = 0, S_{10\_12} = \left(\frac{K_{s4R}}{m_{u4R}}\right), S_{10\_13} = \left(\frac{dK_{s4R}}{m_{u4R}}\right)$$

$$S_{10\_14} = \left(\frac{-tK_{s4R}}{2m_{u4R}}\right), S_{10\_15} = S_{10\_16} = S_{10\_17} = S_{10\_18} = S_{10\_19} = S_{10\_20} = 0$$

$$S_{10\_21} = \left(\frac{-K_{s4R} - K_{t4R}}{m_{u4R}}\right), S_{10\_22} = 0$$

$$\begin{aligned} S_{11\_1}\dot{Z}_s + S_{11\_2}\dot{\theta} + S_{11\_3}\dot{\phi} + S_{11\_4}\dot{Z}_{u1R} + S_{11\_5}\dot{Z}_{u1L} + S_{11\_6}\dot{Z}_{u2R} + S_{11\_7}\dot{Z}_{u2L} \\ + S_{11\_8}\dot{Z}_{u3R} + S_{11\_9}\dot{Z}_{u3L} + S_{11\_10}\dot{Z}_{u4R} + S_{11\_11}\dot{Z}_{u4L} + S_{11\_12}Z_s \\ + S_{11\_13}\theta + S_{11\_14}\phi + S_{11\_15}Z_{u1R} + S_{11\_16}Z_{u1L} + S_{11\_17}Z_{u2R} \\ + S_{11\_18}Z_{u2L} + S_{11\_19}Z_{u3R} + S_{11\_20}Z_{u3L} + S_{11\_21}Z_{u4R} + S_{11\_22}Z_{u4L} \\ + \frac{1}{m_{u4L}}F_{(z4L)c} = \ddot{Z}_{u4L} \end{aligned} \tag{3-72}$$

Where

$$S_{11\_1} = \left(\frac{C_{d4L}}{m_{u4L}}\right), S_{11\_2} = \left(\frac{dC_{d4L}}{m_{u4L}}\right), S_{11\_3} = \left(\frac{tC_{d4L}}{2m_{u4L}}\right), S_{11\_4} = S_{11\_5} = S_{11\_6} = S_{11\_7} = 0$$

$$S_{11\_8} = S_{11\_9} = S_{11\_10} = 0, S_{11\_11} = \left(\frac{-C_{d4L}}{m_{u4L}}\right), S_{11\_12} = \left(\frac{K_{s4L}}{m_{u4L}}\right), S_{11\_13} = \left(\frac{dK_{s4L}}{m_{u4L}}\right)$$

$$S_{11\_14} = \left(\frac{tK_{s4L}}{2m_{u4L}}\right), S_{11\_15} = S_{11\_16} = S_{11\_17} = S_{11\_18} = S_{11\_19} = S_{11\_20} = S_{11\_21} = 0$$

$$S_{11\_22} = \left(\frac{-K_{s4L} - K_{t4L}}{m_{u4L}}\right)$$

By re-arranging equation (3-62) to (3-72) into state-space equations form((3-14) and (3-15)) with a slight modification on the time derivative of state variables equation, to include the disturbance caused by lateral acceleration. The modified state-space equation can be found as follows

$$\dot{X} = AX + BU + Ed_1 \tag{3-73}$$

Where

d_1 is a vector of disturbance variables

Thus, LQR vehicle plant model for SAS can be obtained as follows.

$$\dot{\mathrm{X}} = \begin{bmatrix} \ddot{Z}_s \\ \ddot{\theta} \\ \ddot{\phi} \\ \ddot{Z}_{u1R} \\ \ddot{Z}_{u1L} \\ \ddot{Z}_{u2R} \\ \ddot{Z}_{u2L} \\ \ddot{Z}_{u3R} \\ \ddot{Z}_{u3L} \\ \ddot{Z}_{u4R} \\ \ddot{Z}_{u4L} \\ \dot{Z}_s \\ \dot{\theta} \\ \dot{\phi} \\ \dot{Z}_{u1R} \\ \dot{Z}_{u1L} \\ \dot{Z}_{u2R} \\ \dot{Z}_{u2L} \\ \dot{Z}_{u3R} \\ \dot{Z}_{u3L} \\ \dot{Z}_{u4R} \\ \dot{Z}_{u4L} \end{bmatrix} = A \begin{bmatrix} \dot{Z}_s \\ \dot{\theta} \\ \dot{\phi} \\ \dot{Z}_{u1R} \\ \dot{Z}_{u1L} \\ \dot{Z}_{u2R} \\ \dot{Z}_{u2L} \\ \dot{Z}_{u3R} \\ \dot{Z}_{u3L} \\ \dot{Z}_{u4R} \\ \dot{Z}_{u4L} \\ Z_s \\ \theta \\ \phi \\ Z_{u1R} \\ Z_{u1L} \\ Z_{u2R} \\ Z_{u2L} \\ Z_{u3R} \\ Z_{u3L} \\ Z_{u4R} \\ Z_{u4L} \end{bmatrix} + B \begin{bmatrix} \mathrm{F}_{(z)c} \\ \mathrm{M}_{\theta} \\ \mathrm{M}_{\phi} \\ \mathrm{F}_{(z1R)c} \\ \mathrm{F}_{(z1L)c} \\ \mathrm{F}_{(z2R)c} \\ \mathrm{F}_{(z2L)c} \\ \mathrm{F}_{(z3R)c} \\ \mathrm{F}_{(z3L)c} \\ \mathrm{F}_{(z4R)c} \\ \mathrm{F}_{(z4L)c} \end{bmatrix} + E \begin{bmatrix} 0 \\ 0 \\ a_y \\ 0 \\ 0 \\ 0 \\ 0 \\ 0 \\ 0 \\ 0 \\ 0 \end{bmatrix} \qquad \text{(3-74)}$$

Where

A, B, E, C and D coefficient matrix are as follows

$$\mathrm{A} = \begin{bmatrix} \mathrm{S}_{\mathrm{ij}} & \cdots & \mathrm{S}_{\mathrm{i}_{22}} \\ \vdots & \ddots & \vdots \\ \mathrm{S}_{22_{\mathrm{j}}} & \cdots & \mathrm{S}_{22_{22}} \end{bmatrix}_{22\times 22}$$

Where

$$\mathrm{S}_{\mathrm{i}_{\mathrm{j}}} = \begin{cases} 1, & 11 < \mathrm{i} \leq 22 \text{ and } 1 \leq \mathrm{j} \leq 11 \\ 0, & \text{elsewhere} \end{cases}$$

$$B = \begin{bmatrix}
\frac{1}{m_s} & 0 & 0 & 0 & 0 & 0 & 0 & 0 & 0 & 0 & 0 \\
0 & \frac{1}{I_{YY}} & 0 & 0 & 0 & 0 & 0 & 0 & 0 & 0 & 0 \\
0 & 0 & \frac{1}{I_{XX}} & 0 & 0 & 0 & 0 & 0 & 0 & 0 & 0 \\
0 & 0 & 0 & \frac{1}{m_{u1R}} & 0 & 0 & 0 & 0 & 0 & 0 & 0 \\
0 & 0 & 0 & 0 & \frac{1}{m_{u1L}} & 0 & 0 & 0 & 0 & 0 & 0 \\
0 & 0 & 0 & 0 & 0 & \frac{1}{m_{u2R}} & 0 & 0 & 0 & 0 & 0 \\
0 & 0 & 0 & 0 & 0 & 0 & \frac{1}{m_{u2L}} & 0 & 0 & 0 & 0 \\
0 & 0 & 0 & 0 & 0 & 0 & 0 & \frac{1}{m_{u3R}} & 0 & 0 & 0 \\
0 & 0 & 0 & 0 & 0 & 0 & 0 & 0 & \frac{1}{m_{u3L}} & 0 & 0 \\
0 & 0 & 0 & 0 & 0 & 0 & 0 & 0 & 0 & \frac{1}{m_{u4R}} & 0 \\
0 & 0 & 0 & 0 & 0 & 0 & 0 & 0 & 0 & 0 & \frac{1}{m_{u4L}} \\
0 & 0 & 0 & 0 & 0 & 0 & 0 & 0 & 0 & 0 & 0 \\
0 & 0 & 0 & 0 & 0 & 0 & 0 & 0 & 0 & 0 & 0 \\
0 & 0 & 0 & 0 & 0 & 0 & 0 & 0 & 0 & 0 & 0 \\
0 & 0 & 0 & 0 & 0 & 0 & 0 & 0 & 0 & 0 & 0 \\
0 & 0 & 0 & 0 & 0 & 0 & 0 & 0 & 0 & 0 & 0 \\
0 & 0 & 0 & 0 & 0 & 0 & 0 & 0 & 0 & 0 & 0 \\
0 & 0 & 0 & 0 & 0 & 0 & 0 & 0 & 0 & 0 & 0 \\
0 & 0 & 0 & 0 & 0 & 0 & 0 & 0 & 0 & 0 & 0 \\
0 & 0 & 0 & 0 & 0 & 0 & 0 & 0 & 0 & 0 & 0 \\
0 & 0 & 0 & 0 & 0 & 0 & 0 & 0 & 0 & 0 & 0 \\
0 & 0 & 0 & 0 & 0 & 0 & 0 & 0 & 0 & 0 & 0
\end{bmatrix}$$

$$E = \begin{bmatrix} 0 & 0 & 0 & 0 & 0 & 0 & 0 & 0 & 0 & 0 & 0 \\ 0 & 0 & 0 & 0 & 0 & 0 & 0 & 0 & 0 & 0 & 0 \\ 0 & 0 & \frac{m_s h_{RC}}{I_{XX}} & 0 & 0 & 0 & 0 & 0 & 0 & 0 & 0 \\ 0 & 0 & 0 & 0 & 0 & 0 & 0 & 0 & 0 & 0 & 0 \\ 0 & 0 & 0 & 0 & 0 & 0 & 0 & 0 & 0 & 0 & 0 \\ 0 & 0 & 0 & 0 & 0 & 0 & 0 & 0 & 0 & 0 & 0 \\ 0 & 0 & 0 & 0 & 0 & 0 & 0 & 0 & 0 & 0 & 0 \\ 0 & 0 & 0 & 0 & 0 & 0 & 0 & 0 & 0 & 0 & 0 \\ 0 & 0 & 0 & 0 & 0 & 0 & 0 & 0 & 0 & 0 & 0 \\ 0 & 0 & 0 & 0 & 0 & 0 & 0 & 0 & 0 & 0 & 0 \\ 0 & 0 & 0 & 0 & 0 & 0 & 0 & 0 & 0 & 0 & 0 \\ 0 & 0 & 0 & 0 & 0 & 0 & 0 & 0 & 0 & 0 & 0 \\ 0 & 0 & 0 & 0 & 0 & 0 & 0 & 0 & 0 & 0 & 0 \\ 0 & 0 & 0 & 0 & 0 & 0 & 0 & 0 & 0 & 0 & 0 \\ 0 & 0 & 0 & 0 & 0 & 0 & 0 & 0 & 0 & 0 & 0 \\ 0 & 0 & 0 & 0 & 0 & 0 & 0 & 0 & 0 & 0 & 0 \\ 0 & 0 & 0 & 0 & 0 & 0 & 0 & 0 & 0 & 0 & 0 \\ 0 & 0 & 0 & 0 & 0 & 0 & 0 & 0 & 0 & 0 & 0 \\ 0 & 0 & 0 & 0 & 0 & 0 & 0 & 0 & 0 & 0 & 0 \\ 0 & 0 & 0 & 0 & 0 & 0 & 0 & 0 & 0 & 0 & 0 \\ 0 & 0 & 0 & 0 & 0 & 0 & 0 & 0 & 0 & 0 & 0 \\ 0 & 0 & 0 & 0 & 0 & 0 & 0 & 0 & 0 & 0 & 0 \end{bmatrix}$$

$$C = \begin{bmatrix} 1 & \cdots & 0 \\ \vdots & \ddots & \vdots \\ 0 & \cdots & 1 \end{bmatrix}_{22\times 22}$$

$$D = \begin{bmatrix} 0 & \cdots & 0 \\ \vdots & \ddots & \vdots \\ 0 & \cdots & 0 \end{bmatrix}_{22\times 11}$$

Chapter 4 HIERARCHICAL LQR CONTROL DESIGN

4.1 Introduction

All the proposed control strategies Active-AWS, DYC and SAS are in a hierarchical structure, which has upper and lower controllers. The upper controller for each control strategy is obtained, based on the multi-wheeled Combat Vehicle parameters and control level of motion. For Active-AWS, the upper controller provides the average steering angle for each steering axle, the first, second, third and fourth axle. While, for DYC, the upper controller generates the desired yaw moment needed to prohibit the vehicle from either drifting out or spinning and keep it on the desired trajectory. Moreover, for SAS the upper controller is responsible to generate the desired heave and vertical forces for sprung and un-sprung masses also the desired pitch and roll moment.

Whatever controller allocation strategy is, the lower controller's role is to manage either the desired average steering, corrective roll, pitch and yaw moment or heave and vertical forces determined by the upper controller.

For Active-AWS, the lower controller computes the steering angle needed for each axle's wheels (right and left) through a lockup table.

For DYC, the lower controller conducted in this thesis is TV and DB as a control allocation. The lower controller is designed on two stages for TV and three stages for DB. For TV, the first stage is to generate the optimal tractive forces needed ($F_{X_{tij}}$), based on the friction circle (workload) of each tire for each given axle at a given tire vertical load, while the second stage is a simple on/off slip controller for each tire to prevent exceeding the slip peak ratio. The DB control allocation adopts wheels braking coordination (double wheels braking used) as a first stage. Subsequently, an optimal braking force is obtained based on the normal load for the assigned braking wheels and finally the third stage is an on/off slip controller.

The lower controller of SAS is designed to control the leveling of the sprung and un-sprung masses (heave and bounce) and to reduce the longitudinal and lateral load transfer. By providing the desired damper forces and moments during vehicle maneuvers at limit handling.

The following sections are organized as follows: section (4.2) describes the theory of LQR control followed by the upper and lower controller design for Active-AWS, DYC and SAS in sections (4.3), (4.4) and (4.5) respectively.

4.2 Theory of LQR Controller

The LQR controller is considered to be a multi-input multi-output feedback control system. The LQR aims to minimize the cost function for given controlled state variables through an optimal solution obtained by a quadratic optimal regulator cost function [121] as shown in equation (4-1). While the LQR controller output (lower controller input) and gain matrix are given as follows in equations (4-2) and (4-3).

$$\mathrm{J} = \int_{0}^{\infty} (\mathrm{x}^{\mathrm{T}} * \mathrm{Qx} + \mathrm{u}^{\mathrm{T}} * \mathrm{Ru}\,)\, \mathrm{dt} \tag{4-1}$$

Where Q and R are a positive definite or real symmetric matrix, they are used to determine the proportion importance or as a weighting function for the importance of the state variables that needed to be controlled.

$$\mathrm{u(t)} = -\mathrm{Kx(t)} \tag{4-2}$$

$$\mathrm{K} = \mathrm{R}^{-1}\mathrm{B} * \mathrm{P} \tag{4-3}$$

K is the LQR gain matrix, where it is associated with RICCATI equation that used to minimize the cost function as follows.

$$\mathrm{A}^{*}\mathrm{P} + \mathrm{PA} - \mathrm{PBR}^{-1}\mathrm{B}^{*}\mathrm{P} + \mathrm{Q} = 0 \tag{4-4}$$

<u>Choosing LQR weighting function</u>

One of the major challenges in LQR design is that how to determine the weighting functions Q and R matrix [122]. The general form for the Q and R matrix is shown in equations (4-5) and (4-6). For the Q matrix, each individual $\mathrm{q_n}$ diagonal represents how much weighting value will be given to state variables based on their importance. while for the R matrix each individual ρ_n is chosen in corresponding to each state variables to penalize the control input to the system by giving higher or lower weighting value based on its importance.

$$Q = \begin{bmatrix} \frac{1}{{q_1}^2} & \cdots & 0 \\ \vdots & \ddots & \vdots \\ 0 & \cdots & \frac{1}{{q_n}^2} \end{bmatrix} \tag{4-5}$$

$$R = \begin{bmatrix} \rho_1 & \cdots & 0 \\ \vdots & \ddots & \vdots \\ 0 & \cdots & \rho_n \end{bmatrix} \tag{4-6}$$

4.3 LQR Controller Design for Active-AWS

4.3.1 Upper Controller Design

By considering the generated LQR vehicle plant model for Active-AWS in state-space form as provided in equation (3-16) in section (3.2), A and B matrix can be found. The Q matrix introduced in equation (4-5) is calculated based on the two empirical formulas that are presented in equations (3-39) and (3-40) in section (3.4). Therefore, the Q matrix can be obtained as follows.

$$Q = \begin{bmatrix} \frac{1}{\beta_{des}^2} & 0 \\ 0 & \frac{1}{r_{des}^2} \end{bmatrix} \tag{4-7}$$

While R matrix presented in equation (4-6) is manually tuned as a control input to the system as follows.

$$R = \begin{bmatrix} \rho_{\delta_{1c}} & 0 & 0 & 0 \\ 0 & \rho_{\delta_{2c}} & 0 & 0 \\ 0 & 0 & \rho_{\delta_3} & 0 \\ 0 & 0 & 0 & \rho_{\delta_4} \end{bmatrix} \tag{4-8}$$

After computing Q and R matrix, P can be obtained using RICCATI equation presented in equation (4-4). Hence, the desired LQR controller gain (K) provided in equation (4-3) can be obtained for Active All-AWS ($\mathrm{K}_{\text{Active All-AWS}}$).

4.3.2 Lower Controller Design

As discussed in the previous section, the upper controller level is responsible to generate the desired gains that needed to be allocated by the lower controller level. Accordingly, these obtained gains are multiplied by the state variables errors during the simulation event, forming the average steering angles for each axle as an input for the lower controller level. These average steering angles determine the corrective steering angle needed for the left and right wheel of each axle through a lookup table.

The average steering angle of each axle (δ_{avg}) are calculated as follows in equation (4-10), while the lookup table can be computed based on equation (4-9) considering the inner and outer wheel steering angles δ_{i} and δ_{o} , respectively, whereas t is vehicle's track width and L_i represent the distance from the center of i^{th} axle to the vehicle's center of gravity.

$$\delta_{\mathrm{avg}} = \frac{\delta_{\mathrm{i}} + \delta_{\mathrm{o}}}{2} \tag{4-9}$$

$$\mathrm{Cot}(\delta_{\mathrm{o}}) - \mathrm{Cot}(\delta_{\mathrm{i}}) = \frac{\mathrm{t}}{\mathrm{L}_i} \tag{4-10}$$

By substituting in the previous equations (4-9) and (4-10) [123], the corrective steering angles for the first, second, third and fourth axle left and right wheel can be obtained as illustrated in Figure 4-1, Figure 4-2, Figure 4-3 and Figure 4-4 respectively.

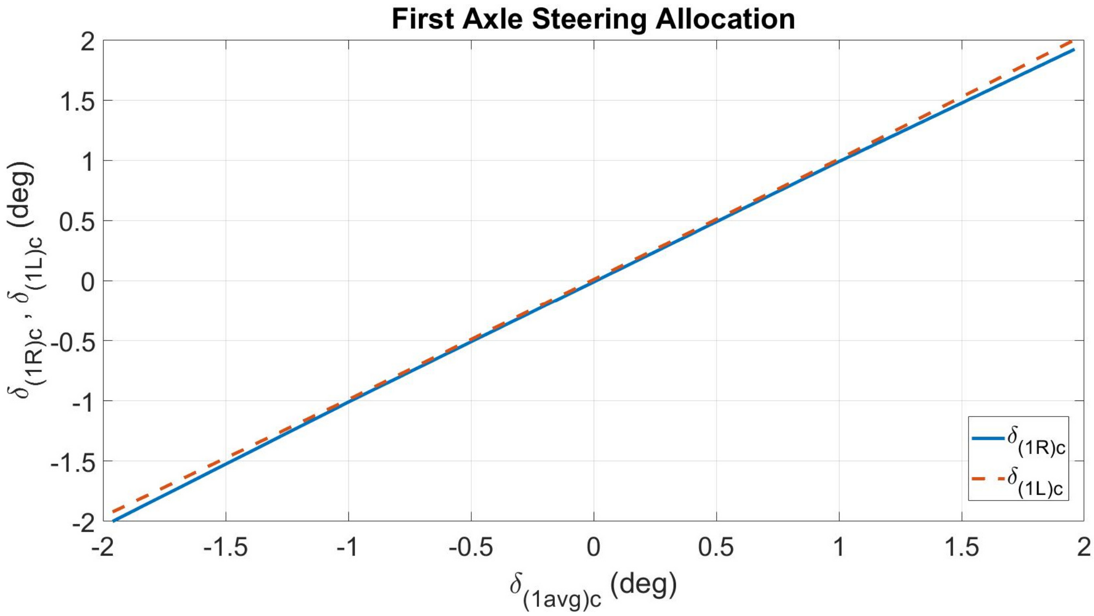

Figure 4-1 First axle left and right corrective wheel steering angles

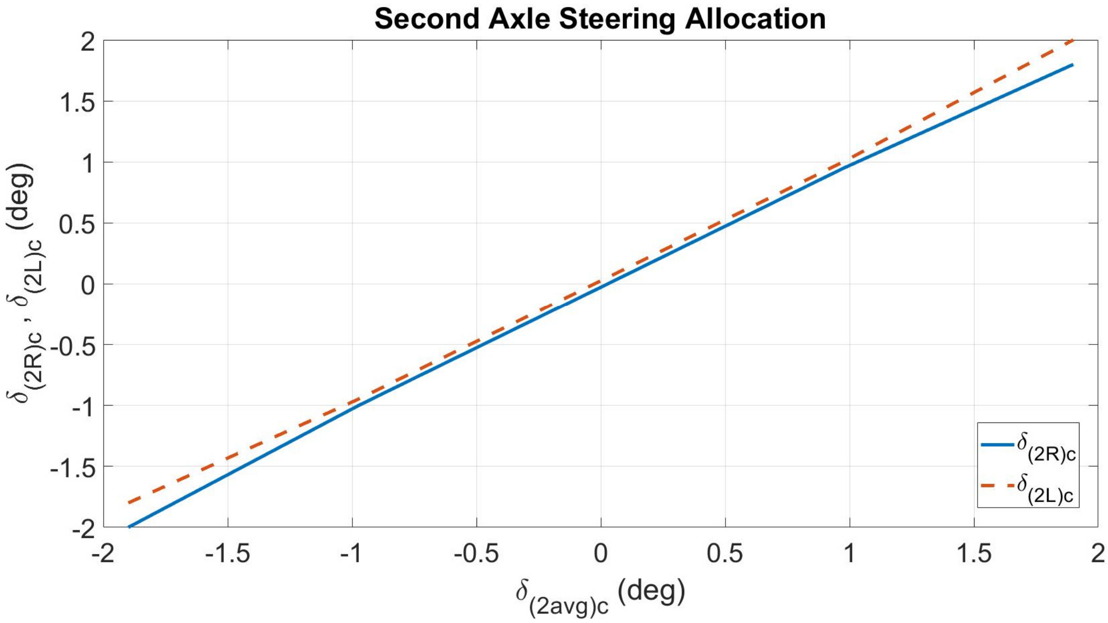

Figure 4-2 Second axle left and right corrective wheel steering angles

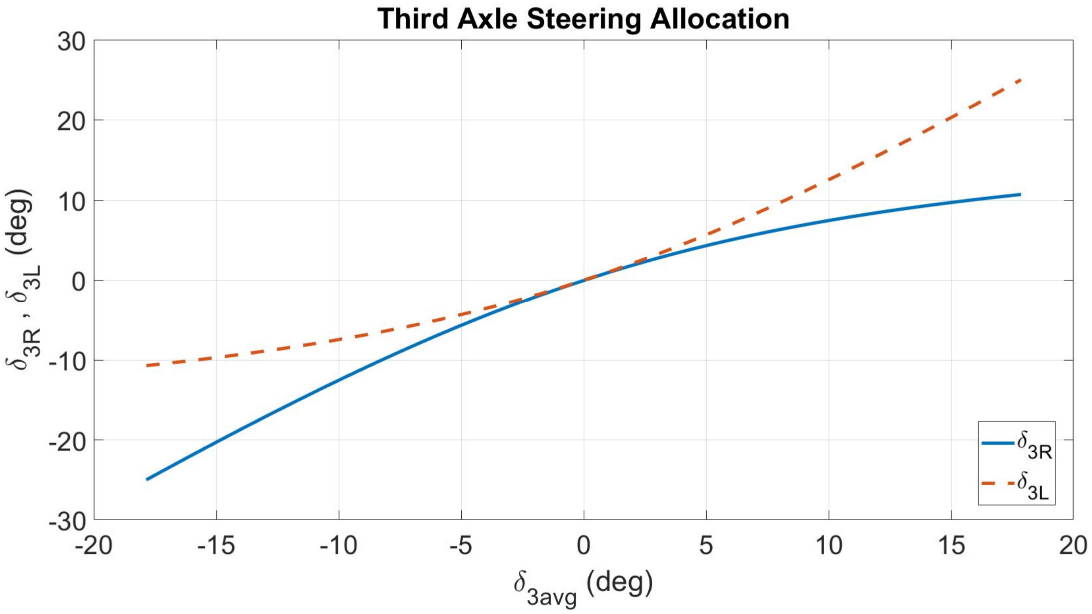

Figure 4-3 Third axle left and right corrective wheel steering angles

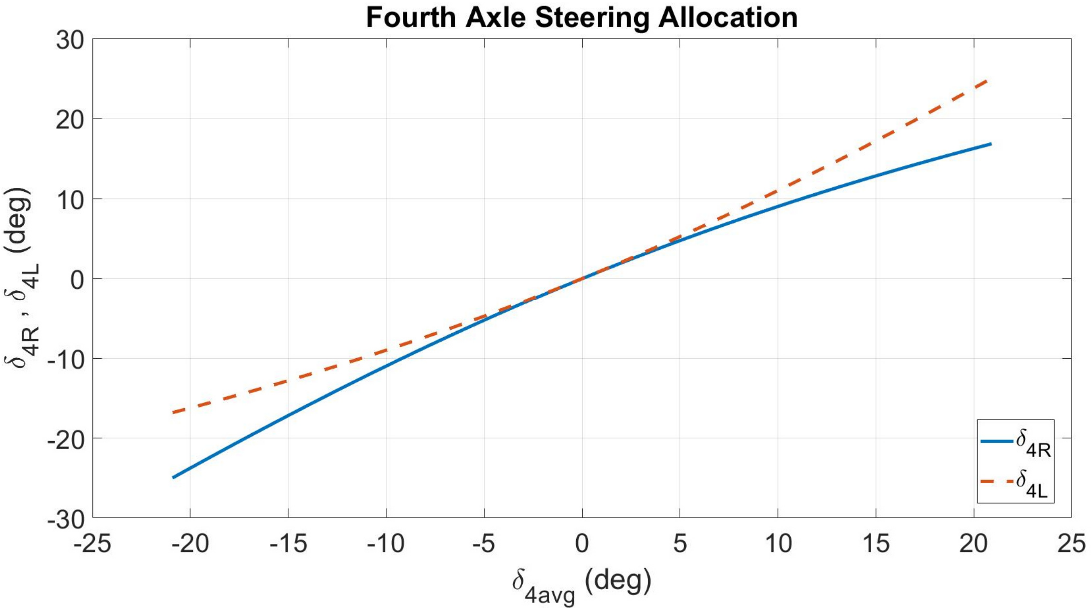

Figure 4-4 Fourth axle left and right corrective wheel steering angles

Note: the maximum allowable corrective steering angle added to the vehicle's first and second axle steering angle is two degrees, while the maximum corrective steering angle of the third and fourth axle are set to be 25 degrees.

4.4 LQR Controller Design for DYC

The proposed direct yaw moment control is a hierarchical control strategy, which has upper and lower controllers. The upper controller is multi-wheeled Combat Vehicle parameters and the control level of motion. The upper controller generates the desired yaw moment needed to prohibit the vehicle from either drifting out or spinning and keep it on the desired trajectory. The lower controller conducted in this thesis is TV and DB as a control allocation. The lower controller is designed on two stages for TV and three stages for DB. For TV, the first stage is to generate the optimal tractive forces needed (F_{Xtij}), based on the friction circle (workload) of each tire for each given axle at a given tire vertical load, while the second stage is a simple on/off slip controller for each tire to prevent exceeding the slip peak ratio. The DB control allocation adopts wheels braking coordination (double wheels braking used) as a first stage. Subsequently, an optimal braking force is obtained based on the normal load for the assigned braking wheels and finally the third stage is an on/off slip controller.

4.4.1 Upper controller design for DYC

By referring to equation (3-32) in section (3.3) generated in state-space form that represents the LQR vehicle plant model for DYC, A and B matrix can be evaluated. The Q matrix presented in equation (4-5) is obtained based on the two empirical formulas that are introduced in equations (3-39) and (3-40) in section (3.4). Consequently, the Q matrix can be found similarly as in equation (4-7).

Nevertheless, R matrix introduced in equation (4-6) is manually tuned as a control input to the system as follows.

$$R = \begin{bmatrix} \rho_{\delta_1} & 0 \\ 0 & \rho_{M_Z} \end{bmatrix} \tag{4-11}$$

Note: since the first axle steering angle is not controlled, accordingly, ρ_{δ_1} is assigned higher weight to neglect its effect.

In similar fashion, after computing Q and R matrix, P can be determined based on RICCATI equation presented in equation (4-4). Thus, the desired LQR controller gain (K) introduced in equation (4-3) can be obtained for DYC (K_{DYC}).

4.4.2 Lower control level design for TV allocation strategy

The lower control level for TV as control allocation strategy is designed to meet the friction circle for each individual tire of the multi-wheeled Combat Vehicle. considering the friction force limitation shared between the longitudinal and lateral forces for each individual tire based on the normal load for each tire. As well as a slip controller is introduced to control and prevent each tire from exceeding slip peak ratio λ_{Peak} and keep each tire to work up to maximum adhesion effort without slipping.

As discussed previously, the lower controller allocation for TV is designed in two stages. The following sub-sections describe the optimal tractive forces distribution as the first stage for TV, followed by wheel dynamics then an ON/Off slip controller is implemented for a driving case as the second stage.

4.4.2.1 Stage 1: Optimal longitudinal tire forces (tractive) distribution for TV

The required corrective yaw moment is dependent on the tire longitudinal forces generated between the tire contact patch and road. During cornering maneuver, the work-load of each individual tire is shared between the longitudinal and lateral forces, so if the longitudinal force (tractive or braking) on each individual tire has exceeded the Friction Circle limitation, as a result, this may lead in increasing the tires slip ratio and decreasing the required lateral forces needed to make the vehicle maintain the cornering maneuver, also if the lateral forces deteriorate, the vehicle may drift out or spin. Therefore, a cost function is developed to compromise between longitudinal and lateral forces for each tire based on the theory of friction circle [109], therefore the chosen cost function is presented as follows.

$$J = \sum W_{ij}\, \mu_{ij}^2 = \sum W_{ij}\, \frac{F_{Xij}^2 + F_{Yij}^2}{F_{Zij}^2} \tag{4-12}$$

$$J = W_{1R}\frac{F_{X1R}^2 + F_{Y1R}^2}{F_{Z1R}^2} + W_{1L}\frac{F_{X1L}^2 + F_{Y1L}^2}{F_{Z1L}^2} + W_{2R}\frac{F_{X2R}^2 + F_{Y2R}^2}{F_{Z2R}^2} + W_{2L}\frac{F_{X2L}^2 + F_{Y2L}^2}{F_{Z2L}^2} + W_{3R}\frac{F_{X3R}^2 + F_{Y3R}^2}{F_{Z3R}^2} + W_{3L}\frac{F_{X3L}^2 + F_{Y3L}^2}{F_{Z3L}^2} + W_{4R}\frac{F_{X4R}^2 + F_{Y4R}^2}{F_{Z4R}^2} + W_{4L}\frac{F_{X4L}^2 + F_{Y4L}^2}{F_{Z4L}^2} \tag{4-13}$$

There are two equally constraints, first constraint is that the total desired longitudinal force needed to satisfy the driver intended traction command, where it should equal the sum of longitudinal force produced by each individual tire is described in as follows.

$$F_{Xdes} = F_{X1R} + F_{X1L} + F_{X2R} + F_{X2L} + F_{X3R} + F_{X3L} + F_{X4R} + F_{X4L} \tag{4-14}$$

Where, $F_{Xdes} = ma_{X-desired}$, and $a_{X-desired}$ can be deceleration in case of braking

The second constraint is that the desired corrective yaw moment that should be equal the sum of the moments produced by each longitudinal force of each individual tire as presented as follows.

$$M_Z = [F_{X1R} - F_{X1L} + F_{X2R} - F_{X2L} + F_{X3R} - F_{X3L} + F_{X4R} - F_{X4L}]\,\frac{t}{2} \tag{4-15}$$

Since the cost function has eight variables and two constraints, hence, it can be used to reduce the number of variables as follows.

$$F_{X3L} = \frac{1}{2}F_{Xdes} - \frac{1}{t}M_Z - F_{X1L} - F_{X2L} - F_{X4L} \tag{4-16}$$

$$F_{X3R} = \frac{1}{2}F_{Xdes} + \frac{1}{t}M_Z - F_{X1R} - F_{X2R} - F_{X4R} \tag{4-17}$$

After plug-in equations (4-16) and (4-17) in cost function equation (4-13), yields an unconstrained cost function as follows.

$$J = W_{1R}\,\frac{F_{X1R}^2 + F_{Y1R}^2}{F_{Z1R}^2} + W_{1L}\,\frac{F_{X1L}^2 + F_{Y1L}^2}{F_{Z1L}^2} + W_{2R}\,\frac{F_{X2R}^2 + F_{Y2R}^2}{F_{Z2R}^2} + W_{2L}\,\frac{F_{X2L}^2 + F_{Y2L}^2}{F_{Z2L}^2} + W_{3R}\,\frac{(\frac{1}{2}F_{Xdes} + \frac{1}{t}M_Z - F_{X1R} - F_{X2R} - F_{X4R})^2 + F_{Y3R}^2}{F_{Z3R}^2} + W_{3L}\,\frac{(\frac{1}{2}F_{Xdes} - \frac{1}{t}M_Z - F_{X1L} - F_{X2L} - F_{X4L})^2 + F_{Y3L}^2}{F_{Z3L}^2} + W_{4R}\,\frac{F_{X4R}^2 + F_{Y4R}^2}{F_{Z4R}^2} + W_{4L}\,\frac{F_{X4L}^2 + F_{Y4L}^2}{F_{Z4L}^2} \tag{4-18}$$

Now, in order to minimize the cost function, it should satisfy the following condition as follows.

$$\frac{\partial J}{\partial F_{X1R}} = \frac{2W_{1R}}{F_{Z1R}^2}\,F_{X1R} - \frac{2W_{3R}\left(\frac{1}{2}F_{Xdes} + \frac{1}{t}M_Z - F_{X1R} - F_{X2R} - F_{X4R}\right)}{F_{Z3R}^2} = 0 \tag{4-19}$$

$$\frac{\partial J}{\partial F_{X1L}} = \frac{2W_{1L}}{F_{Z1L}^2}\,F_{X1L} - \frac{2W_{3L}\left(\frac{1}{2}F_{Xdes} - \frac{1}{t}M_Z - F_{X1L} - F_{X2L} - F_{X4L}\right)}{F_{Z3L}^2} = 0 \tag{4-20}$$

$$\frac{\partial J}{\partial F_{X2R}} = \frac{2W_{2R}}{F_{Z2R}^2}\,F_{X2R} - \frac{2W_{3R}\left(\frac{1}{2}F_{Xdes} + \frac{1}{t}M_Z - F_{X1R} - F_{X2R} - F_{X4R}\right)}{F_{Z3R}^2} = 0 \tag{4-21}$$

$$\frac{\partial J}{\partial F_{X2L}} = \frac{2W_{2L}}{F_{Z2L}^2}\,F_{X2L} - \frac{2W_{3L}\left(\frac{1}{2}F_{Xdes} - \frac{1}{t}M_Z - F_{X1L} - F_{X2L} - F_{X4L}\right)}{F_{Z3L}^2} = 0 \tag{4-22}$$

$$\frac{\partial J}{\partial F_{X4R}} = \frac{2W_{4R}}{F_{Z4R}^2}\,F_{X4R} - \frac{2W_{3R}\left(\frac{1}{2}F_{Xdes} + \frac{1}{t}M_Z - F_{X1R} - F_{X2R} - F_{X4R}\right)}{F_{Z3R}^2} = 0 \tag{4-23}$$

$$\frac{\partial J}{\partial F_{X4L}} = \frac{2W_{4L}}{F_{Z4L}^2}\,F_{X4L} - \frac{2W_{3L}\left(\frac{1}{2}F_{Xdes} - \frac{1}{t}M_Z - F_{X1L} - F_{X2L} - F_{X4L}\right)}{F_{Z3L}^2} = 0 \tag{4-24}$$

After an algebraic manipulation, the optimal longitudinal forces matrix form as follows.

$$\begin{bmatrix} F_{X1R} \\ F_{X1L} \\ F_{X2R} \\ F_{X2L} \\ F_{X4R} \\ F_{X4L} \end{bmatrix} = \begin{bmatrix} H_{1R+3R} & H_0 & H_{3R} & H_0 & H_{3R} & H_0 \\ H_0 & H_{1L+3L} & H_0 & H_{3L} & H_0 & H_{3L} \\ H_{3R} & H_0 & H_{2R+3R} & H_0 & H_{3R} & H_0 \\ H_0 & H_{3L} & H_0 & H_{2L+3L} & H_0 & H_{3L} \\ H_{3R} & H_0 & H_{3R} & H_0 & H_{4R+3R} & H_0 \\ H_0 & H_{3L} & H_0 & H_{3L} & H_0 & H_{4L+3L} \end{bmatrix}^{-1} \times \left(\begin{bmatrix} \frac{H_{3R}}{t} \\ -\frac{H_{3L}}{t} \\ \frac{H_{3R}}{t} \\ -\frac{H_{3L}}{t} \\ \frac{H_{3R}}{t} \\ -\frac{H_{3L}}{t} \end{bmatrix} M_Z + \begin{bmatrix} H_{3R} \\ H_{3L} \\ H_{3R} \\ H_{3L} \\ H_{3R} \\ H_{3L} \end{bmatrix} F_{Xdes} \right) \tag{4-25}$$

Where

$H_0 = 0$, $H_{3R} = \frac{2W_{3R}}{F_{Z3R}^2}$, $H_{3L} = \frac{2W_{3L}}{F_{Z3L}^2}$,

$H_{1R+3R} = \frac{2W_{1R}}{F_{Z1R}^2} + \frac{2W_{3R}}{F_{Z3R}^2}$, $H_{1L+3L} = \frac{2W_{1L}}{F_{Z1L}^2} + \frac{2W_{3L}}{F_{Z3L}^2}$,

$H_{2R+3R} = \frac{2W_{2R}}{F_{Z2R}^2} + \frac{2W_{3R}}{F_{Z3R}^2}$, $H_{2L+3L} = \frac{2W_{2L}}{F_{Z2L}^2} + \frac{2W_{3L}}{F_{Z3L}^2}$,

$H_{4R+3R} = \frac{2W_{4R}}{F_{Z4R}^2} + \frac{2W_{3R}}{F_{Z3R}^2}$, $H_{4L+3L} = \frac{2W_{4L}}{F_{Z4L}^2} + \frac{2W_{3L}}{F_{Z3L}^2}$

Wheel Dynamics

A free body diagram of forces and moments that apply on the tire during the driving case as illustrated in Figure 4-5. Taking the summation of the moment at wheel center, yields the general form of wheel dynamics equation as presented as follows.

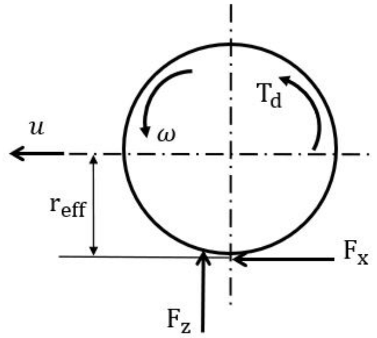

Figure 4-5 free body diagram for wheel during driving case

$$I_{wij}\frac{d\omega}{dt} = T_{dij} - F_{xij}r_{eff} - F_{Zij}f \tag{4-26}$$

where I_w is the mass moment of inertia of the wheel, $\frac{d\omega}{dt}$ is the rate of change of angular velocity of the wheel, r_{eff} is the effective rolling radius of the tire, F_{xij} is the longitudinal force, T_{dij} is the driving torque, F_Z is the normal load applies on tire, f is the rolling resistance coefficient. While subscripts i and j are for axle number and left or right respectively and u is the longitudinal velocity.

Assuming $I_{wij}\frac{d\omega}{dt}$ are small value and rolling resistance, force is not considered in the calculations, therefore they can be neglected. Accordingly based on these assumptions, in case of driving no braking torque $T_b = 0$, the new equation for driving torque may be reduced as follows.

$$T_{dij} = F_{xij}r_{eff} \tag{4-27}$$

4.4.2.2 Stage 2: slip ratio controller

A slip controller is introduced to control and prevent each tire from exceeding slip peak (threshold) ratio λ_{Peak} , which is set to 20 % to keep each tire to work up to maximum adhesion effort without slipping. The governing equation that describes the tire slip ratio in driving scenario is shown as follows.

$$\lambda_{ij} = \frac{w_{ij} r_{eff_{ij}} - v_{ij}}{w_{ij} r_{eff_{ij}}} \quad \text{for driving} \tag{4-28}$$

Where λ is the slip ratio, the angular speed of the wheel is w, the speed at the center of the of wheel is v, r is the effective rolling radius of the tire and finally the subscripts I and j are for axle number and left or right respectively.

4.4.3 Lower control level design for DB allocation strategy

The lower control level for the DB allocation strategy is performed on three stages as follows. Coordination of selection wheels braking logic is introduced as a first stage. Subsequently, the second stage is to generate the optimal braking forces based on the selected double wheels that are carried out in the first stage, followed by wheel dynamics. And finally, an ON/Off slip controller is designed for the braking scenario as a third stage.

4.4.3.1 Stage 1: Wheel braking torque coordination

The first stage introduces coordination of which wheels braking torque should be engaged to maintain the vehicle on the desired trajectory. Double wheels braking is employed in this thesis. The coordination logic is based on the sign of the corrective moment generated by the LQR controller and the difference between the absolute values of desired and actual yaw rate. if the corrective moment is a positive sign and the difference between the absolute values of actual and desired yaw rate is a positive sign, this means that the front axles left braking wheels torque should be activated (wheels 1L,2L) as shown in Figure 4-6. It can be assumed that if the actual yaw rate is bigger than the desired yaw rate, the vehicle exhibits spinning and if the actual yaw rate is smaller than the desired yaw rate, the vehicle is drifting out [86, 87]. Based on this logic, Table 4-1 shows the coordination between wheels braking torque selection.

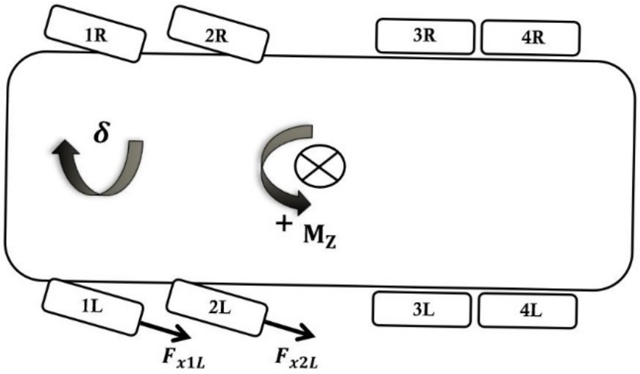

Figure 4-6 Double wheels braking 1L, 2L engaged in case $|r_{actual}| > |r_{desired}|$

Table 4-1 Double wheel braking torque selection logic

	M_Z (+)	M_Z (−)
$\lvert r_{actual}\rvert > \lvert r_{desired}\rvert$	Wheels 1L_2L	Wheels 1R_2R
$\lvert r_{actual}\rvert < \lvert r_{desired}\rvert$	Wheels 3L_4L	Wheels 3R_4R

4.4.3.2 Stage 2: Optimal longitudinal tire forces (braking) for DB

By referring to equation (4-13) and after mathematical manipulations, the final equations for each double wheel braking forces are presented as follows.

$$F_{X1R} = \frac{-\frac{4W_{2R}}{tF_{Z2R}^2}}{\frac{2W_{1R}}{F_{Z1R}^2} + \frac{2W_{2R}}{F_{Z2R}^2}} M_Z \tag{4-29}$$

$$F_{X2R} = -\frac{2}{t} M_Z - F_{X1R} \tag{4-30}$$

$$F_{X1L} = \frac{\frac{4W_{2L}}{tF_{Z2L}^2}}{\frac{2W_{1L}}{F_{Z1L}^2} + \frac{2W_{2L}}{F_{Z2L}^2}} M_Z \tag{4-31}$$

$$F_{X2L} = \frac{2}{t} M_Z - F_{X1L} \tag{4-32}$$

$$F_{X3R} = \frac{-\frac{4W_{4R}}{tF_{Z4R}^2}}{\frac{2W_{3R}}{F_{Z3R}^2} + \frac{2W_{4R}}{F_{Z4R}^2}} M_Z \tag{4-33}$$

$$F_{X4R} = -\frac{2}{t} M_Z - F_{X3R} \tag{4-34}$$

$$F_{X3L} = \frac{\frac{4W_{4L}}{tF_{Z4L}^2}}{\frac{2W_{3L}}{F_{Z3L}^2} + \frac{2W_{4L}}{F_{Z4L}^2}} M_Z \tag{4-35}$$

$$F_{X4L} = \frac{2}{t} M_Z - F_{X3L} \tag{4-36}$$

Wheel Dynamics

A free body diagram demonstrates the forces and moments that apply on the tire during braking case as shown in Figure 4-7, where T_{bij} is the braking torque. Taking summation of moment at wheel center results the general form of wheel dynamics equation as presented as follows.

$$I_{wij}\frac{d\omega}{dt} = -T_{bij} - F_{Zij}f + F_{xij}r_{eff} \tag{4-37}$$

Assuming $I_{wij}\frac{d\omega}{dt}$ are small value and rolling resistance, force is not considered in the calculations, therefore they can be neglected. Accordingly based on these assumptions, in case of braking torque, the new equation for braking torque may be reduced as follows.

$$T_{bij} = F_{xij}r_{eff} \tag{4-38}$$

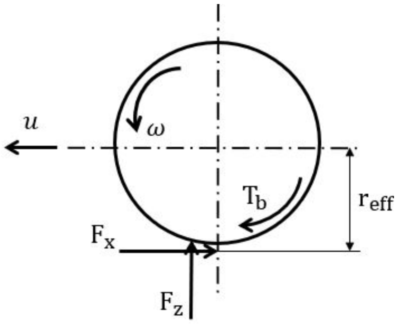

Figure 4-7 free body diagram for wheel during braking case

4.4.3.3 Stage 3: slip ratio controller

The slip controller is simply based on on/off control, which prevents any individual tire from exceeding the slip peak ratio λ_{Peak} , which is set to 20%. In case of braking scenario.

$$\lambda_{ij} = \frac{v_{ij} - w_{ij} r_{eff_{ij}}}{v_{ij}} \quad \text{for braking} \tag{4-39}$$

4.5 LQR Controller Design for SAS

4.5.1 Upper control level design for SAS allocation strategy

By investigating the LQR vehicle plant model for SAS obtained in state-space form in equation (3-74) in section (3.5), A and B coefficients matrix can be obtained. The Q and R matrix presented in equations (4-5) and (4-6) respectively, are tuned manually putting much weight for sprung mass heave (Z_s), pitch (θ) and roll (ϕ) motion and their control inputs as follows.

$$
\begin{aligned}
Q = [&\dot{Z}_s\ 0\ 0\ 0\ 0\ 0\ 0\ 0\ 0\ 0\ 0\ 0\ 0\ 0\ 0\ 0\ 0\ 0\ 0\ 0\ 0\ 0;\\
&0\ \dot{\theta}\ 0\ 0\ 0\ 0\ 0\ 0\ 0\ 0\ 0\ 0\ 0\ 0\ 0\ 0\ 0\ 0\ 0\ 0\ 0\ 0;\\
&0\ 0\ \dot{\phi}\ 0\ 0\ 0\ 0\ 0\ 0\ 0\ 0\ 0\ 0\ 0\ 0\ 0\ 0\ 0\ 0\ 0\ 0\ 0;\\
&0\ 0\ 0\ \dot{Z}_{u1R}\ 0\ 0\ 0\ 0\ 0\ 0\ 0\ 0\ 0\ 0\ 0\ 0\ 0\ 0\ 0\ 0\ 0\ 0;\\
&0\ 0\ 0\ 0\ \dot{Z}_{u1L}\ 0\ 0\ 0\ 0\ 0\ 0\ 0\ 0\ 0\ 0\ 0\ 0\ 0\ 0\ 0\ 0\ 0;\\
&0\ 0\ 0\ 0\ 0\ \dot{Z}_{u2R}\ 0\ 0\ 0\ 0\ 0\ 0\ 0\ 0\ 0\ 0\ 0\ 0\ 0\ 0\ 0\ 0;\\
&0\ 0\ 0\ 0\ 0\ 0\ \dot{Z}_{u2L}\ 0\ 0\ 0\ 0\ 0\ 0\ 0\ 0\ 0\ 0\ 0\ 0\ 0\ 0\ 0;\\
&0\ 0\ 0\ 0\ 0\ 0\ 0\ \dot{Z}_{u3R}\ 0\ 0\ 0\ 0\ 0\ 0\ 0\ 0\ 0\ 0\ 0\ 0\ 0\ 0;\\
&0\ 0\ 0\ 0\ 0\ 0\ 0\ 0\ \dot{Z}_{u3L}\ 0\ 0\ 0\ 0\ 0\ 0\ 0\ 0\ 0\ 0\ 0\ 0\ 0;\\
&0\ 0\ 0\ 0\ 0\ 0\ 0\ 0\ 0\ \dot{Z}_{u4R}\ 0\ 0\ 0\ 0\ 0\ 0\ 0\ 0\ 0\ 0\ 0\ 0;\\
&0\ 0\ 0\ 0\ 0\ 0\ 0\ 0\ 0\ 0\ \dot{Z}_{u4L}\ 0\ 0\ 0\ 0\ 0\ 0\ 0\ 0\ 0\ 0\ 0;\\
&0\ 0\ 0\ 0\ 0\ 0\ 0\ 0\ 0\ 0\ 0\ Z_s\ 0\ 0\ 0\ 0\ 0\ 0\ 0\ 0\ 0\ 0;\\
&0\ 0\ 0\ 0\ 0\ 0\ 0\ 0\ 0\ 0\ 0\ 0\ \theta\ 0\ 0\ 0\ 0\ 0\ 0\ 0\ 0\ 0;\\
&0\ 0\ 0\ 0\ 0\ 0\ 0\ 0\ 0\ 0\ 0\ 0\ 0\ \phi\ 0\ 0\ 0\ 0\ 0\ 0\ 0\ 0;\\
&0\ 0\ 0\ 0\ 0\ 0\ 0\ 0\ 0\ 0\ 0\ 0\ 0\ 0\ Z_{u1R}\ 0\ 0\ 0\ 0\ 0\ 0\ 0;\\
&0\ 0\ 0\ 0\ 0\ 0\ 0\ 0\ 0\ 0\ 0\ 0\ 0\ 0\ 0\ Z_{u1L}\ 0\ 0\ 0\ 0\ 0\ 0;\\
&0\ 0\ 0\ 0\ 0\ 0\ 0\ 0\ 0\ 0\ 0\ 0\ 0\ 0\ 0\ 0\ Z_{u2R}\ 0\ 0\ 0\ 0\ 0;\\
&0\ 0\ 0\ 0\ 0\ 0\ 0\ 0\ 0\ 0\ 0\ 0\ 0\ 0\ 0\ 0\ 0\ Z_{u2L}\ 0\ 0\ 0\ 0;\\
&0\ 0\ 0\ 0\ 0\ 0\ 0\ 0\ 0\ 0\ 0\ 0\ 0\ 0\ 0\ 0\ 0\ 0\ Z_{u3R}\ 0\ 0\ 0;\\
&0\ 0\ 0\ 0\ 0\ 0\ 0\ 0\ 0\ 0\ 0\ 0\ 0\ 0\ 0\ 0\ 0\ 0\ 0\ Z_{u3L}\ 0\ 0;\\
&0\ 0\ 0\ 0\ 0\ 0\ 0\ 0\ 0\ 0\ 0\ 0\ 0\ 0\ 0\ 0\ 0\ 0\ 0\ 0\ Z_{u4R}\ 0;\\
&0\ 0\ 0\ 0\ 0\ 0\ 0\ 0\ 0\ 0\ 0\ 0\ 0\ 0\ 0\ 0\ 0\ 0\ 0\ 0\ 0\ Z_{u4L}]
\end{aligned}
\tag{4-40}
$$

$$
R = \begin{bmatrix}
\rho_{F_{(z)c}} & 0 & 0 & 0 & 0 & 0 & 0 & 0 & 0 & 0 & 0\\
0 & \rho_{M_\theta} & 0 & 0 & 0 & 0 & 0 & 0 & 0 & 0 & 0\\
0 & 0 & \rho_{M_\phi} & 0 & 0 & 0 & 0 & 0 & 0 & 0 & 0\\
0 & 0 & 0 & \rho_{F_{(z1R)c}} & 0 & 0 & 0 & 0 & 0 & 0 & 0\\
0 & 0 & 0 & 0 & \rho_{F_{(z1L)c}} & 0 & 0 & 0 & 0 & 0 & 0\\
0 & 0 & 0 & 0 & 0 & \rho_{F_{(z2R)c}} & 0 & 0 & 0 & 0 & 0\\
0 & 0 & 0 & 0 & 0 & 0 & \rho_{F_{(z2L)c}} & 0 & 0 & 0 & 0\\
0 & 0 & 0 & 0 & 0 & 0 & 0 & \rho_{F_{(z3R)c}} & 0 & 0 & 0\\
0 & 0 & 0 & 0 & 0 & 0 & 0 & 0 & \rho_{F_{(z3L)c}} & 0 & 0\\
0 & 0 & 0 & 0 & 0 & 0 & 0 & 0 & 0 & \rho_{F_{(z4R)c}} & 0\\
0 & 0 & 0 & 0 & 0 & 0 & 0 & 0 & 0 & 0 & \rho_{F_{(z4L)c}}
\end{bmatrix}
\tag{4-41}
$$

In the same manner, after computing Q and R matrix, P can be solved based on RICCATI equation as presented in equation (4-4). Hence, the desired LQR controller gain (K) introduced in equation (4-3) can be obtained for SAS (K_{SAS}).

4.5.2 Lower control level design for SAS allocation strategy

As described in the aforementioned section, the upper control level generates the required gains needed to stabilize and maintain the load-leveling, longitudinal, and lateral load transfer during different maneuvers scenarios (driving, braking, and cornering). Since the vehicle is equipped with eight dampers, that are intended to control eleven state variables, namely sprung mass's heave, pitch and roll motion and unsprung masses' vertical motions. This over-actuation problem can be resolved by merging all the obtained gains to provide the desired dampers force and moments needed to achieve their targets.

The equivalent forces and moments produced by the dampers for sprung mass's heave, pitch and roll motion are presented as follows.

$$F_{(z)c} = F_{d1R} + F_{d1L} + F_{d2R} + F_{d2L} + F_{d3R} + F_{d3L} + F_{d4R} + F_{d4L} \tag{4-42}$$

$$M_{\theta} = -(F_{d1R} + F_{d1L})a - (F_{d2R} + F_{d2L})b + (F_{d3R} + F_{d3L})c + (F_{d4R} + F_{d4L})d \tag{4-43}$$

$$M_{\phi} = (F_{d1L} - F_{d1R})\frac{t}{2} + (F_{d2L} - F_{d2R})\frac{t}{2} + (F_{d3L} - F_{d3R})\frac{t}{2} + (F_{d4L} - F_{d4R})\frac{t}{2} \tag{4-44}$$

By combining the gains obtained for un-sprung masses with equations (4-42), (4-43) and (4-44) and re-arrange them in matrix form yields as follows.

$$\begin{bmatrix} F_{(z)c} \\ M_{\theta} \\ M_{\phi} \\ F_{(z1R)c} \\ F_{(z1L)c} \\ F_{(z2R)c} \\ F_{(z2L)c} \\ F_{(z3R)c} \\ F_{(z3L)c} \\ F_{(z4R)c} \\ F_{(z4L)c} \end{bmatrix} = \begin{bmatrix} 1 & 1 & 1 & 1 & 1 & 1 & 1 & 1 \\ -a & -a & -b & -b & c & c & d & d \\ -\frac{t}{2} & \frac{t}{2} & -\frac{t}{2} & \frac{t}{2} & -\frac{t}{2} & \frac{t}{2} & -\frac{t}{2} & \frac{t}{2} \\ 1 & 0 & 0 & 0 & 0 & 0 & 0 & 0 \\ 0 & 1 & 0 & 0 & 0 & 0 & 0 & 0 \\ 0 & 0 & 1 & 0 & 0 & 0 & 0 & 0 \\ 0 & 0 & 0 & 1 & 0 & 0 & 0 & 0 \\ 0 & 0 & 0 & 0 & 1 & 0 & 0 & 0 \\ 0 & 0 & 0 & 0 & 0 & 1 & 0 & 0 \\ 0 & 0 & 0 & 0 & 0 & 0 & 1 & 0 \\ 0 & 0 & 0 & 0 & 0 & 0 & 0 & 1 \end{bmatrix} \begin{bmatrix} F_{d1R} \\ F_{d1L} \\ F_{d2R} \\ F_{d2L} \\ F_{d3R} \\ F_{d3L} \\ F_{d4R} \\ F_{d4L} \end{bmatrix} \qquad (4\text{-}45)$$

For an equation of linear system $y = Kx$, if $K \in \mathfrak{R}^{m \times n}$ has a full row rank, therefore, a right inverse (pseudo inverse) exists K^{-1} similar to $K^{-1}K = I^{m \times n}$. Accordingly, equation (4-45) can be solved and expressed as follows.

$$\begin{bmatrix} F_{d1R} \\ F_{d1L} \\ F_{d2R} \\ F_{d2L} \\ F_{d3R} \\ F_{d3L} \\ F_{d4R} \\ F_{d4L} \end{bmatrix} = \begin{bmatrix} 1 & 1 & 1 & 1 & 1 & 1 & 1 & 1 \\ -a & -a & -b & -b & c & c & d & d \\ -\frac{t}{2} & \frac{t}{2} & -\frac{t}{2} & \frac{t}{2} & -\frac{t}{2} & \frac{t}{2} & -\frac{t}{2} & \frac{t}{2} \\ 1 & 0 & 0 & 0 & 0 & 0 & 0 & 0 \\ 0 & 1 & 0 & 0 & 0 & 0 & 0 & 0 \\ 0 & 0 & 1 & 0 & 0 & 0 & 0 & 0 \\ 0 & 0 & 0 & 1 & 0 & 0 & 0 & 0 \\ 0 & 0 & 0 & 0 & 1 & 0 & 0 & 0 \\ 0 & 0 & 0 & 0 & 0 & 1 & 0 & 0 \\ 0 & 0 & 0 & 0 & 0 & 0 & 1 & 0 \\ 0 & 0 & 0 & 0 & 0 & 0 & 0 & 1 \end{bmatrix}^{-1} \begin{bmatrix} F_{(z)c} \\ M_{\theta} \\ M_{\phi} \\ F_{(z1R)c} \\ F_{(z1L)c} \\ F_{(z2R)c} \\ F_{(z2L)c} \\ F_{(z3R)c} \\ F_{(z3L)c} \\ F_{(z4R)c} \\ F_{(z4L)c} \end{bmatrix} \qquad (4\text{-}46)$$

Chapter 5 ASSESSMENT OF CONTROLLERS PERFORMANCE

5.1 Introduction

After introducing the implementation of several control strategies in the previous chapter, an evaluation needs to be conducted to determine the benefits of integrating SAS with AWS, TV, and DB at the high and low friction road surfaces. Hence, this evaluation method introduces an assessment of each controller performance through a comparison between each control strategy with and without integration of SAS, as it can be summarized as follows.

- A comparison is carried out between the LQR controller's AWS and AWS+SAS.
- A comparison is performed between the LQR controller's TV and TV+SAS.
- A comparison is conducted between the LQR controller's DB and DB+SAS.

Based on the assessment of each controller performance at limit handling conditions at the different coefficient of friction. A judgement will be made to investigate the merits of each control strategy to improve the vehicle's stability at a highly nonlinear operating range of the tires. Accordingly, a conclusion can be drawn out of this assessment at the end of this chapter.

5.2 Assessment of each controller performance

The assessment of each control strategy was performed in the Slalom test course. This standard test is normally utilized to analyze the vehicles' dynamics performance in the industry. Since the main goal is to evaluate the vehicle's dynamics performance at limit handling scenarios. And to ensure the effectiveness of the proposed controllers under the changes in road surface friction and the variation of vehicle parameters such as cornering stiffness and different steering inputs. Therefore, most of the tests are conducted at high speeds. Moreover, all simulations were performed at high and low road coefficients of friction 0.85 and 0.35, respectively.

Table 5-1 summarizes the two test events conducted to compare each proposed control strategy with and without integration of Semi-active suspension.

Table 5-1 List of Test Events for Assessment of Each Controller's Performance

Test #	**Configuration**	**Test Maneuver**	**Speed (Km/h)**	**Coefficient of friction (μ)**
At High Coefficient of Friction				
5.2.1.1.1	AWS vs AWS+SAS	**Slalom**	65	0.85
5.2.1.1.2	TV vs TV+SAS			
5.2.1.1.3	DB vs DB+SAS			
At Low Coefficient of Friction				
5.2.1.2.1	AWS vs AWS+SAS	**Slalom**	40	0.35
5.2.1.2.2	TV vs TV+SAS			
5.2.1.2.3	DB vs DB+SAS			

5.2.1 30m Constant Step Slalom Test (NATO AVTP-1 03-30)

The NATO AVTP-1 03-30 standard test is maintained at 30 meters constant spacing distance between each pair of cones (d_2). While the lateral offset (d_3) between each cone was set to 5 meters. The test course layout is represented as follows in Figure 5-1.

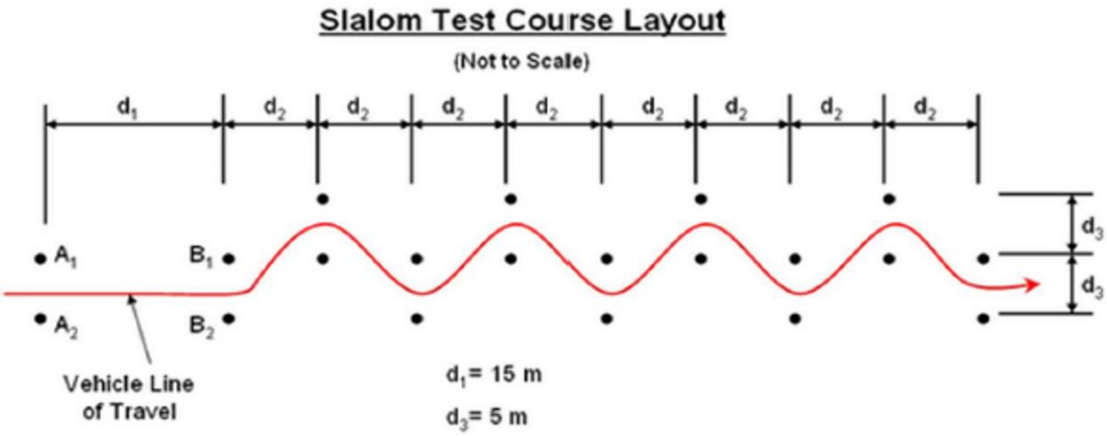

Figure 5-1 NATO AVTP-1 03-30 Constant Step Slalom Test course layout [112]

5.2.1.1 Results and Discussion of the assessment of each controller performance at high coefficient of friction – Constant Step Slalom ($65\ \text{km/h}\ ;\ \mu = 0.85$)

5.2.1.1.1 AWS vs AWS+SAS

Figure 5-2 (a) and (b) show the vehicle trajectory and the corresponding error performed by each control strategy AWS and AWS+SAS, respectively. It can be noticed that AWS+SAS has achieved least error compared to AWS as shown in Table 5-2.

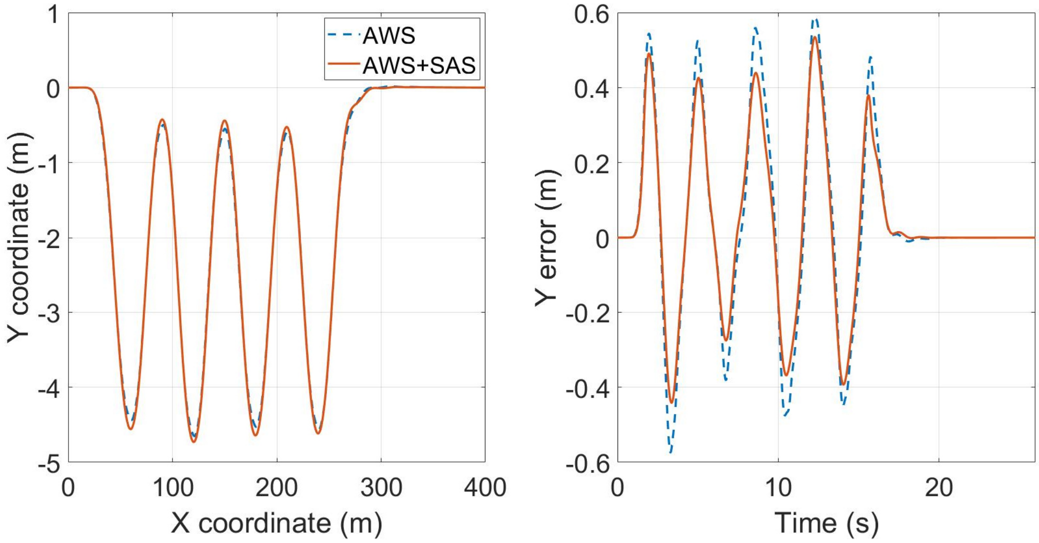

(a) (b)

Figure 5-2 (a) Vehicle trajectory during Slalom at 65 Km/h ($\mu = 0.85$) and (b) Error obtained by AWS and AWS+SAS

Table 5-2 Trajectory Root Mean Square Errors Obtained by AWS and AWS+SAS during Slalom at 65 Km/h (μ = 0.85)

Controller's Configuration	RMSE (m)
AWS	0.2552
AWS+SAS	0.2165

Figure 5-3, Figure 5-4, Figure 5-5 and Figure 5-6 demonstrate the vehicle sideslip, yaw rate, longitudinal speed and lateral acceleration for both AWS and AWS+SAS, respectively. Its notable that AWS+SAS has achieved less sideslip angle than AWS, which considered as a merit for AWS+SAS over AWS in terms of enhancing vehicle's stability at high road friction surface. Regarding to yaw rate response amplitude is approximately maintained the same for both. However, the AWS+SAS has performed smoother peak than AWS, leading to augment the vehicle's maneuverability. Moreover, the AWS+SAS exhibits less drop in vehicle's longitudinal speed compared to AWS, which makes it close to attain the desired speed. Furthermore, it can be observed that AWS+SAS has a tremendous effect in reducing the lateral acceleration compared to AWS, which can increase the vehicle's stability while cornering at high speed.

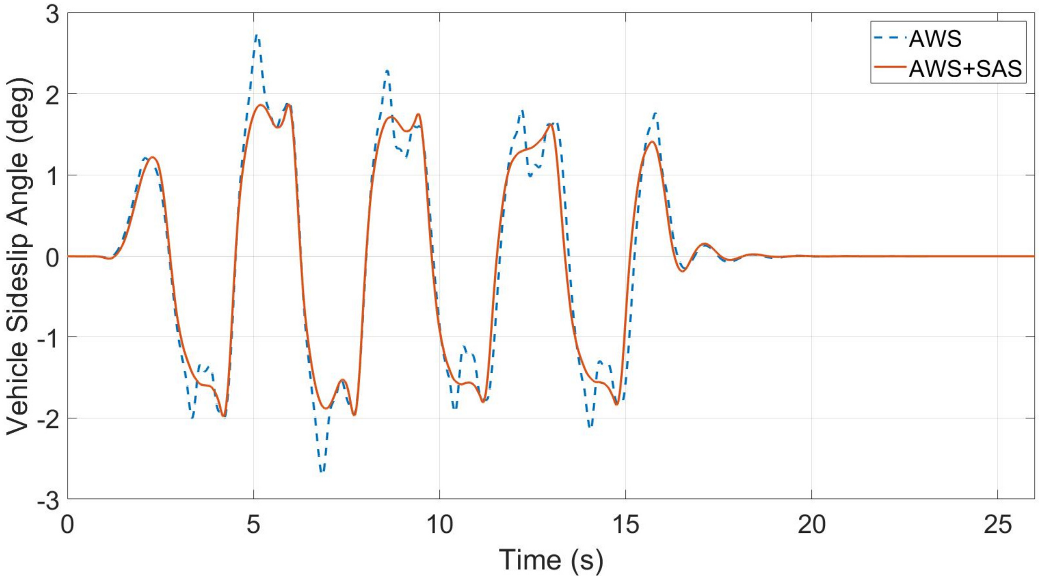

Figure 5-3 Vehicle Sideslip Angle during Slalom at 65 Km/h (μ = 0.85)

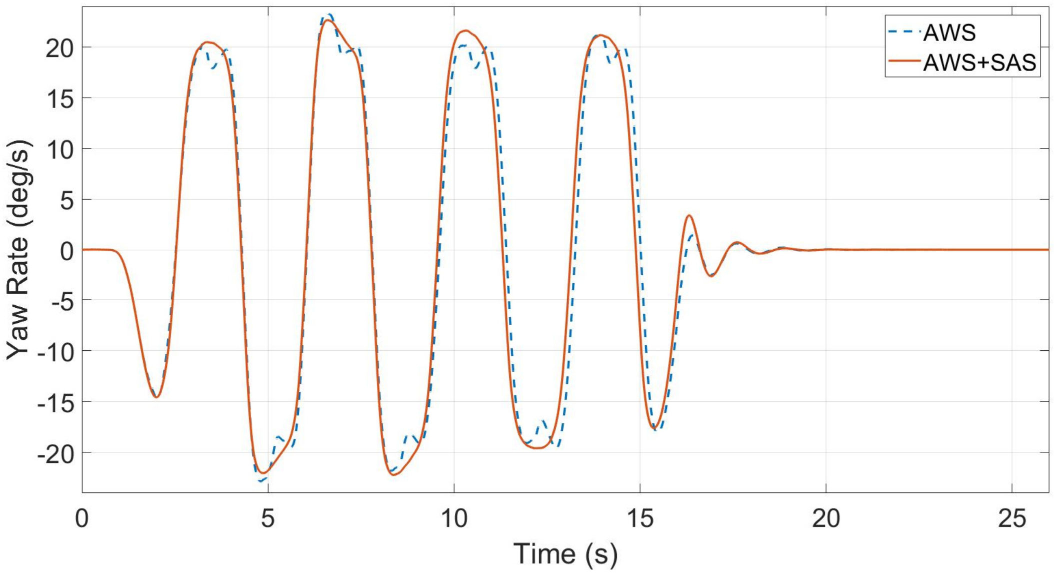

Figure 5-4 Yaw Rate during Slalom at 65 Km/h (μ = 0.85)

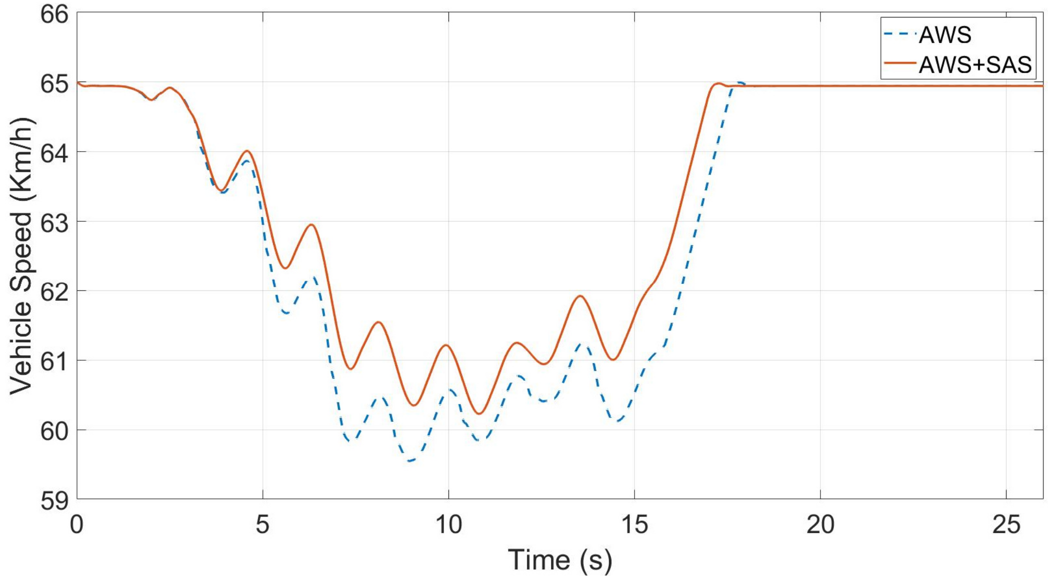

Figure 5-5 Vehicle Speed during Slalom at 65 Km/h (μ = 0.85)

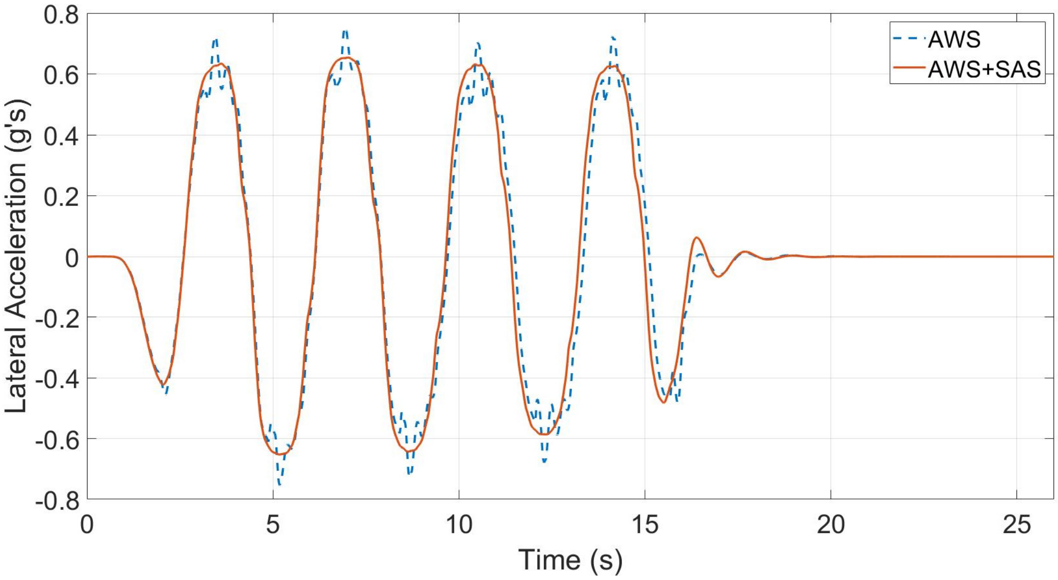

Figure 5-6 Lateral Acceleration during Slalom at 65 Km/h (μ = 0.85)

Figure 5-7, Figure 5-8 and Figure 5-9 illustrate the vehicle's sprung mass displacement, pitch, and roll angle, respectively. It can be observed that AWS+SAS has significantly reduced the vertical displacement at the CG of the sprung mass compared to AWS. Furthermore, AWS+SAS has enormously minimized the pitch and roll angle due to longitudinal and lateral load transfer. Hence, avoiding the grip loss between the tires and the ground at high-speed cornering maneuvers.

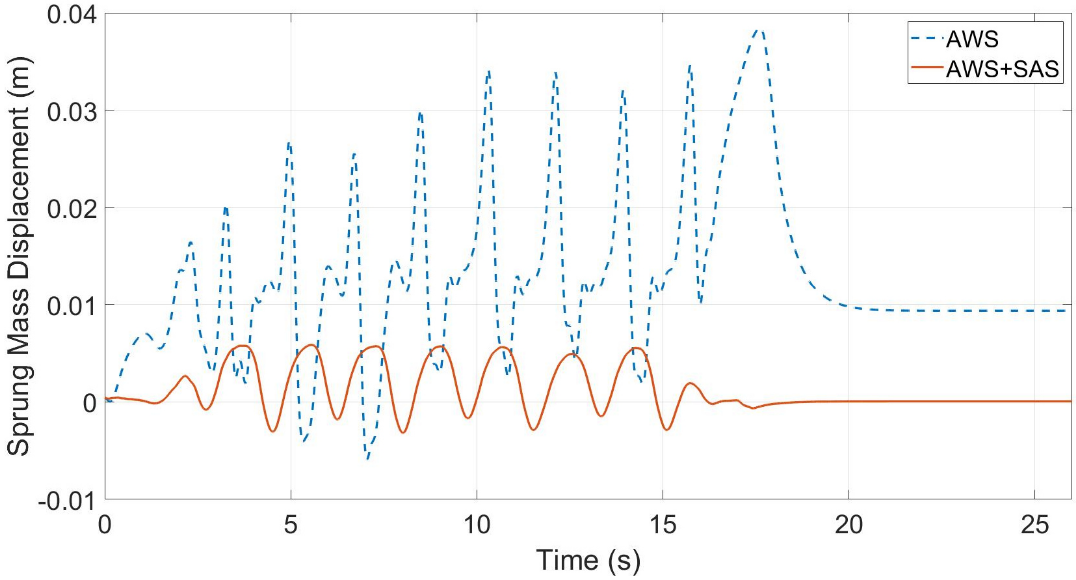

Figure 5-7 Sprung Mass Displacement during Slalom at 65 Km/h (μ = 0.85)

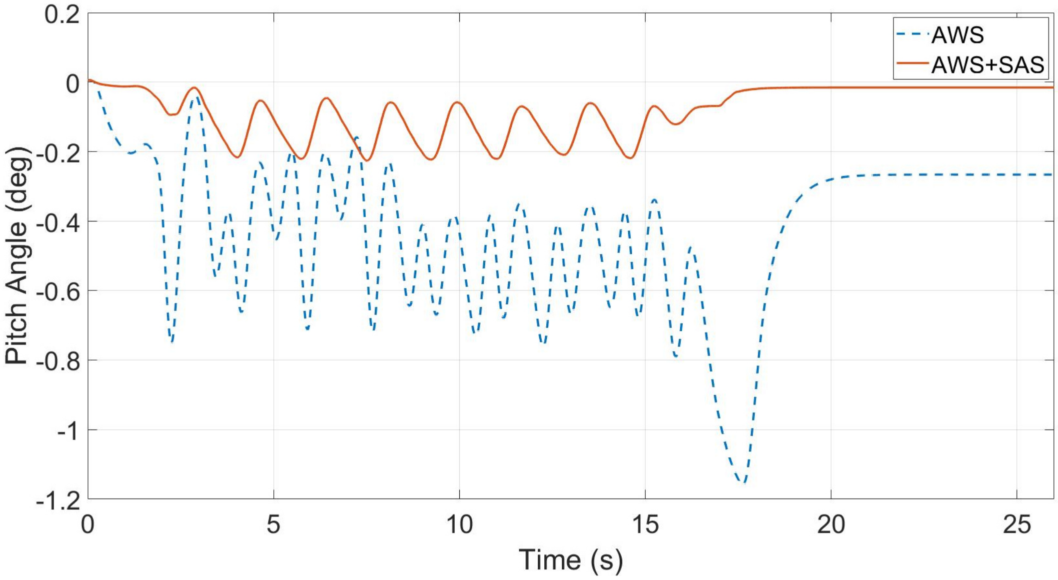

Figure 5-8 Pitch Angle during Slalom at 65 Km/h (μ = 0.85)

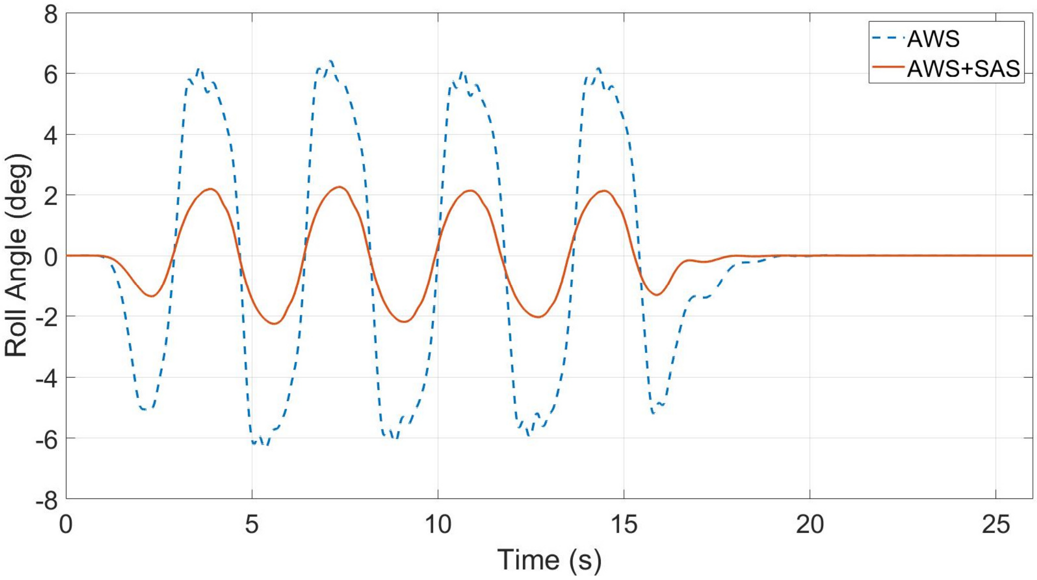

Figure 5-9 Roll Angle during Slalom at 65 Km/h (μ = 0.85)

Figure 5-10 and Figure 5-11demonstrate the front and rear road steer angles in (a) and (b) for AWS and AWS+SAS, respectively. It is remarkable that AWS exhibits larger front and rear steer angle compared to AWS+SAS, which interpreted as the vehicle has tendency to drift out. Thus, the AWS controller deals with that issue by increasing the steering angle to keep the vehicle on the desired trajectory. Moreover, the AWS+SAS has achieved the least front and rear steer wheel angle, which is 21.5 and 5.7 degrees for the front and rear steering angles, respectively. While the AWS has reached 23.4 and 8.7 degrees for the front and rear steering angles, respectively. It should be noted that the rear steer angles for both controllers are performing parallel steering (steering in the same direction as the front steering angles).

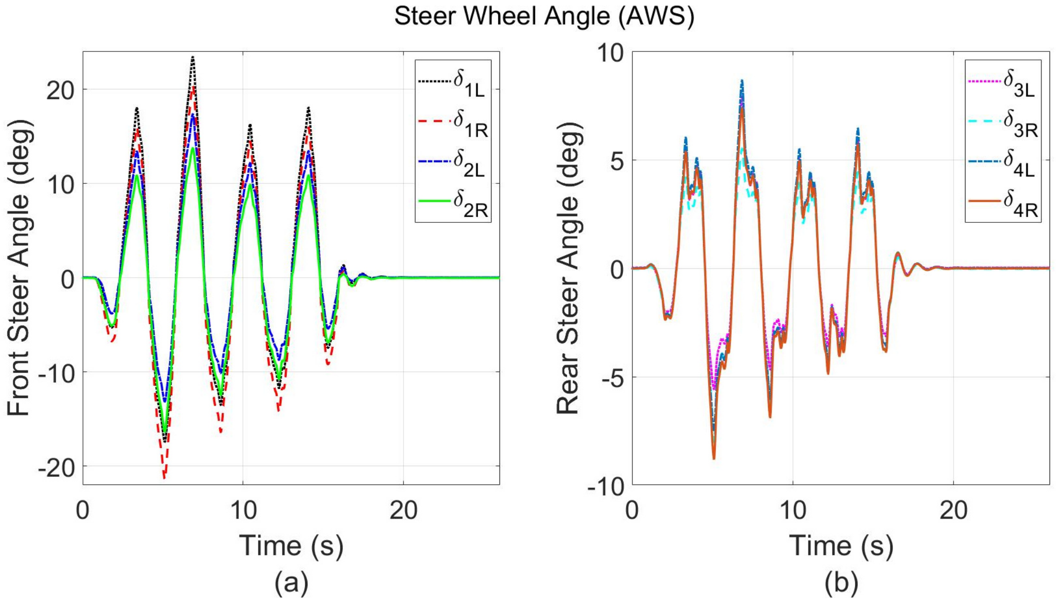

Figure 5-10 (a) Front Steer Angle and (b) Rear Steer Angle for AWS during Slalom at 65 Km/h (μ = 0.85)

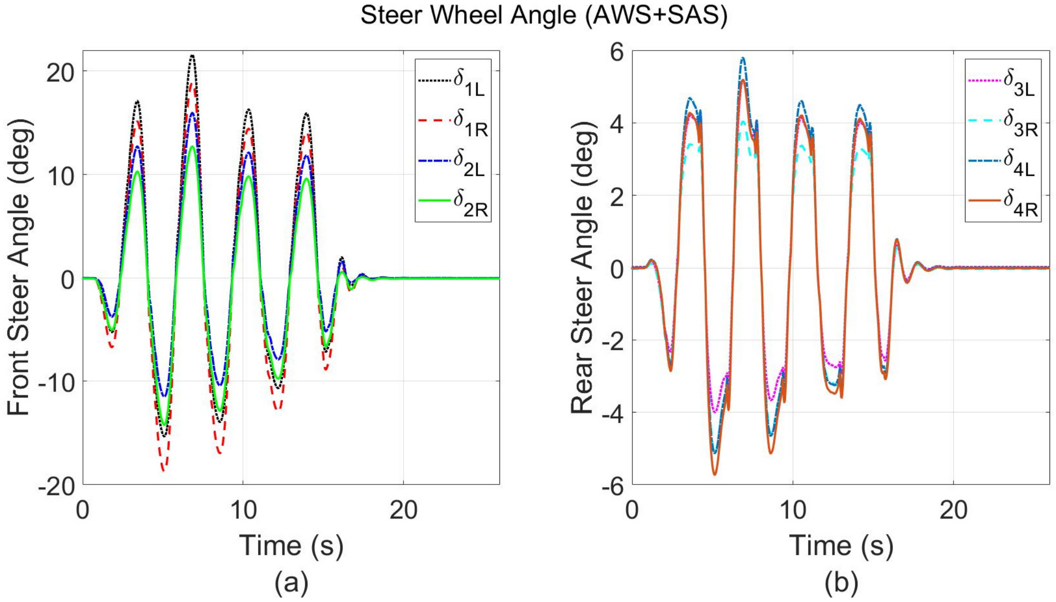

Figure 5-11 (a) Front Steer Angle and (b) Rear Steer Angle for AWS+SAS during Slalom at 65 Km/h (μ = 0.85)

Figure 5-12 and Figure 5-13 show the left and right sides' vehicle dampers 'compressive forces in (a) and (b) respectively for AWS and AWS+SAS. It can be observed that AWS+SAS has obtained largest dampers 'compressive forces varying with time. The largest left side dampers' force was 15479 N and for the right side was 15906 N. while for AWS was 13286.5 N and 13443.4 N for the left and right side, respectively.

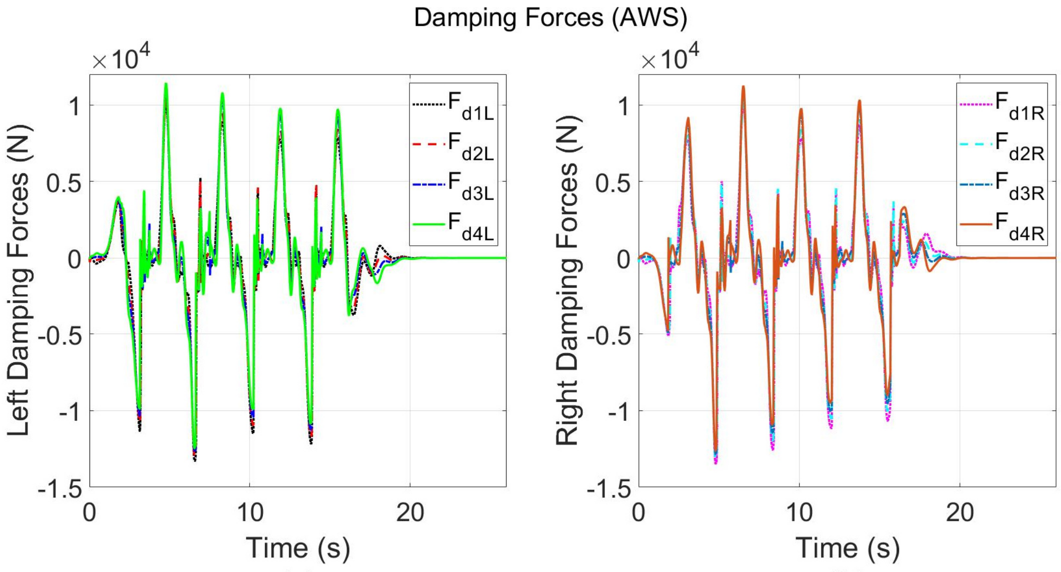

(a) (b)

Figure 5-12 (a) Left Damping Forces and (b) Right Damping Forces for AWS during Slalom at 65 Km/h ($\mu = 0.85$)

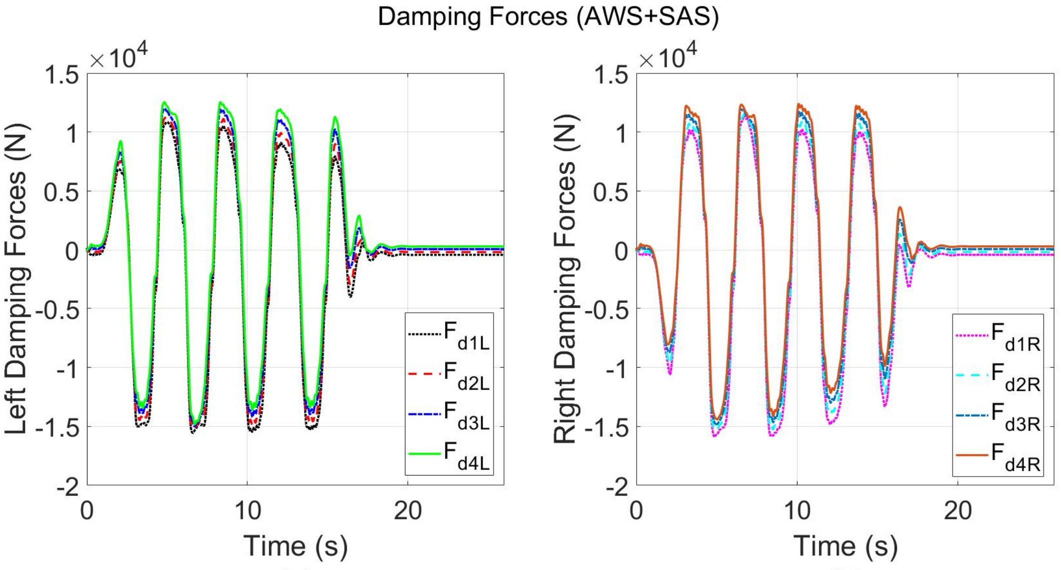

(a) (b)

Figure 5-13 (a) Left Damping Forces and (b) Right Damping Forces for AWS+SAS during Slalom at 65 Km/h ($\mu = 0.85$)

Figure 5-14 and Figure 5-15 express the left and right sides' vehicle normal loads in (a) and (b) respectively for AWS and AWS+SAS. Its notable that AWS+SAS has substantially prevented the vehicle's wheels on both sides to left off the ground during the maneuver event while AWS not. Thus, keeping the tires in contact with the ground, has a significant effect on vehicle's lateral stability in terms of avoiding rollover at high-speed cornering maneuver. Furthermore, minimizing the drop of the lateral forces between the contact patch of tires and the ground due to lateral load transfer.

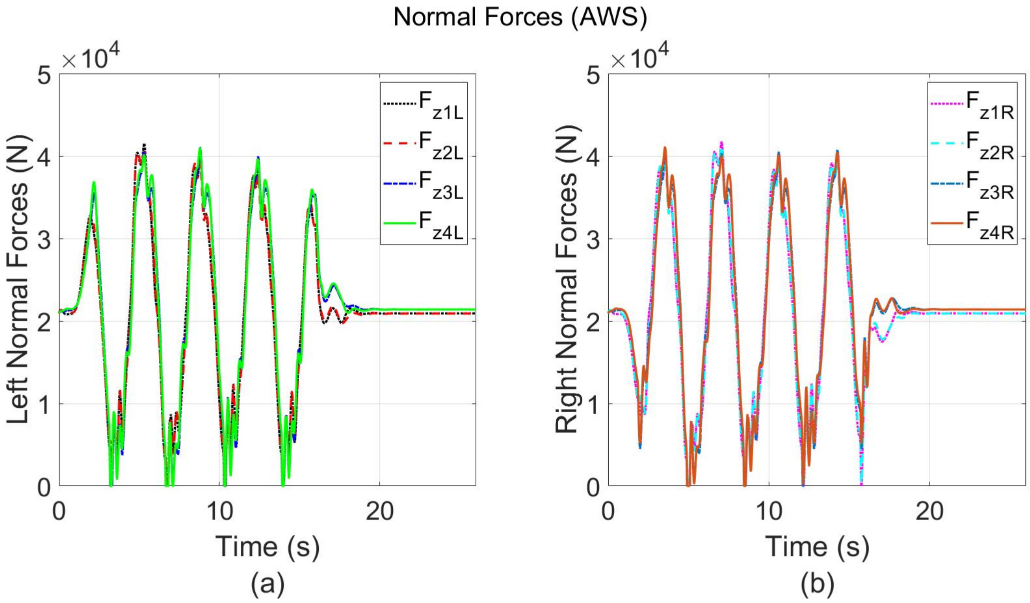

Figure 5-14 (a) Left Normal Forces and (b) Right Normal Forces for AWS during Slalom at 65 Km/h ($\mu = 0.85$)

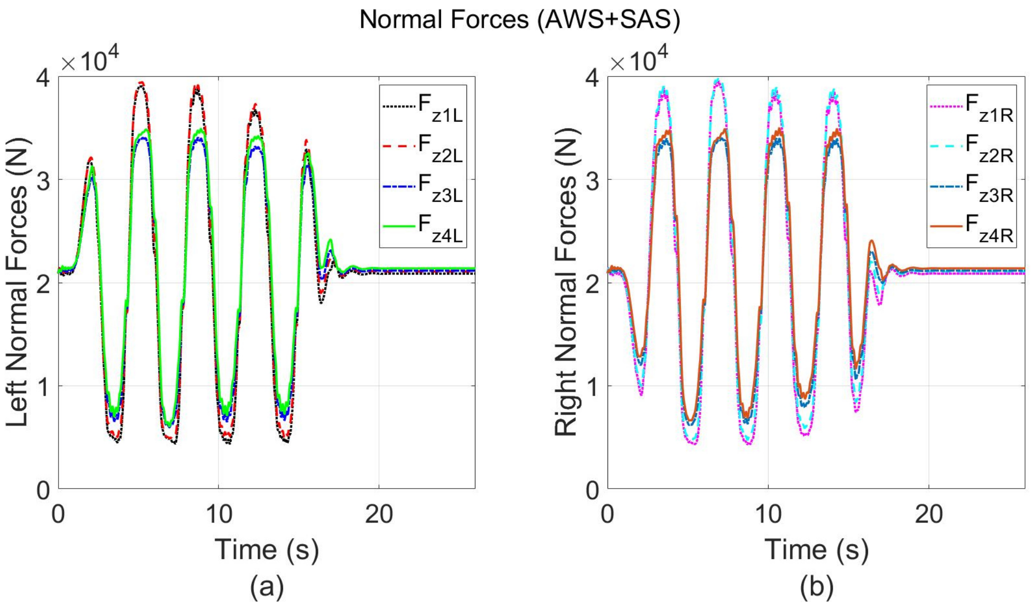

Figure 5-15 (a) Left Normal Forces and (b) Right Normal Forces for AWS+SAS during Slalom at 65 Km/h ($\mu = 0.85$)

5.2.1.1.2 TV vs TV+SAS

The vehicle trajectory and the corresponding error achieved by each control strategy TV and TV+SAS are shown in Figure 5-16 in (a) and (b) respectively. It can be noticed that TV+SAS has maintained less error compared to TV as shown in Table 5-3. Furthermore, the TV+SAS has stabilized the vehicle faster than TV based on the settling time.

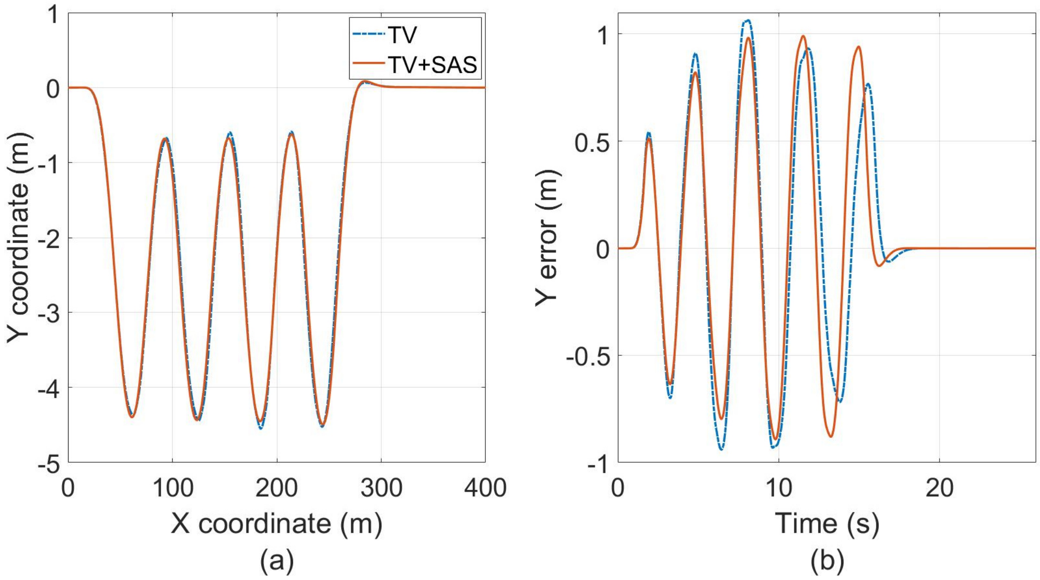

Figure 5-16 (a) Vehicle trajectory during Slalom at 65 Km/h ($\mu = 0.85$) and (b) Error obtained by TV and TV+SAS

Table 5-3 Trajectory Root Mean Square Errors Obtained by TV and TV+SAS during Slalom at 65 Km/h ($\mu = 0.85$)

Controller's Configuration	RMSE (m)
TV	0.4854
TV+SAS	0.4656

Figure 5-17, Figure 5-18, Figure 5-19 and Figure 5-20 illustrate the vehicle sideslip, yaw rate, longitudinal speed and lateral acceleration for both TV and TV+SAS, respectively. It can be remarked that TV+SAS has achieved less sideslip angle and stabilizes the vehicle faster than TV, which considered as a merit for TV+SAS over TV in terms of enhancing vehicle's stability at high road friction surface. The yaw rate response amplitude was varying with respect to time for both control strategies. However, the TV+SAS has performed smoother peak than TV, leading to an enhancement in vehicle's maneuverability. Also, the yaw rate response for TV was slightly shifted and delayed, yielded place to TV+SAS to show a superiority in stabilizing the vehicle faster. As well as the TV+SAS exhibits less drop in vehicle's longitudinal speed compared to TV, which makes it close to achieve the desired speed. Furthermore, it can be observed that TV+SAS has a significant effect in minimizing the lateral acceleration compared to TV, which can increase the vehicle's stability while cornering at high speed.

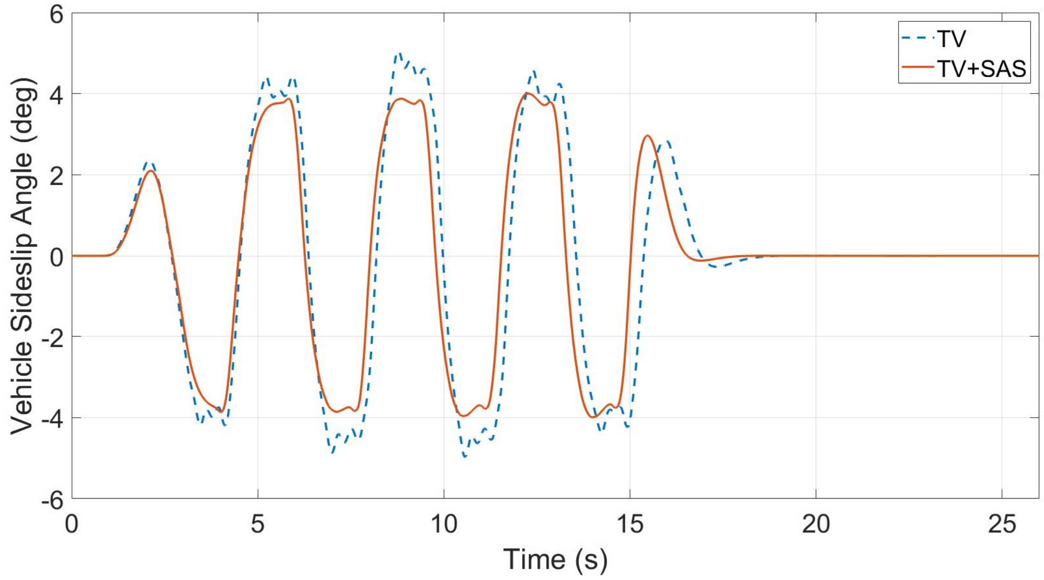

Figure 5-17 Vehicle Sideslip Angle during Slalom at 65 Km/h (μ = 0.85)

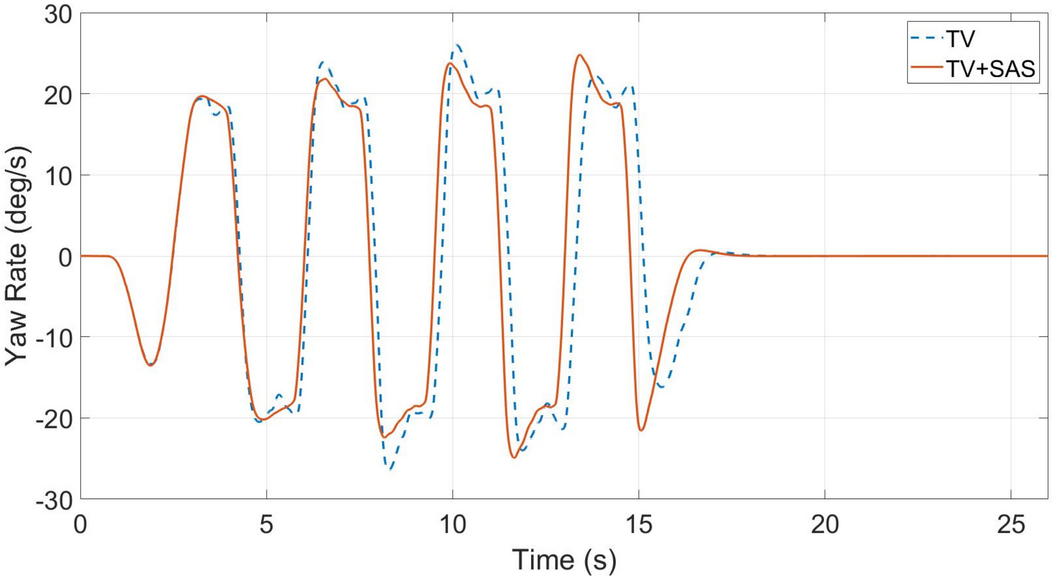

Figure 5-18 Yaw Rate during Slalom at 65 Km/h (μ = 0.85)

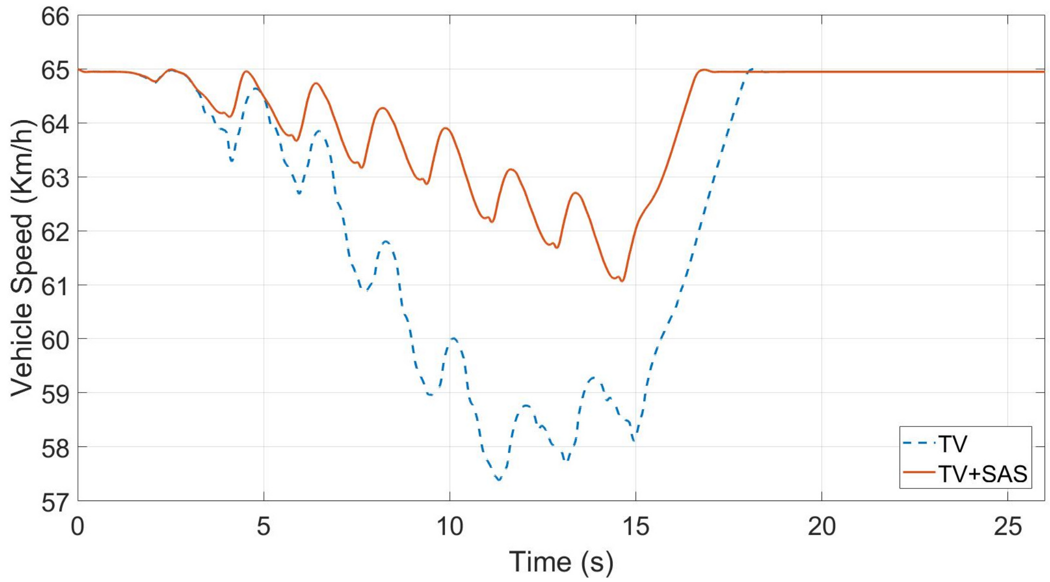

Figure 5-19 Vehicle Speed during Slalom at 65 Km/h (μ = 0.85)

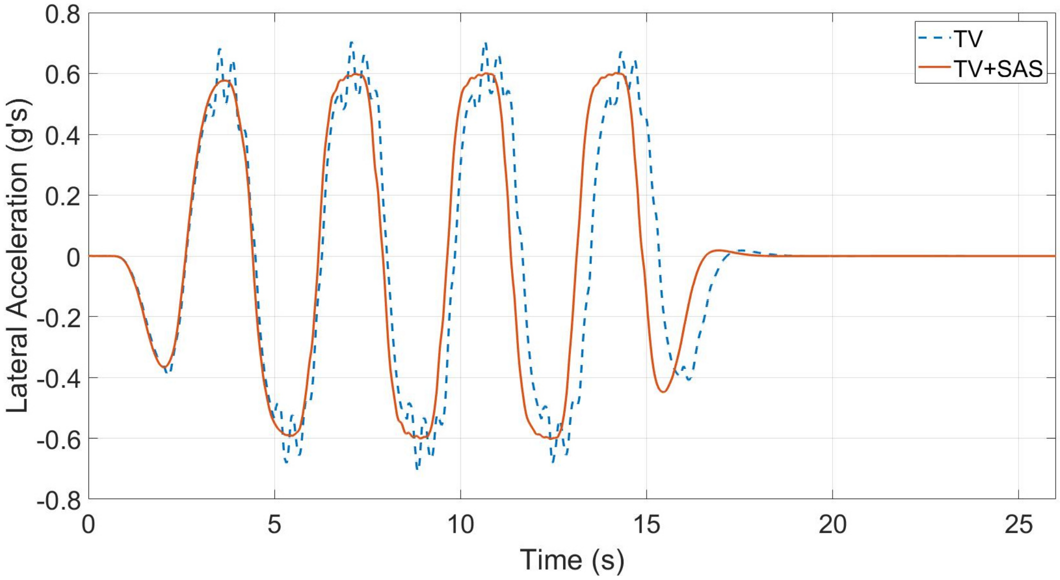

Figure 5-20 Lateral Acceleration during Slalom at 65 Km/h (μ = 0.85)

Figure 5-21, Figure 5-22 and Figure 5-23 demonstrate the vehicle's sprung mass displacement, pitch, and roll angle, respectively. It is notable that TV+SAS has significantly minimized the vertical displacement at the CG of the sprung mass compared to TV. Moreover, TV+SAS has tremendously reduced the pitch and roll angle due to longitudinal and lateral load transfer. Thus, avoiding the grip loss between the tires and the ground at high-speed cornering maneuvers.

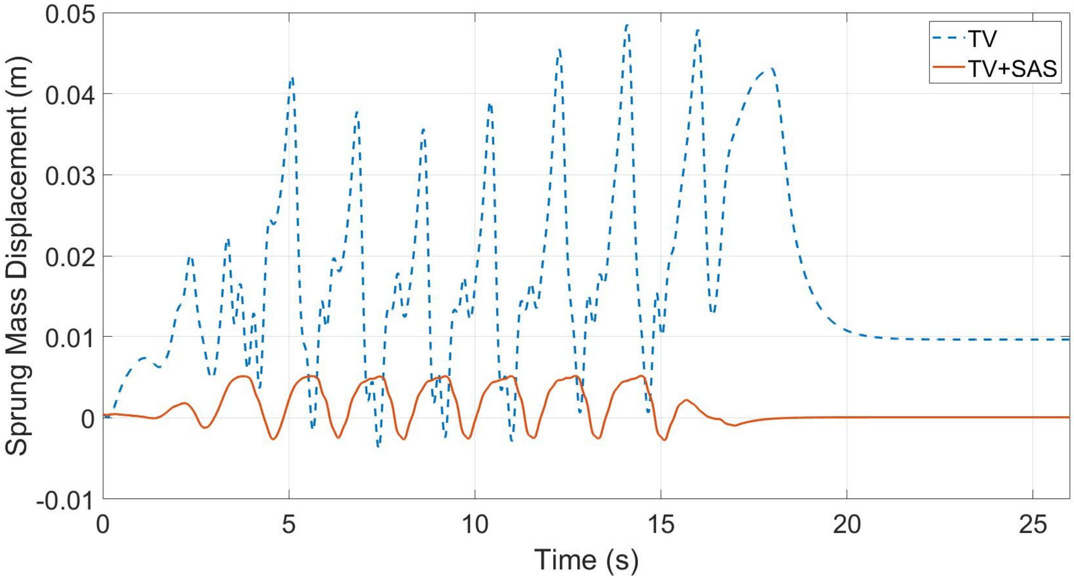

Figure 5-21 Sprung Mass Displacement during Slalom at 65 Km/h ($\mu = 0.85$)

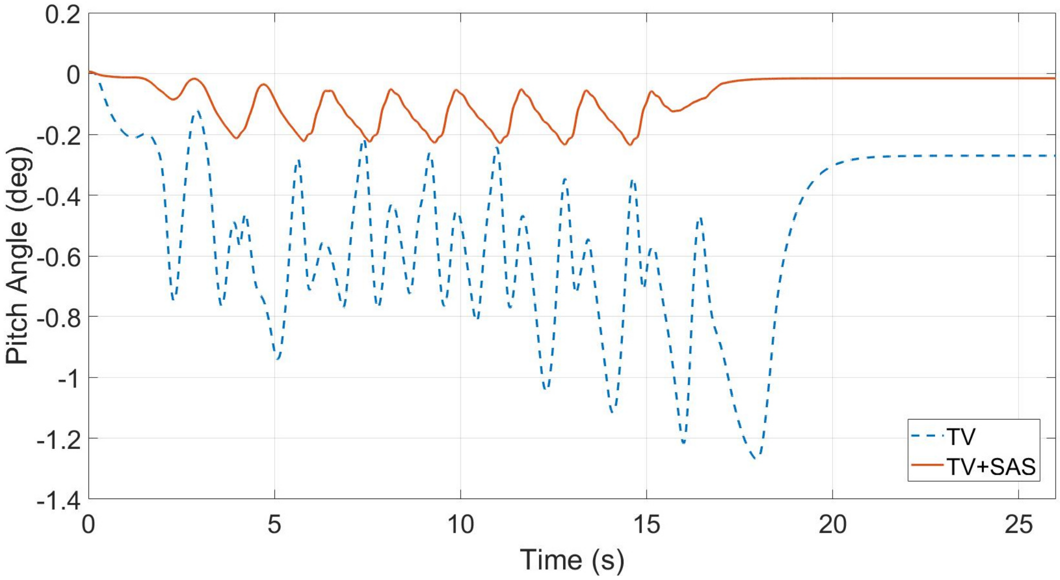

Figure 5-22 Pitch Angle during Slalom at 65 Km/h ($\mu = 0.85$)

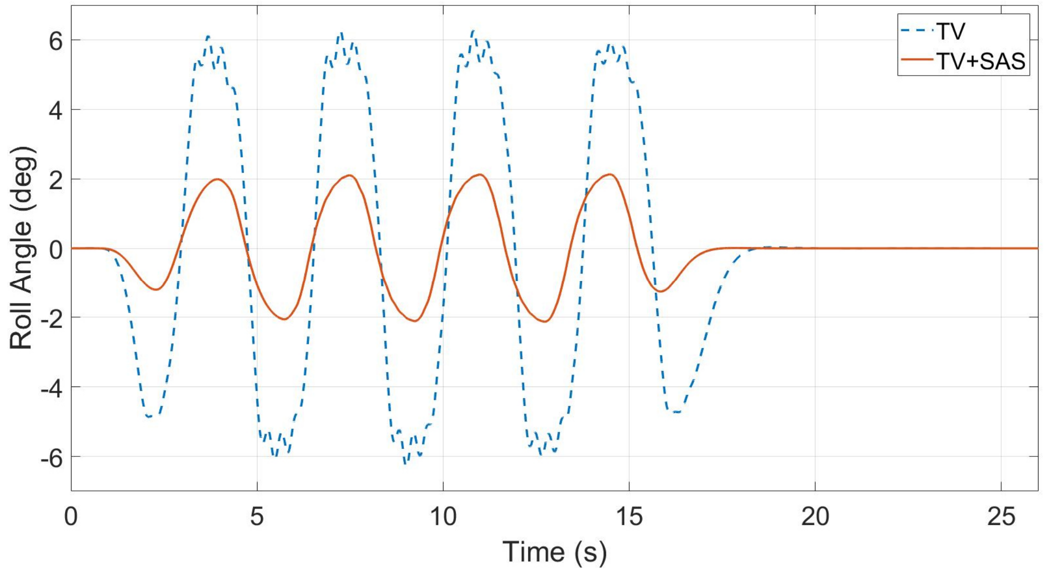

Figure 5-23 Roll Angle during Slalom at 65 Km/h (μ = 0.85)

Figure 5-24 and Figure 5-25 show the left and right sides' vehicle wheels driving torque in (a) and (b) respectively. The maximum obtained driving torque during this maneuver event was same for both control strategies TV and TV+SAS. Nevertheless, it can be noticed that TV+SAS generates less fluctuated and smooth driving torque in both sides compared to TV.

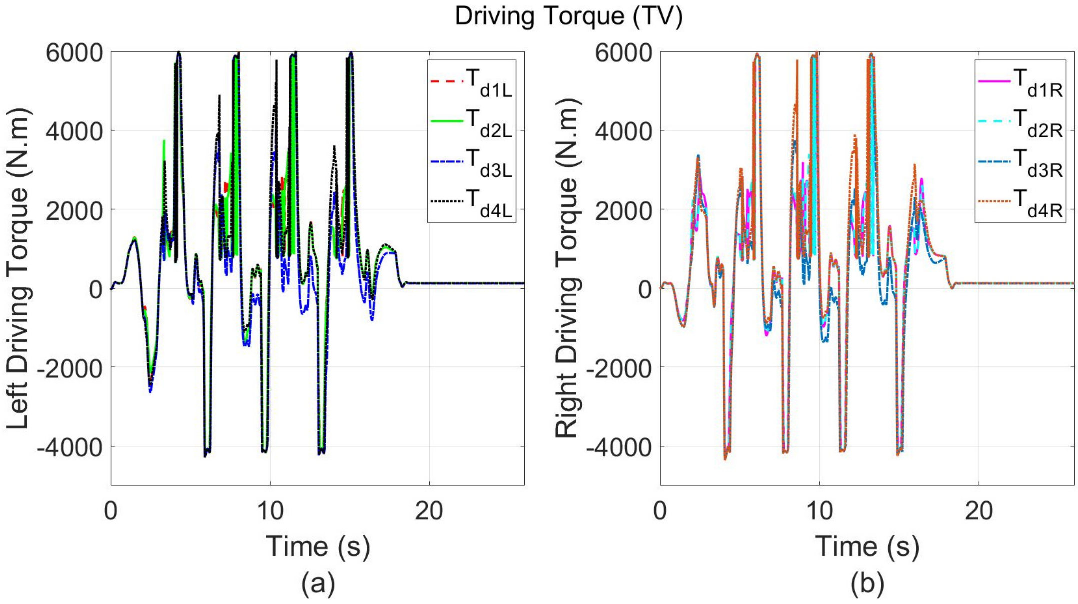

Figure 5-24 (a) Left Driving Wheel Torque and (b) Right Driving Wheel Torque for TV during Slalom at 65 Km/h (μ = 0.85)

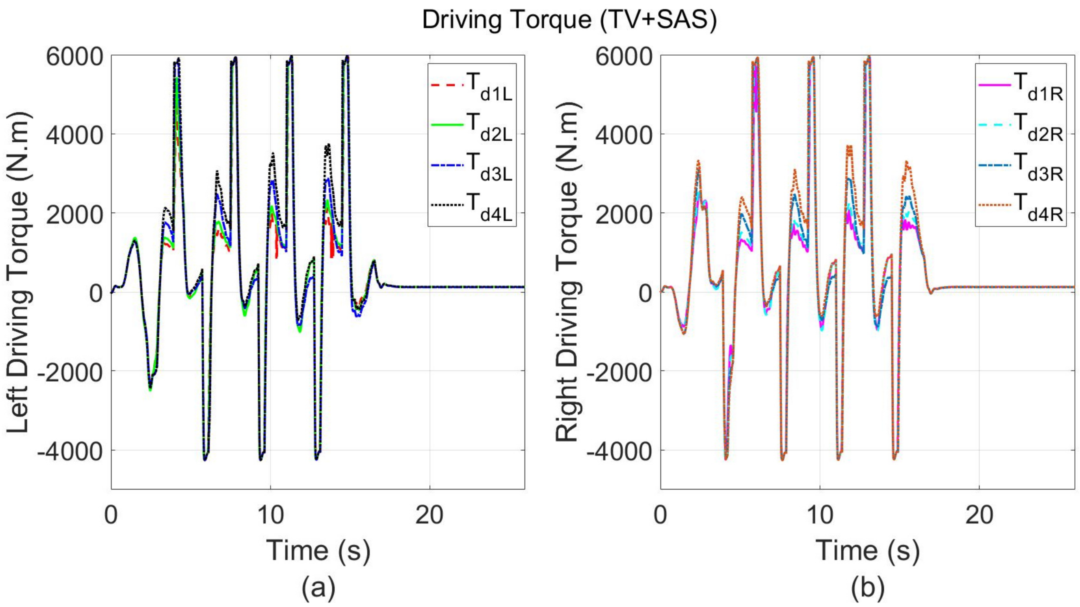

Figure 5-25 (a) Left Driving Wheel Torque and (b) Right Driving Wheel Torque for TV+SAS during Slalom at 65 Km/h ($\mu = 0.85$)

Figure 5-26 and Figure 5-27 represent the left and right sides' vehicle dampers 'compressive forces in (a) and (b) respectively for TV and TV+SAS. It is remarkable that TV+SAS has obtained largest dampers 'compressive forces varying with time. The largest left side dampers' force was almost 15000 N and for both sides. while for TV was 11521.5 N and 11301.5 N for the left and right side, respectively.

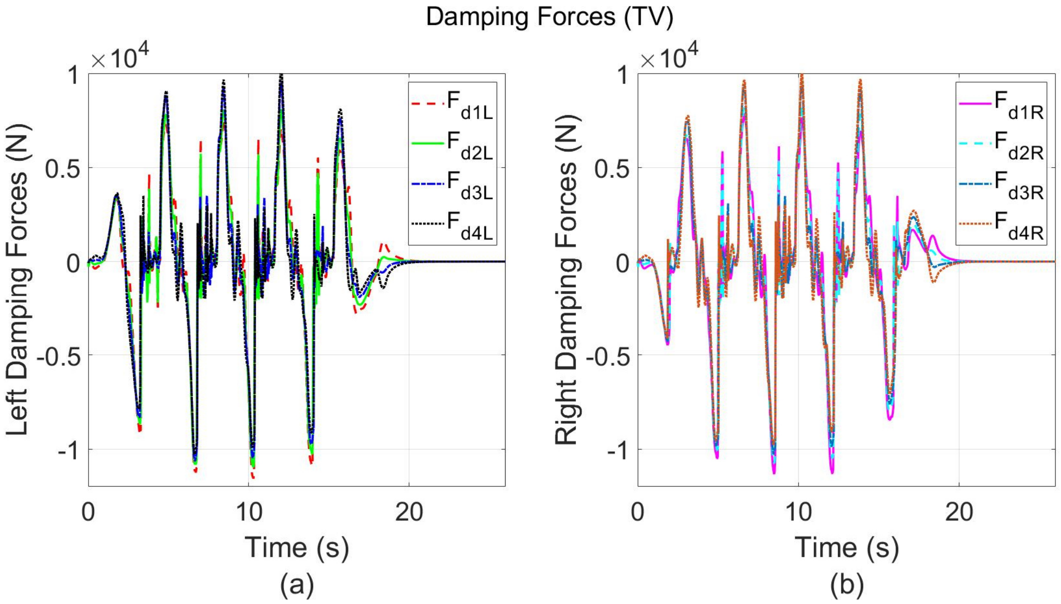

Figure 5-26 (a) Left Damping Forces and (b) Right Damping Forces for TV during Slalom at 65 Km/h ($\mu = 0.85$)

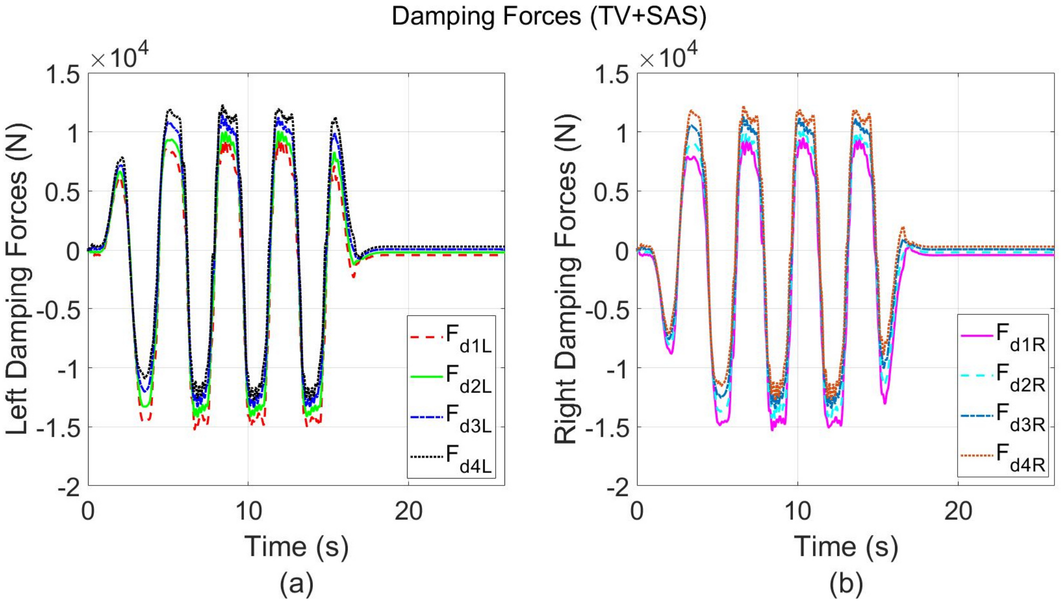

Figure 5-27 (a) Left Damping Forces and (b) Right Damping Forces for TV+SAS during Slalom at 65 Km/h ($\mu = 0.85$)

Figure 5-28 and Figure 5-29 depict the left and right sides' vehicle normal loads in (a) and (b) respectively for TV and TV+SAS. Its notable that TV+SAS has greatly prevented the vehicle's wheels on both sides to left off the ground during the maneuver event while TV not. Hence, keeping the tires in contact with the ground, has a significant effect on vehicle's lateral stability in terms of avoiding rollover at high-speed cornering maneuver. Furthermore, minimizing the drop of the lateral forces between the contact patch of tires and the ground due to lateral load transfer.

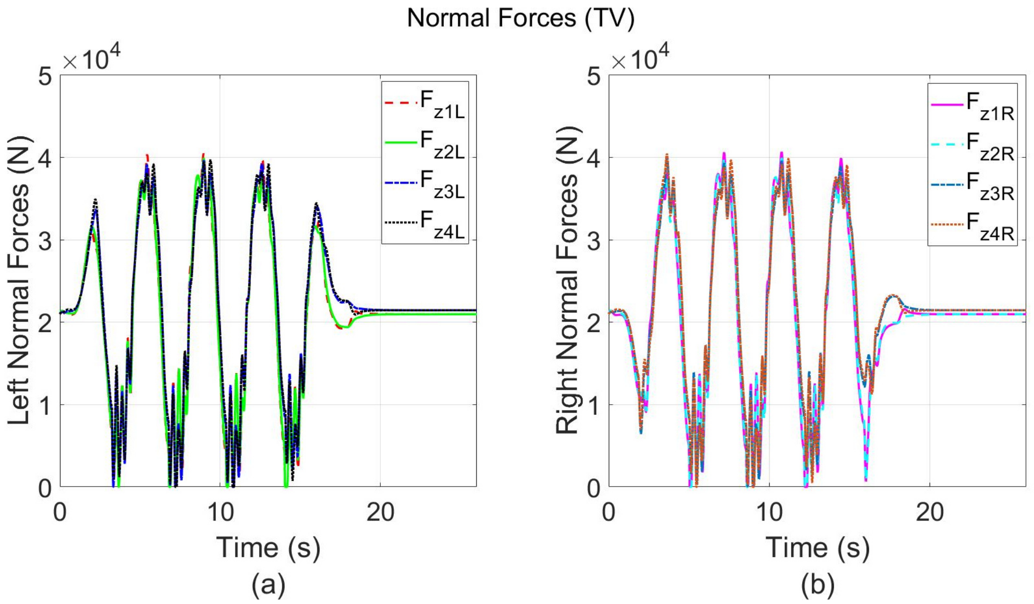

Figure 5-28 (a) Left Normal Forces and (b) Right Normal Forces for TV during Slalom at 65 Km/h (μ = 0.85)

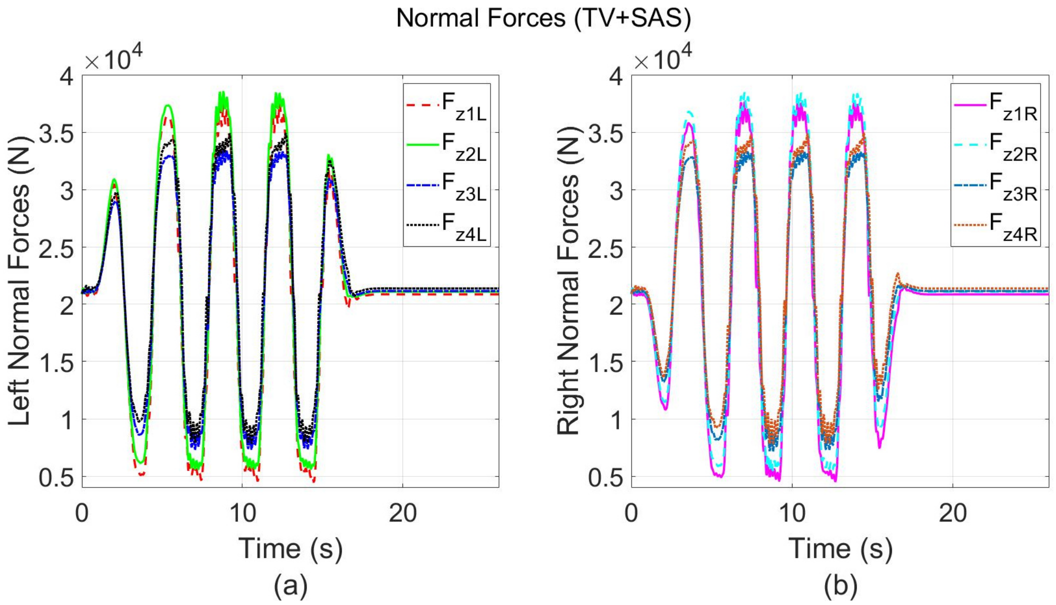

Figure 5-29 (a) Left Normal Forces and (b) Right Normal Forces for TV+SAS during Slalom at 65 Km/h (μ = 0.85)

The slip ratio of the left and right sides' vehicle tires for TV and TV+SAS are shown in Figure 5-30 and Figure 5-31in (a) and (b) respectively. Despite the intervention of slip controller for TV to prevent the slip ratio exceeding 25%, an extent surpassed the desired limit, and this is because of the variation in lateral load transfer. However, it can be observed that the TV+SAS has maintained the slip at 25% where the peak tractive forces can be obtained.

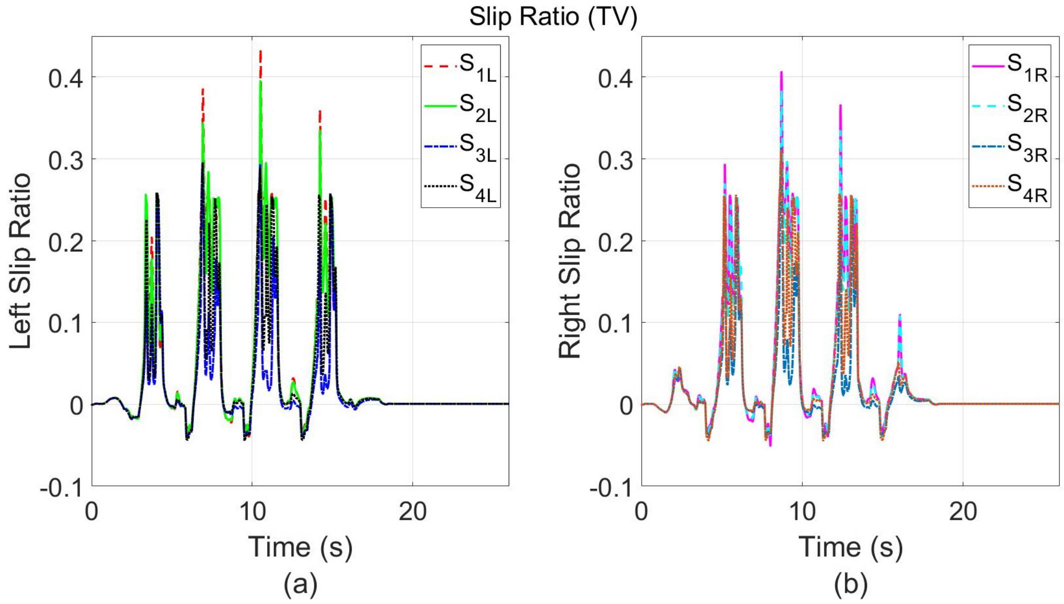

Figure 5-30 (a) Left Tires' Slip Ratio and (b) Right Tires' Slip Ratio for TV during Slalom at 65 Km/h ($\mu = 0.85$)

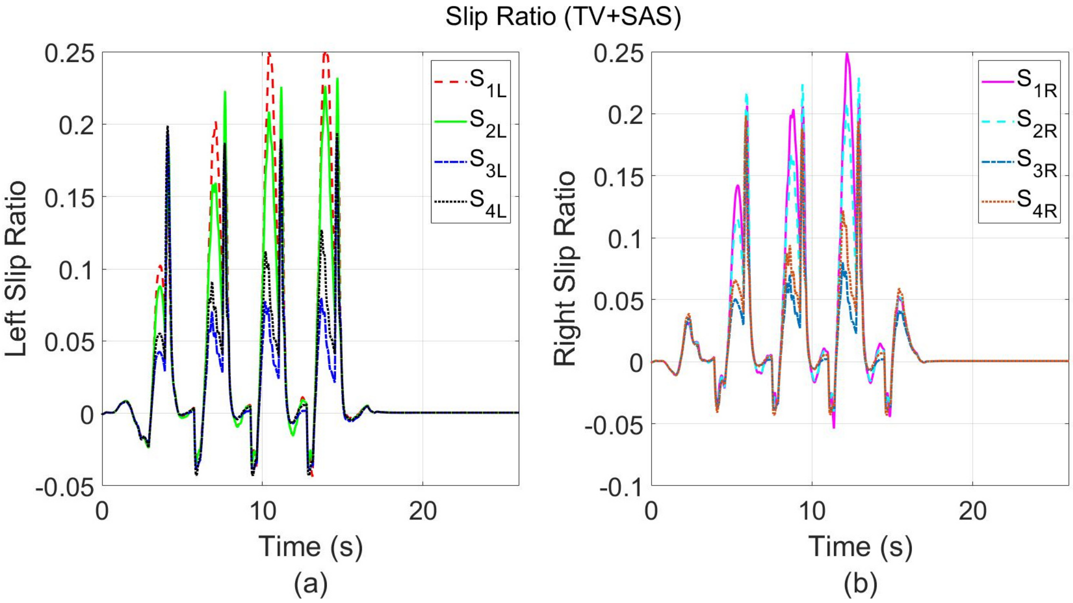

Figure 5-31 (a) Left Tires' Slip Ratio and (b) Right Tires' Slip Ratio for TV+SAS during Slalom at 65 Km/h ($\mu = 0.85$)

5.2.1.1.3 DB vs DB+SAS

The vehicle trajectory and the corresponding error achieved by each control strategy DB and DB+SAS are shown in Figure 5-32 in (a) and (b) respectively. Its notable that there is no significant difference between both control strategies DB and DB+SAS in maintaining trajectory. However, a slight increase in error is observed for DB as shown in Table 5-4.

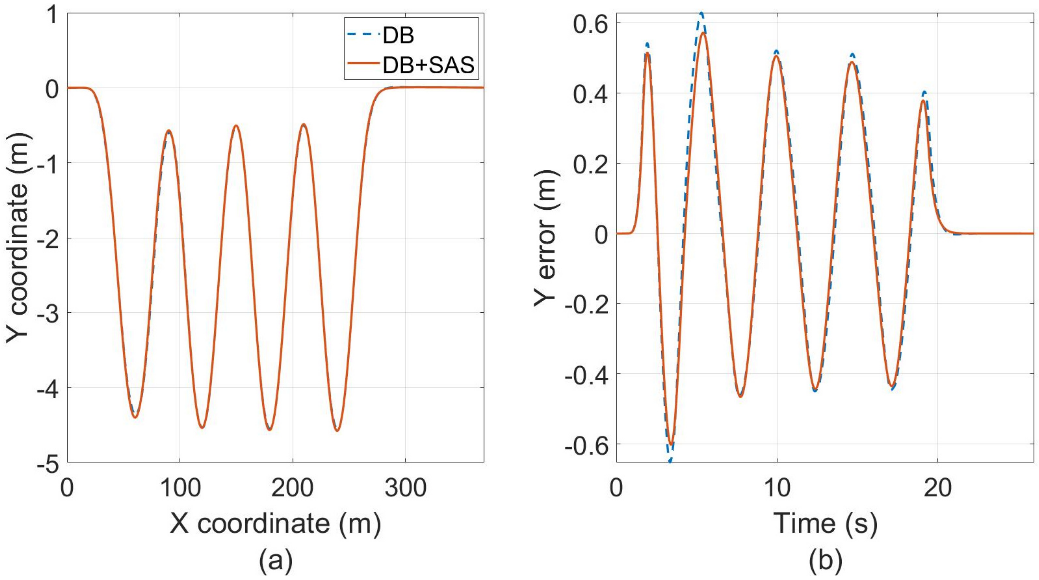

Figure 5-32 (a) Vehicle trajectory during Slalom at 65 Km/h ($\mu = 0.85$) and (b) Error obtained by DB and DB+SAS

Table 5-4 Trajectory Root Mean Square Errors Obtained by DB and DB+SAS during Slalom at 65 Km/h ($\mu = 0.85$)

Controller’s Configuration	RMSE (m)
DB	0.2986
DB+SAS	0.2866

The vehicle sideslip, yaw rate, longitudinal speed and Lateral Acceleration for DB and DB+SAS are shown in Figure 5-33, Figure 5-34, Figure 5-35 and Figure 5-36 respectively. The DB+SAS has achieved less sideslip angle and stabilizes the vehicle faster than DB, which considered as a merit for DB+SAS over DB in terms of enhancing vehicle’s stability at high road friction surface. There is no any significant difference in yaw rate response amplitude between DB and DB+SAS.

However, a slight delay encountered for DB to stabilize the vehicle than DB+SAS. Since the braking is utilized as a control allocation, therefore, a drop in longitudinal speed was expected. Nevertheless, the drop in speed was almost same for both control strategies which is around 45 Km/h. Moreover, it should be noted that DB and DB+SAS have a tremendous effect in minimizing the lateral acceleration compared to any other control allocation strategies. And this due to the reduction in speed occurred as a result of employing the braking as control allocation. Nonetheless, the DB+SAS has displayed a superiority over DB in reducing the lateral acceleration below 0.4 g's. As well as by keeping the peak amplitude smooth and faster in stabilizing the vehicle.

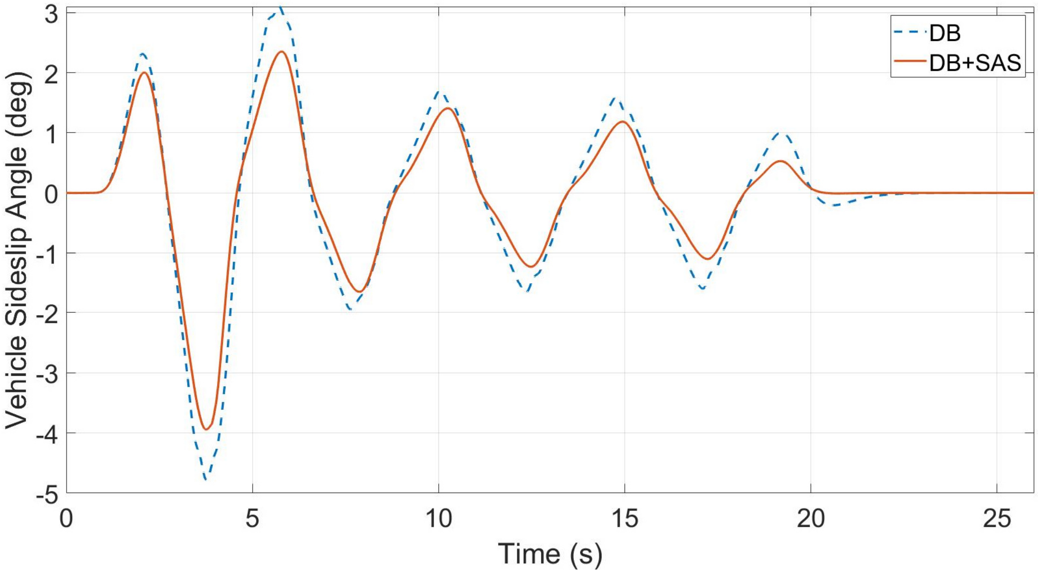

Figure 5-33 Vehicle Sideslip Angle during Slalom at 65 Km/h (μ = 0.85)

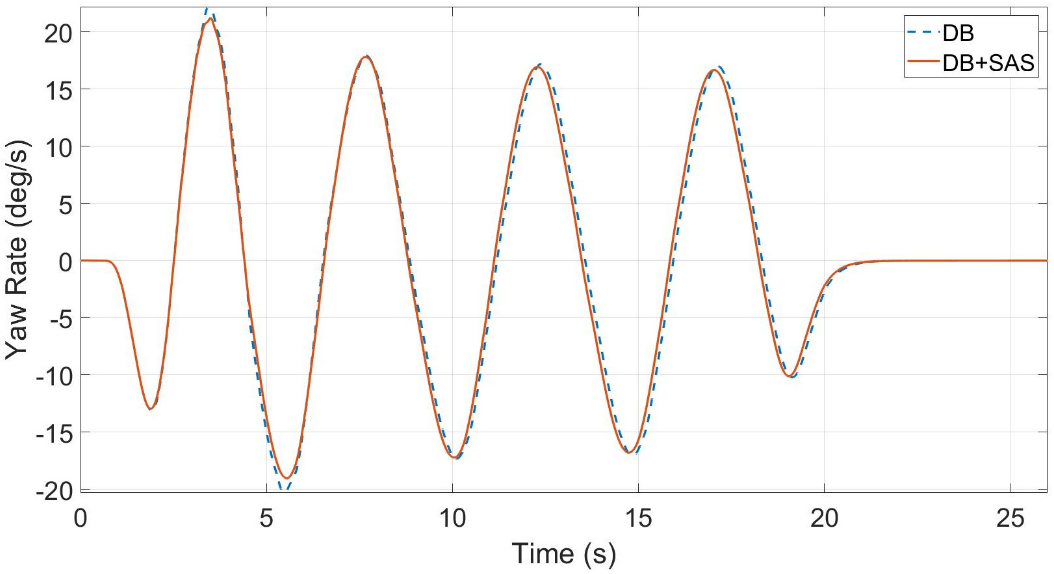

Figure 5-34 Yaw Rate during Slalom at 65 Km/h (μ = 0.85)

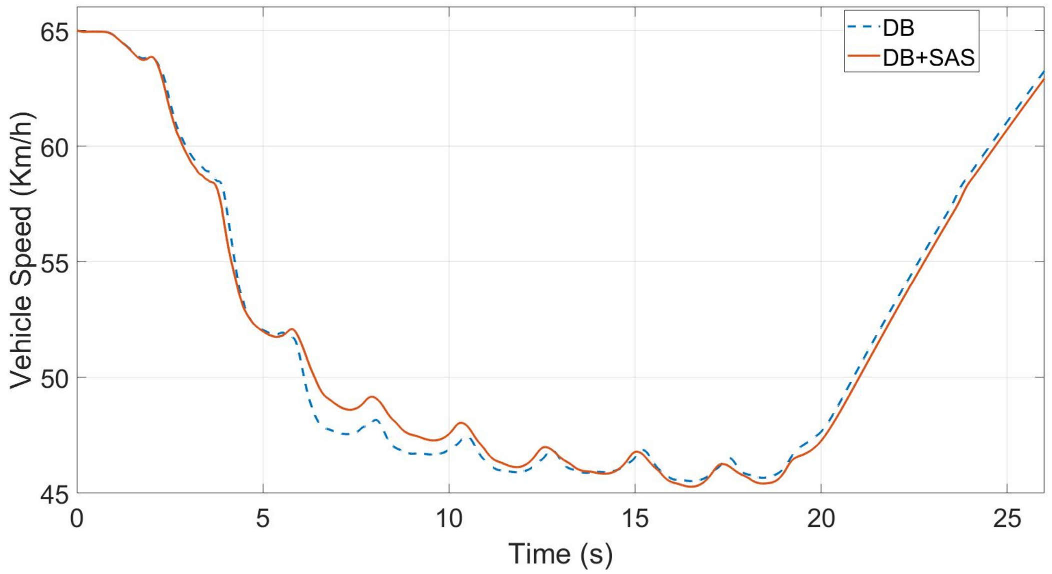

Figure 5-35 Vehicle Speed during Slalom at 65 Km/h (μ = 0.85)

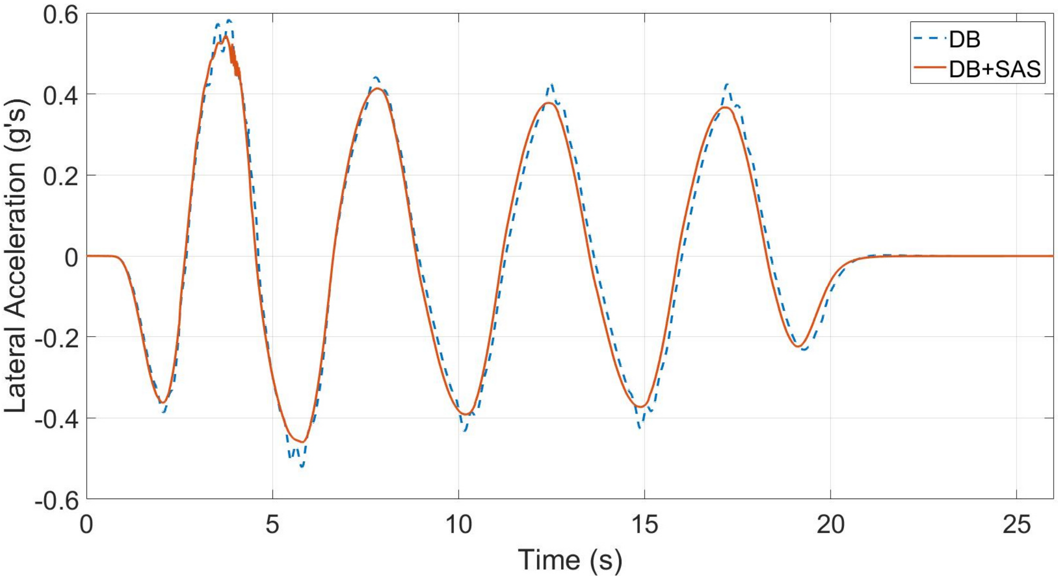

Figure 5-36 Lateral Acceleration during Slalom at 65 Km/h ($\mu = 0.85$)

Figure 5-37, Figure 5-38 and Figure 5-39 depict the sprung mass displacement, pitch and roll angle for DB and DB+SAS, respectively. It can be observed the considerable effect of integrating SAS in particularly with employing the braking as a control allocation strategy. For the sprung mass displacement, the DB+SAS has showed superiority over DB in damping the variation in heave motion to smallest value while DB reached almost 0.06 meters. The variation in longitudinal load transfer due to braking and recuperating the speed by the driver, can be demonstrated through pitch angle plot. Accordingly, the DB+SAS has dampened the pitch angle at smallest value -0.08 degree, while -1.7 degree for DB. Furthermore, the DB+SAS has succeeded to maintain the roll angle at smallest value below 2 degrees, while reached 6 degrees for DB. Consequently, leading to minimizing the drop in total lateral forces due to lateral load transfer caused by roll angle.

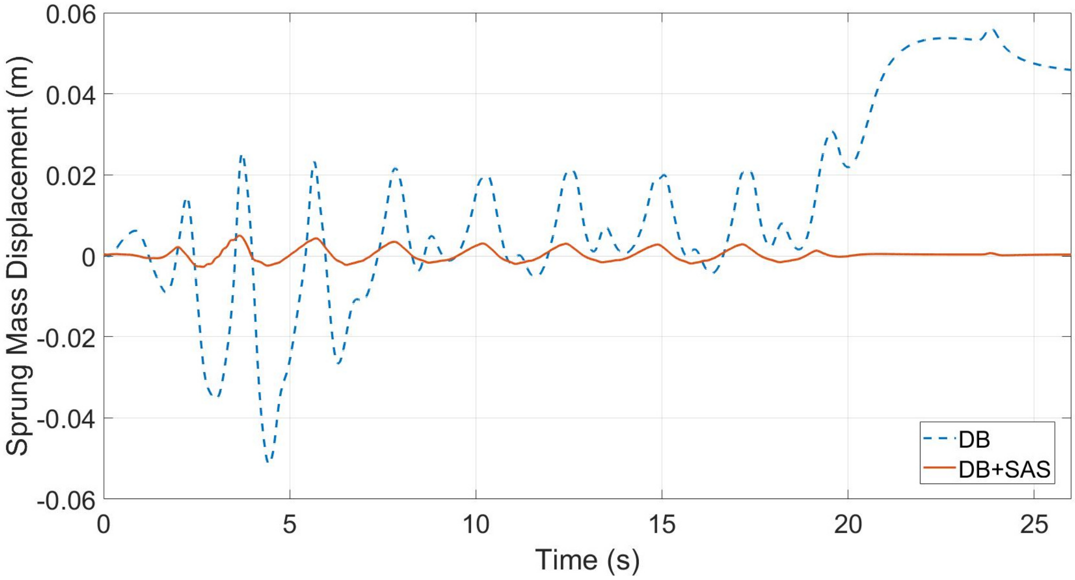

Figure 5-37 Sprung Mass Displacement during Slalom at 65 Km/h (μ = 0.85)

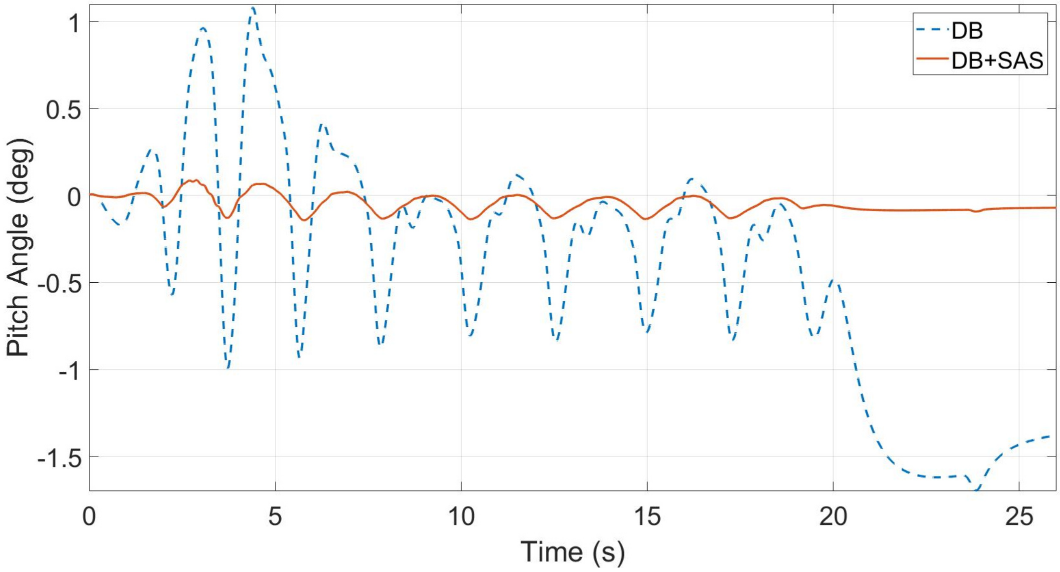

Figure 5-38 Pitch Angle during Slalom at 65 Km/h (μ = 0.85)

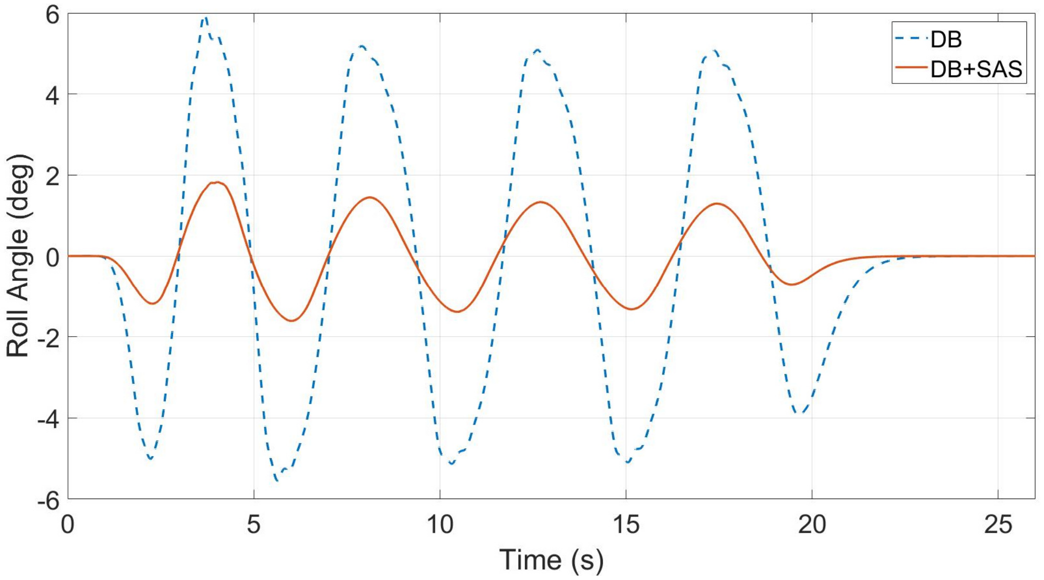

Figure 5-39 Roll Angle during Slalom at 65 Km/h (μ = 0.85)

Figure 5-40 and Figure 5-41 show the left and right braking wheel torque in (a) and (b) for DB and DB+SAS. There is no any significant difference can be observed in braking torque magnitude between DB and DB+SAS. However, a smooth braking torque was induced for DB+SAS than in DB.

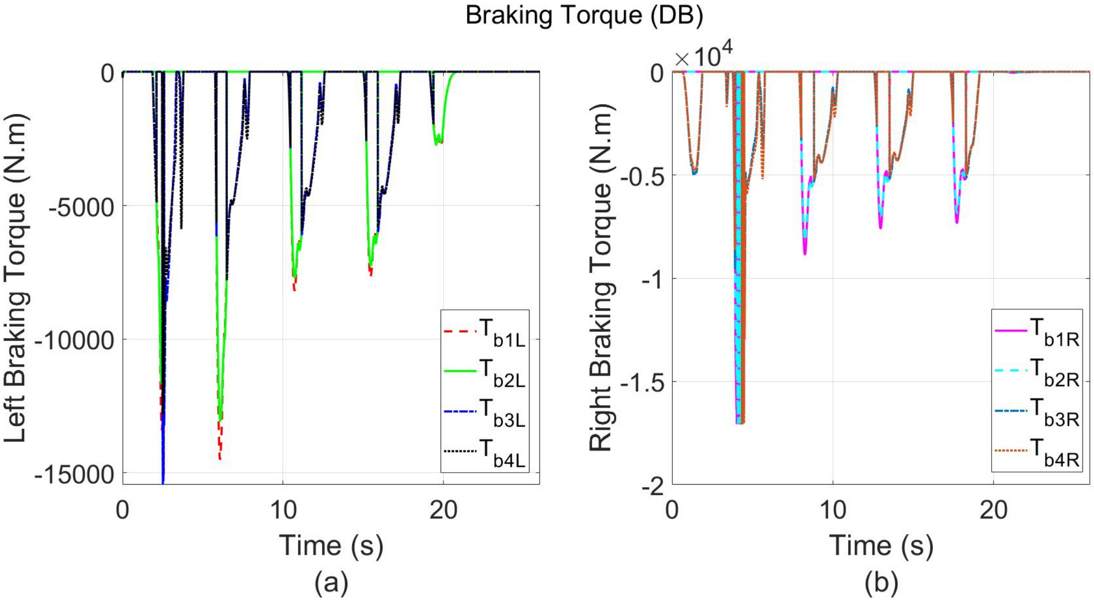

(a)

(b)

Figure 5-40 (a) Left Braking Wheel Torque and (b) Right Braking Wheel Torque for DB during Slalom at 65 Km/h (μ = 0.85)

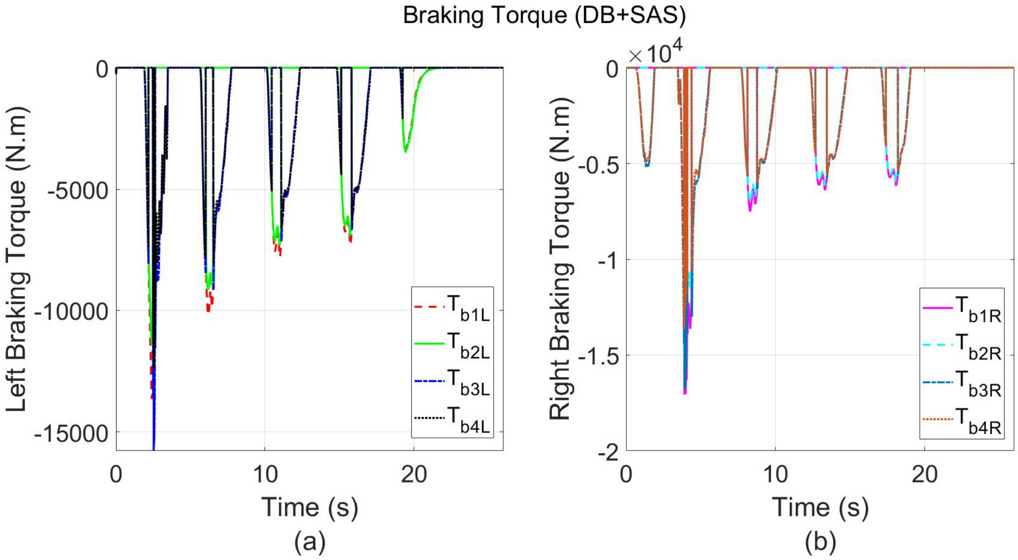

Figure 5-41 (a) Left Braking Wheel Torque and (b) Right Braking Wheel Torque for DB+SAS during Slalom at 65 Km/h ($\mu = 0.85$)

Figure 5-42 and Figure 5-43 illustrate the left and right sides' vehicle dampers 'compressive forces in (a) and (b) respectively for DB and DB+SAS. It is notable that DB+SAS has obtained largest dampers 'compressive forces varying with time. The largest left side dampers' force was 15970.1 N and 14607.1 N for left and right sides, respectively. while for DB was 7916.4 N and 8082.1 N for the left and right side, respectively.

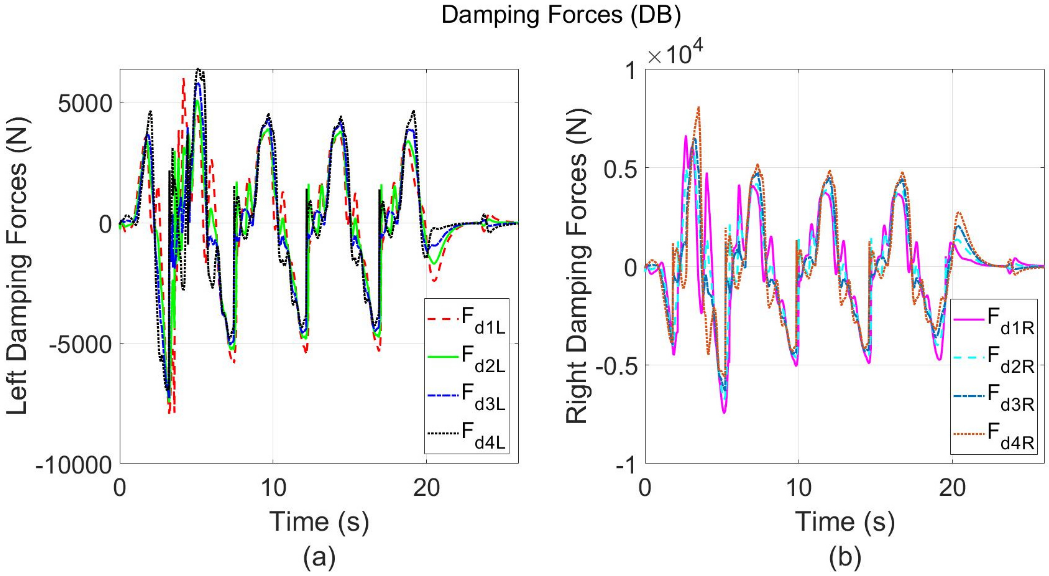

Figure 5-42 (a) Left Damping Forces and (b) Right Damping Forces for DB during Slalom at 65 Km/h ($\mu = 0.85$)

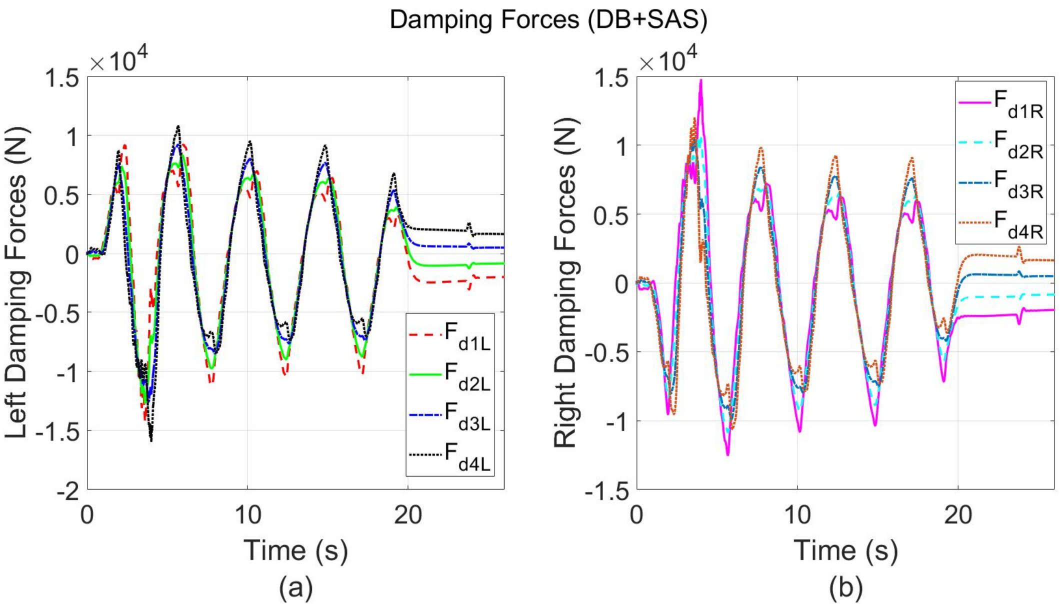

Figure 5-43 (a) Left Damping Forces and (b) Right Damping Forces for DB+SAS during Slalom at 65 Km/h ($\mu = 0.85$)

Figure 5-44 and Figure 5-45 demonstrate the left and right sides' vehicle normal loads in (a) and (b) respectively for DB and DB+SAS. It is remarkable that DB+SAS has greatly prevented the vehicle's wheels on both sides to left off the ground during the maneuver event while DB not. Hence, keeping the tires in contact with the ground, has a great effect on vehicle's lateral stability in terms of avoiding rollover at high-speed cornering maneuver. Moreover, minimizing the drop of the lateral forces between the contact patch of tires and the ground due to lateral load transfer.

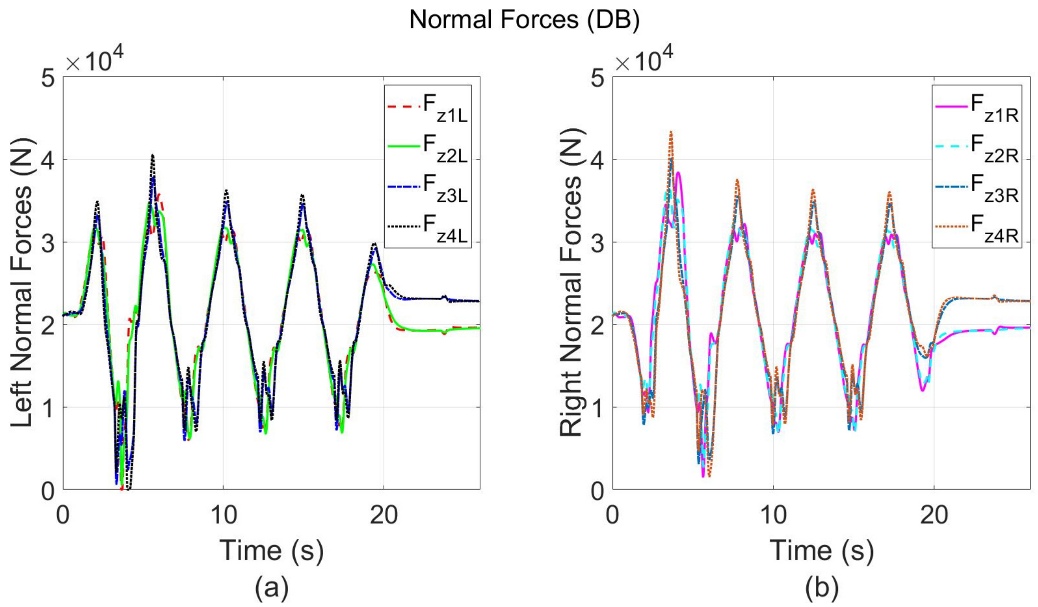

(a) (b)

Figure 5-44 (a) Left Normal Forces and (b) Right Normal Forces for DB during Slalom at 65 Km/h ($\mu = 0.85$)

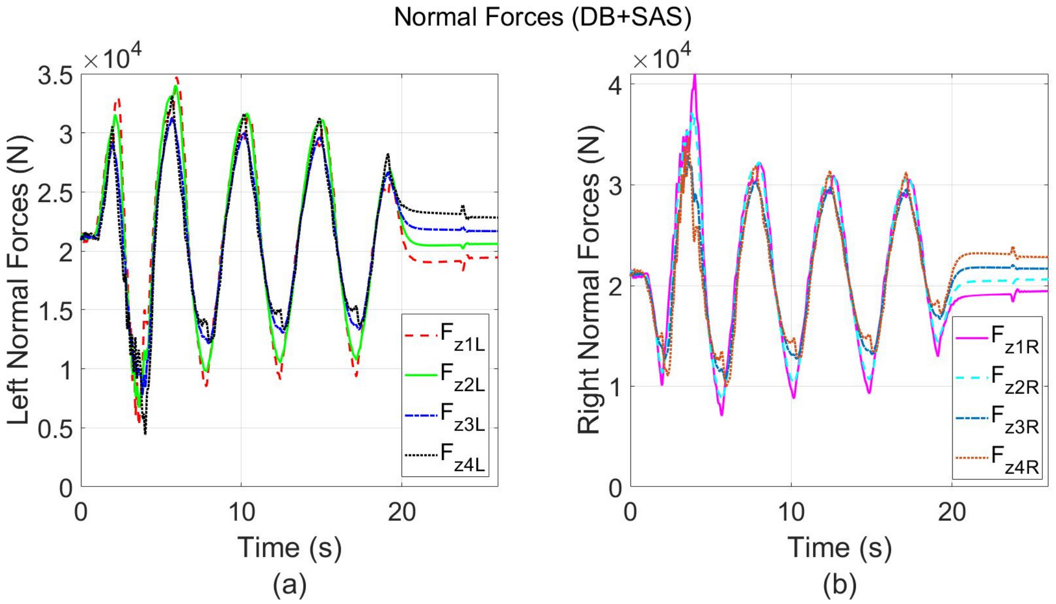

(a) (b)

Figure 5-45 (a) Left Normal Forces and (b) Right Normal Forces for DB+SAS during Slalom at 65 Km/h ($\mu = 0.85$)

Figure 5-46 and Figure 5-47 represent the slip ratio of the left and right sides' vehicle tires (a) and (b) for DB and DB+SAS. It can be noticed the intervention of slip controller in both control strategies to prevent the slip ratio exceeding 25% while braking is engaged, where the peak braking forces can be obtained. However, a remarkable arise in slip ratio nearly 45% during recuperating speed (driving) encountered for DB and this due to the effect of the lateral load transfer while the DB+SAS not. It should be noted that there is no slip controller on the driving torque when employing the braking as a control allocation.

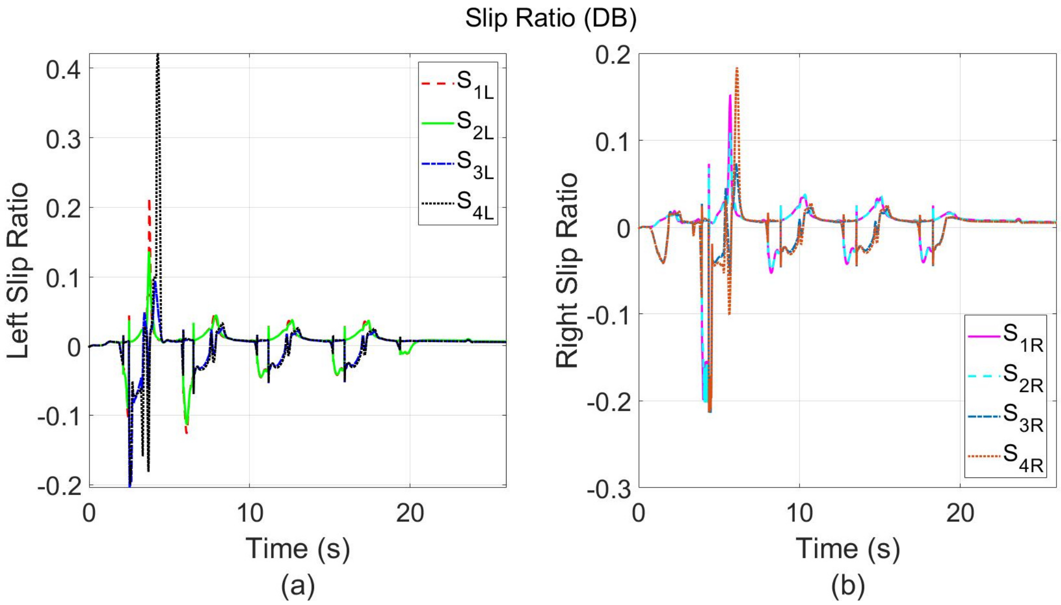

(a) (b)

Figure 5-46 (a) Left Tires' Slip Ratio and (b) Right Tires' Slip Ratio for DB during Slalom at 65 Km/h (μ = 0.85)

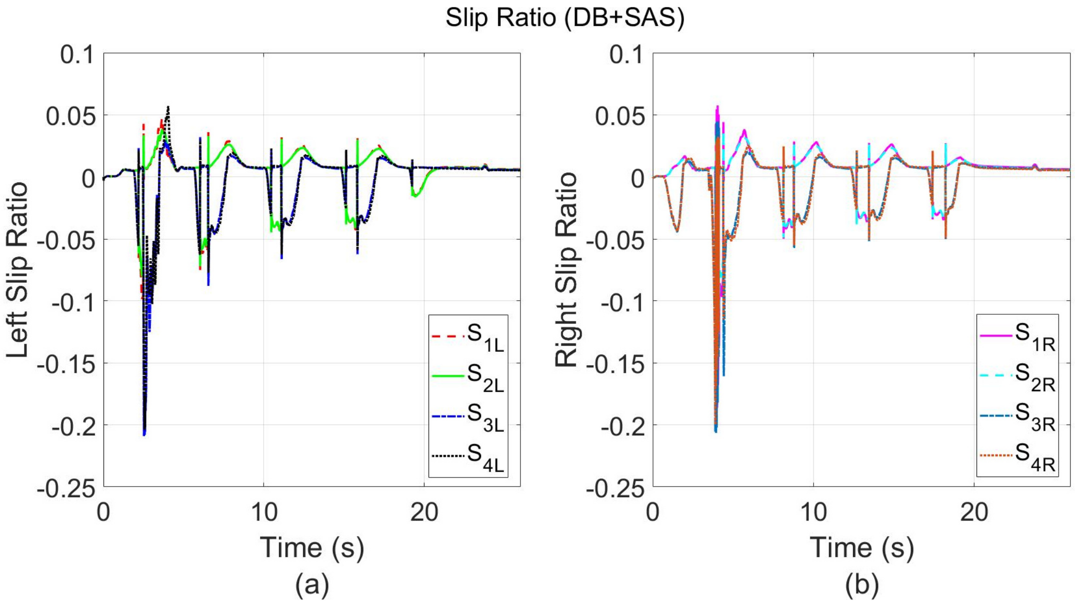

(a) (b)

Figure 5-47 (a) Left Tires' Slip Ratio and (b) Right Tires' Slip Ratio for DB+SAS during Slalom at 65 Km/h (μ = 0.85)

5.2.1.2 Results and Discussion of the assessment of each controller performance at low coefficient of friction – Constant Step Slalom ($40\ km/h\ ;\ \mu = 0.35$)

5.2.1.2.1 AWS vs AWS+SAS

Figure 5-48 show the vehicle trajectory and the corresponding error performed by each control strategy AWS and AWS+SAS, respectively. It can be noticed that AWS+SAS has achieved slightly least error compared to AWS as shown in Table 5-5. As well as AWS+SAS stabilizes the vehicle faster than AWS.

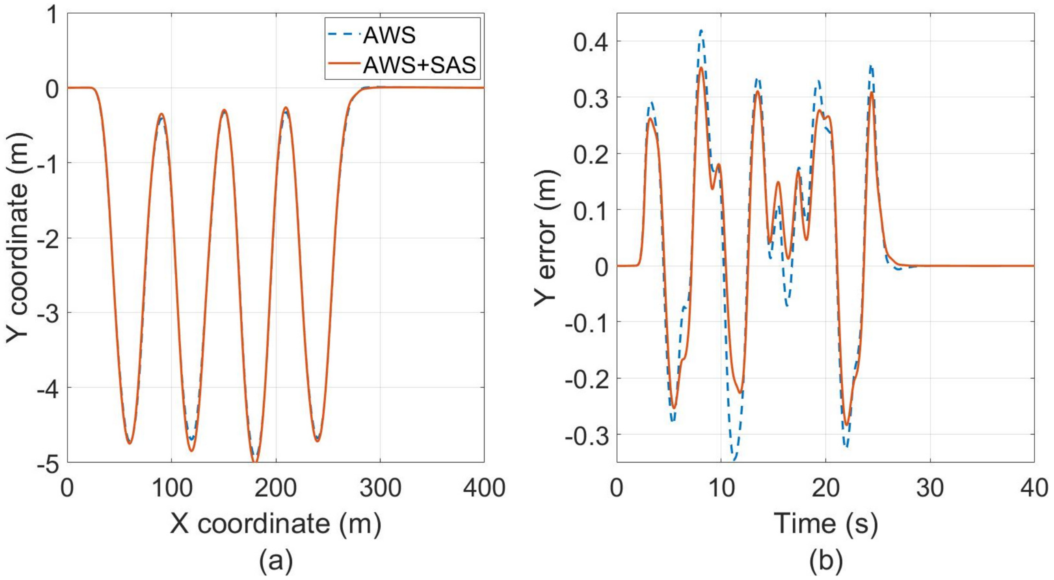

Figure 5-48 (a) Vehicle trajectory during Slalom at 40 Km/h (μ = 0.35) and (b) Error obtained by AWS and AWS+SAS

Table 5-5 Trajectory Root Mean Square Errors Obtained by AWS and AWS+SAS during Slalom at 40 Km/h (μ = 0.35)

Controller's Configuration	RMSE (m)
AWS	0.1642
AWS+SAS	0.1452

Figure 5-49, Figure 5-50, Figure 5-51 and Figure 5-52 demonstrate the vehicle sideslip, yaw rate, longitudinal speed and lateral acceleration for both AWS and AWS+SAS, respectively. Its notable that AWS and AWS+SAS have achieved almost the same peak amplitude sideslip angle. However, a slight difference is observed in terms of stabilizing fast the vehicle for AWS+SAS. As for yaw rate response amplitude is approximately maintained the same for both control strategies. Furthermore, regarding to the longitudinal speed and lateral acceleration it can be observed that both control strategies have obtained identical results concerning the variation in speed and the stabilization time.

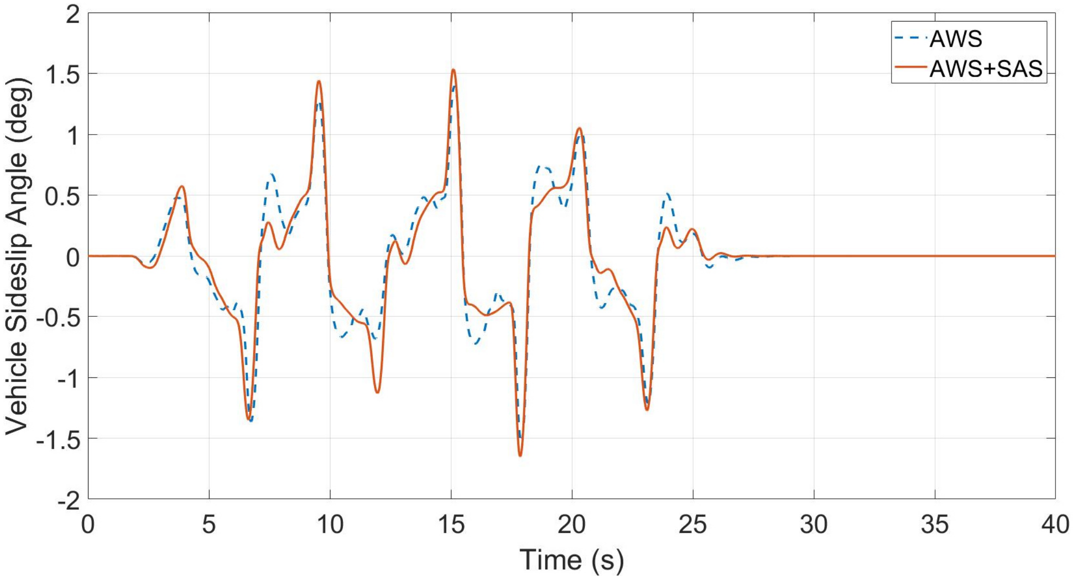

Figure 5-49 Vehicle Sideslip Angle during Slalom at 40 Km/h (μ = 0.35)

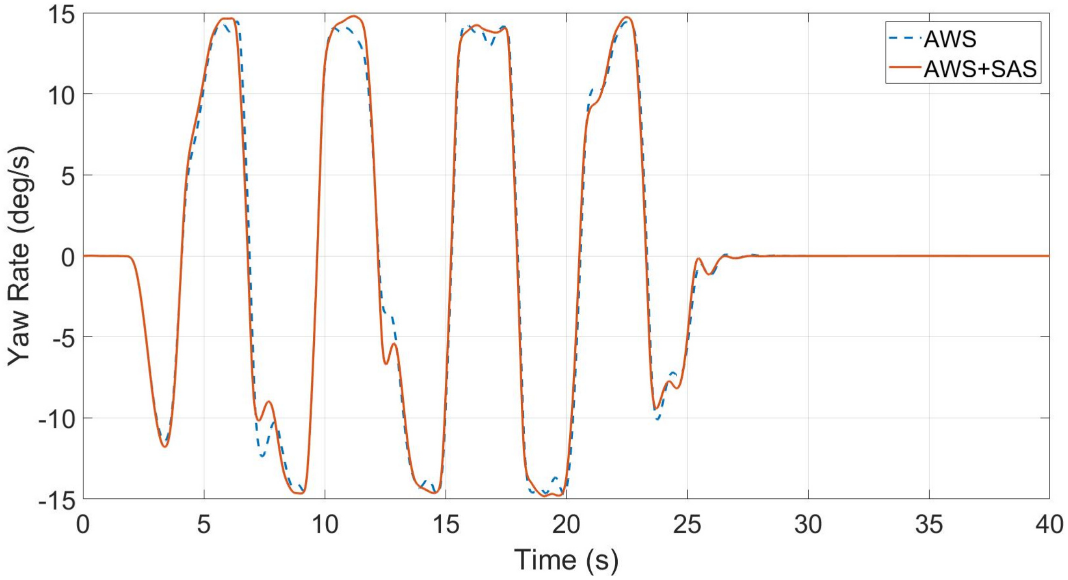

Figure 5-50 Yaw Rate during Slalom at 40 Km/h (μ = 0.35)

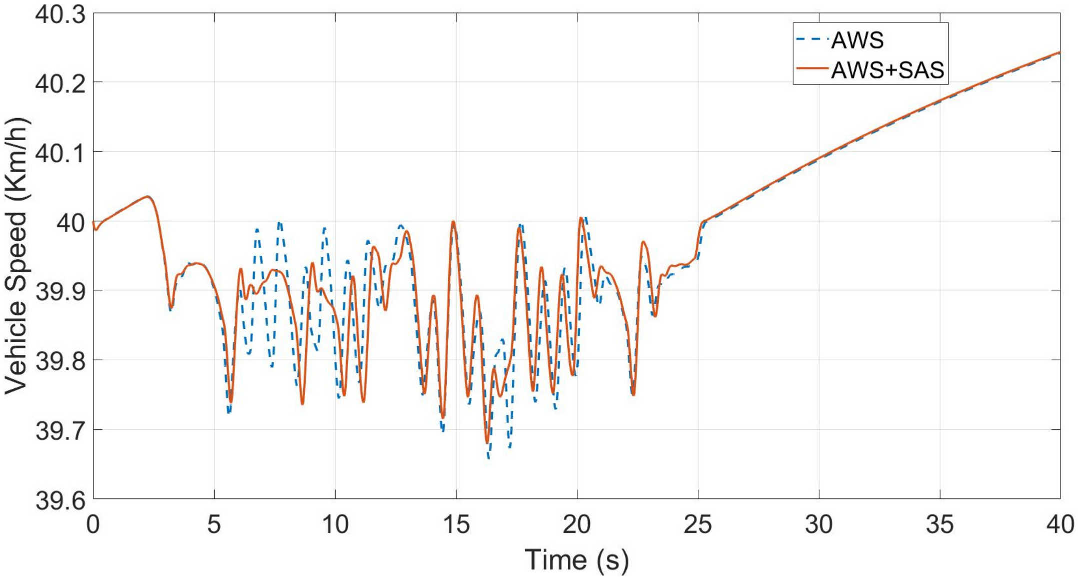

Figure 5-51 Vehicle Speed during Slalom at 40 Km/h (μ = 0.35)

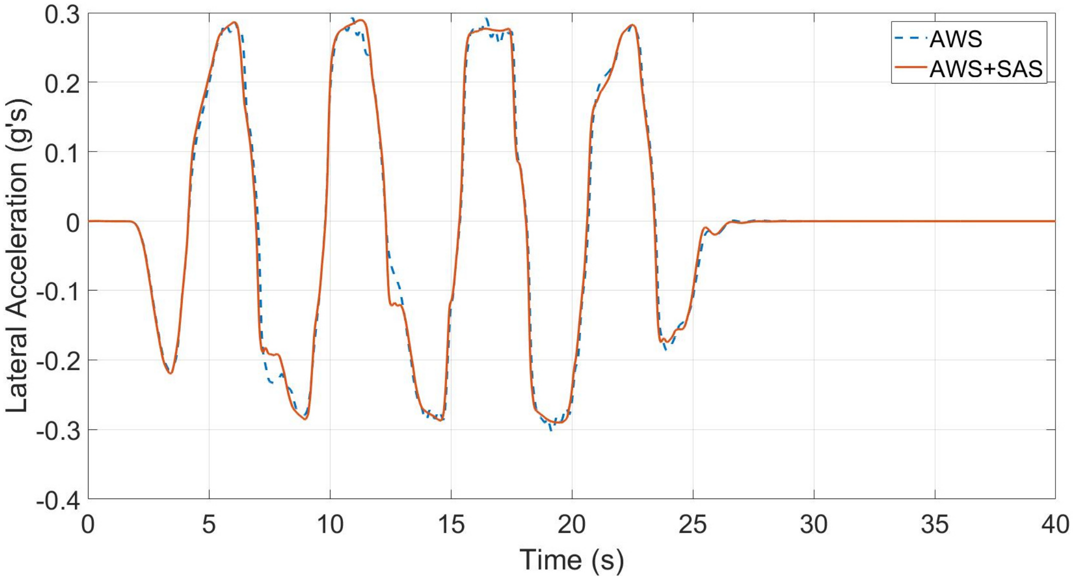

Figure 5-52 Lateral Acceleration during Slalom at 40 Km/h (μ = 0.35)

Figure 5-53, Figure 5-54 and Figure 5-55 illustrate the vehicle's sprung mass displacement, pitch, and roll angle, respectively. It can be observed that AWS+SAS has significantly reduced the vertical displacement at the CG of the sprung mass to smallest value compared to AWS. Furthermore, AWS+SAS has enormously minimized the pitch and roll angle due to longitudinal and lateral load transfer.

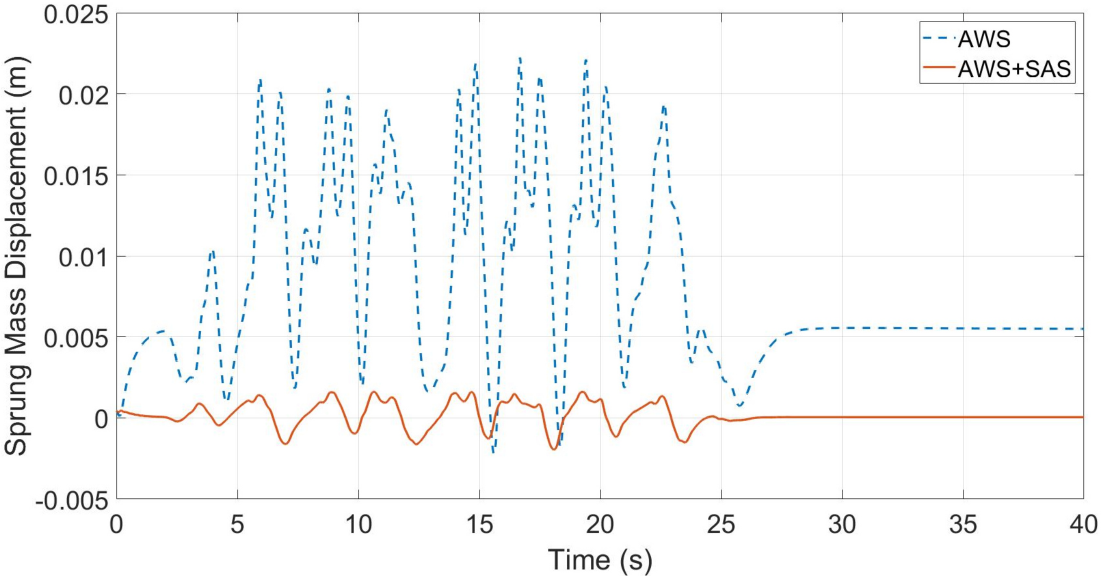

Figure 5-53 Sprung Mass Displacement during Slalom at 40 Km/h ($\mu = 0.35$)

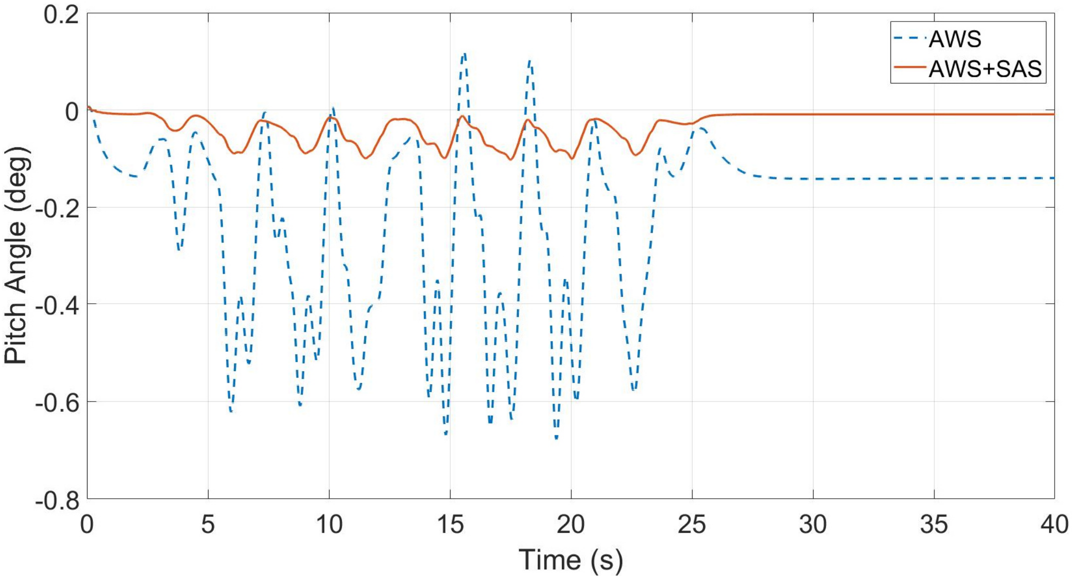

Figure 5-54 Pitch Angle during Slalom at 40 Km/h ($\mu = 0.35$)

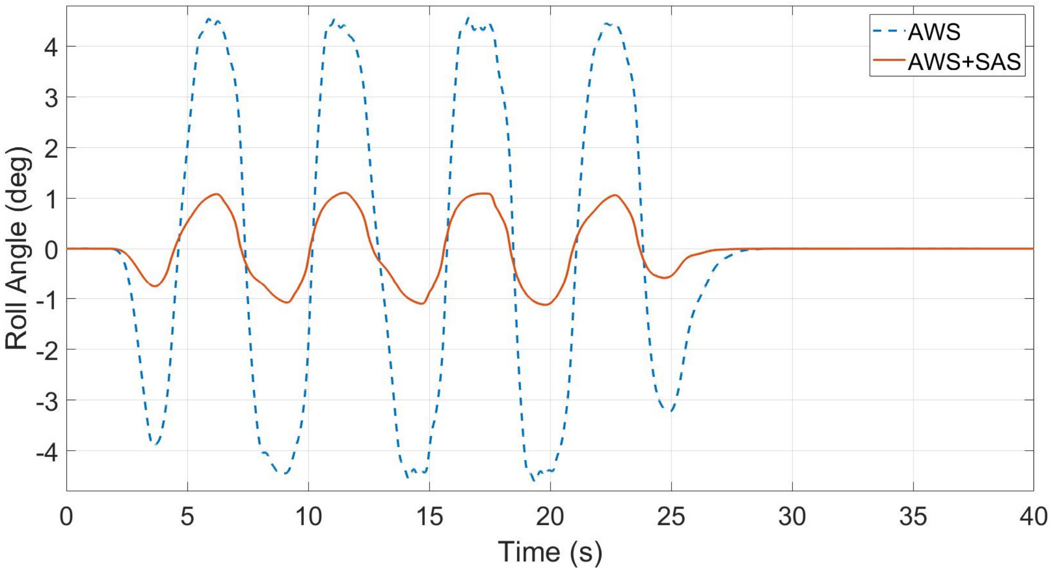

Figure 5-55 Roll Angle during Slalom at 40 Km/h ($\mu = 0.35$)

Figure 5-56 and Figure 5-57 demonstrate the front and rear road steer angles in (a) and (b) for AWS and AWS+SAS, respectively. It is remarkable that AWS+SAS exhibits larger front and rear steer angle compared to AWS, which interpreted as the vehicle has tendency to drift out. Thus, the AWS+SAS controller deals with that issue by increasing the steering angle to keep the vehicle on the desired trajectory. Moreover, the AWS+SAS has achieved the largest front and rear steer wheel angle, which is 19.1 and 5 degrees, respectively. While the AWS has reached 18.6 and 4.5 degrees for the front and rear steering angles, respectively. It should be noted that the rear steer angles for both controllers are performing parallel steering (steering in the same direction as the front steering angles).

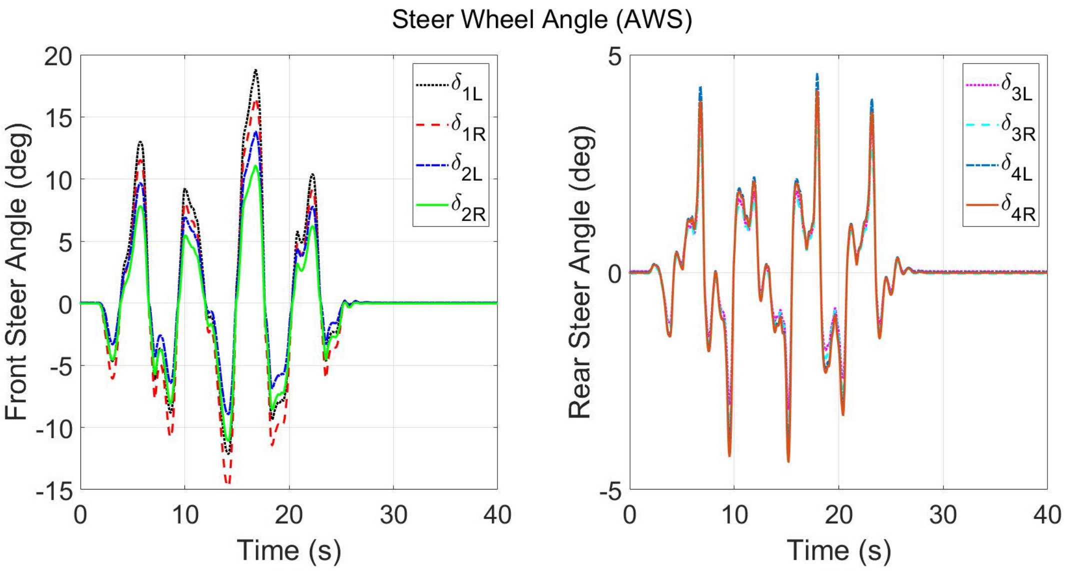

(a) (b)

Figure 5-56 (a) Front Steer Angle and (b) Rear Steer Angle for AWS during Slalom at 40 Km/h (μ = 0.35)

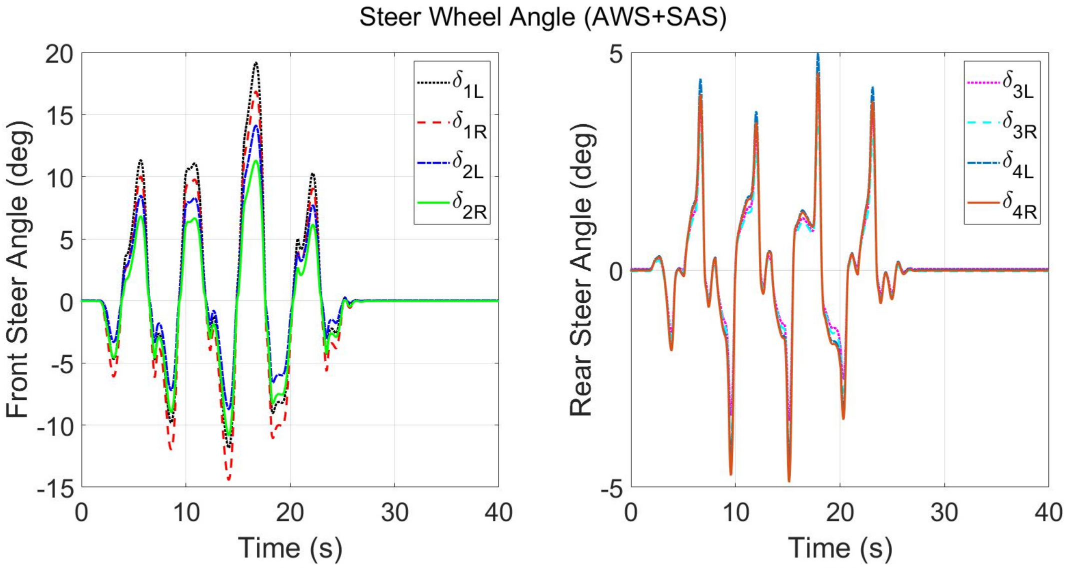

(a) (b)

Figure 5-57 (a) Front Steer Angle and (b) Rear Steer Angle for AWS+SAS during Slalom at 40 Km/h (μ = 0.35)

Figure 5-58 and Figure 5-59 show the left and right sides' vehicle dampers 'compressive forces in (a) and (b) respectively for AWS and AWS+SAS. It can be observed that AWS and AWS+SAS have obtained approximately the same dampers 'compressive forces. The largest left side dampers' force was 7169.6 N and for the right side was 7277.4 N. while for AWS+SAS was 7566.5 N and 7630.5 N for the left and right side, respectively.

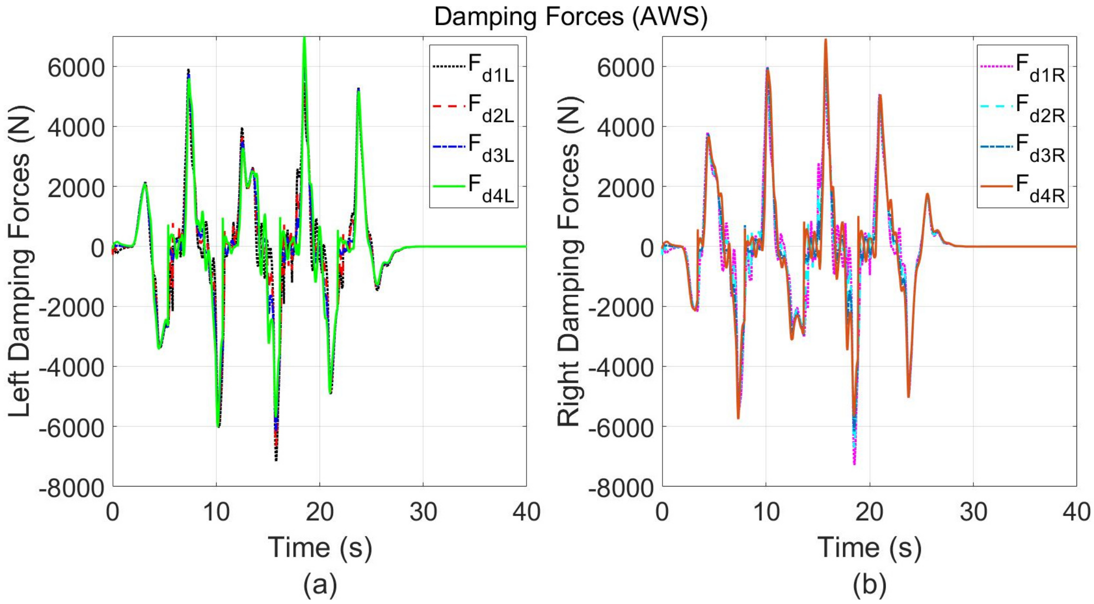

Figure 5-58 (a) Left Damping Forces and (b) Right Damping Forces for AWS during Slalom at 40 Km/h ($\mu = 0.35$)

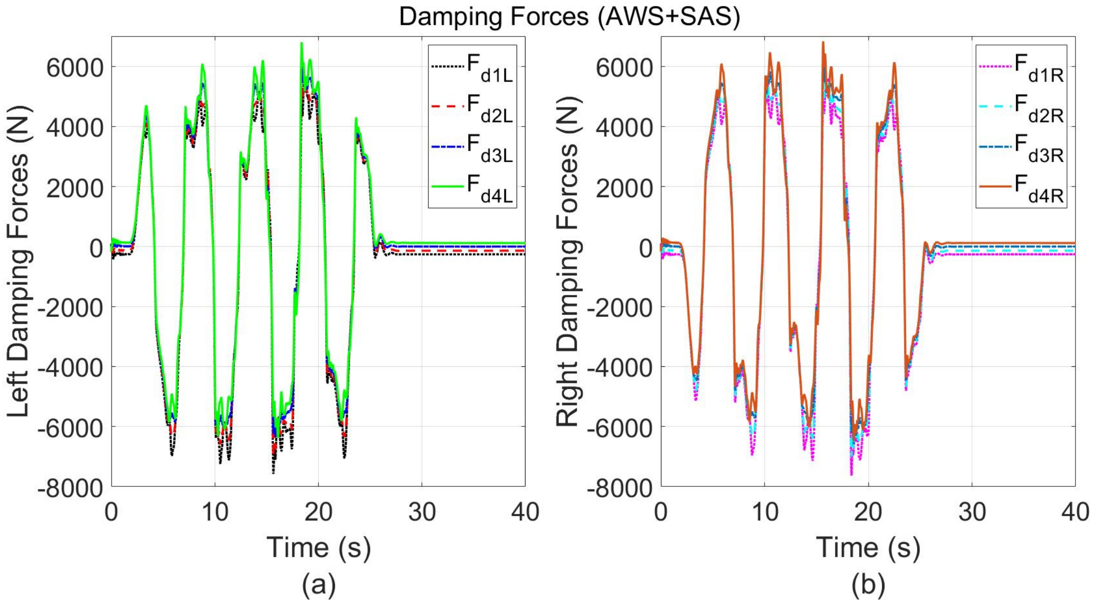

Figure 5-59 (a) Left Damping Forces and (b) Right Damping Forces for AWS+SAS during Slalom at 40 Km/h ($\mu = 0.35$)

Figure 5-60 and Figure 5-61 express the left and right sides' vehicle normal loads in (a) and (b) respectively for AWS and AWS+SAS. Its notable that AWS+SAS has substantially prevented the vehicle's wheels normal loads from dropping beyond 10000 N for both sides compared to AWS that dropped below the indicated value. For the left and right sides normal load values are 12792.6 and 12633.8 N respectively for AWS+SAS, while 8961.4 and 8655.7 N respectively for AWS.

However, this drop in the normal load is not considered significant, since the vehicle is running at low friction road surface.

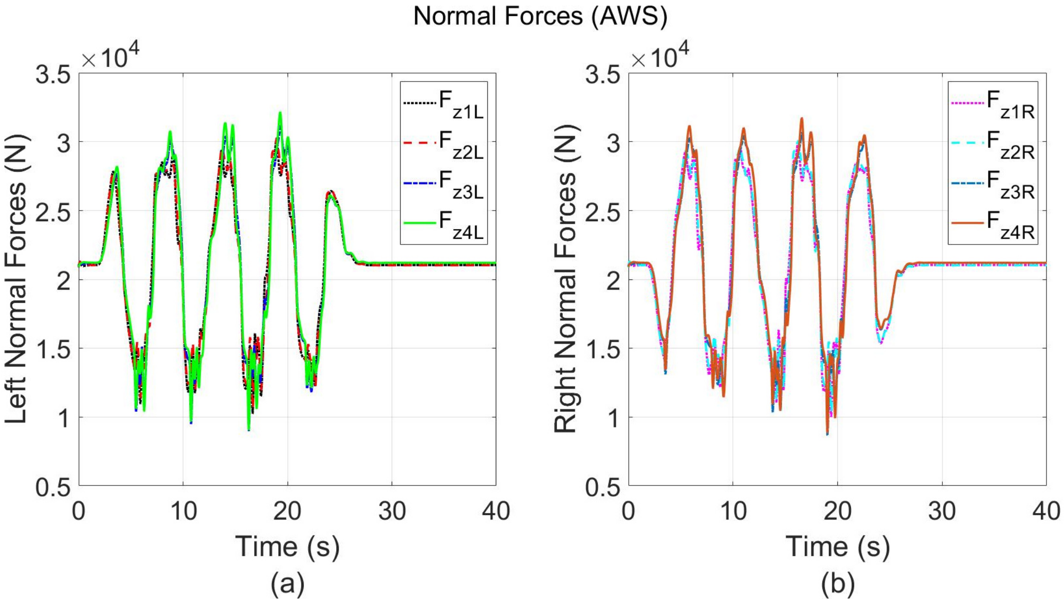

Figure 5-60 (a) Left Normal Forces and (b) Right Normal Forces for AWS during Slalom at 40 Km/h $(\mu = 0.35)$

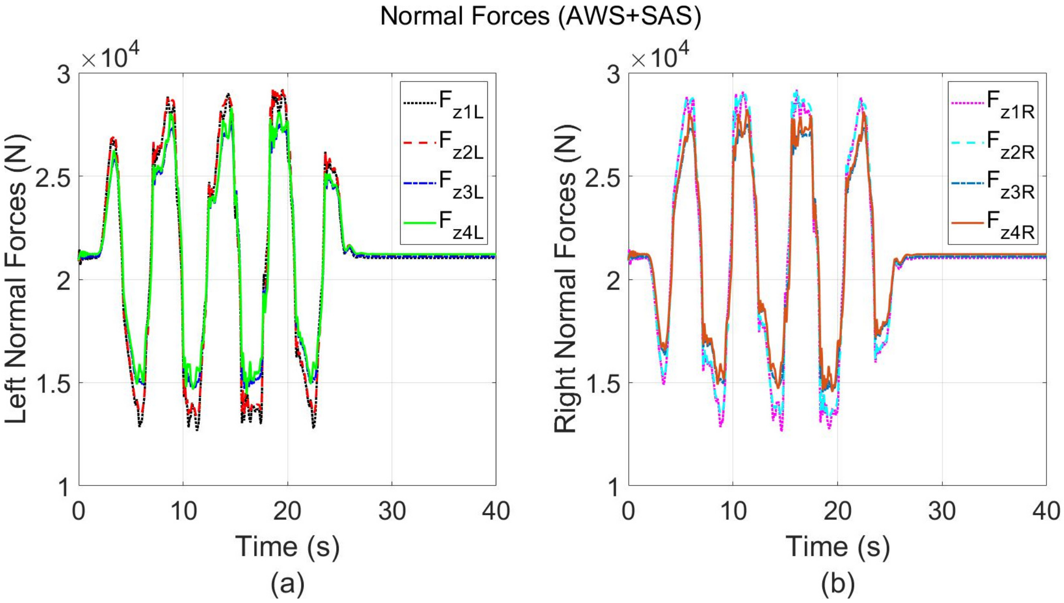

Figure 5-61 (a) Left Normal Forces and (b) Right Normal Forces for AWS+SAS during Slalom at 40 Km/h $(\mu = 0.35)$

5.2.1.2.2 TV vs TV+SAS

The vehicle trajectory and the corresponding error achieved by each control strategy TV and TV+SAS are shown in Figure 5-62 in (a) and (b) respectively. It can be noticed that TV+SAS has slightly maintained less error compared to TV as depicted in Table 5-6. Furthermore, the TV has stabilized the vehicle faster than TV+SAS based on the settling time.

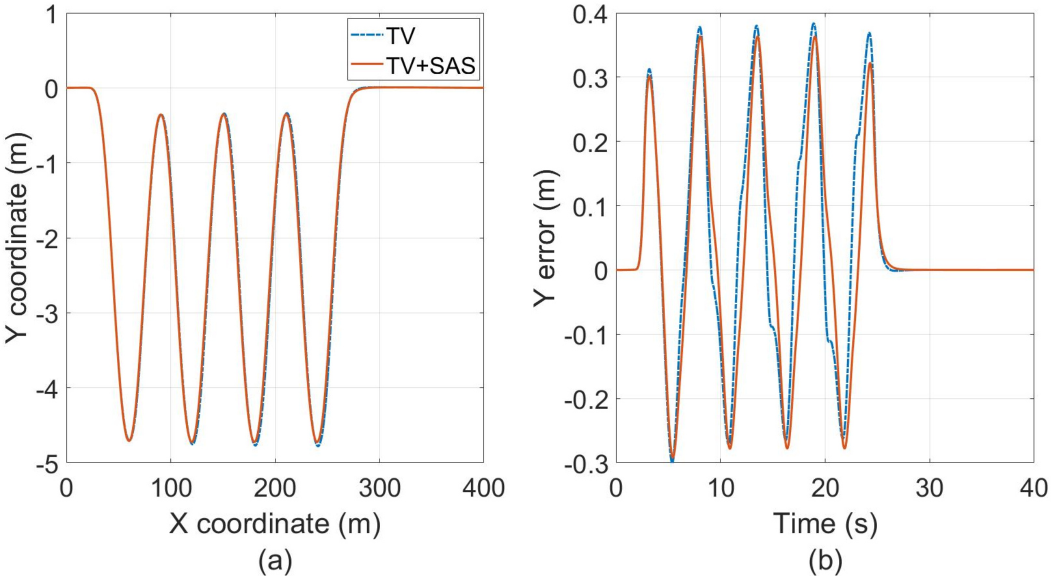

Figure 5-62 (a) Vehicle trajectory during Slalom at 40 Km/h ($\mu = 0.35$) and (b) Error obtained by TV and TV+SAS

Table 5-6 Trajectory Root Mean Square Errors Obtained by TV and TV+SAS during Slalom at 40 Km/h ($\mu = 0.35$)

Controller's Configuration	RMSE (m)
TV	0.1651
TV+SAS	0.1564

Figure 5-63, Figure 5-64, Figure 5-65 and Figure 5-66 represent the vehicle sideslip, yaw rate, longitudinal speed and lateral acceleration for both TV and TV+SAS, respectively. It can be observed that TV+SAS have slightly achieved less sideslip angle than TV which are 1.2 and 1.5 degrees, respectively. Also, a smooth peak amplitude response is obtained by TV+SAS and faster in stabilizing the vehicle than TV. In view of yaw rate response amplitude is approximately maintained the same for both control strategies. Moreover, concerning the longitudinal speed and lateral acceleration it can be noticed that both control strategies have attained approximately identical results concerning the variation in speed, except very slight difference in a quick stabilizing time for lateral acceleration encountered for TV+SAS.

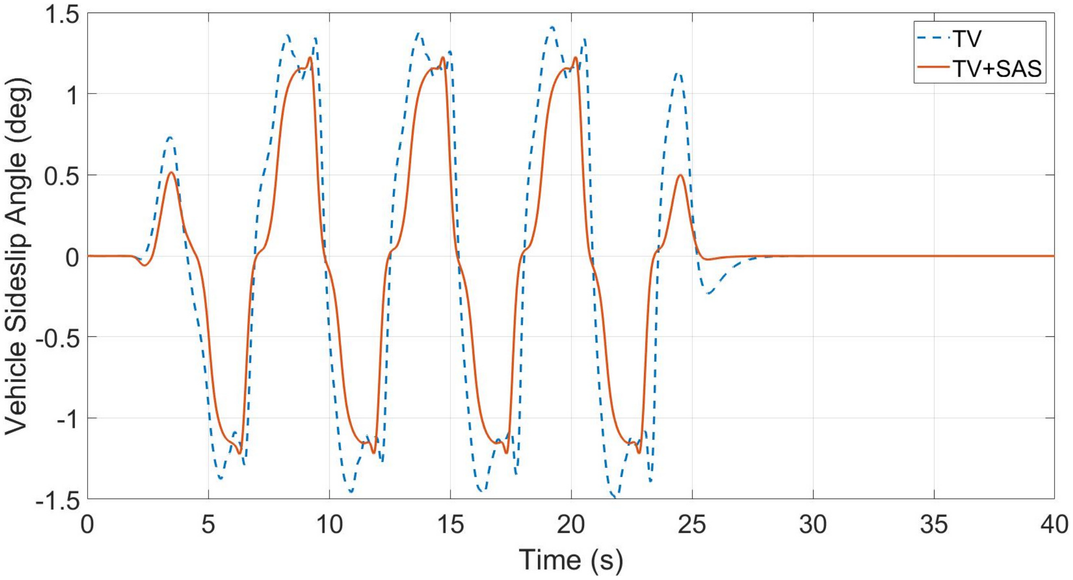

Figure 5-63 Vehicle Sideslip Angle during Slalom at 40 Km/h (μ = 0.35)

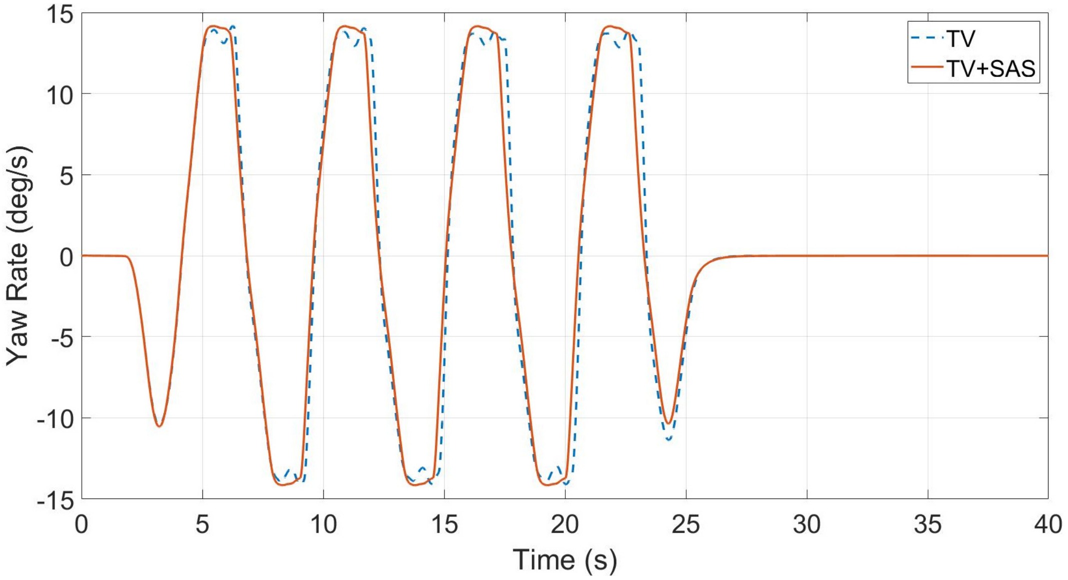

Figure 5-64 Yaw Rate during Slalom at 40 Km/h (μ = 0.35)

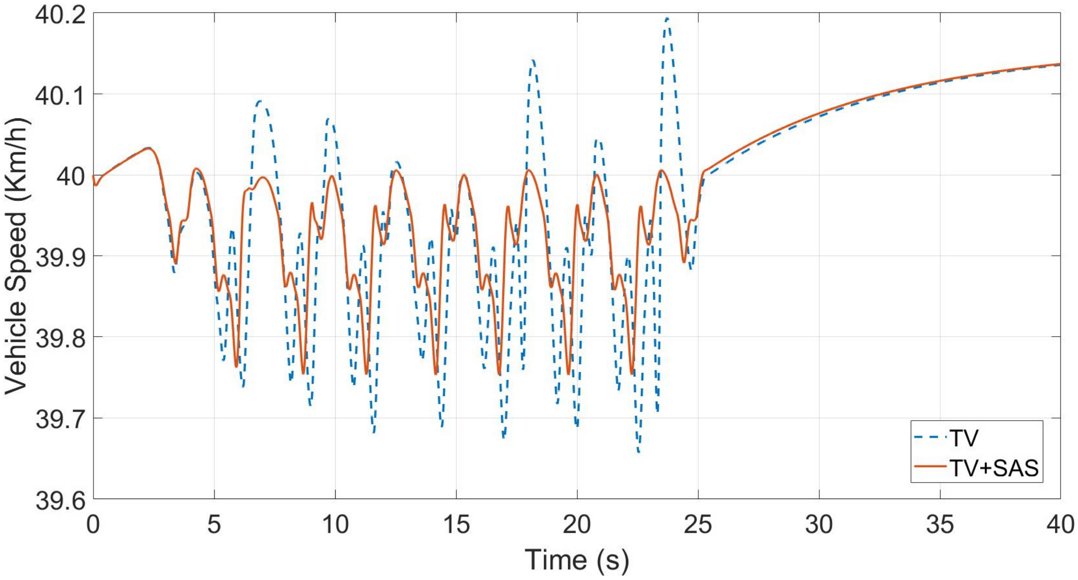

Figure 5-65 Vehicle Speed during Slalom at 40 Km/h ($\mu = 0.35$)

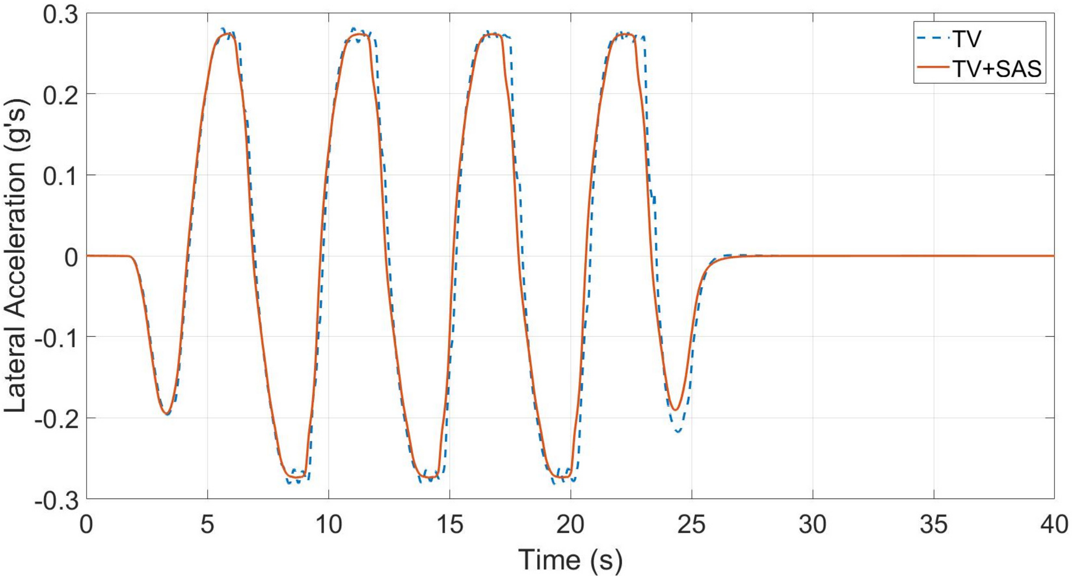

Figure 5-66 Lateral Acceleration during Slalom at 40 Km/h ($\mu = 0.35$)

Figure 5-67, Figure 5-68 and Figure 5-69 depict the vehicle's sprung mass displacement, pitch, and roll angle, respectively. It can be observed that TV+SAS has minimized the vertical displacement at the CG of the sprung mass to smallest value compared to TV. Furthermore, TV+SAS has substantially reduced the pitch and roll angle due to longitudinal and lateral load transfer.

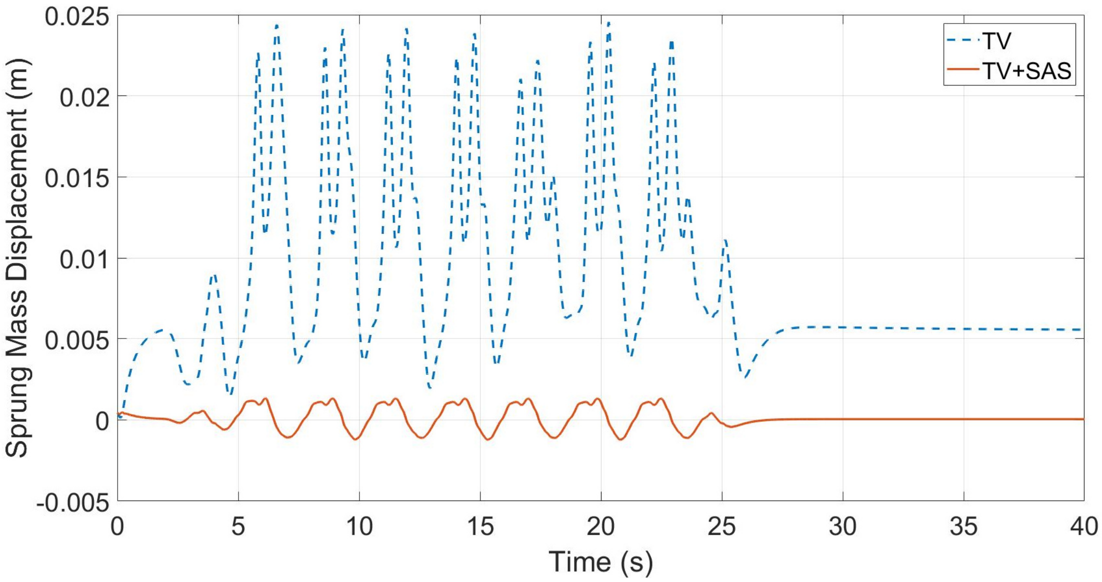

Figure 5-67 Sprung Mass Displacement during Slalom at 40 Km/h ($\mu = 0.35$)

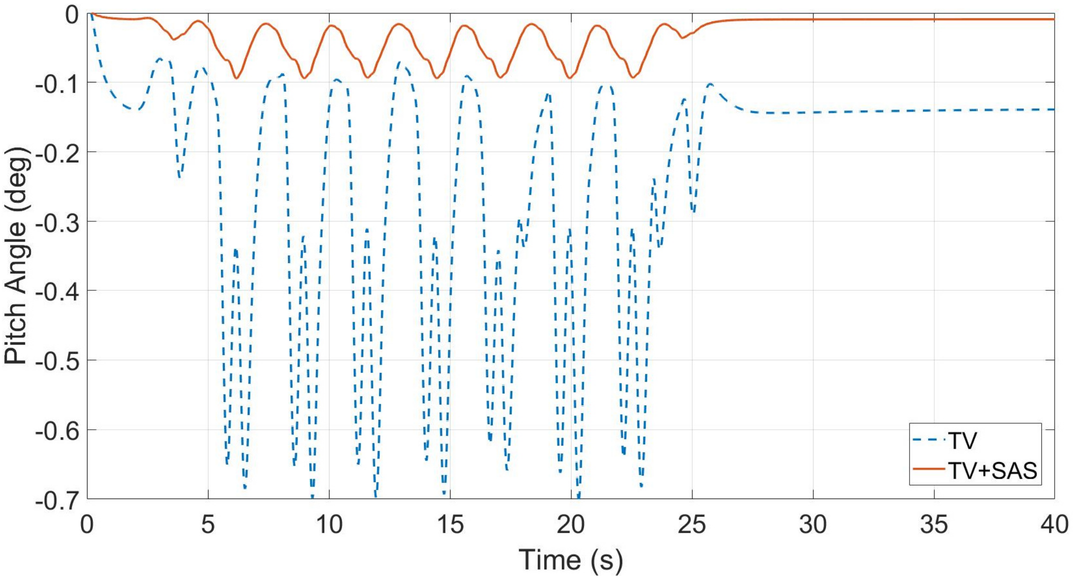

Figure 5-68 Pitch Angle during Slalom at 40 Km/h ($\mu = 0.35$)

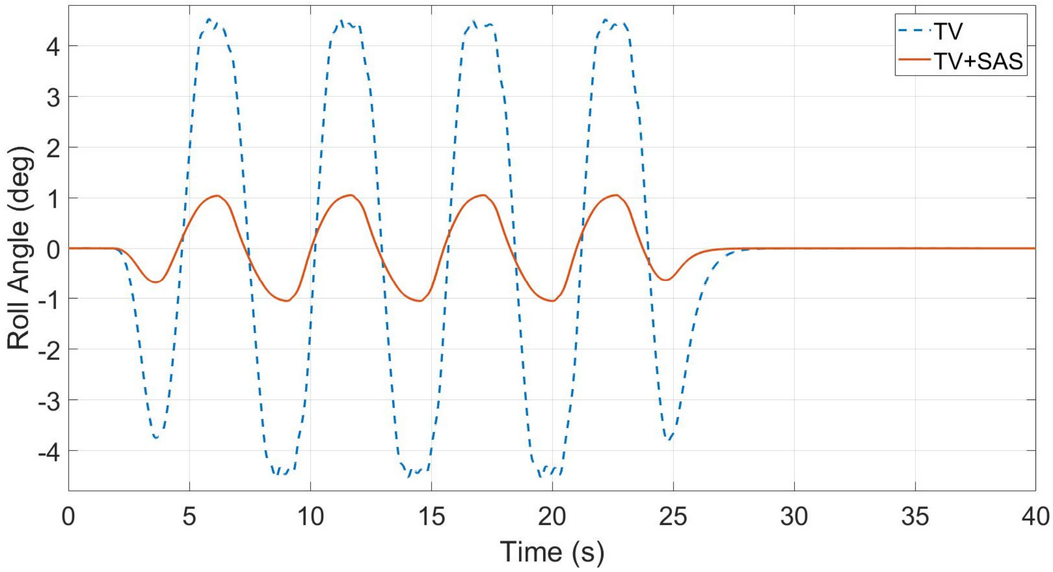

Figure 5-69 Roll Angle during Slalom at 40 Km/h (μ = 0.35)

Figure 5-70 and Figure 5-71express the left and right sides' vehicle wheels driving torque in (a) and (b) respectively. Its notable that TV+SAS have obtained less driving wheel torque for both sides which are 2388.9 Nm and 2495.4 NM, While TV attained 4687.6 Nm. and 3853.8 Nm for left and right sides, respectively. Furthermore, TV+SAS generates less fluctuated and smooth driving torque in both sides compared to TV.

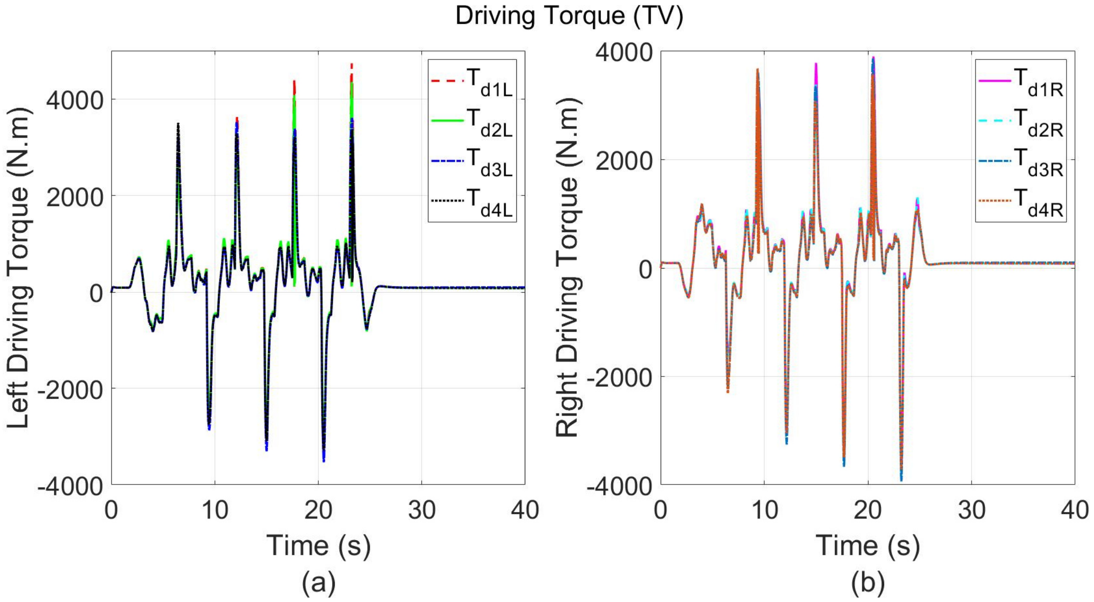

Figure 5-70 (a) Left Driving Wheel Torque and (b) Right Driving Wheel Torque for TV during Slalom at 40 Km/h (μ = 0.35)

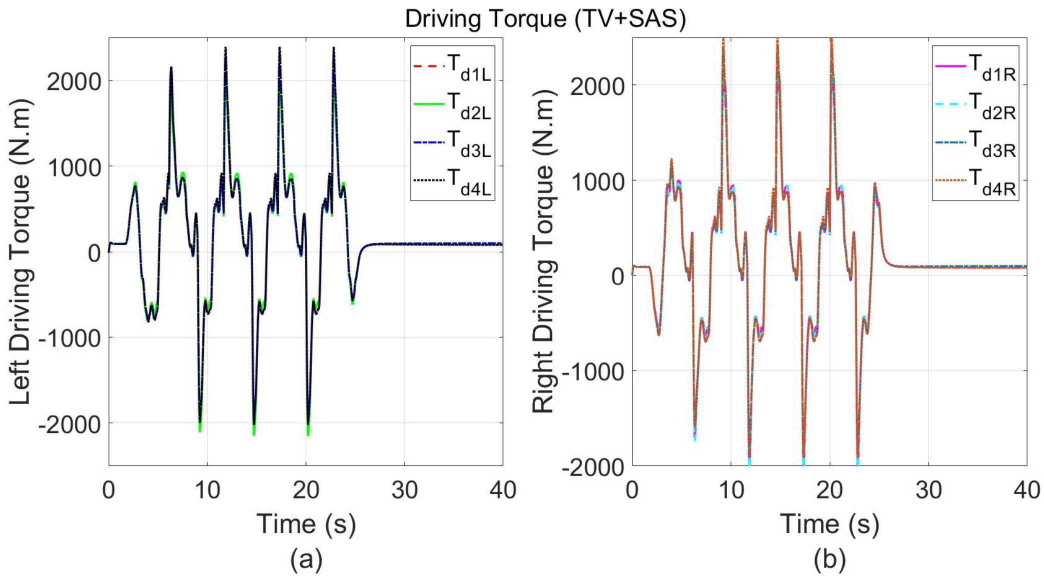

Figure 5-71 (a) Left Driving Wheel Torque and (b) Right Driving Wheel Torque for TV+SAS during Slalom at 40 Km/h (μ = 0.35)

Figure 5-72 and Figure 5-73 demonstrate the left and right sides' vehicle dampers 'compressive forces in (a) and (b) respectively for TV and TV+SAS. It can be observed that TV+SAS has obtained largest dampers 'compressive forces varying with time. The largest left side dampers' force was nearly 6000 N and for both sides. while for TV was 4511.0 N and 4419.4 N for the left and right side, respectively.

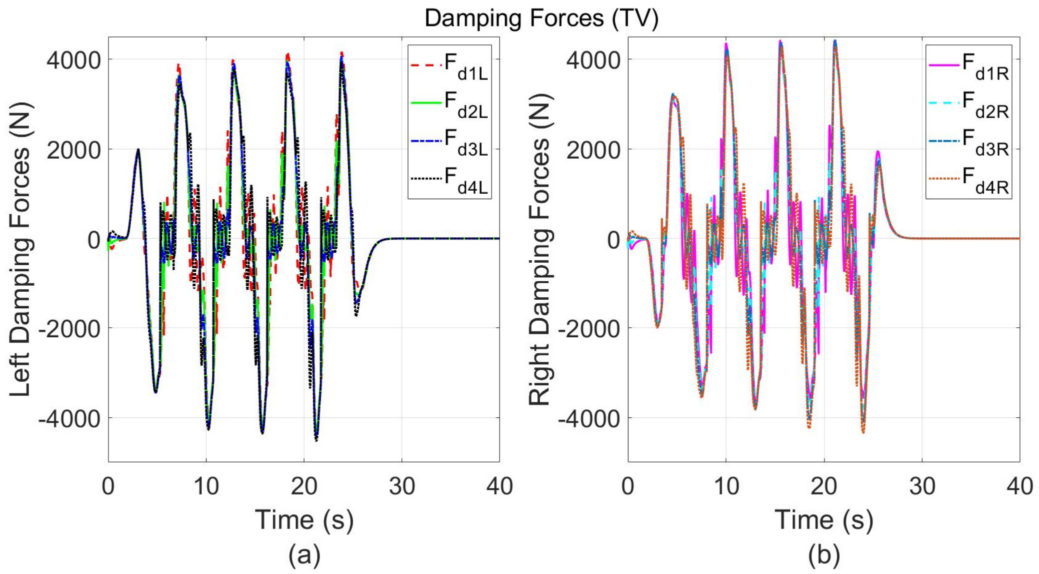

Figure 5-72 (a) Left Damping Forces and (b) Right Damping Forces for TV during Slalom at 40 Km/h (μ = 0.35)

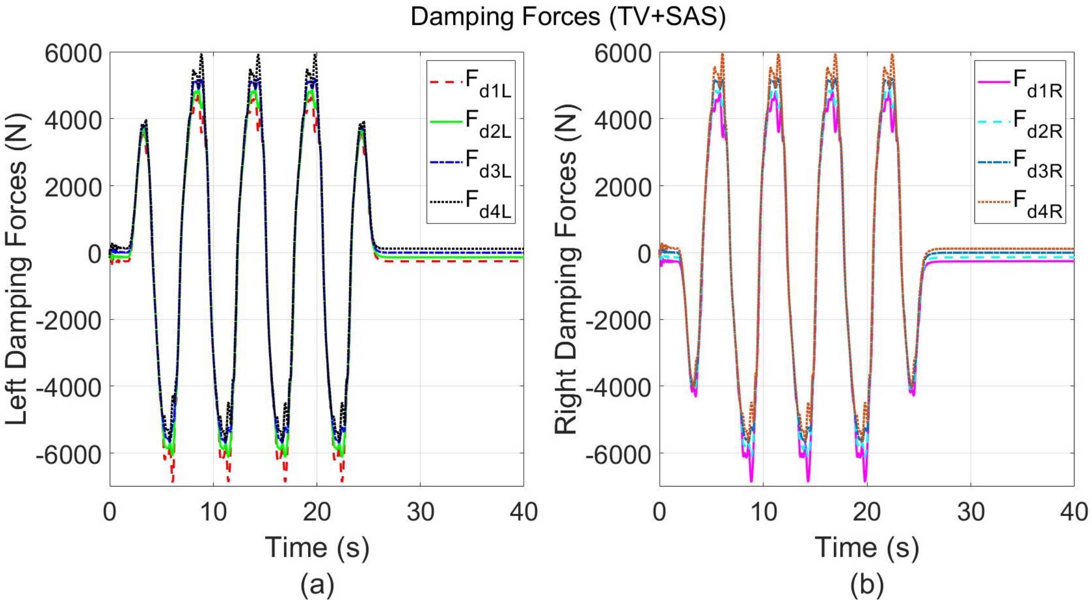

Figure 5-73 (a) Left Damping Forces and (b) Right Damping Forces for TV+SAS during Slalom at 40 Km/h ($\mu = 0.35$)

Figure 5-74 and Figure 5-75 show the left and right sides' vehicle normal loads in (a) and (b) respectively for TV and TV+SAS. It can be noticed that TV+SAS has significantly prevented the vehicle's wheels normal loads from dropping beyond 12000 N for both sides compared to TV that dropped up 9500 N. For the left and right sides normal load values are 12947.8 and 12961.2 N respectively for TV+SAS, while 10199.4 and 9513.0 N for TV. However, this drop in the normal load is not considered significant, since the vehicle is running at low friction road surface.

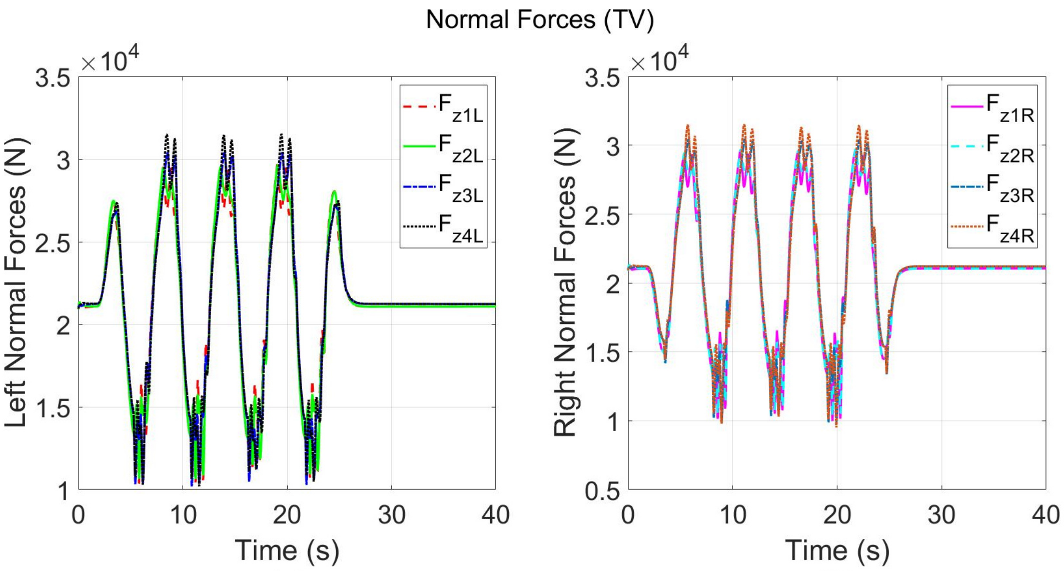

(a) (b)

Figure 5-74 (a) Left Normal Forces and (b) Right Normal Forces for TV during Slalom at 40 Km/h ($\mu = 0.35$)

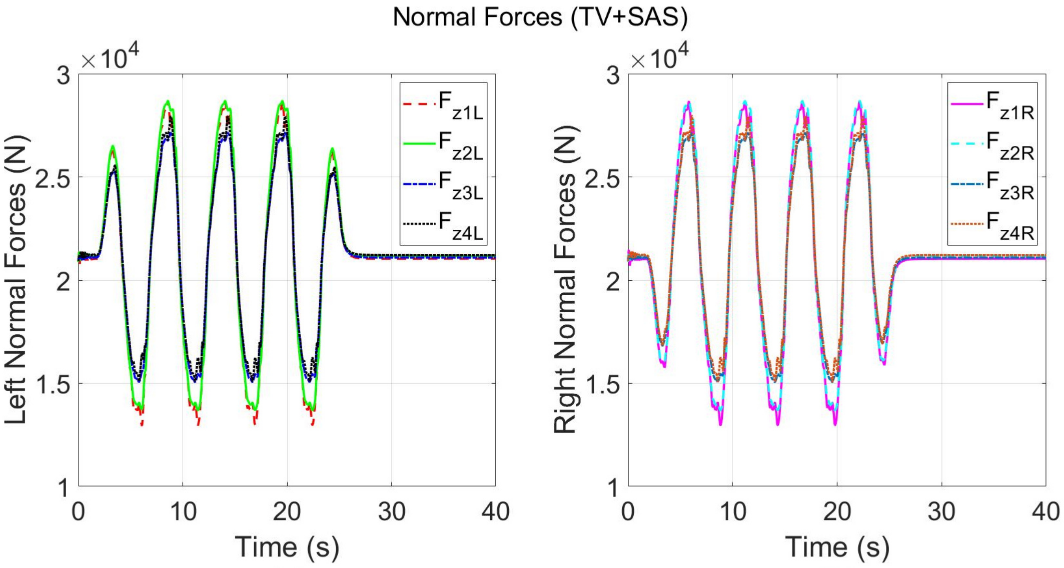

(a) (b)

Figure 5-75 (a) Left Normal Forces and (b) Right Normal Forces for TV+SAS during Slalom at 40 Km/h ($\mu = 0.35$)

The slip ratio of the left and right sides' vehicle tires for TV and TV+SAS are shown in Figure 5-76 and Figure 5-77 in (a) and (b) respectively. The intervention of slip controller can be observed to prevent the slip ratio from exceeding the desired limit 25% for TV. On the contrary no intervention of the slip controller of the TV+SAS, where the maximum slip ratio attained is 0.06 and this is because of the reduction of lateral load transfer achieved by integrating SAS.

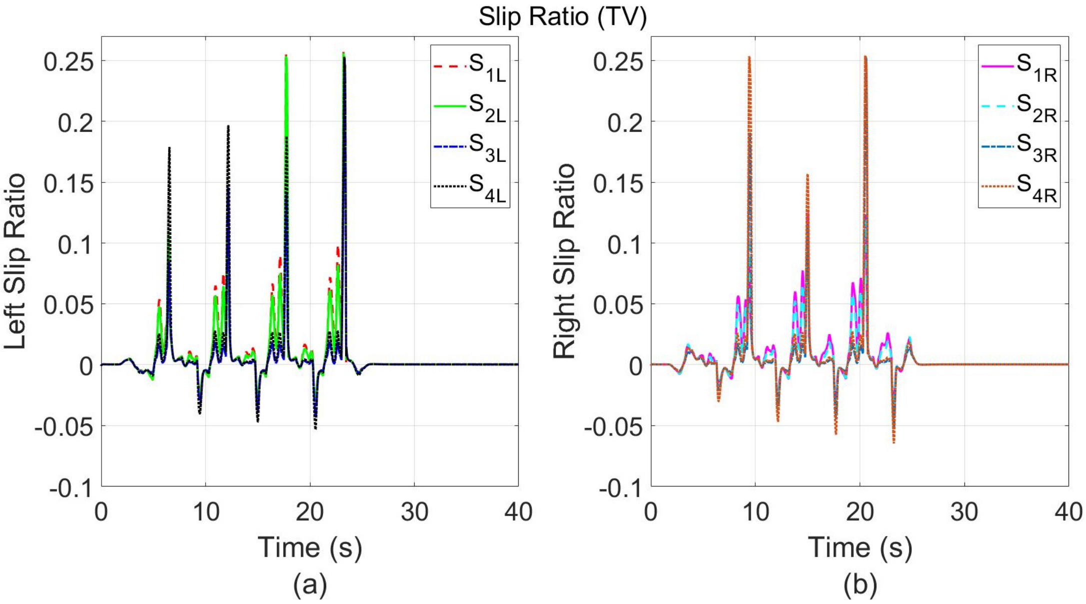

Figure 5-76 (a) Left Tires' Slip Ratio and (b) Right Tires' Slip Ratio for TV during Slalom at 40 Km/h ($\mu = 0.35$)

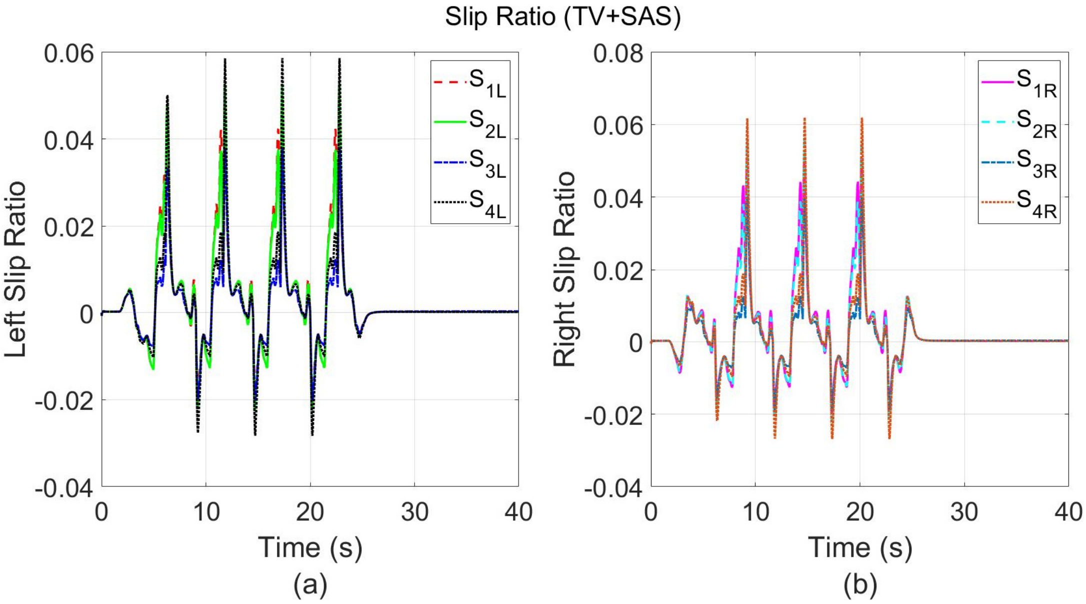

Figure 5-77 (a) Left Tires' Slip Ratio and (b) Right Tires' Slip Ratio for TV+SAS during Slalom at 40 Km/h ($\mu = 0.35$)

5.2.1.2.3 DB vs DB+SAS

The vehicle trajectory and the corresponding error achieved by each control strategy DB and DB+SAS are shown in Figure 5-78 in (a) and (b) respectively. It can be noticed that DB+SAS and DB have almost maintained same error as represented in Table 5-7. Furthermore, the DB has stabilized the vehicle faster than DB+SAS based on the settling time.

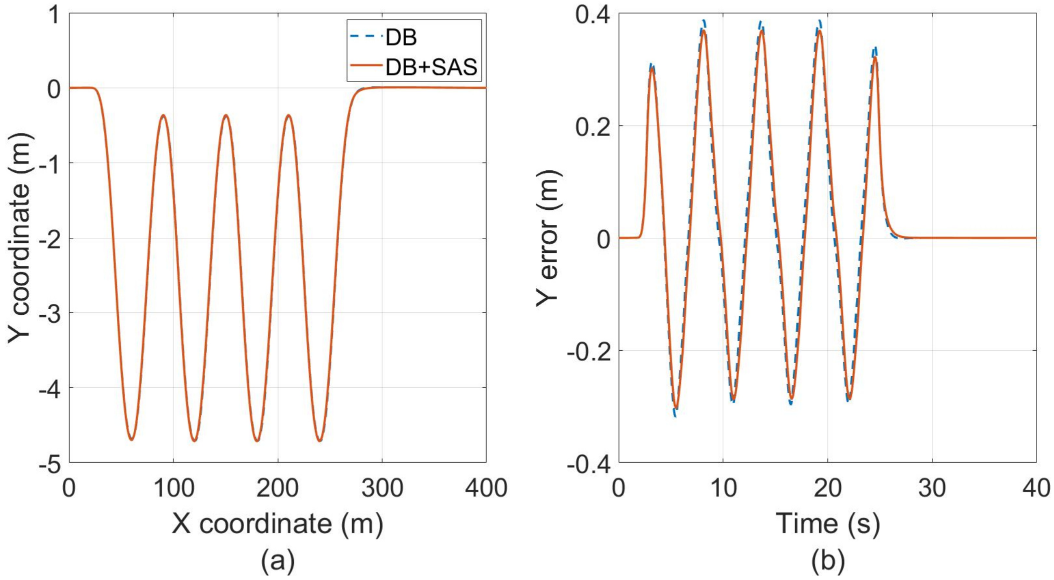

Figure 5-78 (a) Vehicle trajectory during Slalom at 40 Km/h ($\mu = 0.35$) and (b) Error obtained by DB and DB+SAS

Table 5-7 Trajectory Root Mean Square Errors Obtained by DB and DB+SAS during Slalom at 40 Km/h ($\mu = 0.35$)

Controller's Configuration	RMSE (m)
DB	0.1654
DB+SAS	0.1617

Figure 5-79, Figure 5-80, Figure 5-81 and Figure 5-82 illustrate the vehicle sideslip, yaw rate, longitudinal speed and lateral acceleration for both DB and DB+SAS, respectively. Its notable that DB+SAS have slightly achieved less sideslip angle than DB which are 1.6 and 1.9 degrees, respectively. Also, a smooth peak amplitude response is obtained by DB+SAS and faster in stabilizing the vehicle than DB. Regarding to the yaw rate response amplitude is approximately maintained the same for both control strategies. Furthermore, concerning the longitudinal speed it can be noticed that both control strategies have attained the same drop variation in speed. Nevertheless, a slight reduction difference in lateral acceleration is observed encountered for DB+SAS which is 0.27 g's while 0.3 g's for DB.

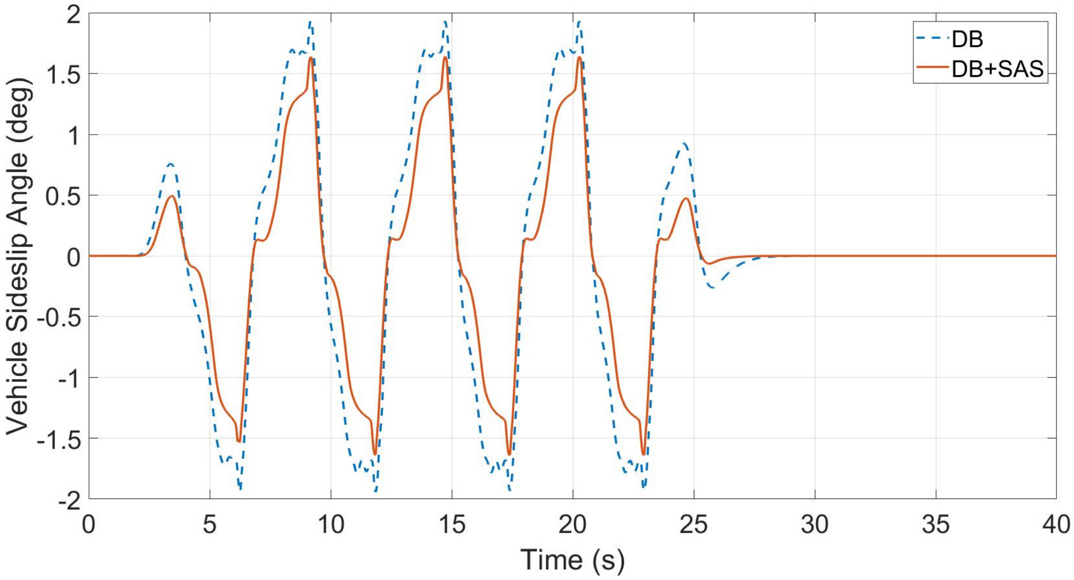

Figure 5-79 Vehicle Sideslip Angle during Slalom at 40 Km/h (μ = 0.35)

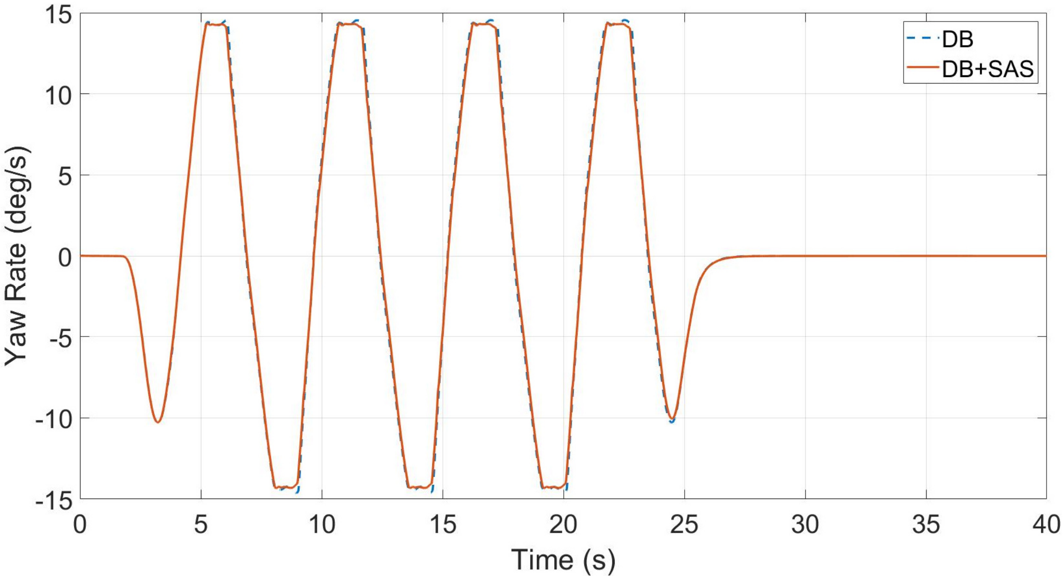

Figure 5-80 Yaw Rate during Slalom at 40 Km/h (μ = 0.35)

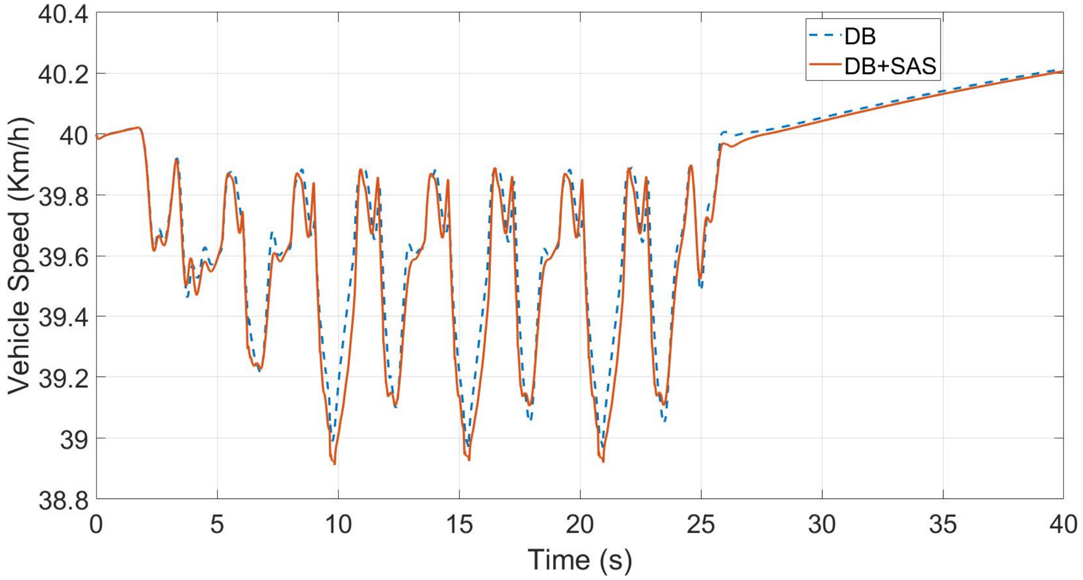

Figure 5-81 Vehicle Speed during Slalom at 40 Km/h ($\mu = 0.35$)

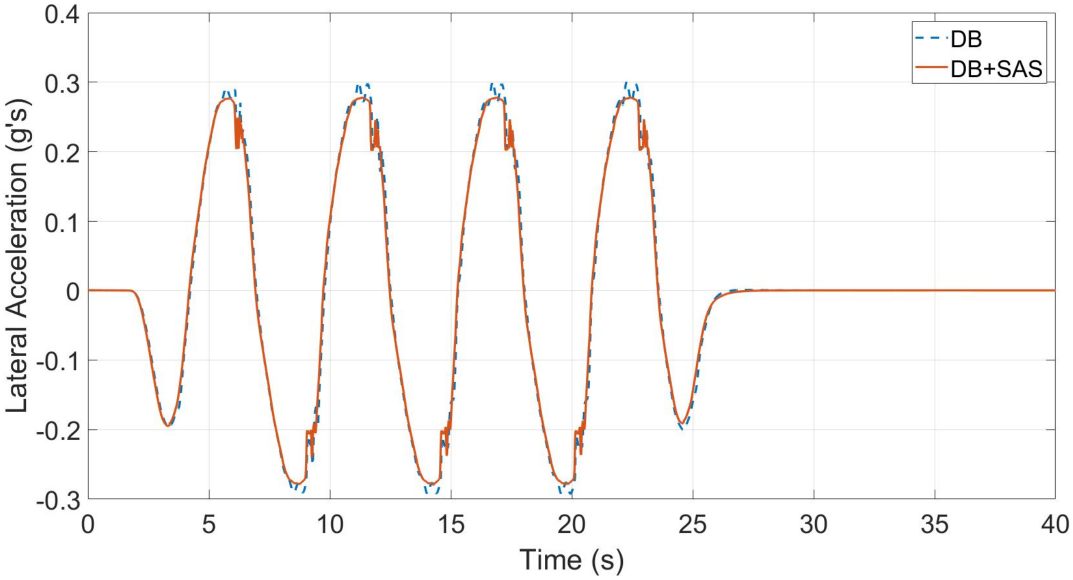

Figure 5-82 Lateral Acceleration during Slalom at 40 Km/h ($\mu = 0.35$)

Figure 5-83, Figure 5-84 and Figure 5-85 demonstrate the vehicle's sprung mass displacement, pitch, and roll angle, respectively. It can be observed that DB+SAS has minimized the vertical displacement at the CG of the sprung mass to smallest value compared to DB. Moreover, DB+SAS has substantially reduced the pitch and roll angle due to longitudinal and lateral load transfer.

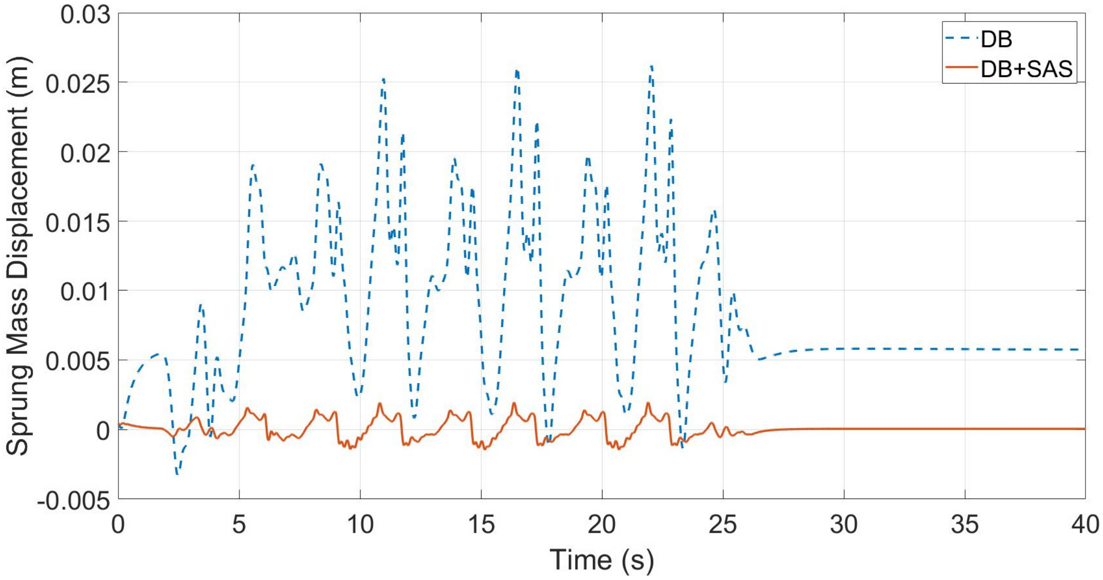

Figure 5-83 Sprung Mass Displacement during Slalom at 40 Km/h ($\mu = 0.35$)

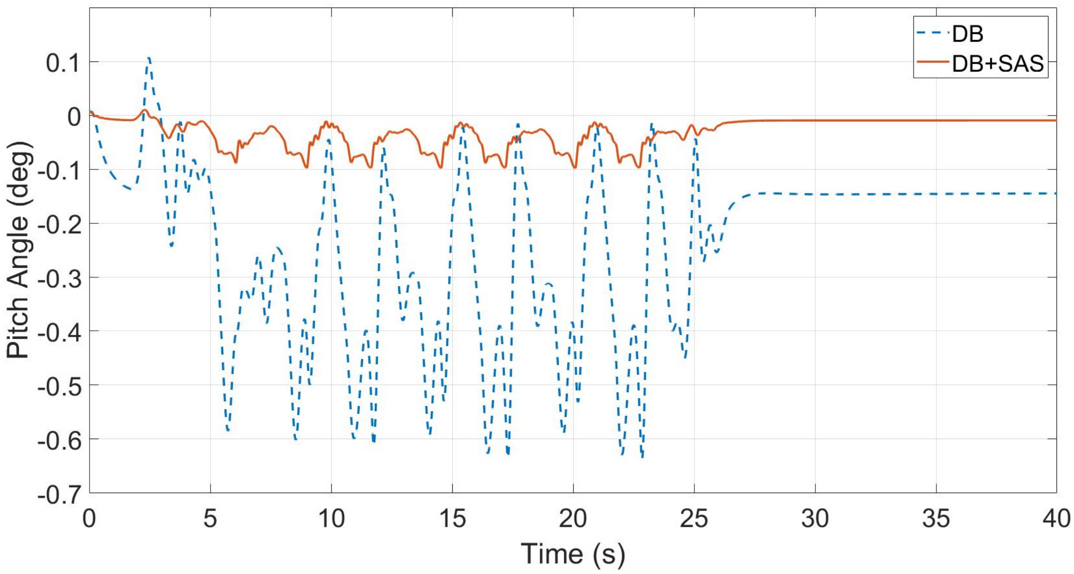

Figure 5-84 Pitch Angle during Slalom at 40 Km/h ($\mu = 0.35$)

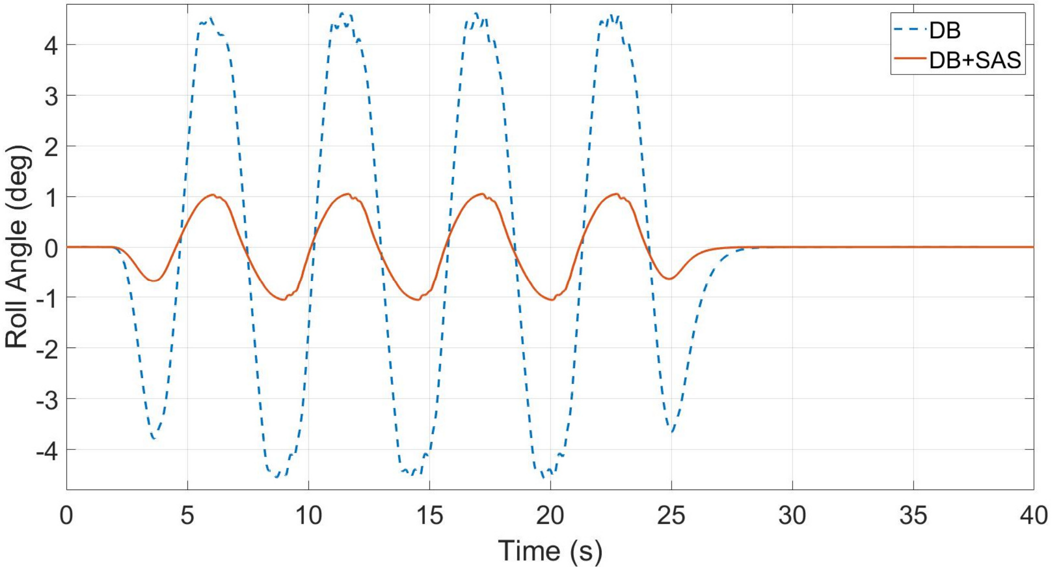

Figure 5-85 Roll Angle during Slalom at 40 Km/h (μ = 0.35)

Figure 5-86 and Figure 5-87 show the left and right braking wheel torque in (a) and (b) for DB and DB+SAS. It can be remarked that DB has obtained less braking wheel torque in both sides than DB+SAS. DB has achieved 8000 Nm and 7835.5 Nm, while DB+SAS attained 9948.2 Nm and 9125.1 Nm for left and right sides, respectively.

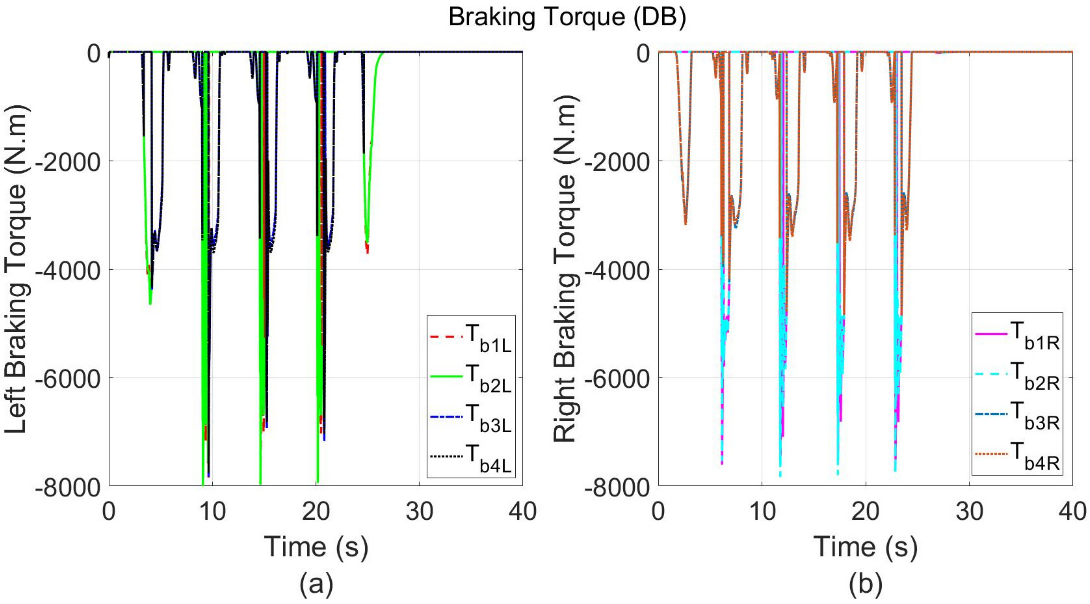

(a) (b)

Figure 5-86 (a) Left Braking Wheel Torque and (b) Right Braking Wheel Torque for DB during Slalom at 40 Km/h (μ = 0.35)

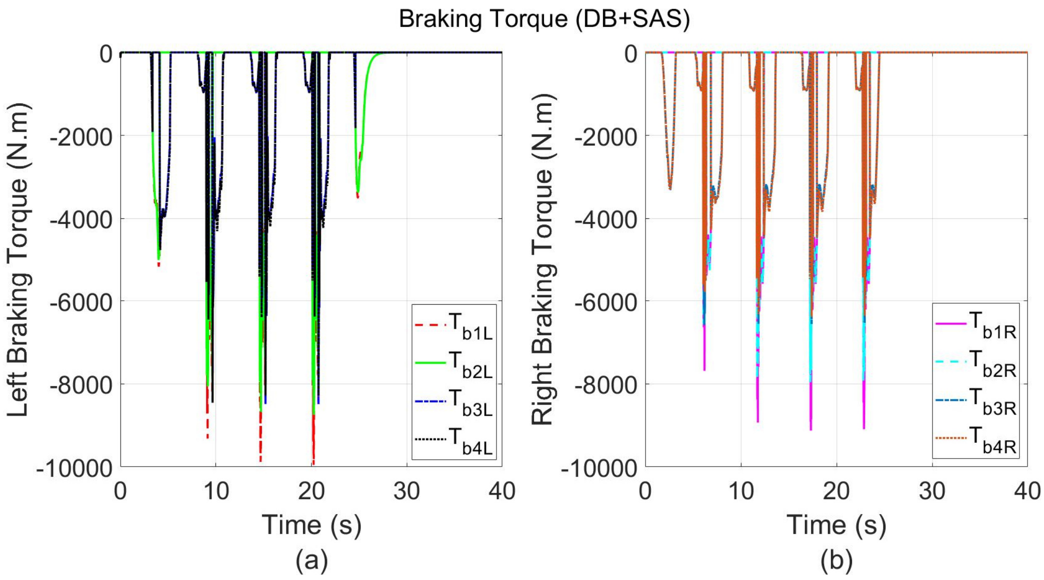

Figure 5-87 (a) Left Braking Wheel Torque and (b) Right Braking Wheel Torque for DB+SAS during Slalom at 40 Km/h ($\mu = 0.35$)

Figure 5-88 and Figure 5-89 demonstrate the left and right sides' vehicle dampers 'compressive forces in (a) and (b) respectively for DB and DB+SAS. It can be observed that DB+SAS has obtained largest dampers 'compressive forces varying with time. The largest left side dampers' force was nearly 8490.6 N and 7404.5 N for left and right sides, respectively. while for DB was 4343.6 N and 4390.5 N for the left and right side, respectively.

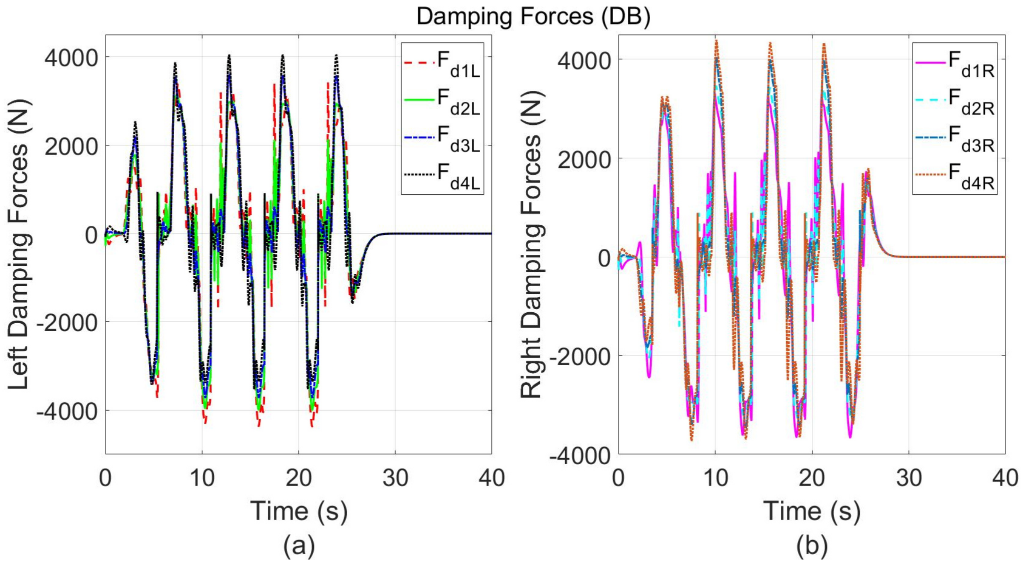

Figure 5-88 (a) Left Damping Forces and (b) Right Damping Forces for DB during Slalom at 40 Km/h ($\mu = 0.35$)

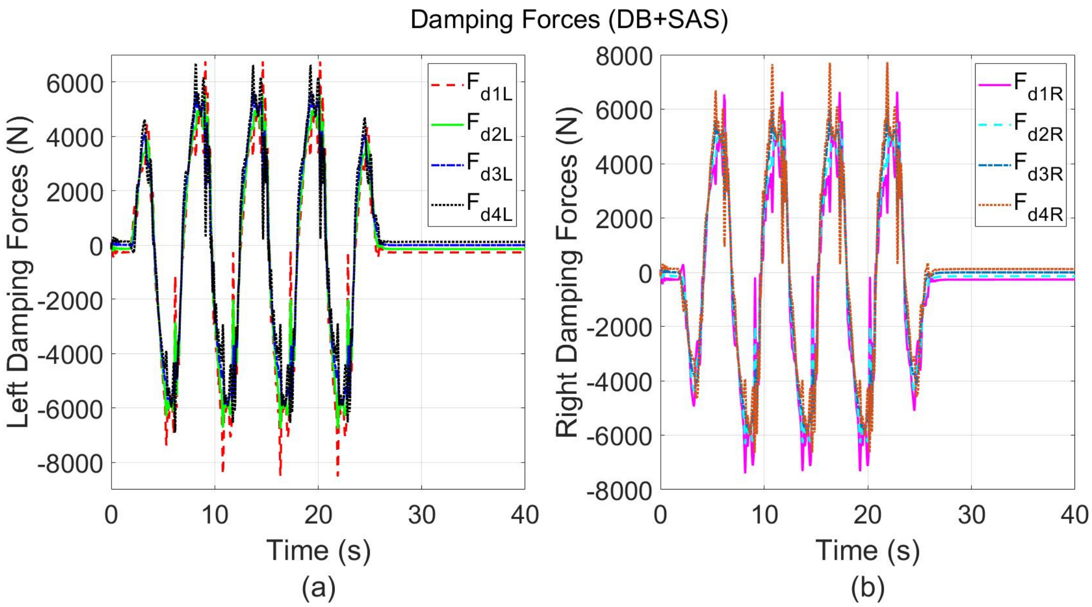

Figure 5-89 (a) Left Damping Forces and (b) Right Damping Forces for DB+SAS during Slalom at 40 Km/h ($\mu = 0.35$)

Figure 5-90 and Figure 5-91 show the left and right sides' vehicle normal loads in (a) and (b) respectively for DB and DB+SAS. It can be noticed that DB+SAS has significantly prevented the vehicle's wheels normal loads from dropping beyond 11000 N for both sides compared to DB that dropped up 9000 N. For the left and right sides normal load values are 11304.0 N and 12372.0 N respectively for DB+SAS, while 9022.8 N and 10762.1 N for DB. However, this drop in the normal load is not considered significant, since the vehicle is running at low friction road surface.

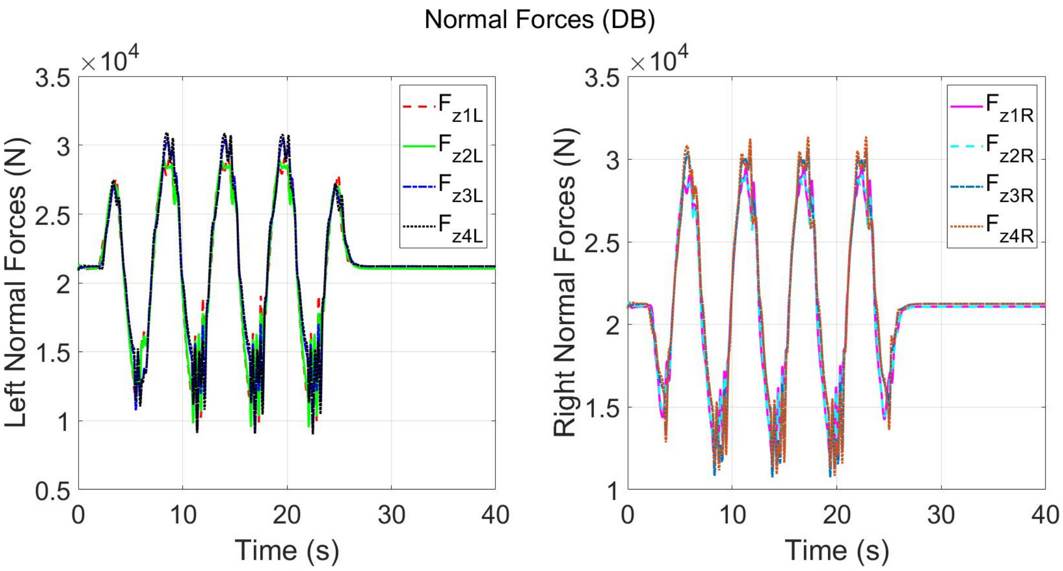

(a) (b)

Figure 5-90 (a) Left Normal Forces and (b) Right Normal Forces for DB during Slalom at 40 Km/h ($\mu = 0.35$)

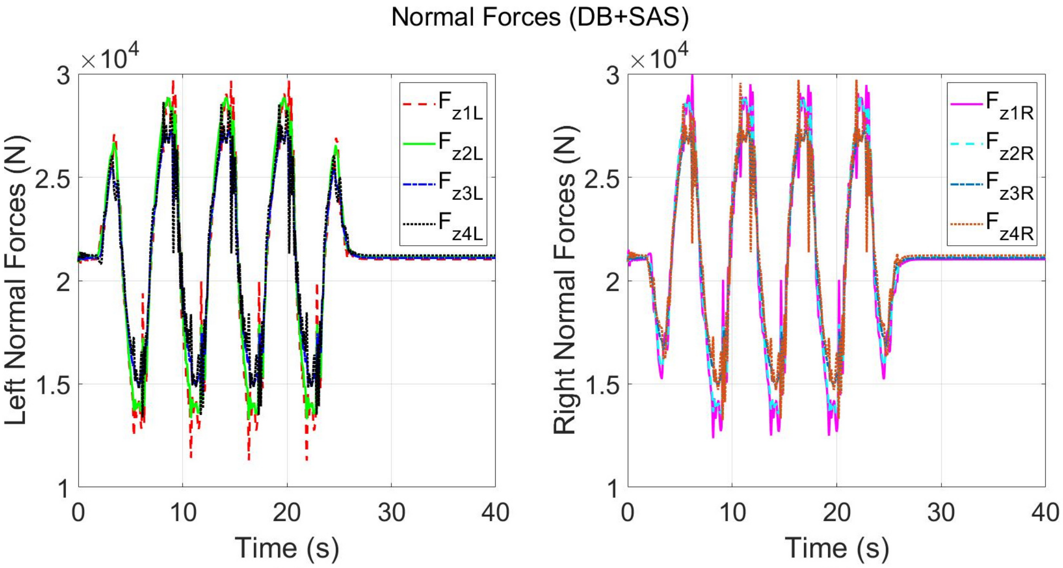

(a) (b)

Figure 5-91 (a) Left Normal Forces and (b) Right Normal Forces for DB+SAS during Slalom at 40 Km/h ($\mu = 0.35$)

The slip ratio of the left and right sides' vehicle tires for DB and DB+SAS are shown in Figure 5-92Figure 5-93 in (a) and (b) respectively. Its notable the slip control intervention in both control strategies to prevent the slip ratio to exceed the desired limit 25% where the peak braking forces can be generated.

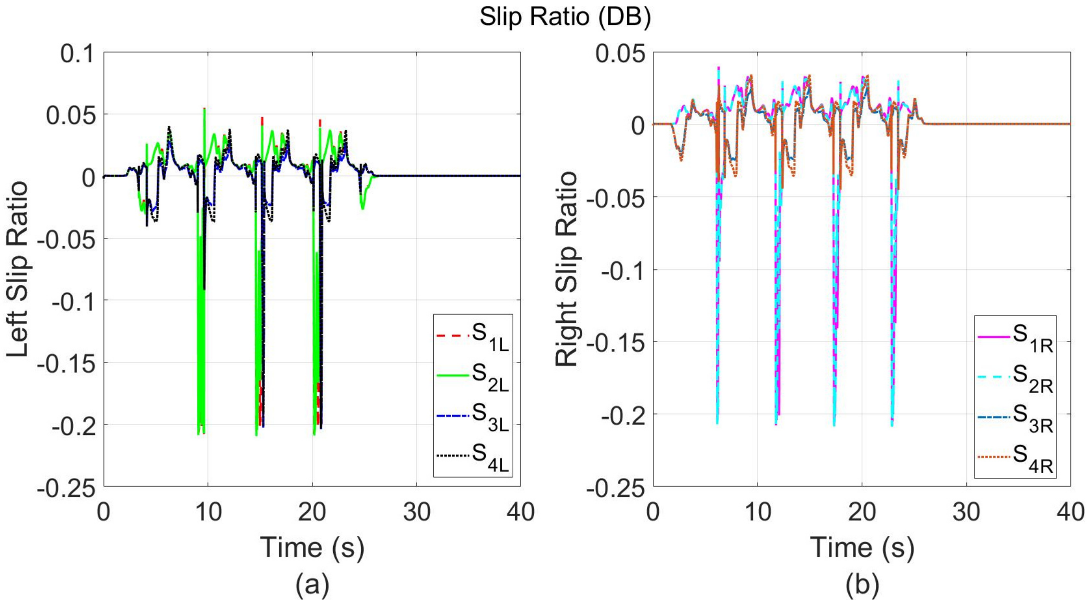

Figure 5-92 (a) Left Tires' Slip Ratio and (b) Right Tires' Slip Ratio for DB during Slalom at 40 Km/h ($\mu = 0.35$)

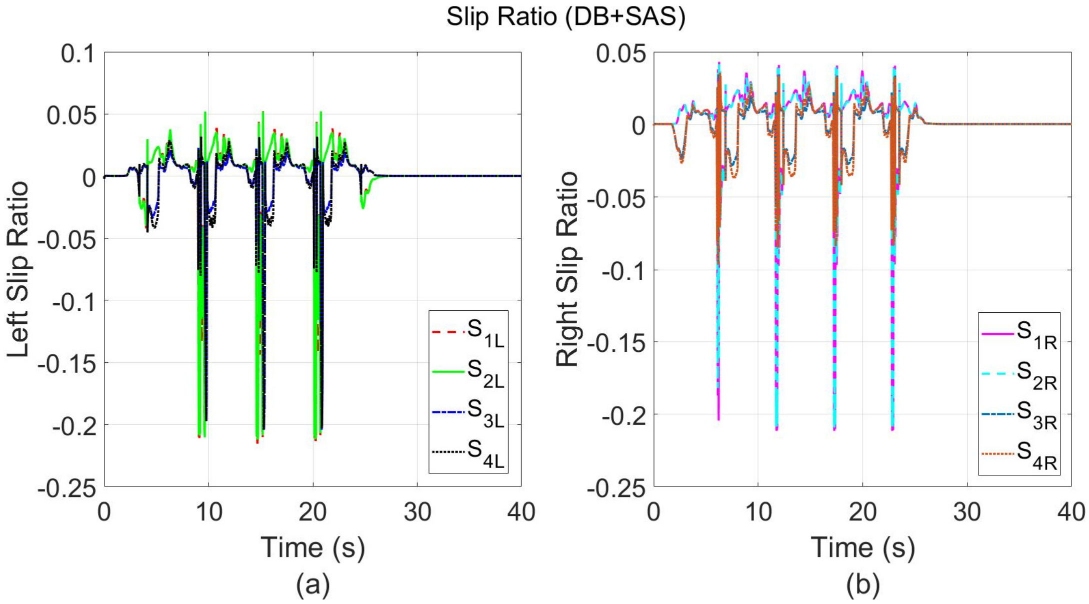

Figure 5-93 (a) Left Tires' Slip Ratio and (b) Right Tires' Slip Ratio for DB+SAS during Slalom at 40 Km/h ($\mu = 0.35$)

5.3 Summary and Conclusion

A comprehensive comparison has been conducted between each control strategy with and without integration of SAS during slalom test events. The first event was at speed 65 Km/h and coefficient of friction 0.85, while the second event was at 40 Km/h and low friction road surface 0.35. The aim of this comparison was to investigate the benefits of integrating the SAS with AWS, TV and DB and its effect on vehicle's lateral dynamics. The first comparison was carried out between AWS vs AWS+SAS, followed by TV vs TV+SAS then DB vs DB+SAS. As it can be summarized as follows.

At speed 65 Km/h and high coefficient of friction 0.85

- All control strategies integrated with SAS have shown superiority against all control strategies without integration of SAS in enhancing vehicle's lateral stability.
- It was observed that the integration of SAS has assisted in minimizing the error that occurred during performing the intended trajectory.
- It succeeded to achieve less sideslip angle, leading to an improvement in terms of vehicle stability at a high friction road surface.
- It was found that the yaw rate peak response was noticed smoother.
- It helped in maintaining the speed close to the desired speed with less drop,
- A significant reduction in lateral acceleration has been remarked with the integration of SAS.
- A tremendous reduction in sprung mass vertical displacement. Furthermore, the integration of SAS has significantly reduced the pitch and roll angles at the smallest possible values resulting from longitudinal and lateral load transfer at high-speed cornering. Consequently, maintaining the tires with contact with the ground during the severe maneuvers and preventing the drop of total lateral forces due to load transfer. Also minimizing the possible chances of a rollover.
- It was remarked that AWS+SAS was exhibiting less front and rear steering wheel angles than AWS. Moreover, in the case of TV+SAS, less fluctuation was observed in generating the driving torque, as well as less in driving torque magnitude achieved than TV. In the

same manner the DB+SAS was found to attain less braking torque and oscillations than DB.

- The integration of SAS had a substantial effect in preventing the tires from losing grip with the ground and keep them at high values based on the normal load plots. Nevertheless, gives it an advantage over all control strategies without integration of SAS that reached zero values during high-speed cornering maneuver.
- It was found that the integration of SAS had helped the slip controllers in the case of TV+SAS and DB+SAS to maintain either the tractive or braking peak effort at the desired values of slip ratio of $20 - 25\%$. While the TV and DB surpassed these values, which can badly reduce the lateral forces, and this is because of load transfer.
- In terms of stabilization time, it was observed that the integration of SAS stabilizes faster the vehicle than the control strategies without integration of SAS based on the settling time in all the plots.

At speed 40 Km/h and low coefficient of friction 0.35

- All control strategies with and without integration of SAS have relatively obtained the same error during performing the desired trajectory. However, the control strategies integrated with SAS were observed slightly performing less error than the control strategies without integration of SAS.
- Regarding vehicle sideslip angle, yaw rate, longitudinal speed and lateral acceleration, the performance of all control strategies were noticed the same, no significant remarks can be observed.
- It’s true that all the control strategies integrated with SAS have succeeded to minimize the sprung mass displacement, pitch, and roll angles at the lowest possible values than the control strategies without integration of SAS. However, the enhancements applied to the vehicle’s stability and maneuverability were not that quite significant except for TV+SAS and DB+SAS have slightly stabilized the vehicle faster than TV and DB in terms of sideslip angle plots.
- It should be noted that AWS+SAS exhibited larger front and rear steering angles than AWS. Furthermore, the braking torque generated was observed larger for DB+SAS than

in the case of DB. However, TV+SAS attained less driving torque achieved than in the case of TV.

- No significant drop in normal loads has been detected since the vehicle was running at a low coefficient of friction, therefore the lateral acceleration was below 0.4 g's.
- It was found that TV had maintained the driving torque to be generated at peak effort of slip ratio 25%, unlike TV+SAS that was at 6%. While in the case of DB+SAS and DB the braking peak effort was at slip ratios 25%.

The final remark can be drawn as the integration of SAS can greatly enhance vehicle lateral dynamics at high friction road surfaces. while at low coefficient of friction its not effective, in particularly in case if the control allocation utilized as by steering or braking.

Chapter 6 SIMULATION RESULTS AND DISCUSSION

6.1 Introduction

Various standard test maneuvers have been conducted at limit handling conditions at different coefficients of friction to evaluate the effectiveness of each proposed control strategy using the TRUCKSIM full vehicle model. Based on the conclusion and results obtained in the previous chapter, the evaluation method in this chapter presents a comparison between the conventional vehicle (no control) versus each proposed control strategy with and without integration of SAS based on the friction road surface. As it can be summarized as follows.

- A comparison is conducted between LQR controllers (AWS+SAS vs TV+SAS vs DB+SAS) vs conventional vehicle at high friction road surfaces.
- A comparison is performed between LQR controllers (AWS vs TV vs DB) vs conventional vehicle at low friction road surfaces.

The evaluation method of each control strategy was carried out in Slalom, Standard Double Lane Change (DLC), Federal Motors Vehicle Safety Standard (FMVSS 126 ESC), Modified J-Turn and Open-Loop Step Slalom test maneuvers. These standard tests are normally utilized to analyze the vehicles' dynamics performance in the industry. Since the main goal is to evaluate the vehicle's dynamics performance at limit handling scenarios. And to ensure the effectiveness of the proposed controllers under the changes in road surface friction and the variation of vehicle parameters such as cornering stiffness and different steering inputs. Therefore, most of the tests are conducted at high speeds. Moreover, all simulations were performed at average and high dry road coefficient of friction 0.85 and 1.0 respectively and then duplicated at a low coefficient of friction 0.2 and 0.35, respectively.

Table 6-1 outlines all the test maneuvers that were conducted at various speeds and road coefficient of friction for all the proposed control strategies and the conventional vehicle.

Table 6-1 List of Various Test Events for Controllers' Evaluation

Test #	Configuration	Test Maneuver	Speed (Km/h)	Coefficient of friction (μ)
1	No Control vs AWS+SAS vs TV+SAS vs DB+SAS	**Slalom**	65	0.85
			75	1.0
	No Control vs AWS vs TV vs DB		40	0.35
			30	0.2
2	No Control vs AWS+SAS vs TV+SAS vs DB+SAS	**DLC**	100	0.85
	No Control vs AWS vs TV vs DB		80	0.35
3	No Control vs AWS+SAS vs TV+SAS vs DB+SAS	**FMVSS 126 ESC**	100	0.85
	No Control vs AWS vs TV vs DB		80	0.35
4	No Control vs AWS+SAS vs TV+SAS vs DB+SAS	**Modified J-Turn**	100	0.85
	No Control vs AWS vs TV vs DB		80	0.35
5	No Control vs AWS+SAS vs TV+SAS vs DB+SAS	**Open-Loop Step Slalom**	65	1.0

6.2 Simulation Results and Discussion at Various Test Events

6.2.1 30m Constant Step Slalom Test (NATO AVTP-1 03-30)

6.2.1.1 Results and Discussion of Evaluation Method at high coefficient of friction – Constant Step Slalom (65 km/h ; $\mu = 0.85$)

The vehicle trajectory and the corresponding error achieved by each control strategy AWS+SAS, TV+SAS and DB+SAS and Vehicle (No Control) are shown in Figure 6-1 in (a) and (b) respectively. It can be noticed that all the proposed control strategies have succeeded to maintain the vehicle on the desired trajectory, while vehicle (No Control) failed and lost stability. However, TV+SAS has achieved the largest error among the proposed control strategies while AWS+SAS has obtained the smallest error as shown in Table 6-2. Furthermore, TV+SAS and AWS+SAS have stabilized the vehicle faster than DB+SAS based on the settling time and this is because of the reduction in speed caused by braking.

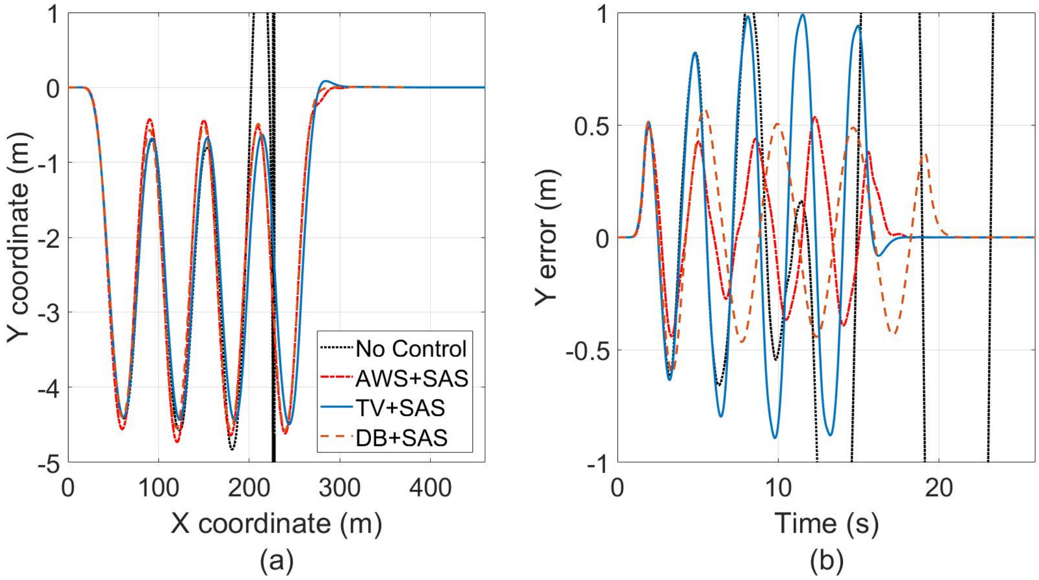

Figure 6-1 Vehicle trajectory during Slalom at 65 Km/h ($\mu = 0.85$) and (b) Error obtained by vehicle (No Control), AWS+SAS, TV+SAS and DB+SAS

Table 6-2 Trajectory Root Mean Square Errors Obtained by Uncontrolled Vehicle, AWS+SAS, TV+SAS and DB+SAS during Slalom at 65 Km/h ($\mu = 0.85$)

Controller's Configuration	RMSE (m)
No Control	3.4906
AWS+SAS	0.2165
TV+SAS	0.4656
DB+SAS	0.2866

Figure 6-2, Figure 6-3, Figure 6-4 and Figure 6-5 illustrate the vehicle sideslip, yaw rate, longitudinal speed and lateral acceleration for AWS+SAS, TV+SAS and DB+SAS and Vehicle (No Control), respectively. It is notable that TV+SAS has achieved the largest sideslip angle compared to the other control strategies, while DB+SAS have obtained the smallest value. The yaw rate response amplitude was varying with respect to time for all control strategies. However, the TV+SAS has performed the largest peak value, leading to an enhancement in vehicle's maneuverability. Also, the yaw rate response for DB+SAS was shifted and delayed, yielded place to AWS+SAS and TV+SAS to show a superiority in stabilizing the vehicle faster. Moreover, the TV+SAS has succeeded to reasonably maintain the vehicle's longitudinal speed close to the desired value compared to AWS+SAS and DB+SAS, the lowest drop in speed attained by each are 61.1, 60.2 and 45.3 Km/h, respectively. Furthermore, it can be observed that DB+SAS has a significant effect in minimizing the lateral acceleration compared to other control strategies and this is due to the reduction in speed caused by braking. However, TV+SAS has stabilized the vehicle faster than the other control strategies in all mentioned plots followed by AWS+SAS.

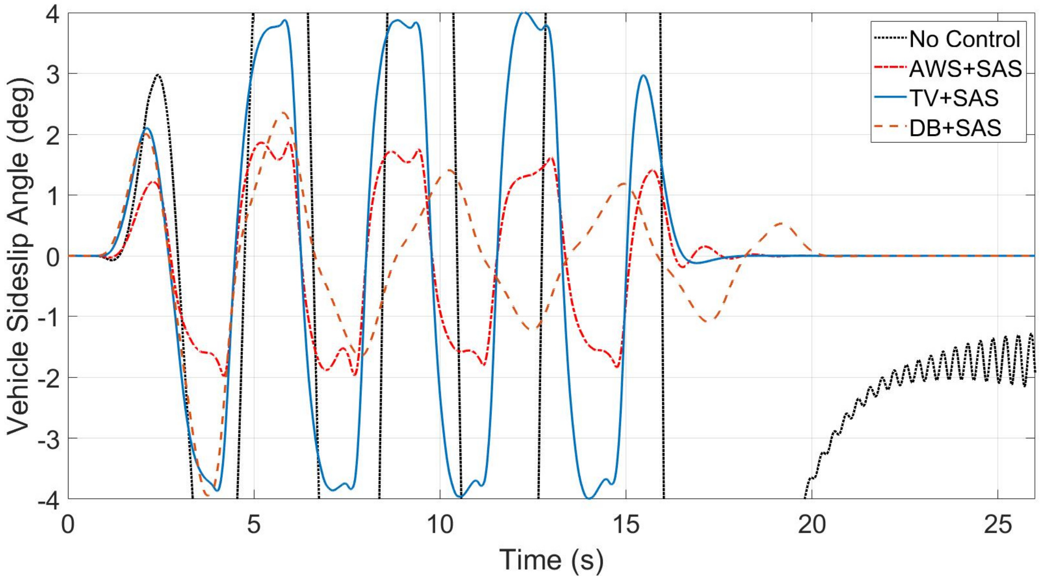

Figure 6-2 Vehicle Sideslip Angle during Slalom at 65 Km/h ($\mu = 0.85$)

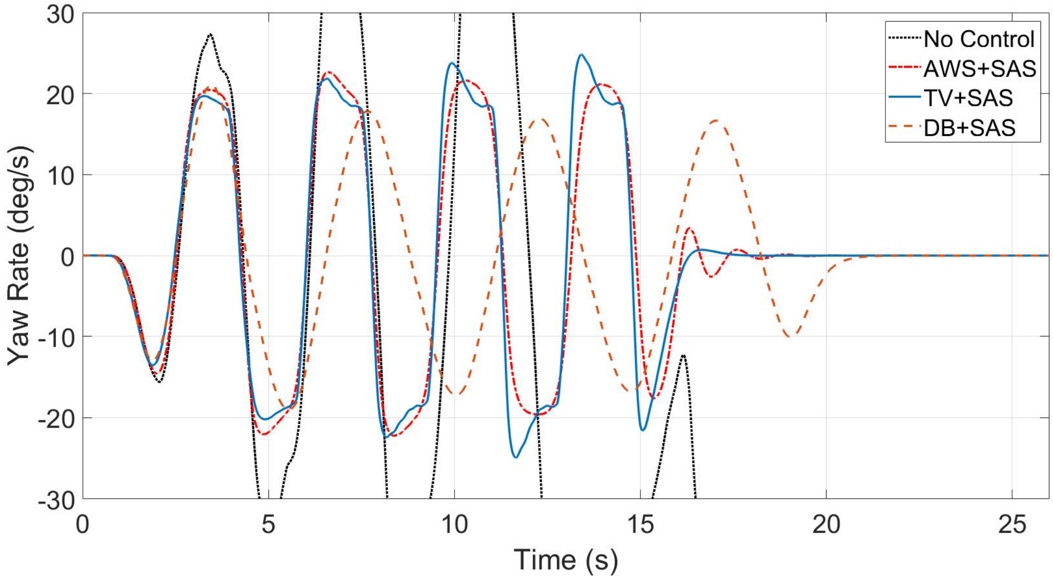

Figure 6-3 Yaw Rate during Slalom at 65 Km/h ($\mu = 0.85$)

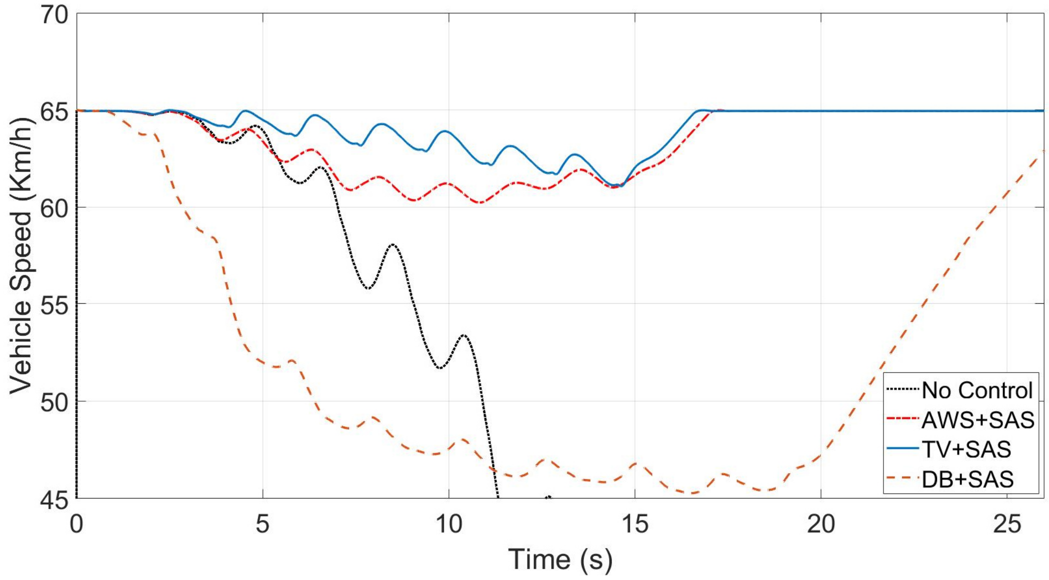

Figure 6-4 Vehicle Speed during Slalom at 65 Km/h (μ = 0.85)

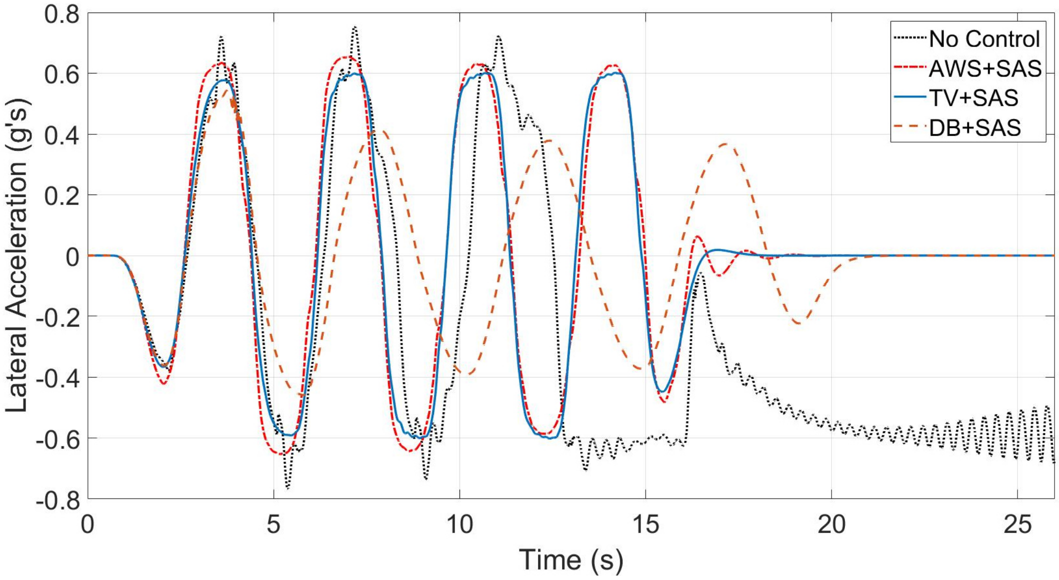

Figure 6-5 Lateral Acceleration during Slalom at 65 Km/h (μ = 0.85)

Figure 6-6, Figure 6-7 and Figure 6-8 demonstrate the vehicle's sprung mass displacement, pitch, and roll angle, respectively. It can be remarked that all control strategies have significantly minimized the vertical displacement at the CG of the sprung mass compared to the vehicle with no control whose lost stability. However, AWS+SAS has obtained the largest displacement compared to the other control strategies, while DB+SAS has performed the smallest value. As well as AWS+SAS and TV+SAS have stabilized and maintained the sprung mass leveling to zero faster than DB+SAS. Although, DB+SAS has tremendously reduced the pitch and roll angle due to longitudinal and lateral load transfer compared to AWS+SAS and TV+SAS, it requires time to stabilize the vehicle based on the settling time.

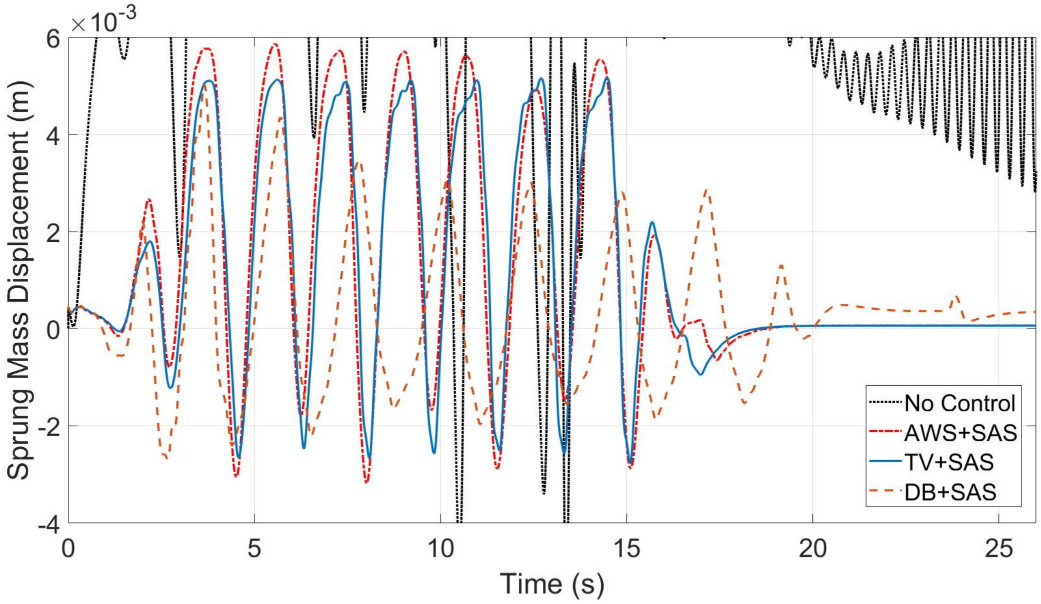

Figure 6-6 Sprung Mass Displacement during Slalom at 65 Km/h (μ = 0.85)

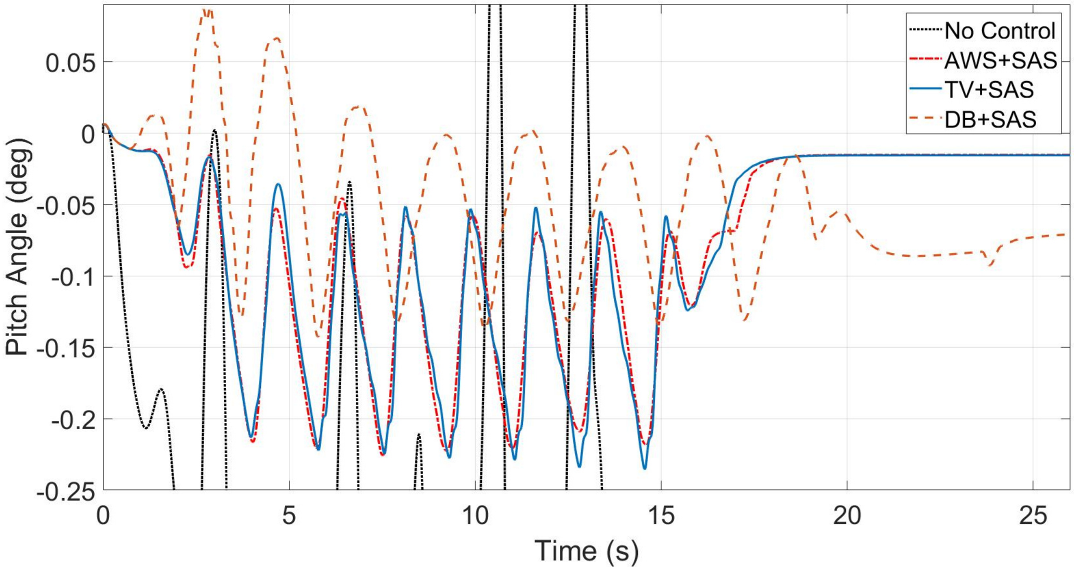

Figure 6-7 Pitch Angle during Slalom at 65 Km/h (μ = 0.85)

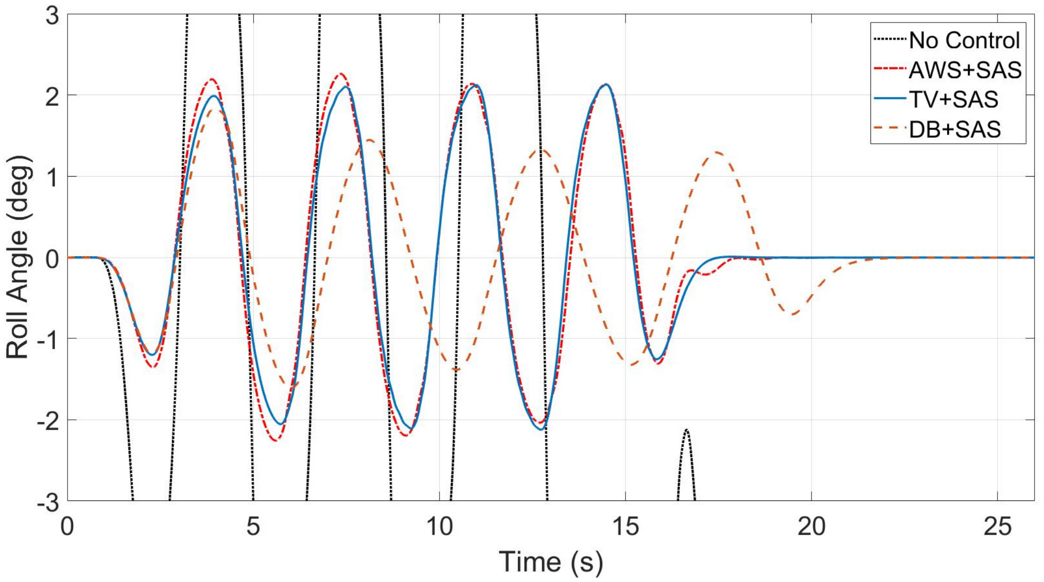

Figure 6-8 Roll Angle during Slalom at 65 Km/h ($\mu = 0.85$)

6.2.1.2 Results and Discussion of Second Evaluation Method at high coefficient of friction – Constant Step Slalom ($75\ \mathrm{km/h}\ ;\ \mu = 1.0$)

The vehicle trajectory and the corresponding error achieved by each control strategy AWS+SAS, TV+SAS and DB+SAS and Vehicle (No Control) are shown in Figure 6-9 in (a) and (b) respectively. It can be observed that TV+SAS and DB+SAS have succeeded to maintain the vehicle on the desired trajectory, while AWS+SAS and vehicle with no control failed and lost stability. However, TV+SAS has achieved the largest error compared to DB+SAS as presented in Table 6-3. Furthermore, TV+SAS has stabilized the vehicle faster than DB+SAS based on the settling time and this is because of the reduction in speed caused by braking.

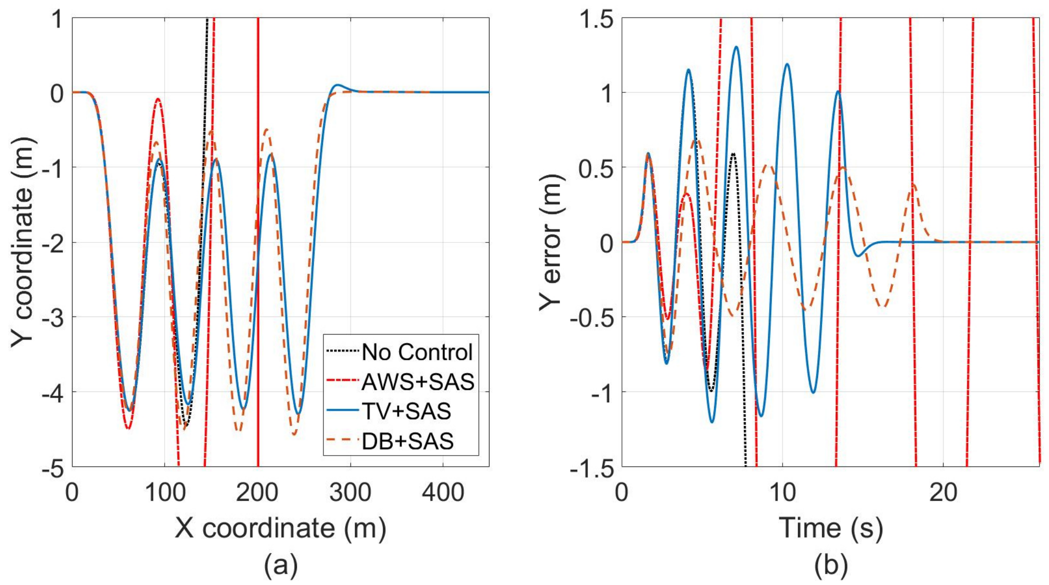

Figure 6-9 Vehicle trajectory during Slalom at 75 Km/h (μ = 1.0) and (b) Error obtained by vehicle (No Control), AWS+SAS, TV+SAS and DB+SAS

Table 6-3 Trajectory Root Mean Square Errors Obtained by Uncontrolled Vehicle, AWS+SAS, TV+SAS and DB+SAS during Slalom at 75 Km/h (μ = 1.0)

Controller's Configuration	RMSE (m)
No Control	17.0994
AWS+SAS	8.9898
TV+SAS	0.5557
DB+SAS	0.3089

Figure 6-10, Figure 6-11, Figure 6-12 and Figure 6-13 demonstrate the vehicle sideslip, yaw rate, longitudinal speed and lateral acceleration for AWS+SAS, TV+SAS and DB+SAS and Vehicle with no control, respectively. It can be noticed that TV+SAS has achieved the largest sideslip angle compared to DB+SAS, while AWS+SAS and vehicle with no control have lost stability. Nevertheless, TV+SAS has shown superiority over DB+SAS in stabilizing faster the vehicle at 16.1 seconds while 19.4 seconds by DB+SAS. The yaw rate response amplitude was varying with respect to time for both control strategies. However, the TV+SAS has performed the largest peak value, leading to an improvement in vehicle's maneuverability. Also, the yaw rate response for DB+SAS was shifted and delayed, yielded place to TV+SAS to show a supremacy in stabilizing the vehicle faster based on the settling time. Furthermore, the TV+SAS has succeeded to relatively maintain the vehicle's longitudinal speed close to the desired value compared to DB+SAS, the lowest drop in speed attained by each are 66.2 and 45.7 Km/h, respectively. Nonetheless, it can be observed that DB+SAS has a significant effect in minimizing the lateral acceleration compared to TV+SAS and this is due to the reduction in speed caused by braking. However, TV+SAS has stabilized the vehicle faster than DB+SAS in all mentioned plots based on the settling time.

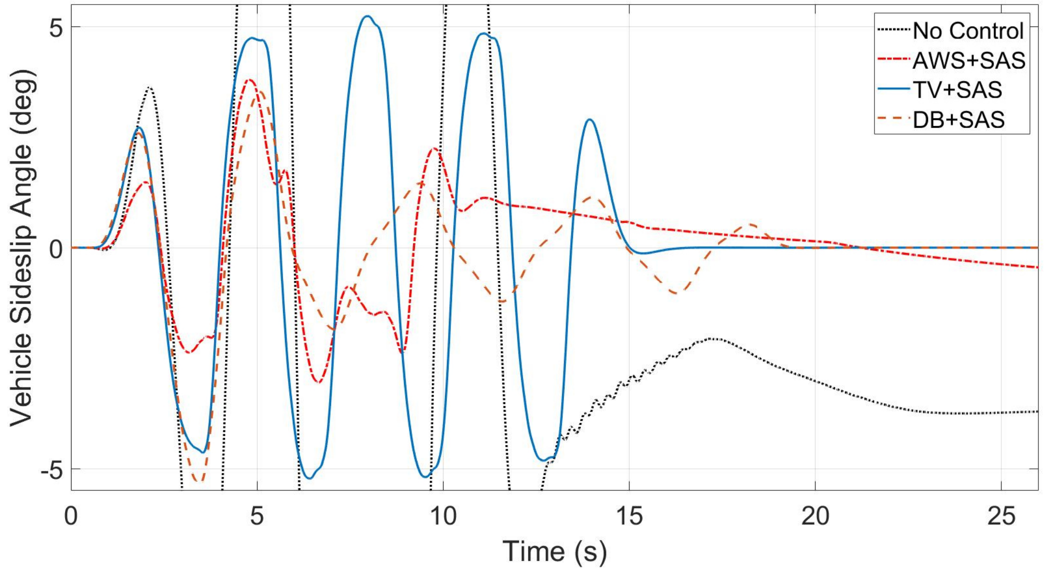

Figure 6-10 Vehicle Sideslip Angle during Slalom at 75 Km/h (μ = 1.0)

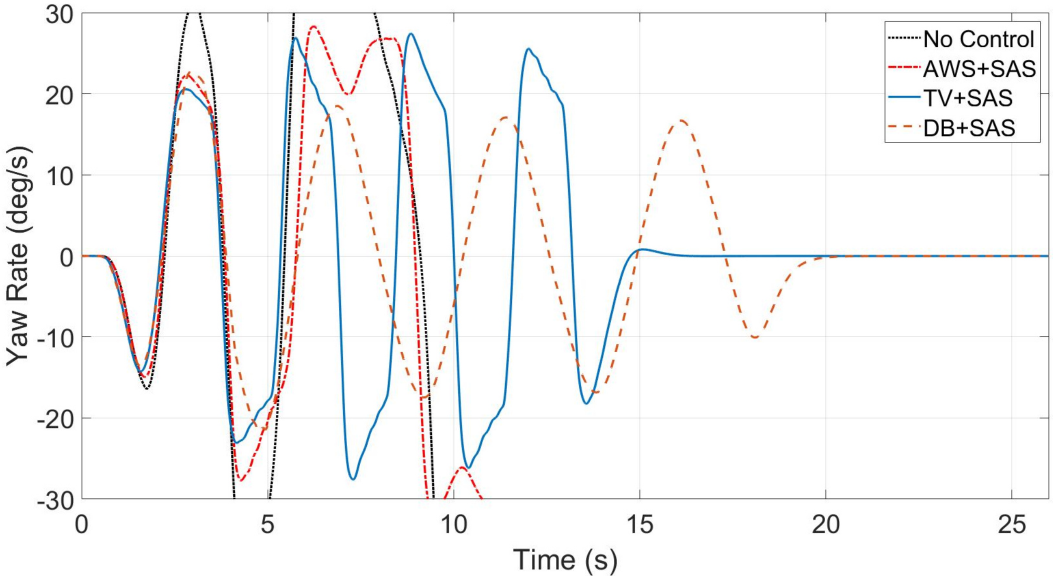

Figure 6-11 Yaw Rate during Slalom at 75 Km/h (μ = 1.0)

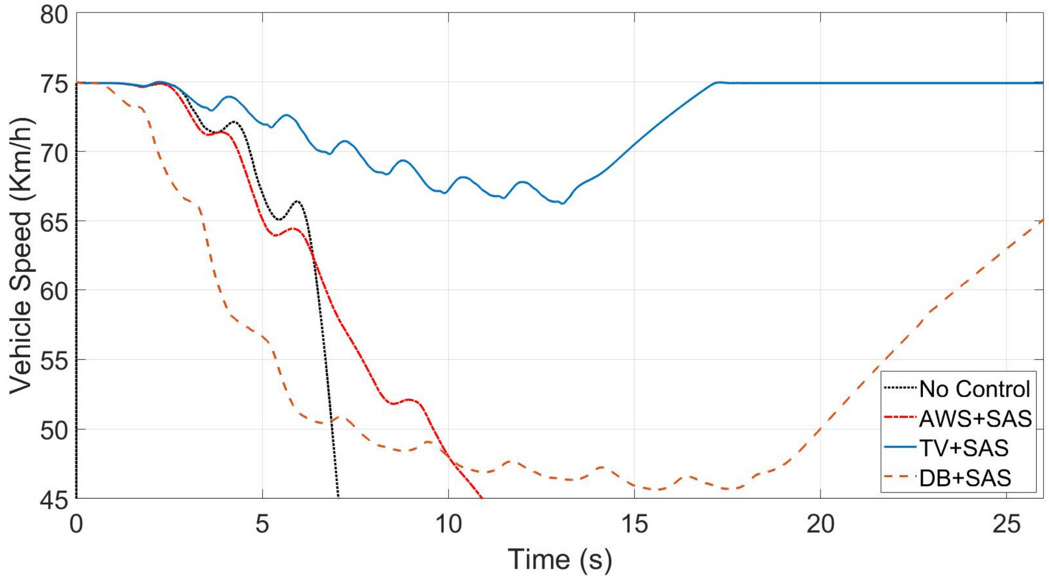

Figure 6-12 Vehicle Speed during Slalom at 75 Km/h (μ = 1.0)

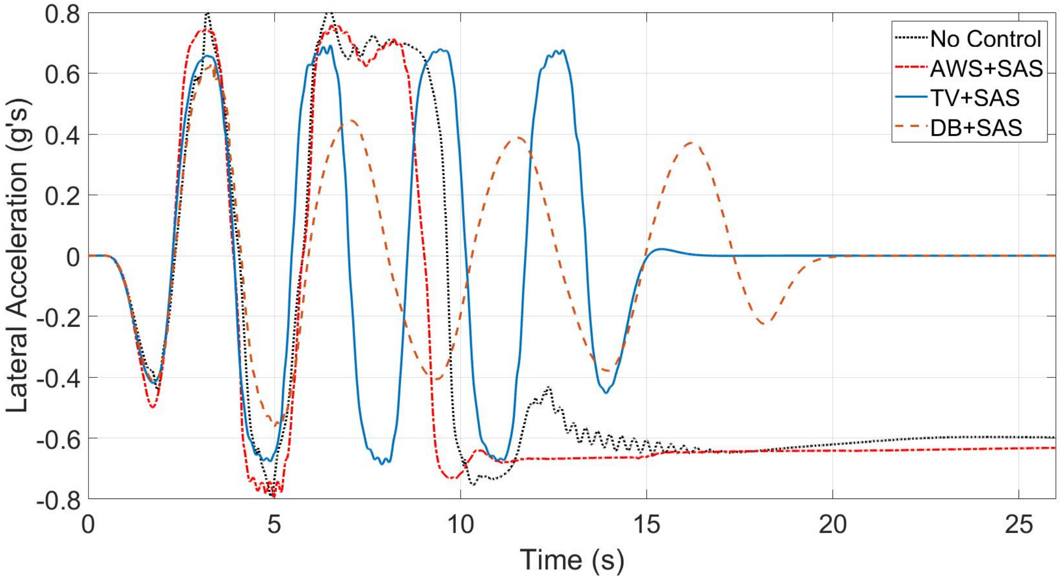

Figure 6-13 Lateral Acceleration during Slalom at 75 Km/h (μ = 1.0)

Figure 6-14, Figure 6-15 and Figure 6-16 depict the vehicle's sprung mass displacement, pitch, and roll angle, respectively. It can be remarked that TV+SAS and DB+SAS have tremendously minimized the vertical displacement at the CG of the sprung mass compared to AWS+SAS and the vehicle with no control whose lost stability. However, TV+SAS has obtained the largest displacement compared to DB+SAS. Nevertheless, TV+SAS have stabilized and maintained the sprung mass leveling to zero faster than DB+SAS. Although, DB+SAS has significantly reduced the pitch and roll angle due to longitudinal and lateral load transfer compared TV+SAS, it requires time to stabilize the vehicle based on the settling time.

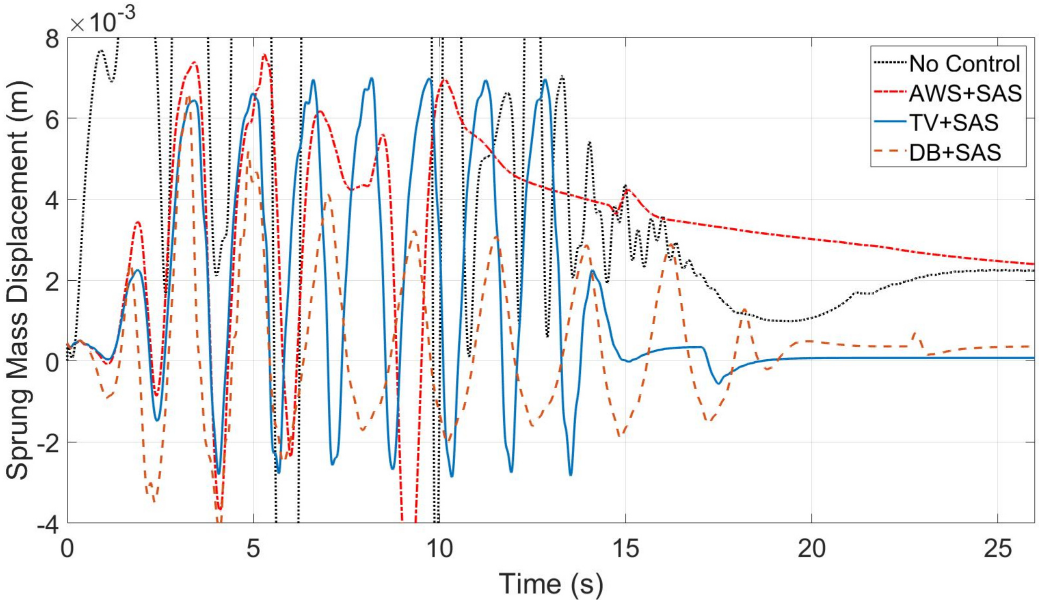

Figure 6-14 Sprung Mass Displacement during Slalom at 75 Km/h (μ = 1.0)

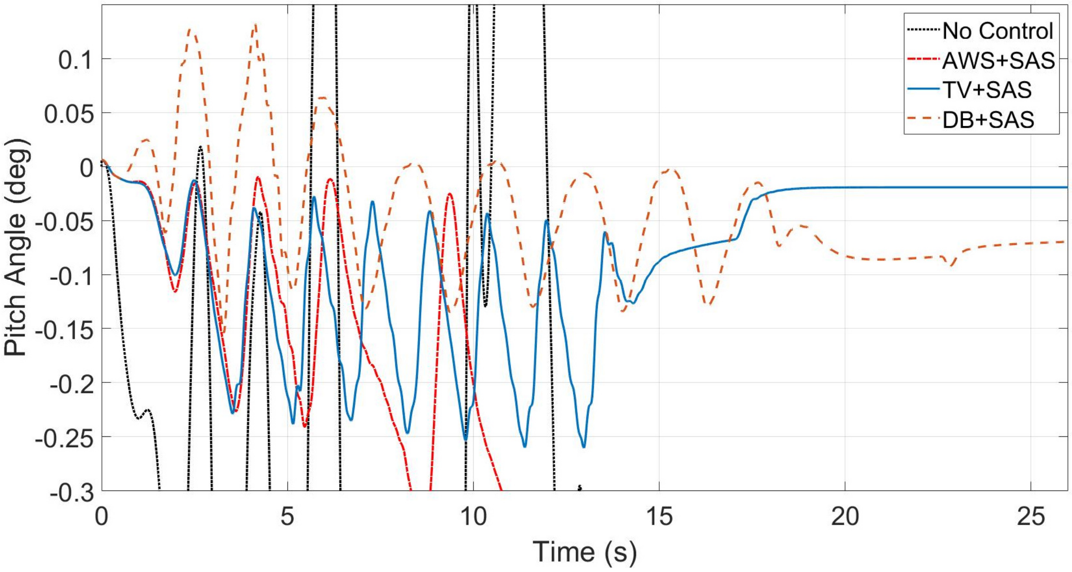

Figure 6-15 Pitch Angle during Slalom at 75 Km/h (μ = 1.0)

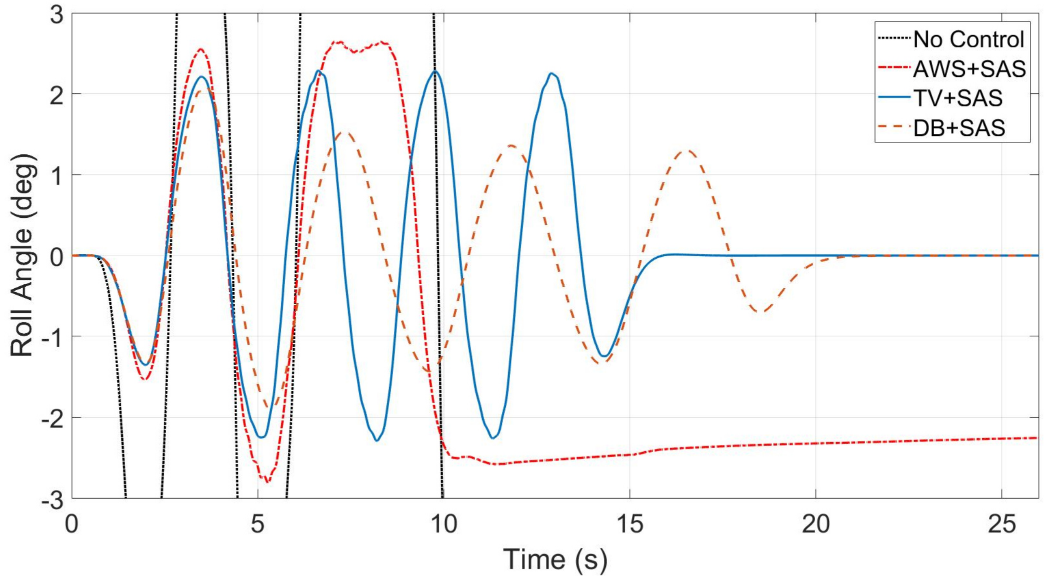

Figure 6-16 Roll Angle during Slalom at 75 Km/h (μ = 1.0)

Figure 6-17 shows the left and right sides' vehicle wheels driving torque for TV+SAS in (a) and (b) respectively. The maximum obtained driving torque during this test event was almost the same for left and right sides which are 5922.3 Nm and -4339.4 Nm for left side, while 5953.8 Nm and -4313.0 Nm for right side. However, a slight fluctuation in driving torque is observed during this test event.

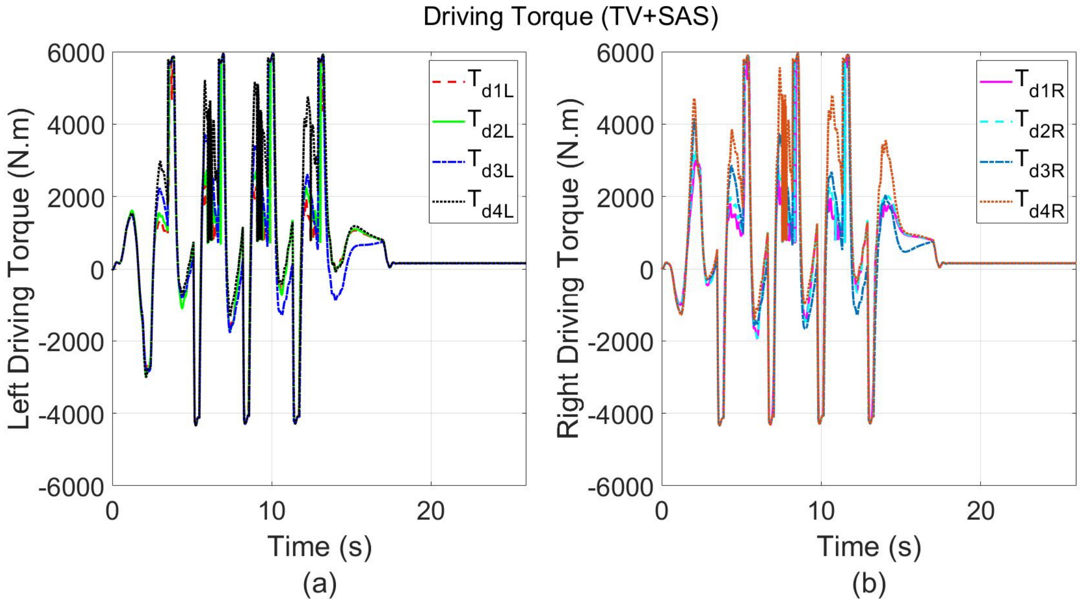

Figure 6-17 (a) Left Wheels Driving Torque and (b) Right Wheels Driving Torque for TV+SAS during Slalom at 75 Km/h (μ = 1.0)

Figure 6-18 illustrates the left and right braking wheel torque in (a) and (b) respectively for DB+SAS. There is no any significant remark can be observed regarding to wheels 'braking torque magnitude for the left and right side.

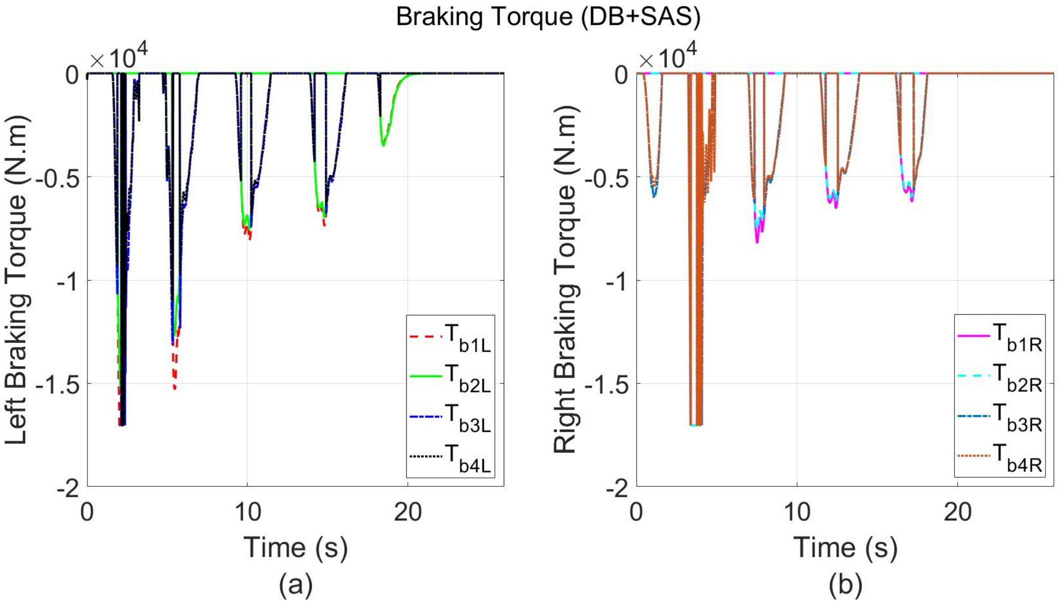

Figure 6-18 (a) Left Wheels Braking Torque and (b) Right Wheels Braking Torque for DB+SAS during Slalom at 75 Km/h (μ = 1.0)

Figure 6-19 and Figure 6-20 represent the left and right sides' vehicle dampers 'compressive forces in (a) and (b) respectively for TV+SAS and DB+SAS. It is remarkable that DB+SAS has obtained the largest left dampers' forces, while TV+SAS has attained largest right dampers' force varying with time. The DB+SAS dampers' force was -19733.4 N and 15358.4 N for left and right respectively. While -18722.4 N and -18173.6 N for the left and right side, respectively for TV+SAS.

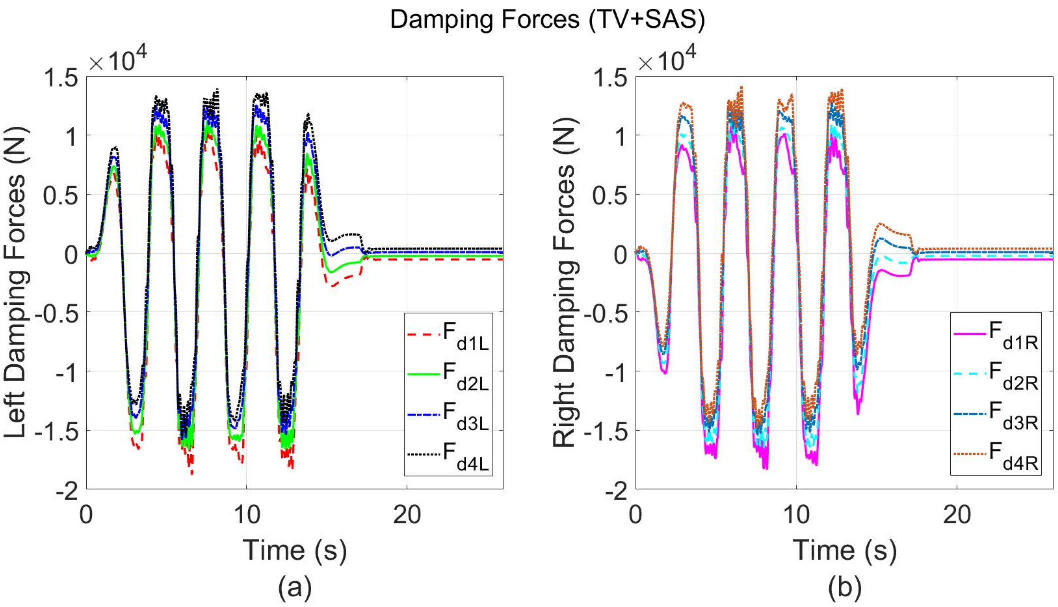

Figure 6-19 (a) Left Damping Forces and (b) Right Damping Forces for TV+SAS during Slalom at 75 Km/h ($\mu = 1.0$)

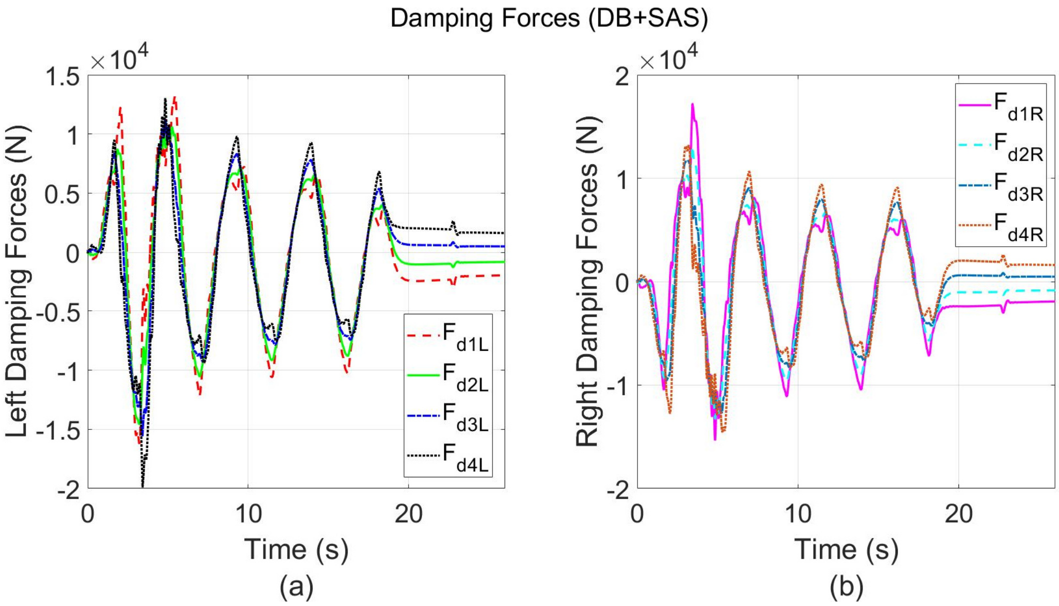

Figure 6-20 (a) Left Damping Forces and (b) Right Damping Forces for DB+SAS during Slalom at 75 Km/h ($\mu = 1.0$)

Figure 6-21 and Figure 6-22 demonstrate the left and right sides' vehicle normal loads in (a) and (b) respectively for TV+SAS and DB+SAS. Its notable that TV+SAS and DB+SAS have reasonably prevented the vehicle's wheels on both sides to left off the ground during the maneuver event. However, the DB+SAS has obtained lowest left side normal load which is 398 N for the left fourth tire. While 706.2 N for the left first tire for TV+SAS. Hence, this drop in normal load can justify the increasing of the dampers' force in the previous plots in Figure 6-19Figure 6-20 respectively.

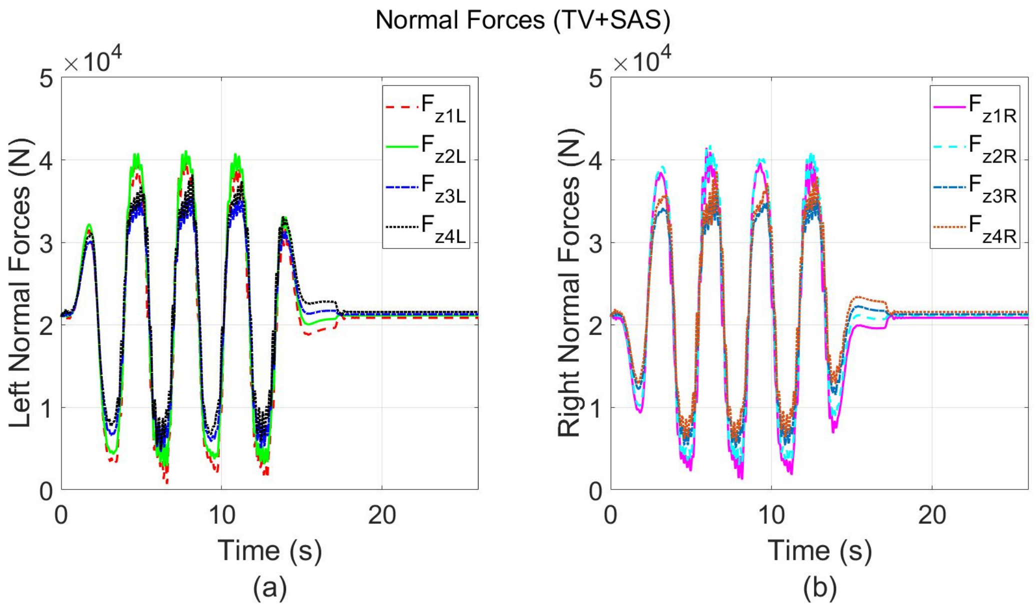

(a)

(b)

Figure 6-21(a) Left Side Normal Forces and (b) Right Side Normal Forces for TV+SAS during Slalom at 75 Km/h (μ = 1.0)

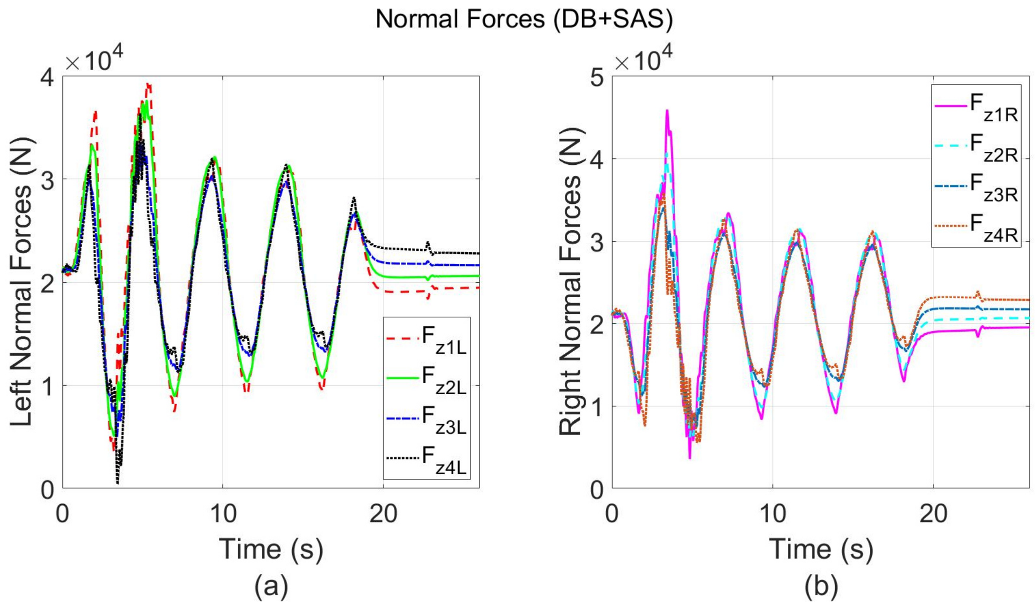

(a)

(b)

Figure 6-22 (a) Left Side Normal Forces and (b) Right Side Normal Forces for DB+SAS during Slalom at 75 Km/h (μ = 1.0)

The slip ratio of the left and right sides' vehicle tires for TV+SAS and DB+SAS are shown in Figure 6-23Figure 6-24 in (a) and (b) respectively. It can be observed that the minimization of the longitudinal and lateral load transfer can significantly assist the slip controller to maintain either the peak tractive or braking force at the desired limit $(20 - 25\%)$.

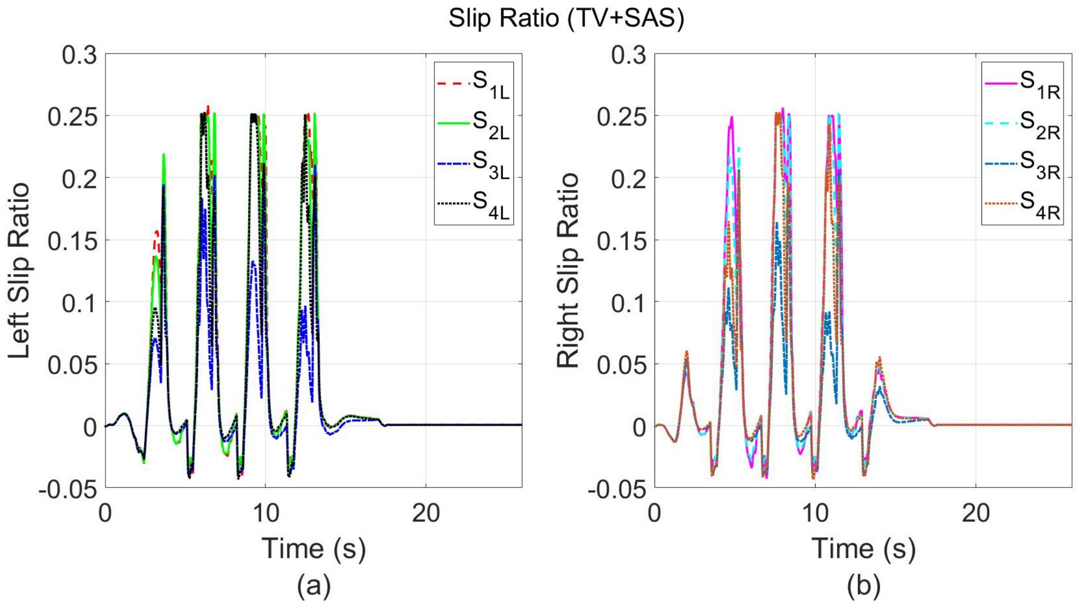

(a) (b)

Figure 6-23 (a) Left Tires' Slip Ratio and (b) Right Tires' Slip Ratio for TV+SAS during Slalom at 75 Km/h ($\mu = 1.0$)

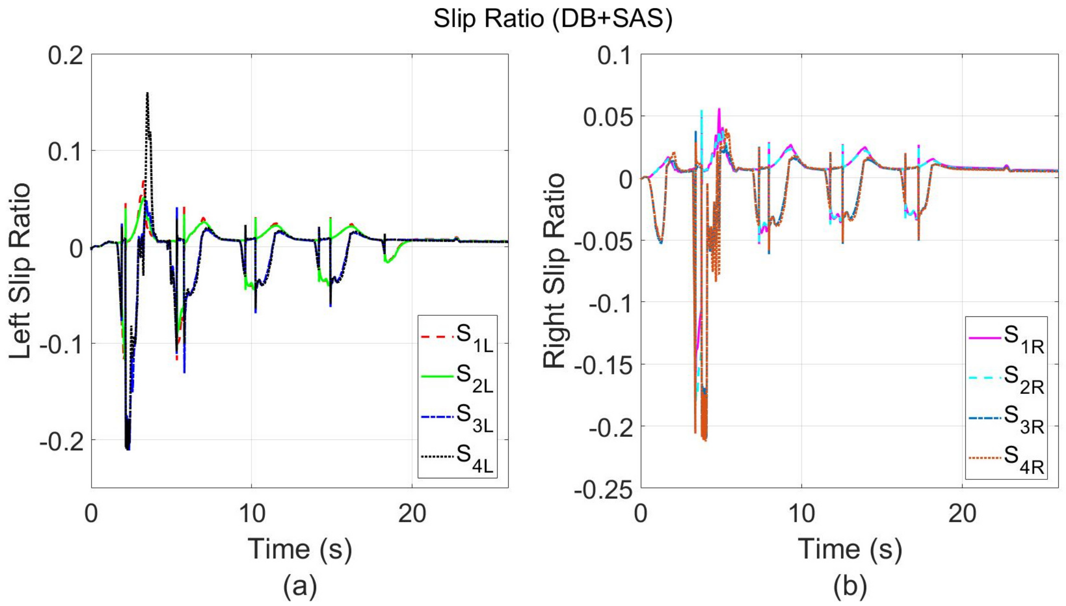

(a) (b)

Figure 6-24 (a) Left Tires' Slip Ratio and (b) Right Tires' Slip Ratio for DB+SAS during Slalom at 75 Km/h ($\mu = 1.0$)

6.2.1.3 Results and Discussion of Evaluation Method at Low coefficient of friction – Constant Step Slalom ($40\ \mathrm{km/h}\ ;\ \mu = 0.35$)

The vehicle trajectory and the corresponding error achieved by each control strategy AWS, TV, DB, and vehicle with no control are shown in Figure 6-25 in (a) and (b) respectively. It can be noticed that all the proposed control strategies and vehicle with no control have succeeded to perform the trajectory without any failure. Also, the uncontrolled vehicle has relatively obtained the least error as shown in Table 6-4.

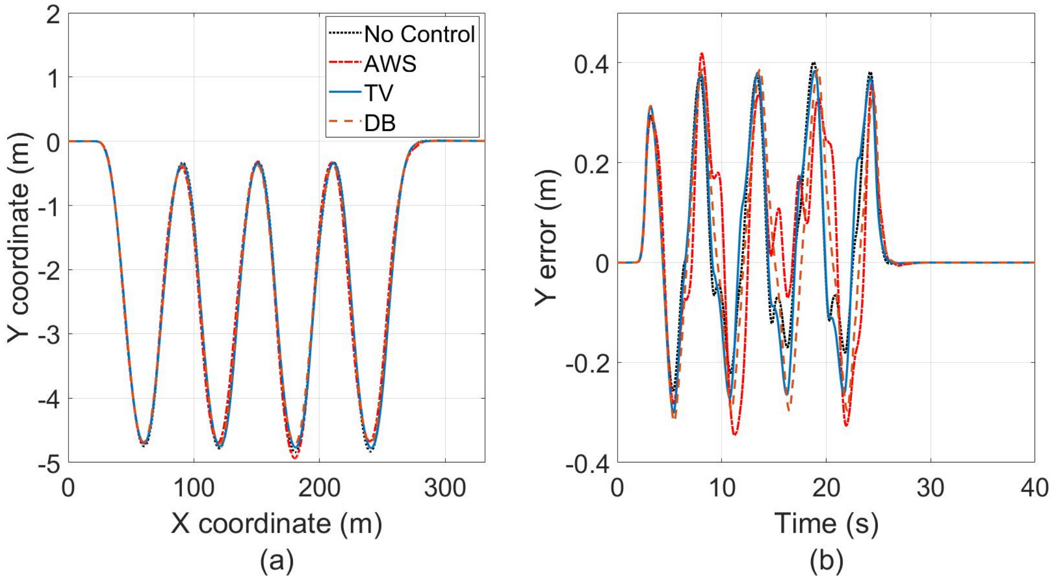

Figure 6-25 Vehicle trajectory during Slalom at 40 Km/h ($\mu = 0.35$) and (b) Error obtained by vehicle (No Control), AWS, TV, and DB

Table 6-4 Trajectory Root Mean Square Errors Obtained by Uncontrolled Vehicle, AWS, TV, and DB during Slalom at 40 Km/h ($\mu = 0.35$)

Controller’s Configuration	RMSE (m)
No Control	0.1530
AWS	0.1642
TV	0.1651
DB	0.1654

Figure 6-26, Figure 6-27, Figure 6-28 and Figure 6-29 illustrate the vehicle sideslip, yaw rate, longitudinal speed, and lateral acceleration respectively for AWS, TV, DB, and vehicle with no control. Its notable that AWS has achieved the smallest value for sideslip angle followed by TV then DB, 0.9, 1.3 and 2 degrees, respectively. While vehicle with no control has attained the largest value -5.6 degrees. which considered as a merit for AWS over the other control strategies in terms of enhancing vehicle's stability at low road friction surface. The yaw rate response amplitude was maintained relatively same for all control strategies around 15 degree/s, while the vehicle with no control attained the largest value 19 degree/s. Moreover, AWS, TV and vehicle with no control exhibit less drop in vehicle's longitudinal speed compared to DB, which makes it close to achieve the desired speed. For lateral acceleration there is no any significant observation can be remarked since all the configurations have reasonably same peak amplitude except the vehicle with no control has slightly attained the largest value.

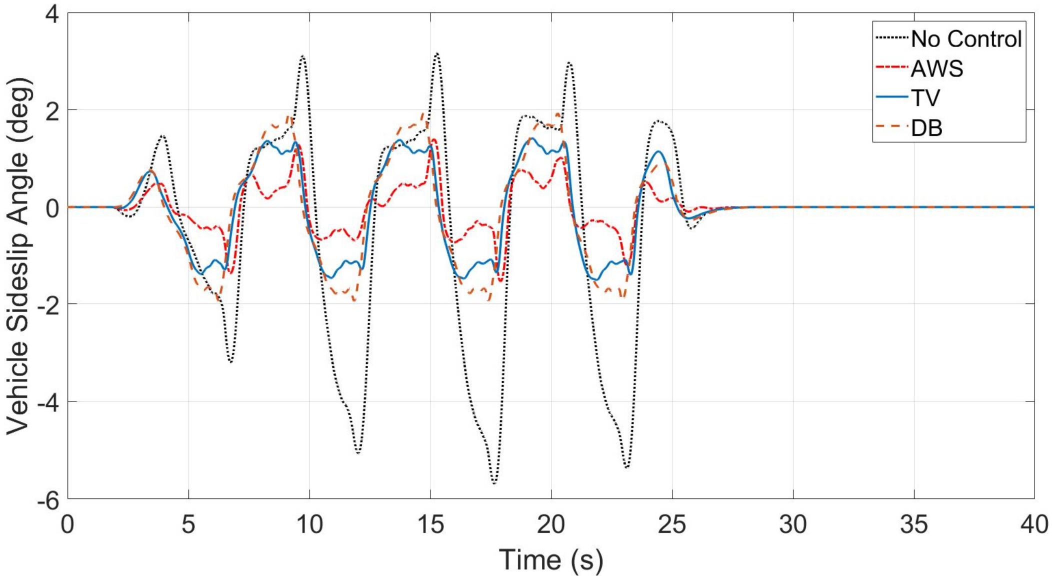

Figure 6-26 Vehicle Sideslip Angle during Slalom at 40 Km/h ($\mu = 0.35$)

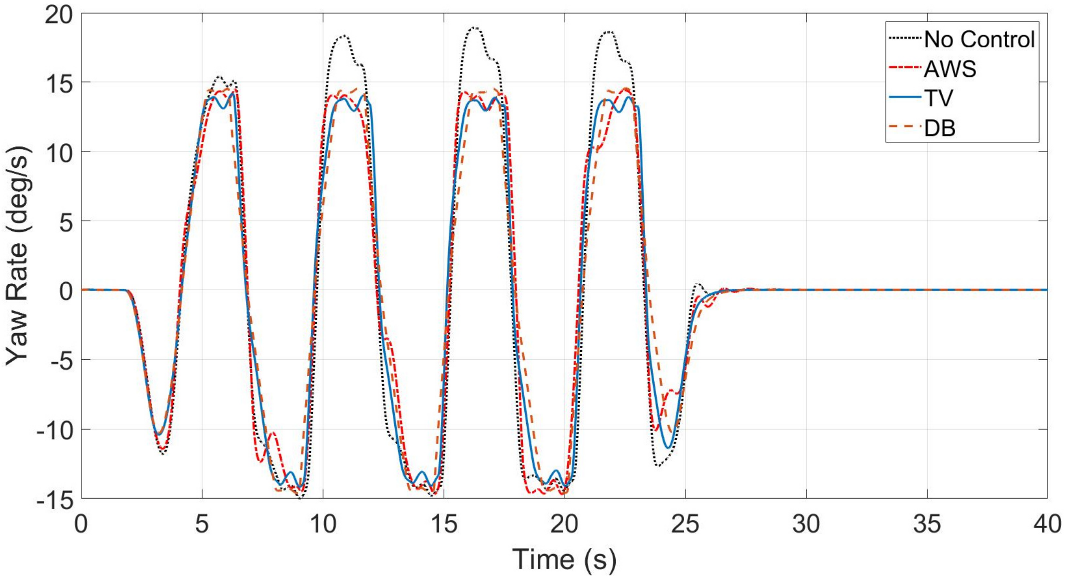

Figure 6-27 Yaw Rate during Slalom at 40 Km/h (μ = 0.35)

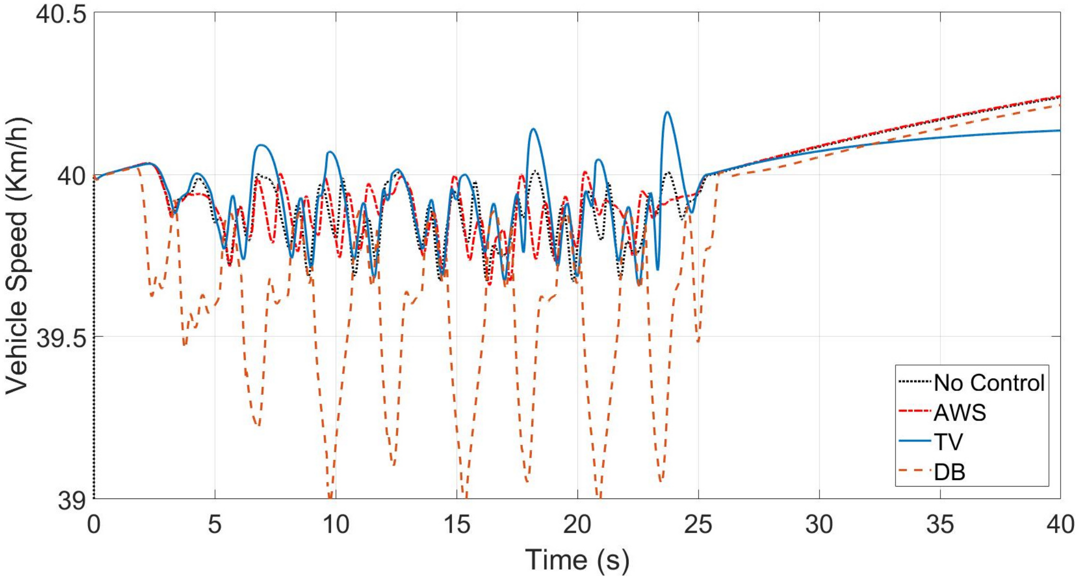

Figure 6-28 Vehicle Speed during Slalom at 40 Km/h (μ = 0.35)

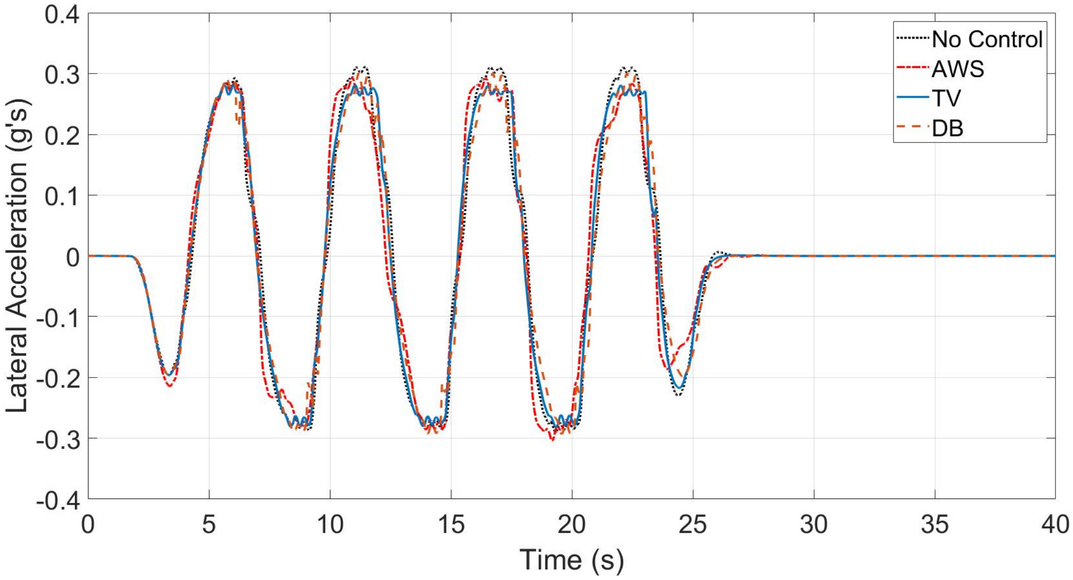

Figure 6-29 Lateral Acceleration during Slalom at 40 Km/h (μ = 0.35)

Figure 6-30 and Figure 6-31demonstrate the front and rear road steer angles in (a) and (b) for vehicle with no control and AWS, respectively. A maximum front steering angle of 18.7 degrees and 4.5 degrees for rear steering angle are observed for AWS, while -15 degrees for vehicle with no control. It should be noted that the rear steer angles for AWS are performing parallel steering (steering in the same direction as the front steering angles).

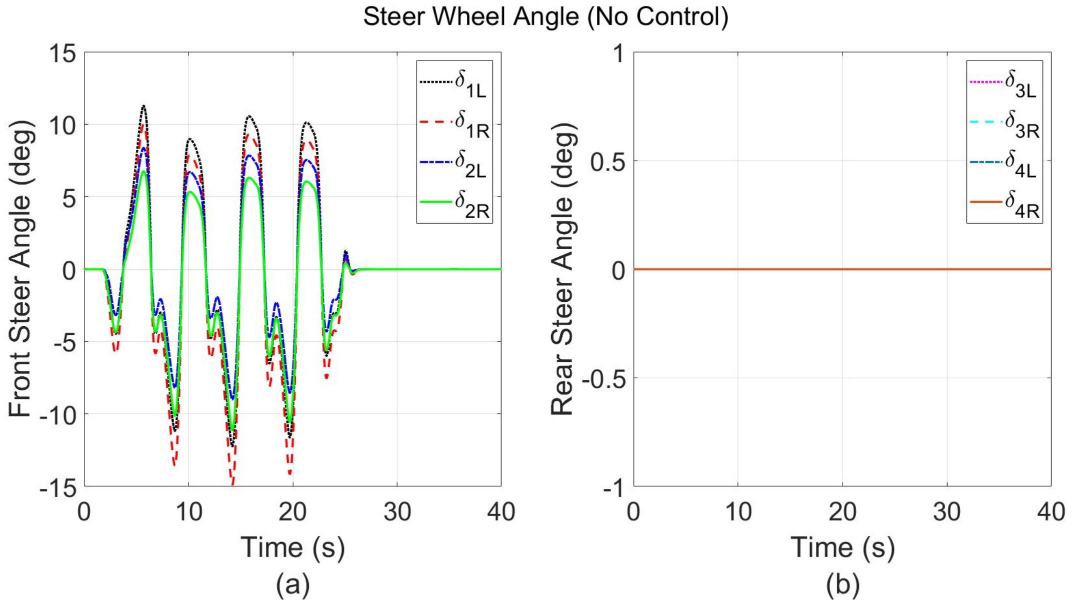

Figure 6-30 (a) Front Steer Angle and (b) Rear Steer Angle for Vehicle (No Control) during Slalom at 40 Km/h (μ = 0.35)

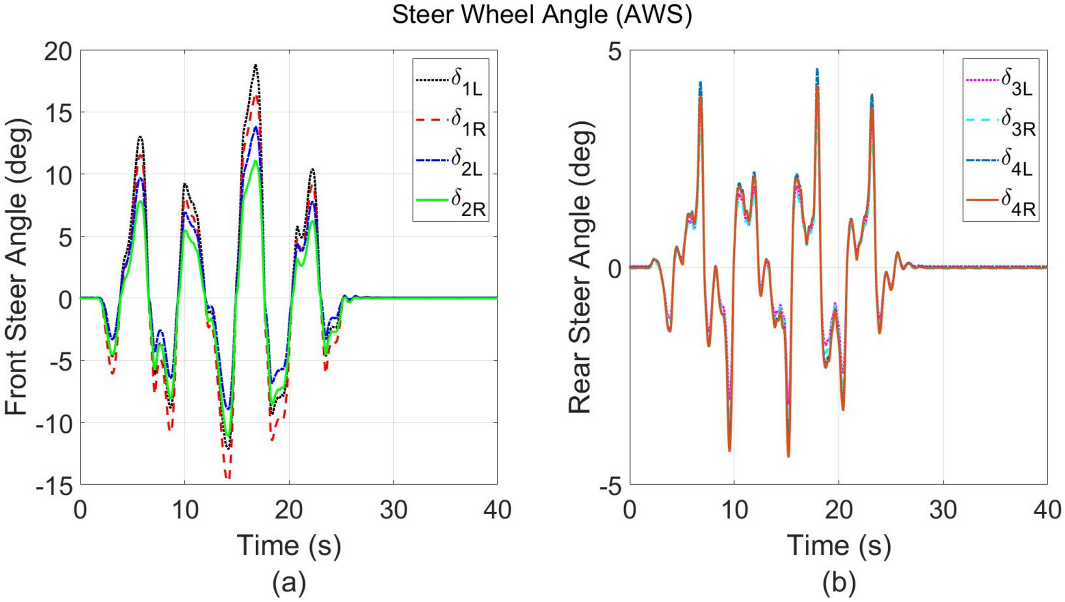

(a) (b)

Figure 6-31(a) Front Steer Angle and (b) Rear Steer Angle for AWS during Slalom at 40 Km/h ($\mu = 0.35$)

Figure 6-32 and Figure 6-33 show the left and right sides' vehicle wheels driving torque in (a) and (b) for vehicle with no control and TV, respectively. The maximum achieved driving wheel torque in the left and right side for TV is 4683.3 Nm and 3937.6 Nm, respectively. While 800 Nm in both sides for vehicle with no control.

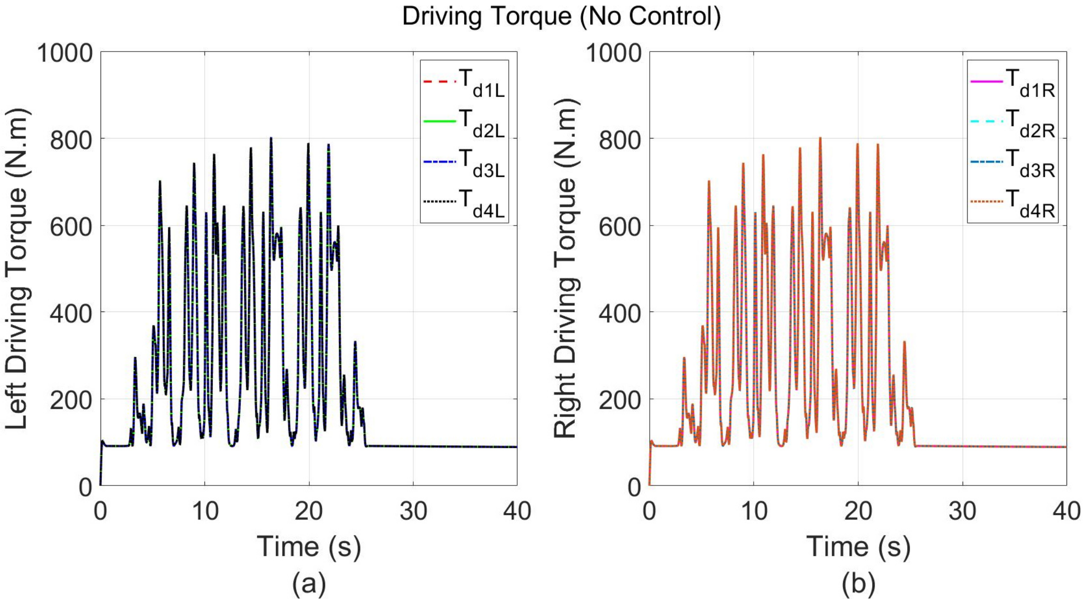

(a) (b)

Figure 6-32 (a) Left Wheels Driving Torque and (b) Right Wheels Driving Torque for Vehicle (No Control) during Slalom at 40 Km/h ($\mu = 0.35$)

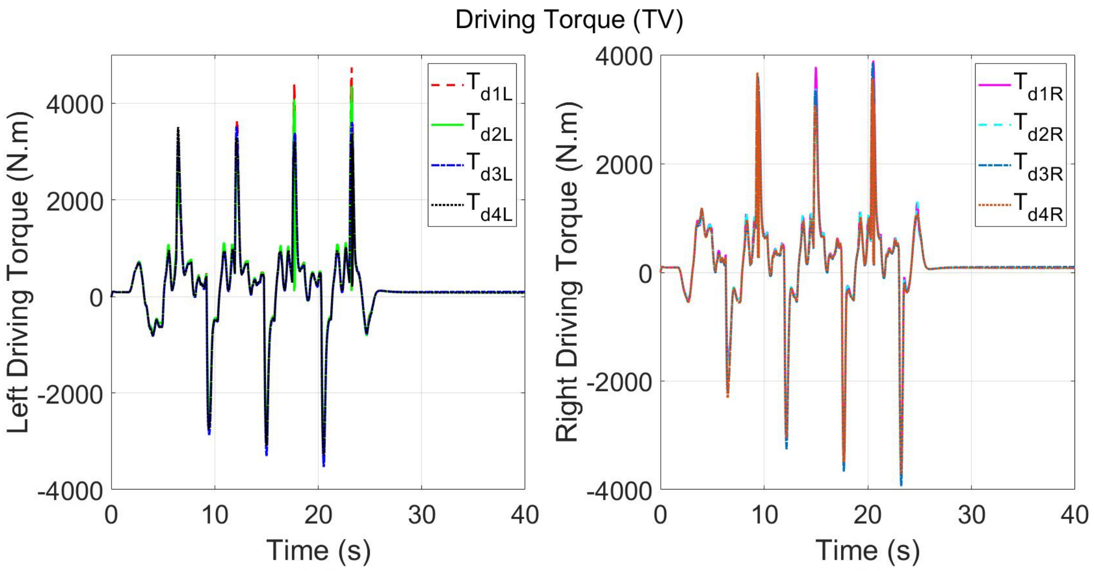

(a) (b)

Figure 6-33 (a) Left Wheels Driving Torque and (b) Right Wheels Driving Torque for TV during Slalom at 40 Km/h ($\mu = 0.35$)

Figure 6-34 presents the left and right sides' braking wheel torque in (a) and (b) for DB. The maximum attained wheel braking torque is observed to be relatively same for both sides, for the left side is 8007.3 Nm, while 7835.5 Nm for the right side.

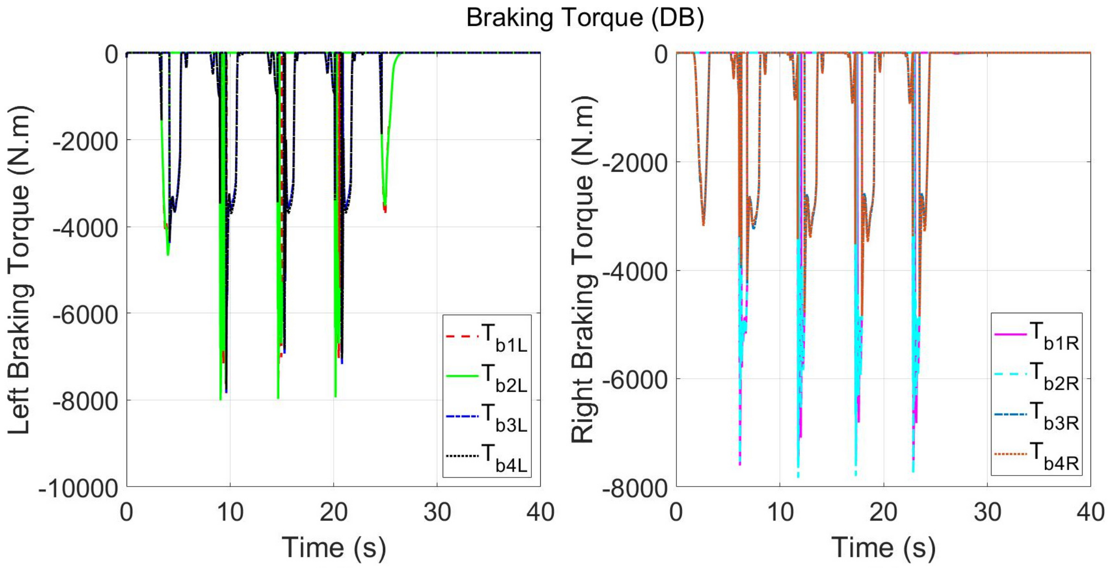

(a) (b)

Figure 6-34 (a) Left Wheels Braking Torque and (b) Right Wheels Braking Torque for DB during Slalom at 40 Km/h ($\mu = 0.35$)

6.2.1.4 Results and Discussion of Evaluation Method at Low coefficient of friction – Constant Step Slalom ($30\ \mathrm{km/h}\ ;\ \mu = 0.2$)

The vehicle trajectory and the corresponding error achieved by each control strategy AWS, TV, DB, and vehicle with no control are shown in Figure 6-35. Its notable that TV and DB have successfully maintained the trajectory, while AWS and vehicle with no control failed to achieve it. However, DB has slightly obtained the largest error compared to TV as shown in Table 6-5.

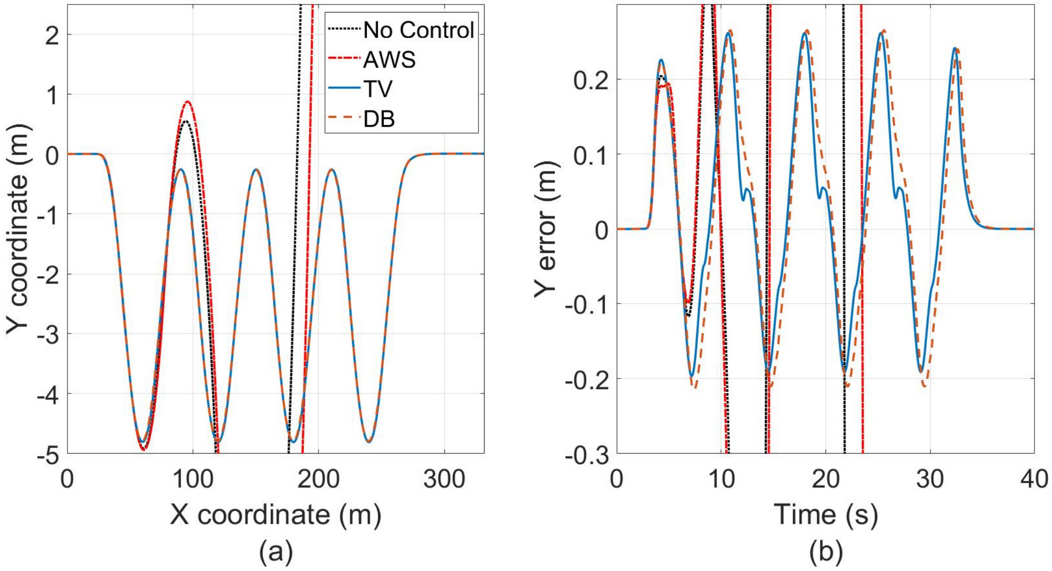

Figure 6-35 Vehicle trajectory during Slalom at 30 Km/h ($\mu = 0.2$) and (b) Error obtained by vehicle (No Control), AWS, TV, and DB

Table 6-5 Trajectory Root Mean Square Errors Obtained by Uncontrolled Vehicle, AWS, TV, and DB during Slalom at 30 Km/h ($\mu = 0.2$)

Controller's Configuration	RMSE (m)
No Control	22.7483
AWS	26.5756
TV	0.1239
DB	0.1348

Figure 6-36, Figure 6-37, Figure 6-38 and Figure 6-39 depict the vehicle sideslip, yaw rate, longitudinal speed, and lateral acceleration respectively for AWS, TV, DB, and vehicle with no control. TV has showed superiority in minimizing the vehicle sideslip and keep it stable at very low friction road surface followed by DB, while AWS and vehicle with no control failed and lost stability. The yaw rate is observed to be same for both TV and DB. However, DB has slightly achieved larger peak amplitude than TV, also the response is shifted and delayed, makes TV to stabilize the vehicle faster. The longitudinal speed and lateral acceleration were approximately maintained the same for both control strategies. However, TV is faster than DB in stabilizing the vehicle based on the settling time.

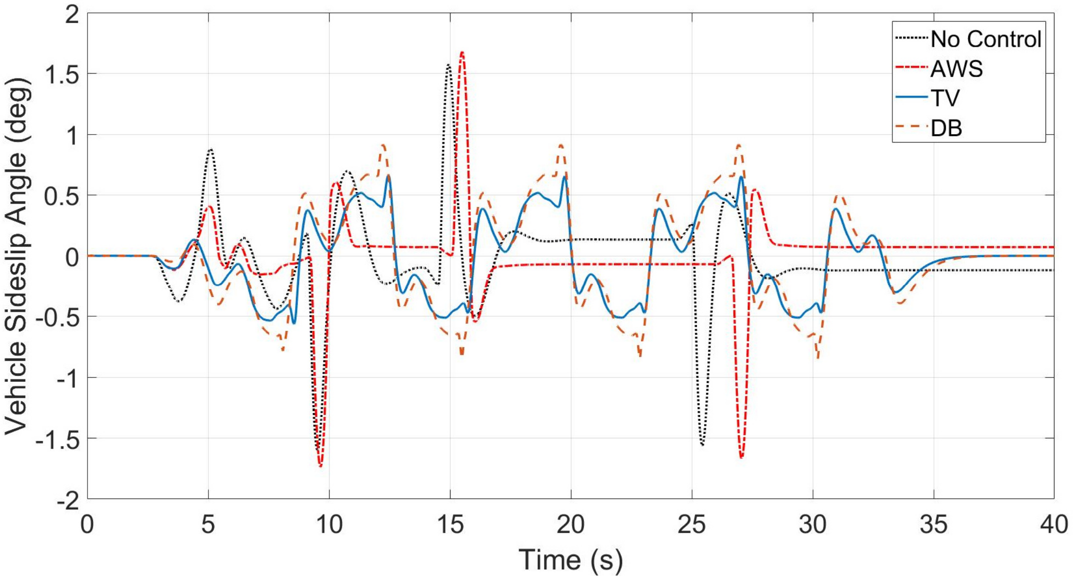

Figure 6-36 Vehicle Sideslip Angle during Slalom at 30 Km/h (μ = 0.2)

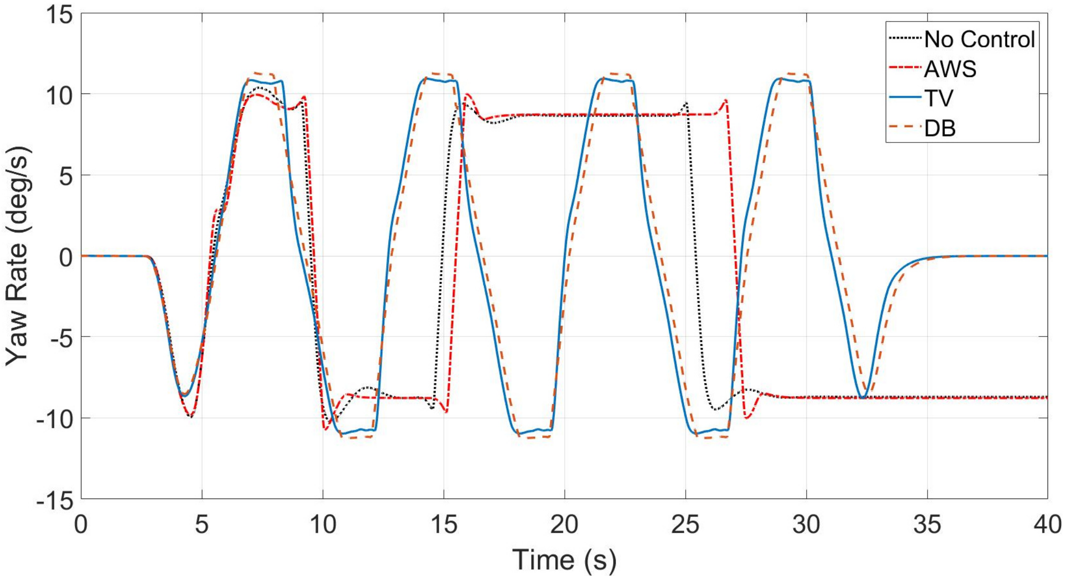

Figure 6-37 Yaw Rate during Slalom at 30 Km/h (μ = 0.2)

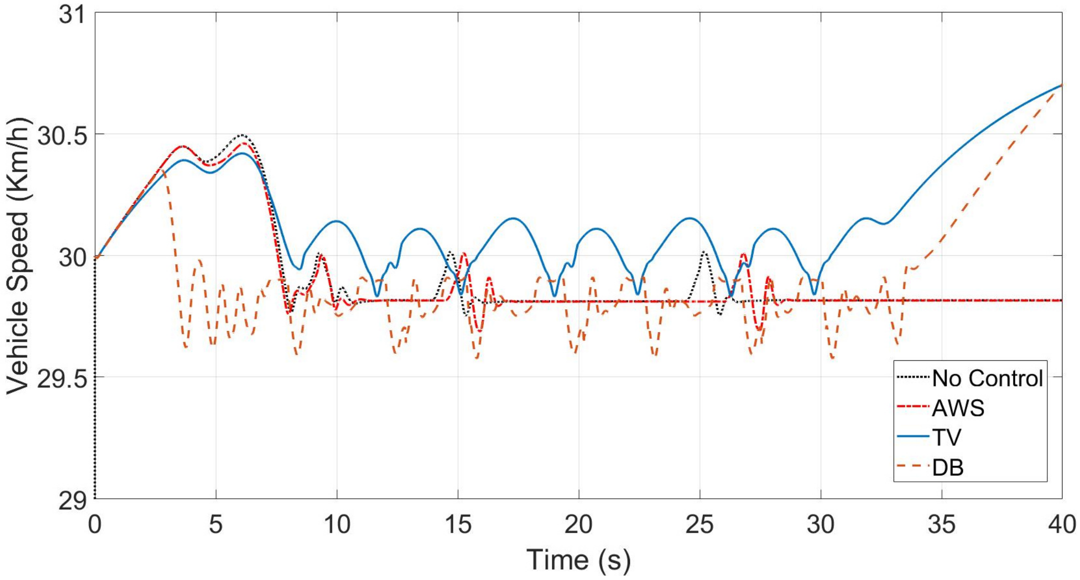

Figure 6-38 Vehicle Speed during Slalom at 30 Km/h (μ = 0.2)

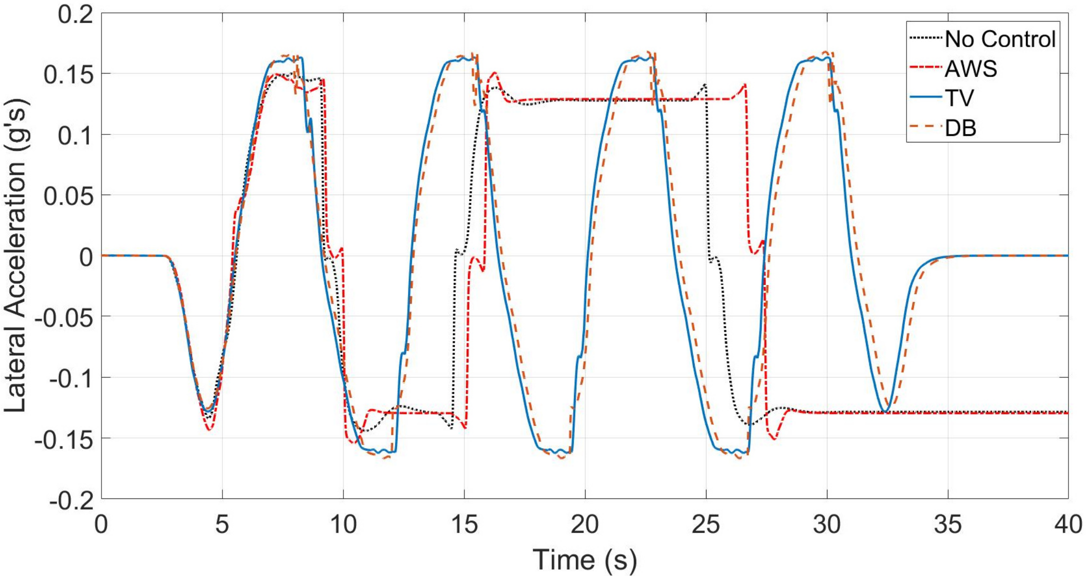

Figure 6-39 Lateral Acceleration during Slalom at 30 Km/h (μ = 0.2)

Figure 6-40 express the left and right sides' vehicle wheels driving torque in (a) and (b) for TV. The maximum achieved driving wheel torque in the left and right side is 1849.0 Nm and 1978.0 Nm, respectively.

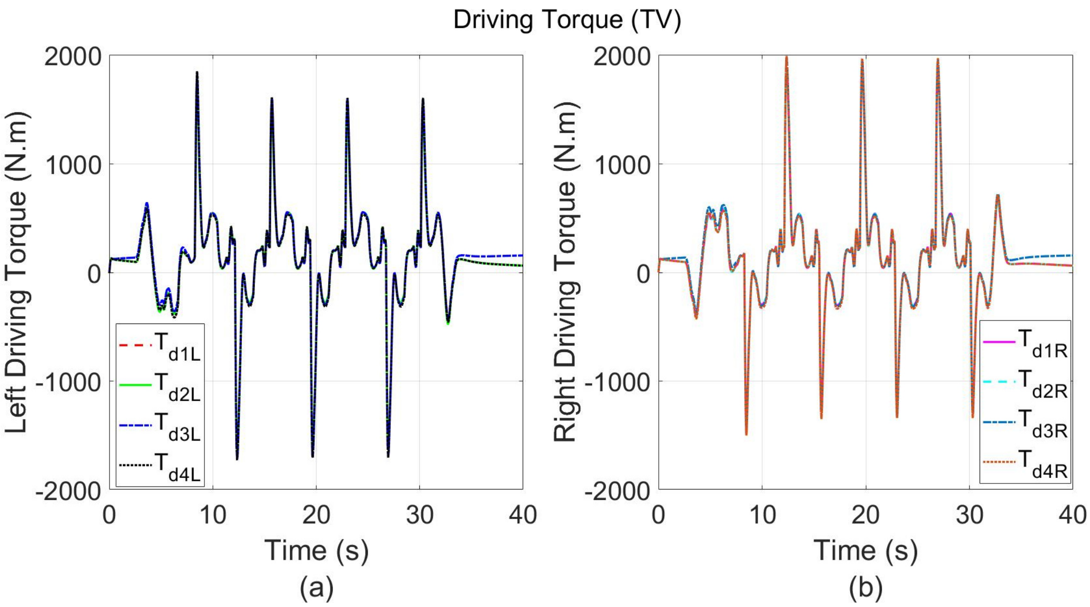

Figure 6-40 (a) Left Wheels Driving Torque and (b) Right Wheels Driving Torque for TV during Slalom at 30 Km/h (μ = 0.2)

Figure 6-41 express the left and right sides' wheels braking torque in (a) and (b) for DB. The maximum achieved braking wheel torque in the left and right side is -7897.3 Nm and -3301.7 Nm, respectively.

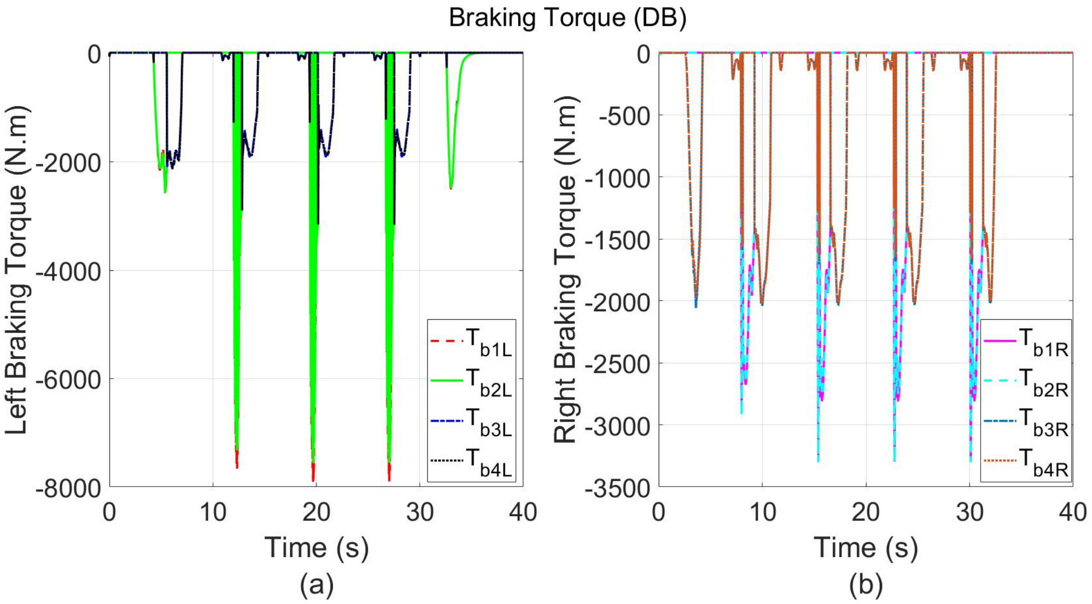

Figure 6-41 (a) Left Wheels Braking Torque and (b) Right Wheels Braking Torque for DB during Slalom at 30 Km/h (μ = 0.2)

6.2.2 Double Lane Change Test (DLC) (NATO AVTP 03-160W)

The NATO AVTP 03-160W standard test is designed to evaluate the vehicle's lateral dynamics behaviour through a lane change with a rapidly return to original lane. The maneuver course layout is represented as follows in Figure 6-42.

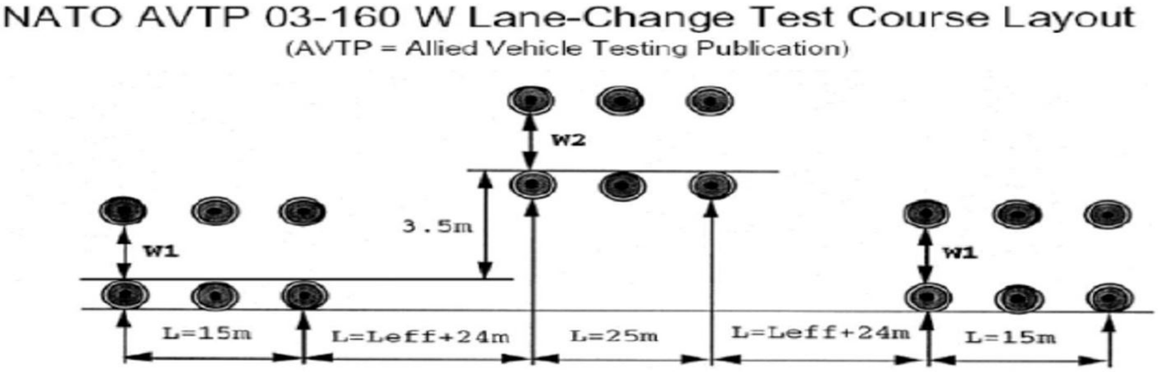

Figure 6-42 NATO AVTP 03-160 W Lane-Change Test Course Layout (Courtesy of GDLS-C) [112]

6.2.2.1 Results and Discussion of Evaluation Method at high coefficient of friction – NATO Double Lane Change ($100\ \mathrm{km/h}\ ;\ \mu = 0.85$)

The vehicle trajectory and the corresponding error achieved by each control strategy AWS+SAS, TV+SAS, DB+SAS, and vehicle with no control are shown in Figure 6-43 in (a) and (b) respectively. Its notable that all proposed control strategies and vehicle with no control have performed the trajectory. AWS+SAS has achieved the least error compared to the other control strategies and uncontrolled vehicle as presented in Table 6-6.

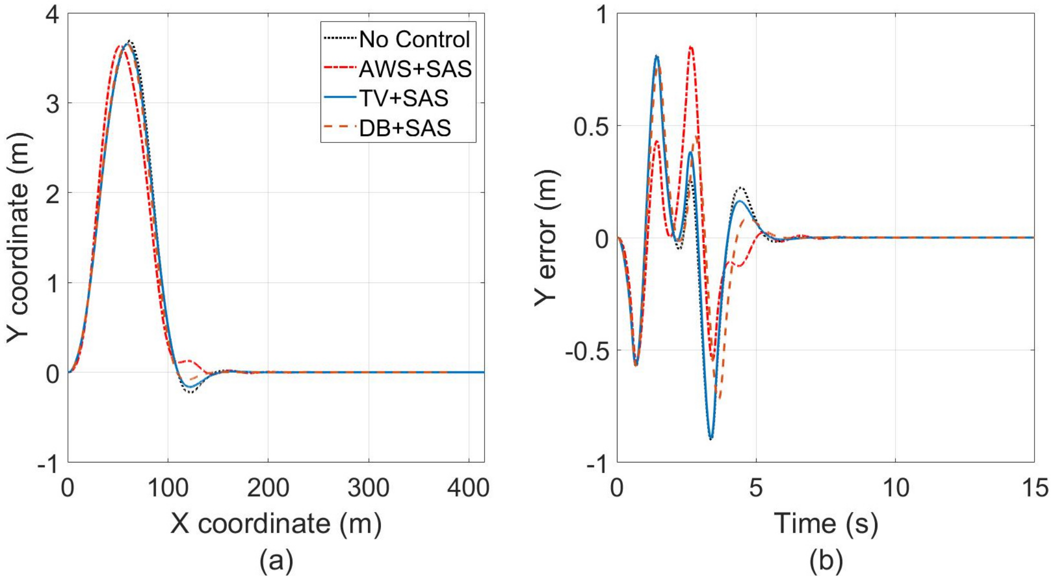

Figure 6-43 Vehicle trajectory during DLC at 100 Km/h (μ = 0.85) and (b) Error obtained by vehicle (No Control), AWS+SAS, TV+SAS and DB+SAS

Table 6-6 Trajectory Root Mean Square Errors Obtained by Uncontrolled Vehicle, AWS+SAS, TV+SAS and DB+SAS during DLC at 100 Km/h (μ = 0.85)

Controller's Configuration	RMSE (m)
No Control	0.2273
AWS+SAS	0.1975
TV+SAS	0.2251
DB+SAS	0.2111

Figure 6-44, Figure 6-45, Figure 6-46 and Figure 6-47 illustrate the vehicle sideslip, yaw rate, longitudinal speed and lateral acceleration respectively for vehicle with no control, AWS+SAS, TV+SAS and DB+SAS. It can be observed that AWS+SAS have maintained the smallest value for sideslip angle compared to the other control strategies and vehicle with no control. AWS+SAS has achieved maximum sideslip angle 2.3 degrees, while 3.3, 3.0 and 5.3 degrees for TV+SAS, DB+SAS and vehicle with no control, respectively. The yaw rate response amplitude was varying with respect to time for all control strategies. However, TV+SAS and DB+SAS stabilized the vehicle faster than AWS+SAS and vehicle with no control. Also, TV+SAS has achieved less drop in longitudinal speed among all other control strategies and vehicle with no control, makes it close to maintain the desired speed. Furthermore, the largest lateral acceleration peak amplitude was attained by AWS+SAS, while the smallest value was performed by DB+SAS and this is because the reduction of speed caused by braking followed by TV+SAS. It should be noted that TV+SAS and DB+SAS have stabilized the vehicle faster than AWS+SAS in all the mentioned plots.

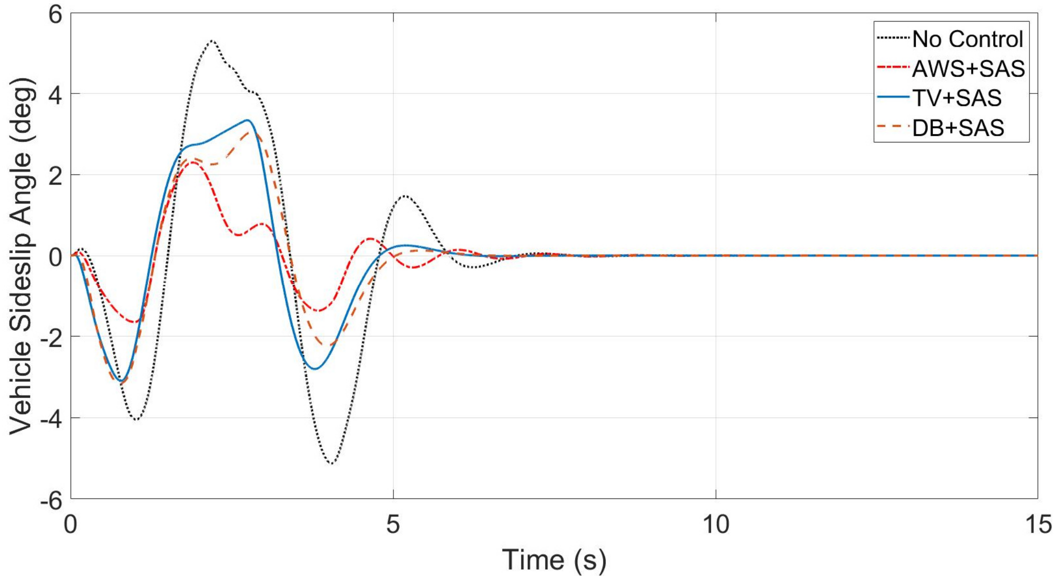

Figure 6-44 Vehicle Sideslip Angle during DLC at 100 Km/h (μ = 0.85)

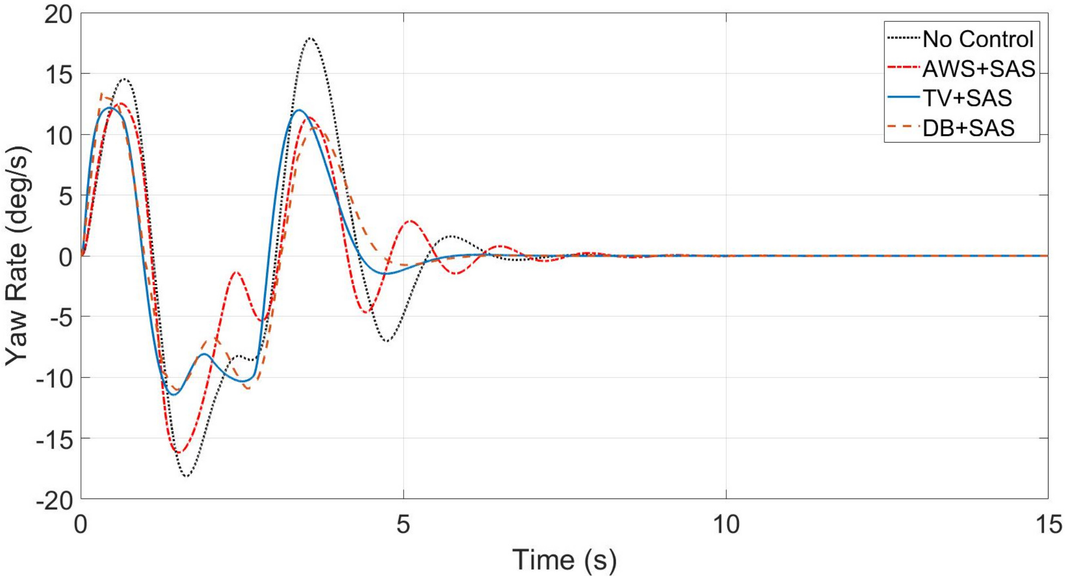

Figure 6-45 Yaw Rate during DLC at 100 Km/h (μ = 0.85)

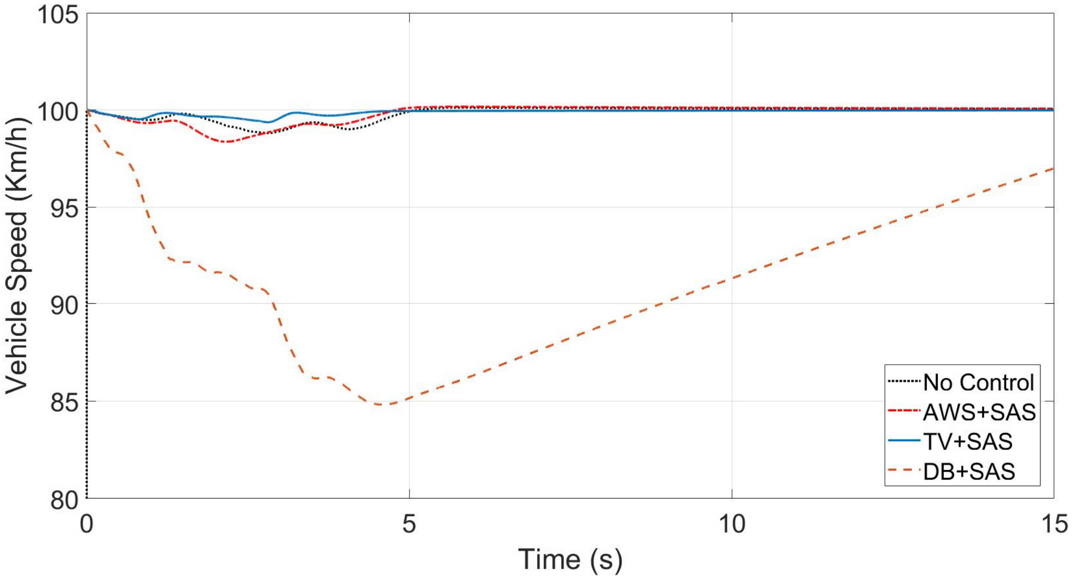

Figure 6-46 Vehicle Speed during DLC at 100 Km/h (μ = 0.85)

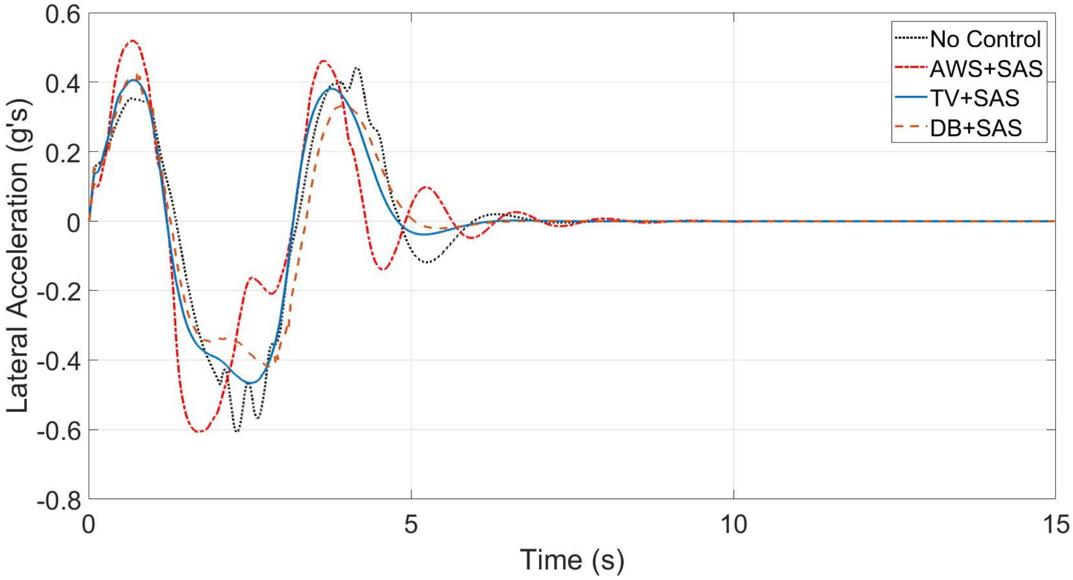

Figure 6-47 Lateral Acceleration during DLC at 100 Km/h (μ = 0.85)

Figure 6-48, Figure 6-49 and Figure 6-50 demonstrate the vehicle's sprung mass displacement, pitch, and roll angle, respectively. It is notable that AWS+SAS, TV+SAS and DB+SAS have significantly minimized the vertical displacement at the CG of the sprung mass compared to vehicle with no control. Furthermore, all the proposed control strategies have tremendously reduced the pitch and roll angle due to longitudinal and lateral load transfer. Hence, avoiding the grip loss between the tires and the ground at high-speed cornering maneuvers.

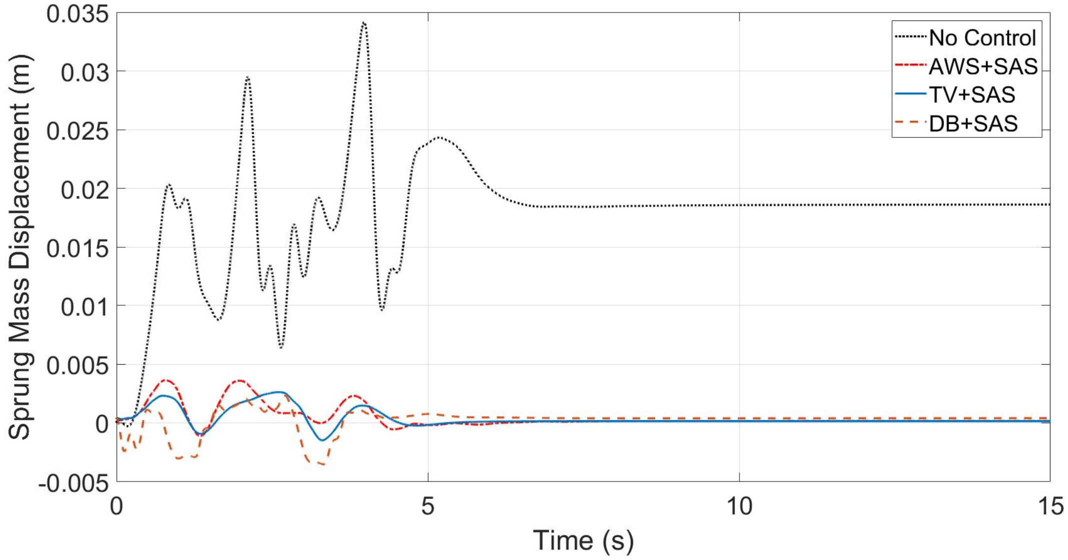

Figure 6-48 Sprung Mass Displacement during DLC at 100 Km/h (μ = 0.85)

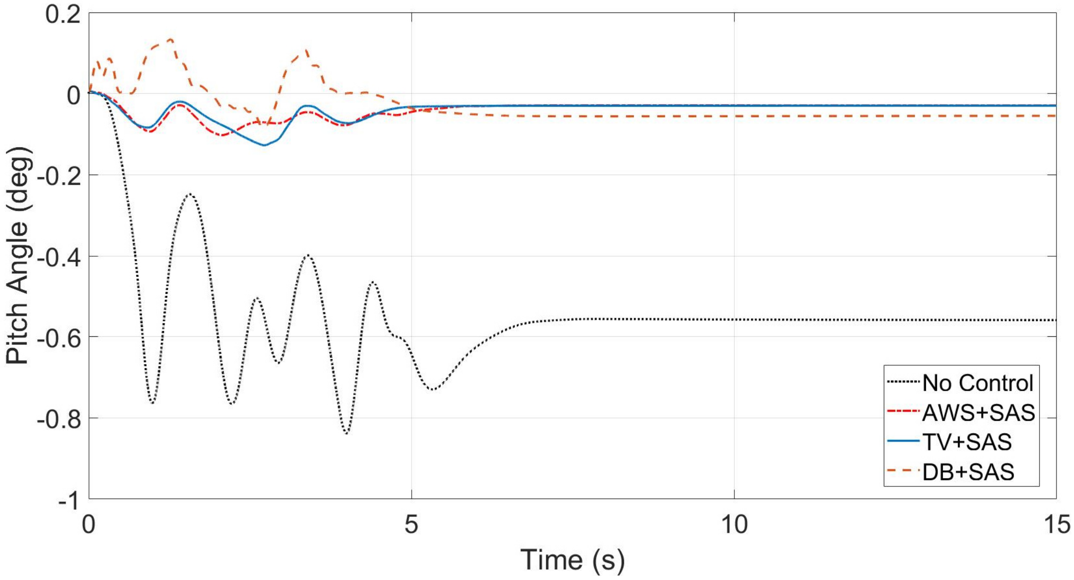

Figure 6-49 Pitch Angle during DLC at 100 Km/h (μ = 0.85)

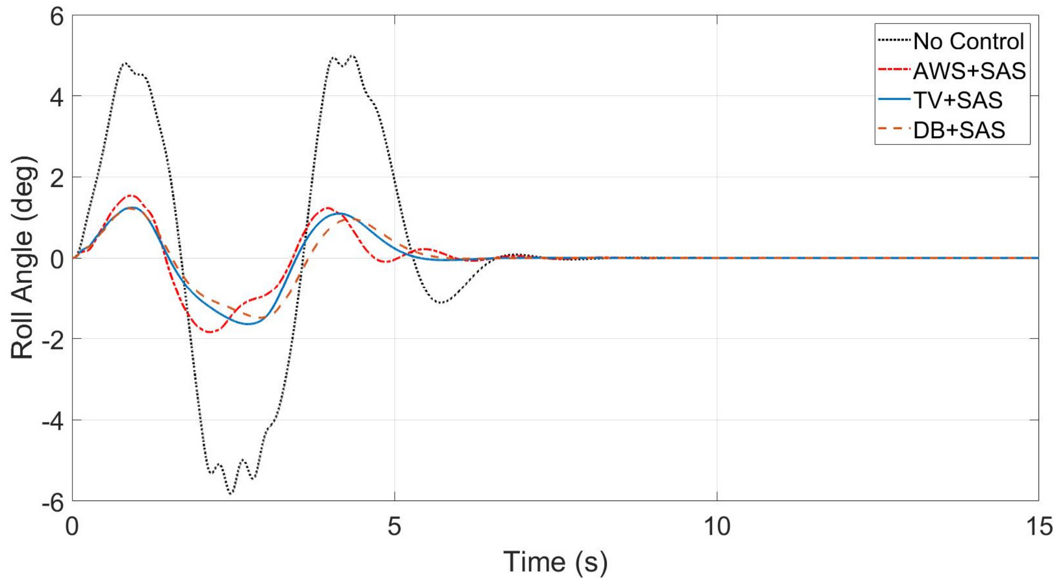

Figure 6-50 Roll Angle during DLC at 100 Km/h (μ = 0.85)

Figure 6-51 and Figure 6-52 (a) and (b) present the front and rear road steer angles in (a) and (b) for vehicle with no control and AWS+SAS, respectively. A maximum front steering angle of -10 degrees and -7.2 degrees for rear steering angle are observed for AWS+SAS, while -7 degrees for vehicle with no control. It should be noted that the rear steer angles for AWS are performing parallel steering (steering in the same direction as the front steering angles).

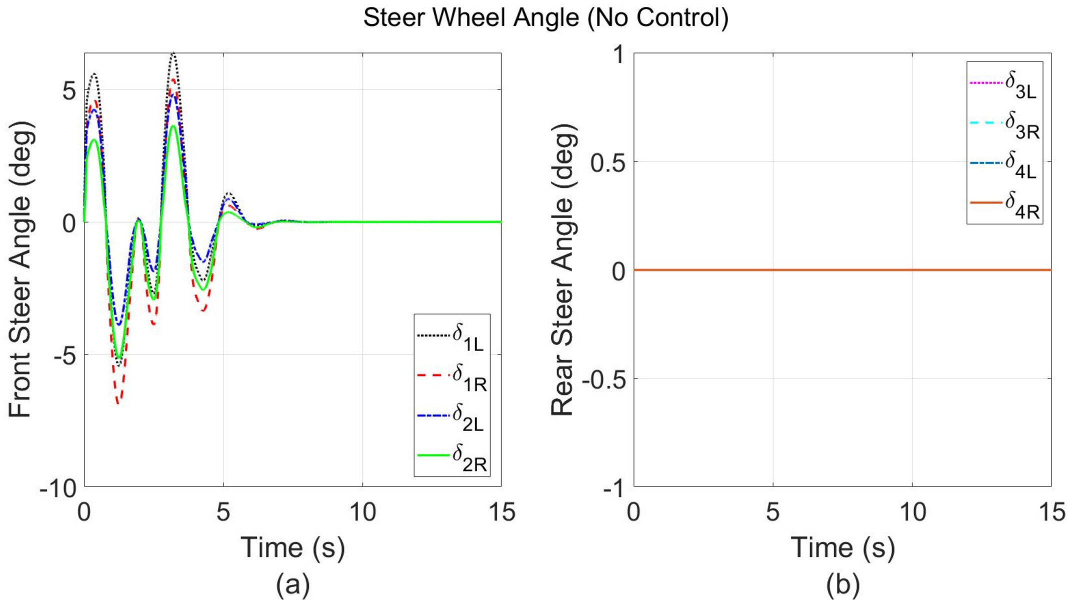

Figure 6-51 (a) Front Steer Angle and (b) Rear Steer Angle for Vehicle (No Control) during DLC at 100 Km/h (μ = 0.85)

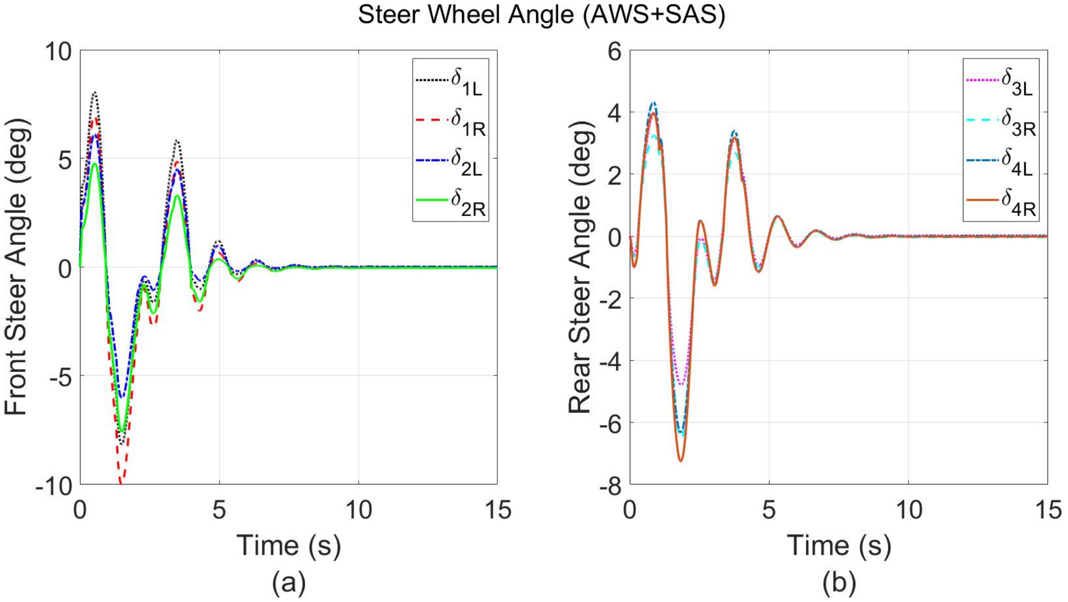

Figure 6-52 (a) Front Steer Angle and (b) Rear Steer Angle for AWS+SAS during DLC at 100 Km/h (μ = 0.85)

Figure 6-53 and Figure 6-54 show the left and right sides' vehicle wheels driving torque in (a) and (b) for vehicle with no control and TV+SAS, respectively. The maximum achieved driving wheel torque in the left and right side for TV+SAS is -5000 Nm and 5465.0 Nm, respectively. While 600 Nm in both sides for vehicle with no control.

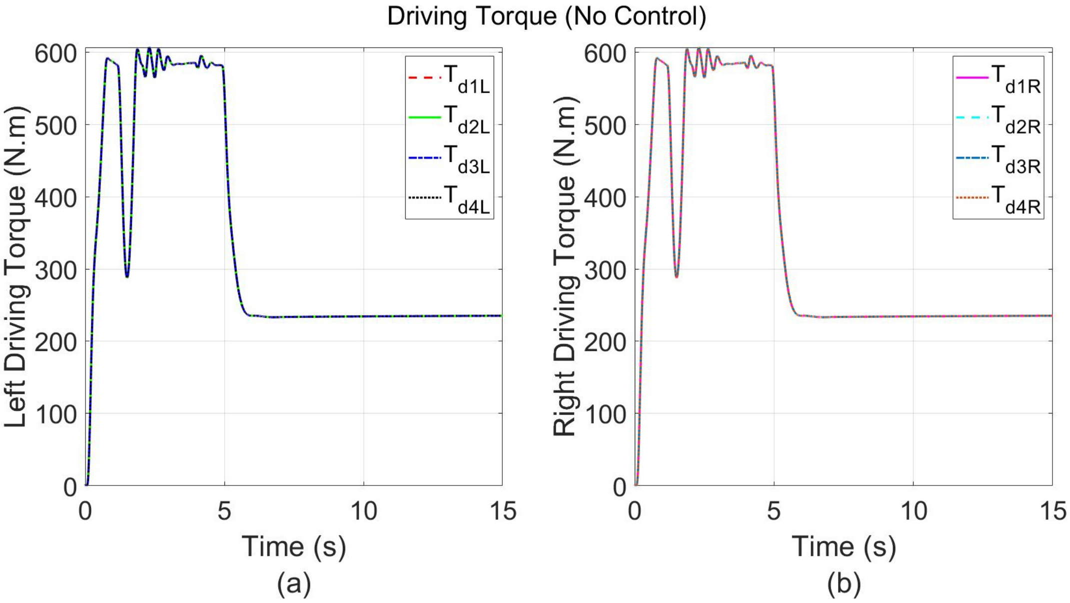

Figure 6-53 (a) Left Wheels Driving Torque and (b) Right Wheels Driving Torque for Vehicle (No Control) during DLC at 100 Km/h (μ = 0.85)

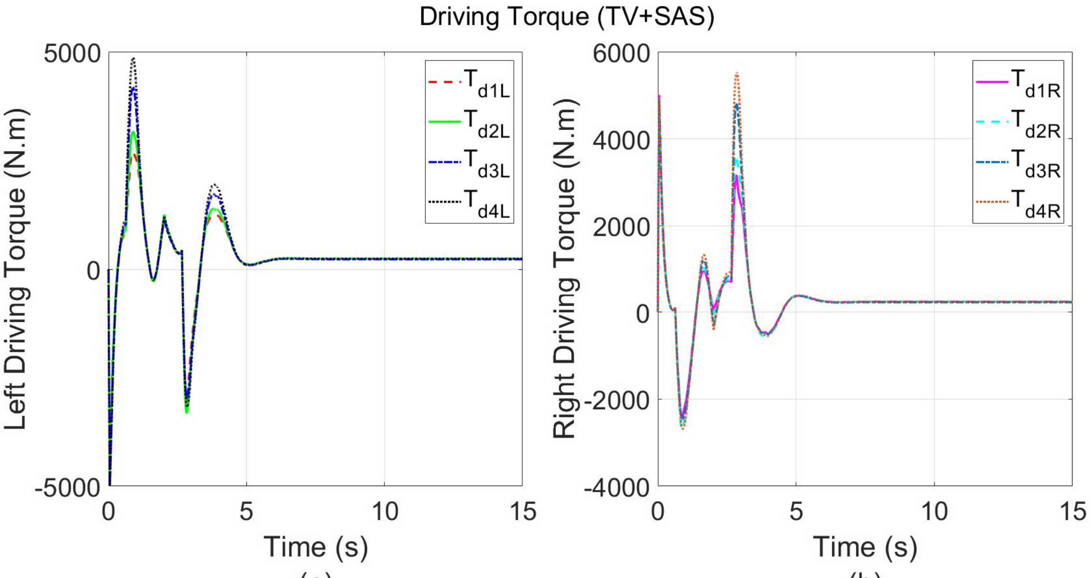

(a) (b)

Figure 6-54 (a) Left Wheels Driving Torque and (b) Right Wheels Driving Torque for TV+SAS during DLC at 100 Km/h ($\mu = 0.85$)

Figure 6-55 express the left and right sides' wheels braking torque in (a) and (b) for DB. The maximum achieved braking wheel torque in the left and right side is -17033.0 Nm for both, respectively.

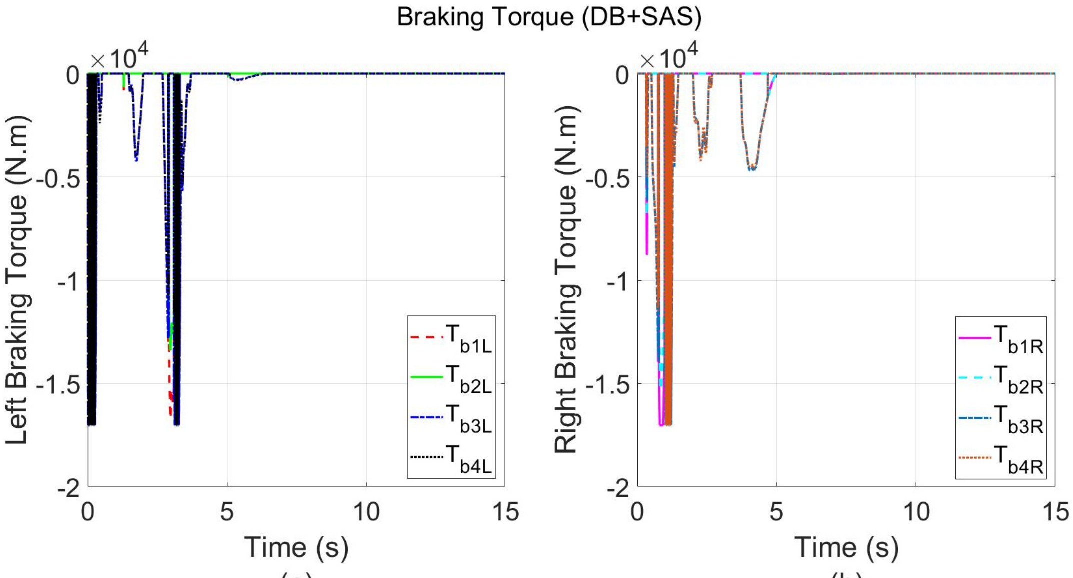

(a) (b)

Figure 6-55 (a) Left Wheels Braking Torque and (b) Right Wheels Braking Torque for TV+SAS during DLC at 100 Km/h ($\mu = 0.85$)

Figure 6-56,Figure 6-57, Figure 6-58 and Figure 6-59 depict the left and right sides' vehicle damper forces in (a) and (b) for vehicle with no control, AWS+SAS, TV+SAS and DB+SAS respectively. It is remarkable that all proposed control strategies have obtained largest dampers' forces varying with time compared to vehicle with no control. However, DB+SAS have induced the largest dampers' forces followed by AWS+SAS compared to TV+SAS.

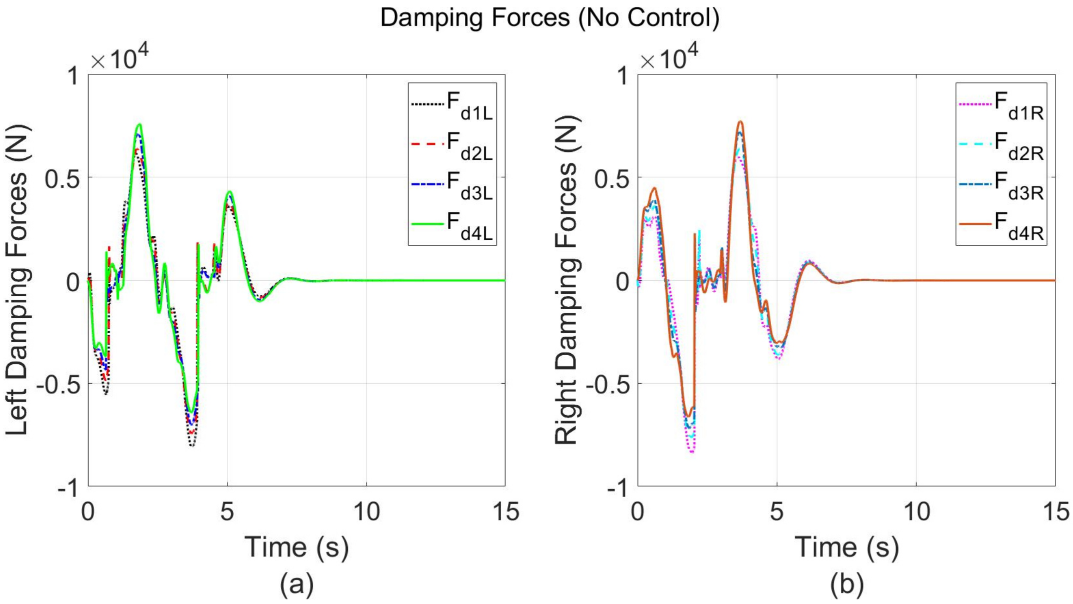

Figure 6-56 (a) Left Damping Forces and (b) Right Damping Forces for Vehicle (No Control) during DLC at 100 Km/h (μ = 0.85)

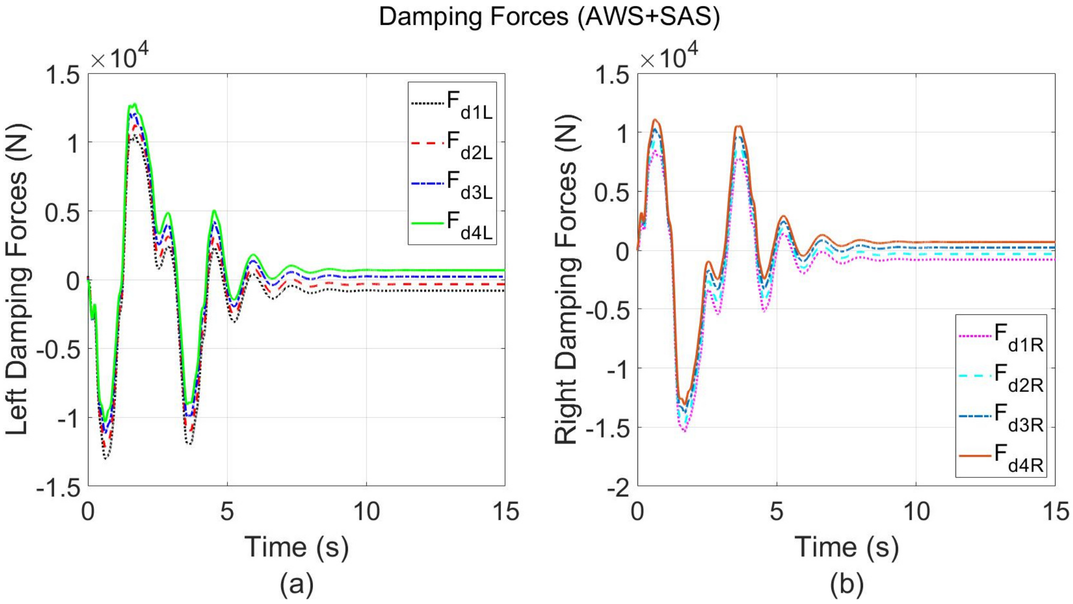

Figure 6-57 (a) Left Damping Forces and (b) Right Damping Forces for AWS+SAS during DLC at 100 Km/h (μ = 0.85)

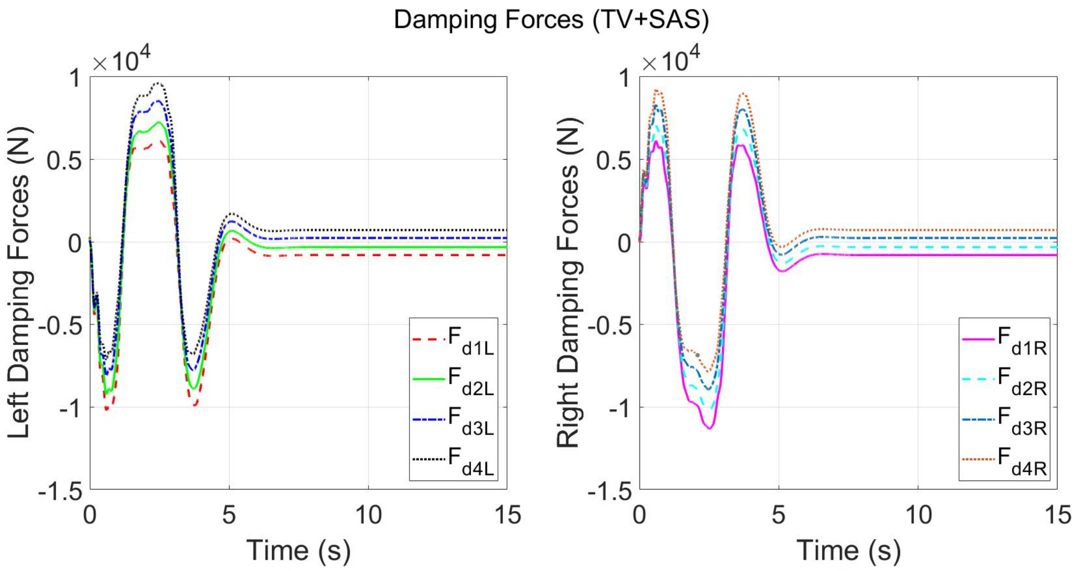

(a) (b)

Figure 6-58 (a) Left Damping Forces and (b) Right Damping Forces for TV+SAS during DLC at 100 Km/h ($\mu = 0.85$)

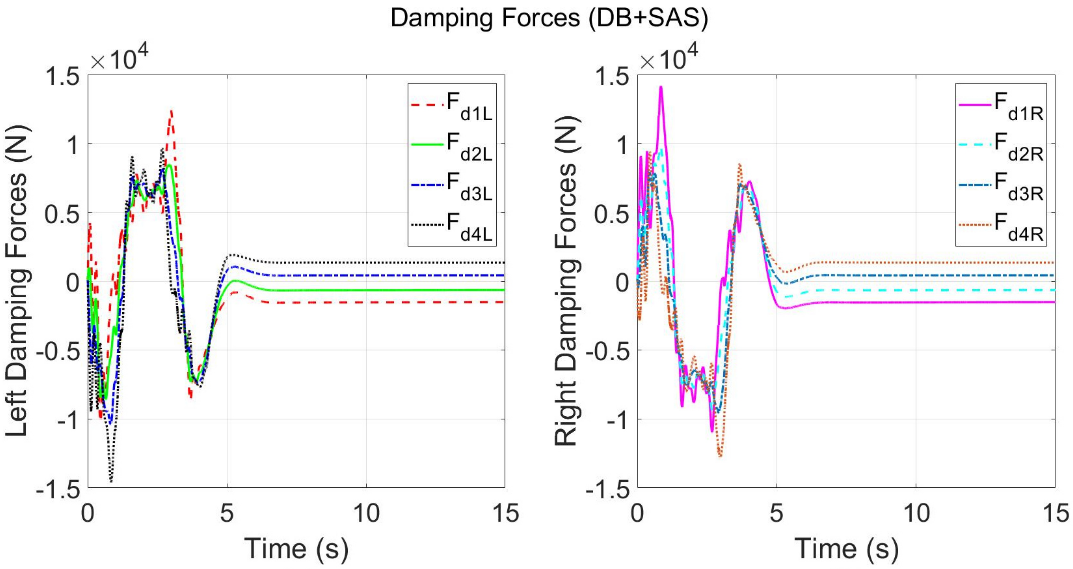

(a) (b)

Figure 6-59 (a) Left Damping Forces and (b) Right Damping Forces for DB+SAS during DLC at 100 Km/h ($\mu = 0.85$)

6.2.2.2 Results and Discussion of Evaluation Method at Low coefficient of friction – NATO Double Lane Change ($80\ \mathrm{km/h}\ ;\ \mu = 0.35$)

The vehicle trajectory and the corresponding error achieved by each control strategy AWS, TV, DB, and vehicle with no control are shown in Figure 6-60 in (a) and (b) respectively. Although all control strategies have maintained the trajectory without losing stability at low friction road surface, they obtained relatively the same error as shown in Table 6-7.

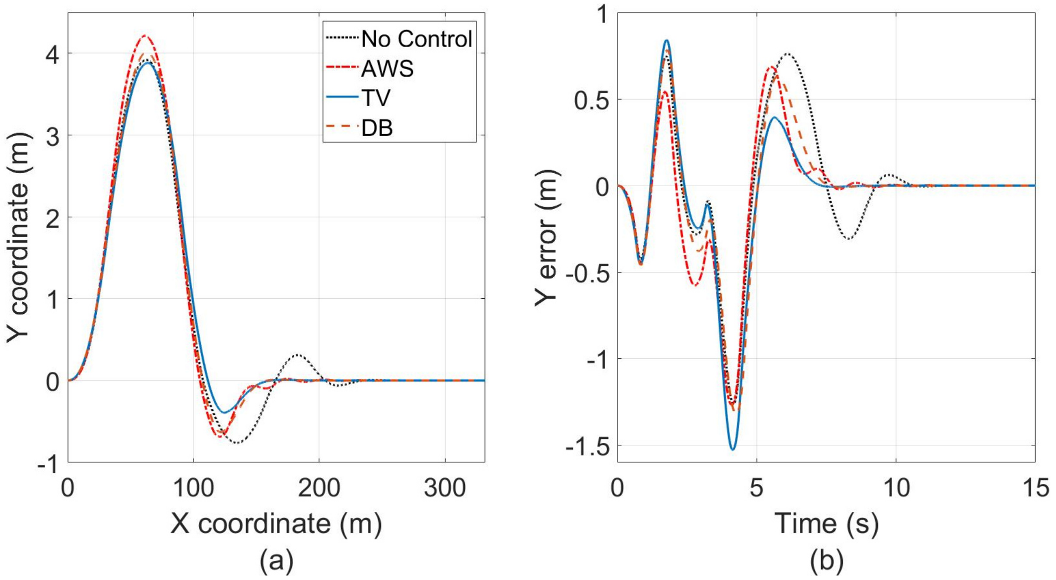

Figure 6-60 Vehicle trajectory during DLC at 80 Km/h ($\mu = 0.35$) and (b) Error obtained by vehicle (No Control), AWS, TV, and DB

Table 6-7 Trajectory Root Mean Square Errors Obtained by Uncontrolled Vehicle, AWS, TV, and DB during DLC at 80 Km/h ($\mu = 0.35$)

Controller's Configuration	RMSE (m)
No Control	0.3889
AWS	0.3613
TV	0.3879
DB	0.3773

Figure 6-61, Figure 6-62, Figure 6-63 and Figure 6-64 show the vehicle sideslip, yaw rate, longitudinal speed, and lateral acceleration respectively for AWS, TV, DB, and vehicle with no control. It should be observed that all proposed control strategies have tremendously minimized the sideslip angle compared to the vehicle with no control whose obtained maximum value -20.3 degrees. In addition, the yaw rate response amplitude was observed the largest for AWS compared to TV and DB. However, TV is the fastest in stabilizing the vehicle based on the settling time followed by DB compared to AWS. Moreover, the TV and AWS were approximately close to perform the desired speed while DB achieved the lowest speed which is 72.6 Km/h. for lateral acceleration, AWS has attained the largest value compared to TV and DB which is 0.32 g's. it should be noted that TV and DB showed a superiority in stabilizing the vehicle faster than AWS.

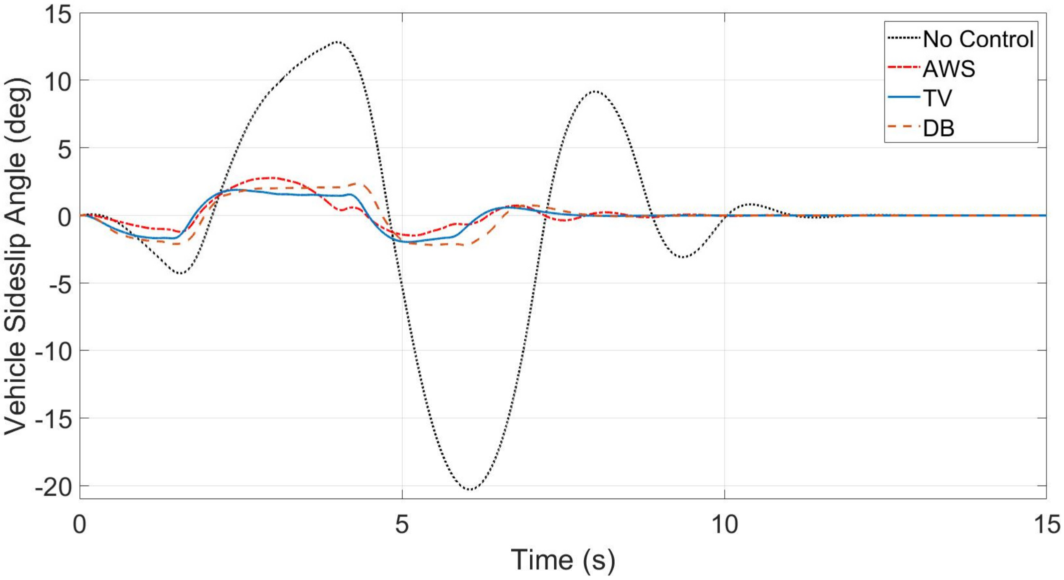

Figure 6-61 Vehicle Sideslip Angle during DLC at 80 Km/h ($\mu = 0.35$)

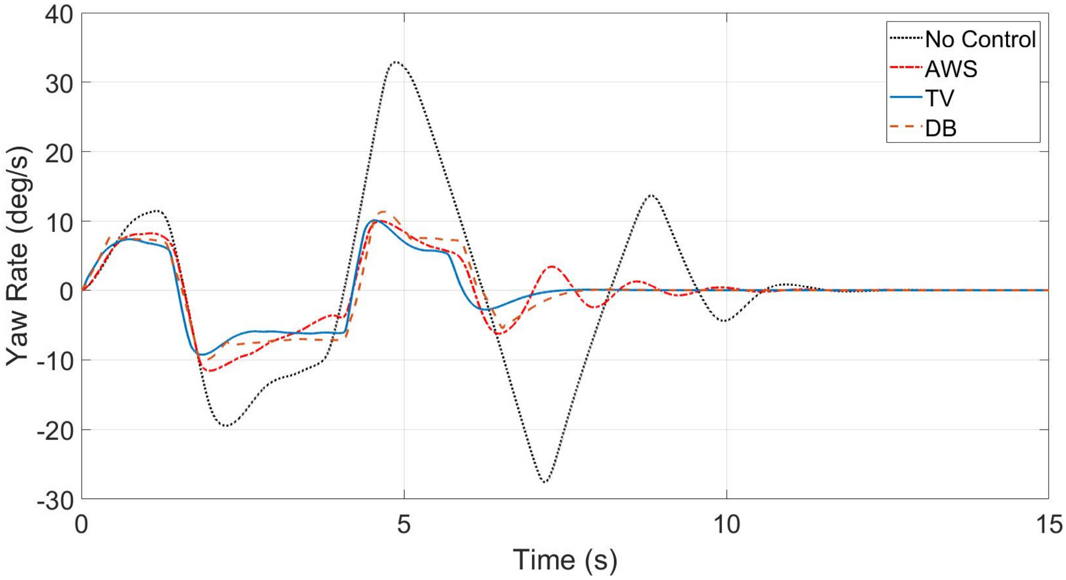

Figure 6-62 Yaw Rate during DLC at 80 Km/h (μ = 0.35)

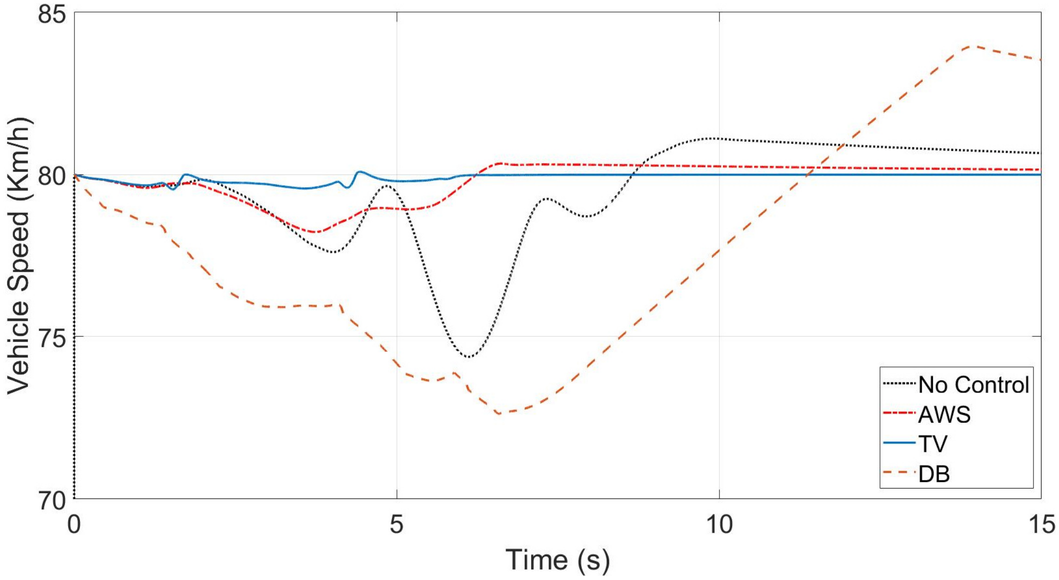

Figure 6-63 Vehicle Speed during DLC at 80 Km/h (μ = 0.35)

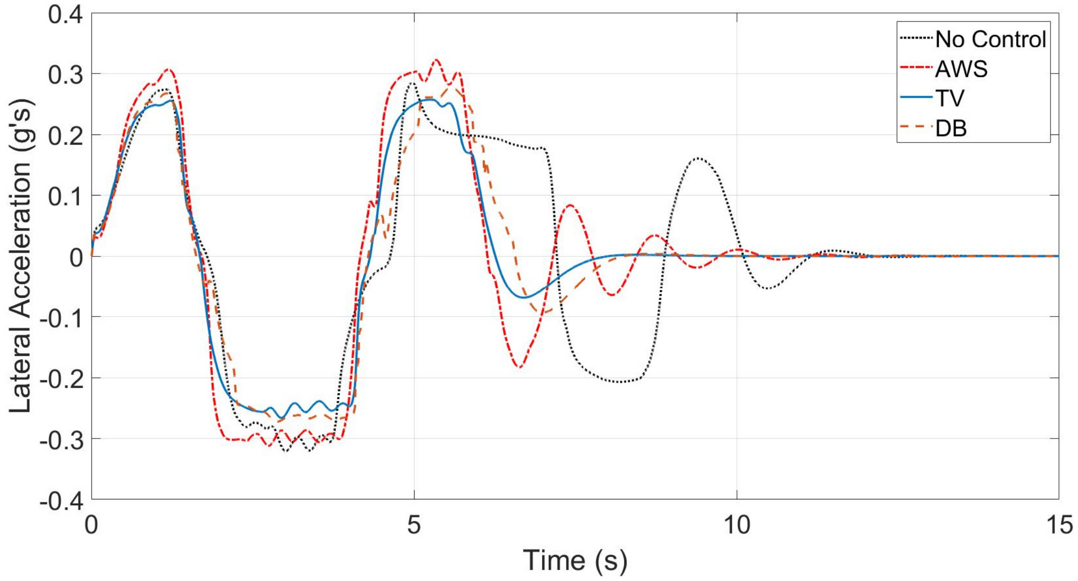

Figure 6-64 Lateral Acceleration during DLC at 80 Km/h (μ = 0.35)

Figure 6-65 and Figure 6-66 demonstrate the front and rear road steer angles in (a) and (b) for vehicle with no control and AWS, respectively. A maximum front steering angle of -23 degrees and -9.3 degrees for rear steering angle are observed for AWS, while -23.7 degrees for vehicle with no control. It should be noted that the rear steer angles for AWS are performing parallel steering (steering in the same direction as the front steering angles).

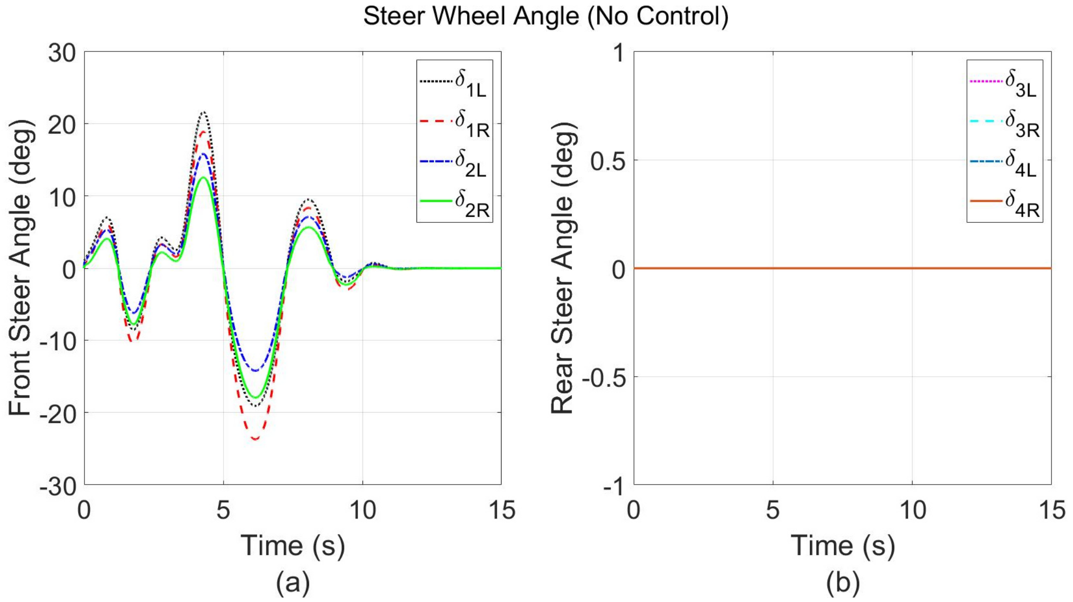

Figure 6-65 (a) Front Steer Angle and (b) Rear Steer Angle for Vehicle (No Control) during DLC at 80 Km/h (μ = 0.35)

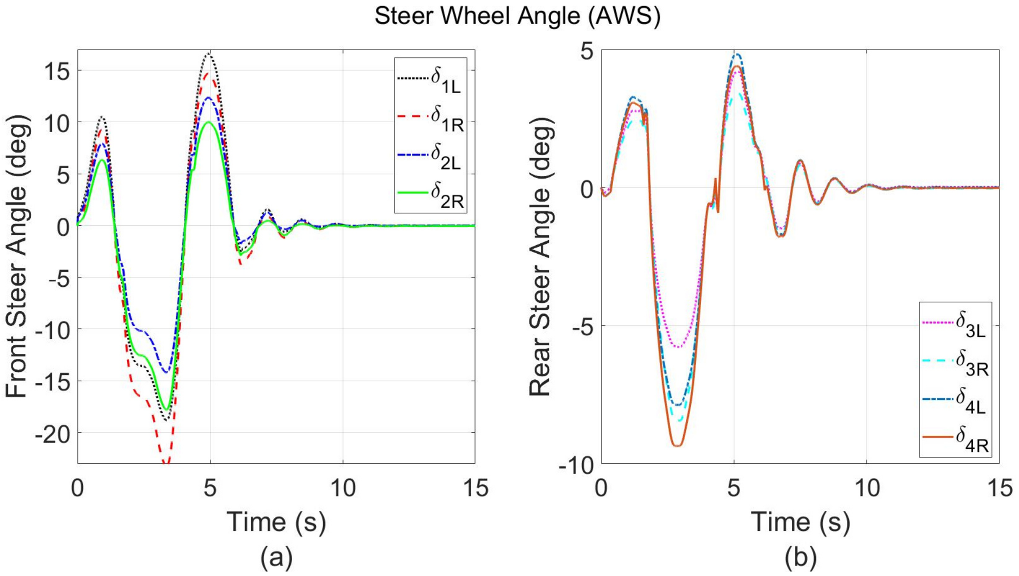

Figure 6-66 (a) Front Steer Angle and (b) Rear Steer Angle for AWS during DLC at 80 Km/h (μ = 0.35)

Figure 6-67 and Figure 6-68 illustrate the left and right sides' vehicle wheels driving torque in (a) and (b) for vehicle with no control and TV, respectively. The maximum achieved driving wheel torque in the left and right side for TV is 5304.5 Nm and 5353.0 Nm, respectively. While 686.0 Nm in both sides for vehicle with no control.

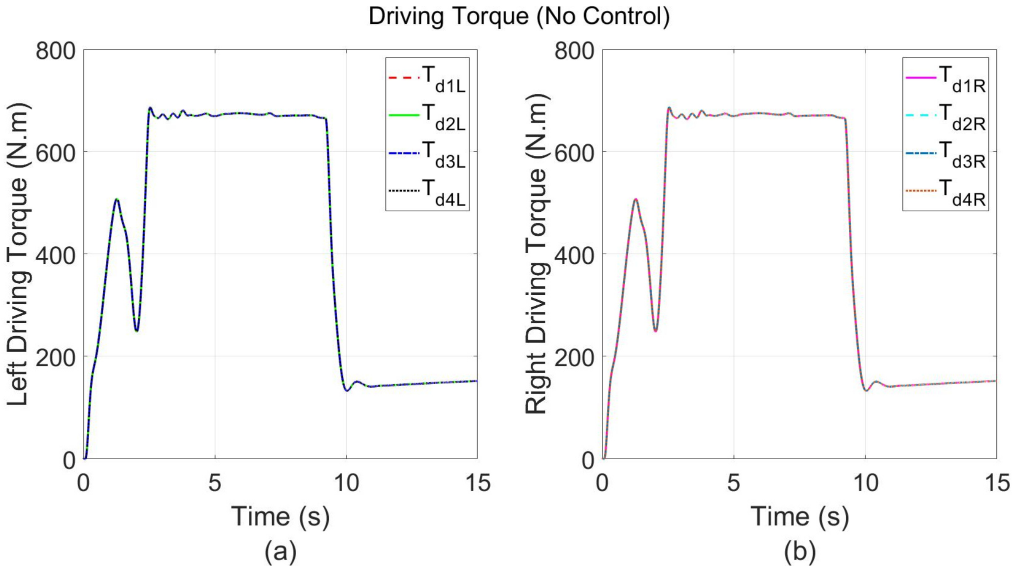

Figure 6-67 (a) Left Wheels Driving Torque and (b) Right Wheels Driving Torque for Vehicle (No Control) during DLC at 80 Km/h (μ = 0.35)

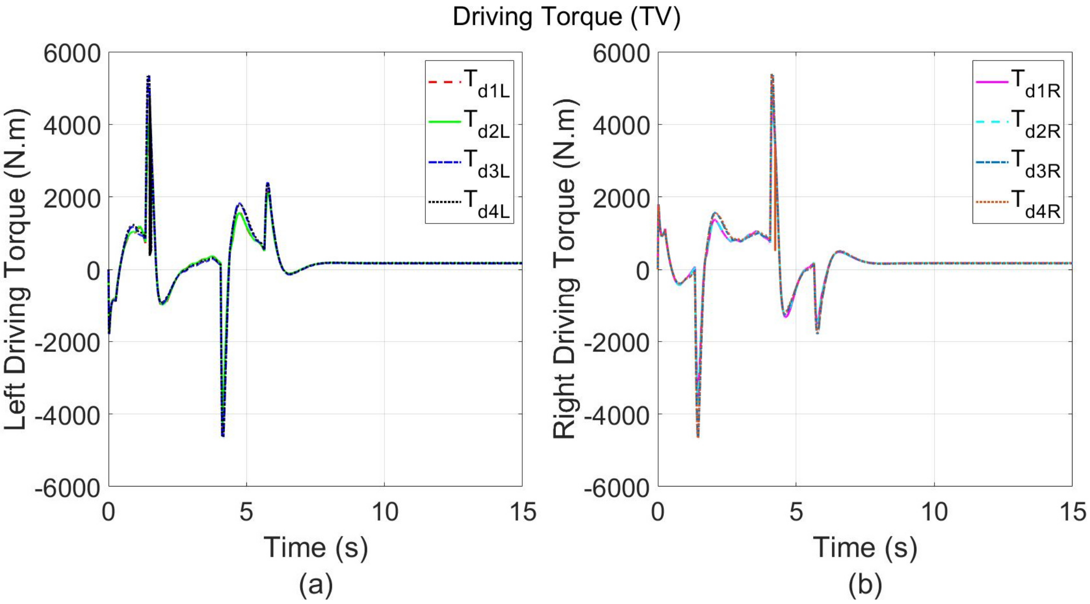

Figure 6-68 (a) Left Wheels Driving Torque and (b) Right Wheels Driving Torque for TV during DLC at 80 Km/h (μ = 0.35)

Figure 6-69 shows the left and right sides' wheels braking torque in (a) and (b) for DB. The maximum attained braking wheel torque in the left and right side is -17033.0 Nm for both, respectively.

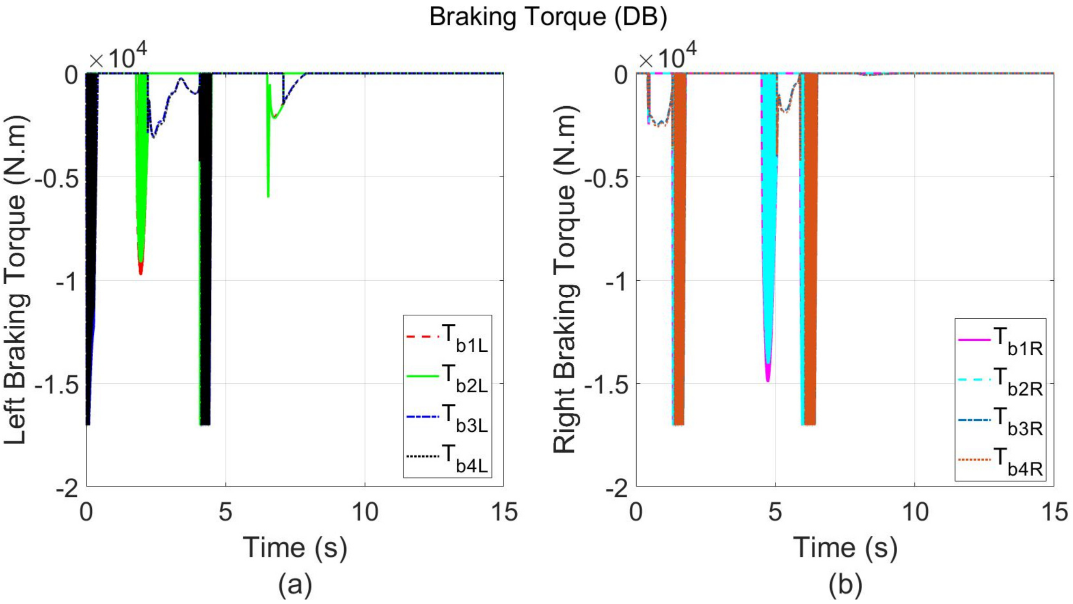

Figure 6-69 (a) Left Wheels Braking Torque and (b) Right Wheels Braking Torque for DB during DLC at 80 Km/h (μ = 0.35)

6.2.3 Federal Motors Vehicle Safety Standard (FMVSS 126 ESC)

The Federal Motors Vehicle Safety Standard (FMVSS 126 ESC) is considered as an open-loop test course, where no target path to be follow. This test is also known as Sine with Dwell maneuver, where it is constructed on a modified 0.7 Hz sinusoidal steering input to evaluate the ESC oversteer intervention performance [124]. The steering wheel input is function of time with a peak value of 234 degrees as shown in Figure 6-70.

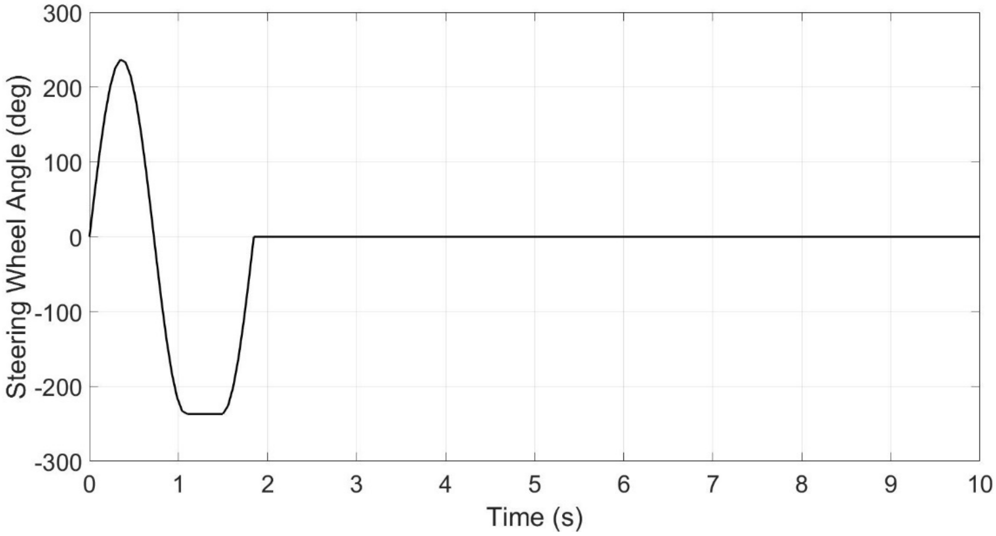

Figure 6-70 Steering Wheel Angle Input For FMVSS 126 ESC Test Course

6.2.3.1 Results and Discussion of Evaluation Method at high coefficient of friction – FMVSS 126 ESC ($100\ \mathrm{km/h}\ ;\ \mu = 0.85$)

The vehicle trajectory performed by each control strategy AWS+SAS, TV+SAS, DB+SAS, and vehicle with no control are shown in Figure 6-71. It can be noticed that TV+SAS has achieved the smallest lateral displacement followed by DB+SAS then AWS+SAS, while vehicle with no control attained the largest value.

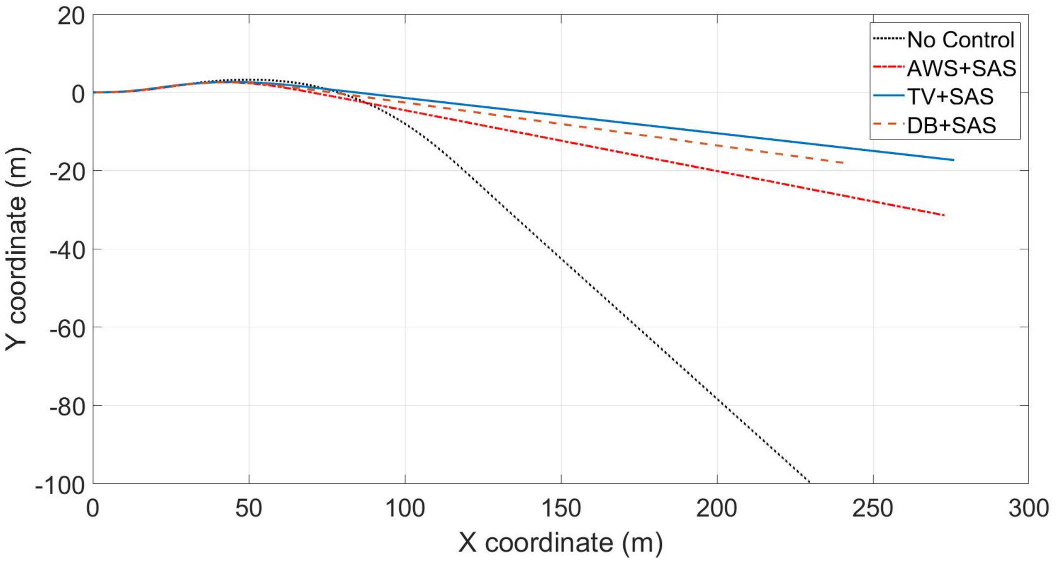

Figure 6-71 Vehicle trajectory during FMVSS 126 ESC at 100 Km/h ($\mu = 0.85$)

Figure 6-72, Figure 6-73, Figure 6-74 and Figure 6-75 depict the vehicle sideslip, yaw rate, longitudinal speed and lateral acceleration respectively for vehicle with no control, AWS+SAS, TV+SAS and DB+SAS. It can be observed that the proposed control strategies have significantly minimized the sideslip angle compared to the vehicle with no control. TV+SAS has attained the largest yaw rate response amplitude among the proposed control strategies, as well as TV+SAS and DB+SAS stabilized the vehicle faster than AWS+SAS. The vehicle with no control took 6.1 seconds to stabilize while 2.7 seconds for TV+SAS and DB+SAS and 3.1 seconds for AWS+SAS. Furthermore, TV+SAS has achieved less drop in longitudinal speed among all other control strategies and vehicle with no control, makes it close to maintain the desired speed. Moreover, the largest lateral acceleration peak amplitude was attained by AWS+SAS among all the control strategies. Also, it should be noted that TV+SAS and DB+SAS have stabilized the vehicle faster than AWS+SAS in all the mentioned plots.

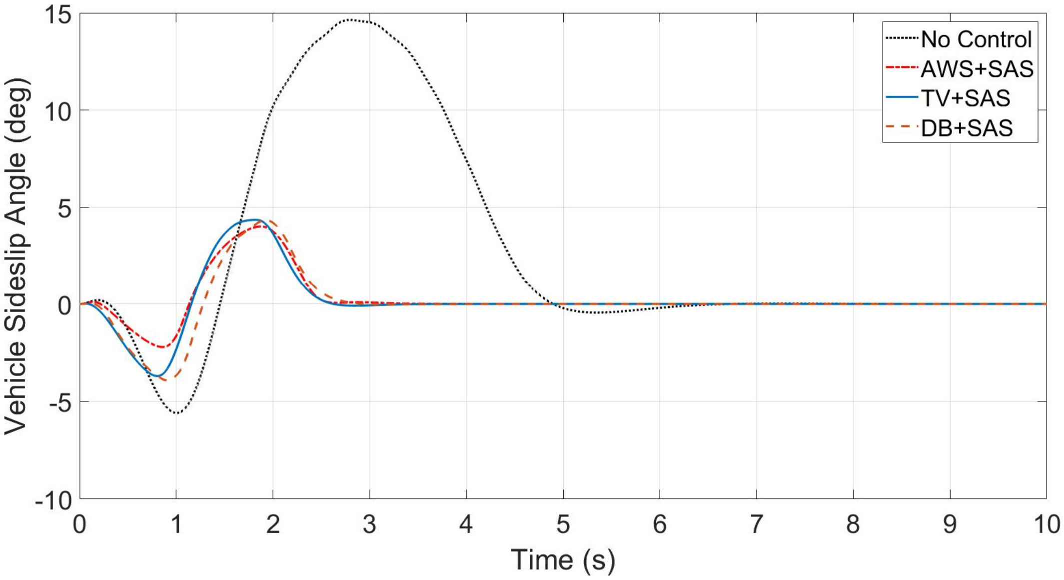

Figure 6-72 Vehicle Sideslip Angle during FMVSS 126 ESC at 100 Km/h (μ = 0.85)

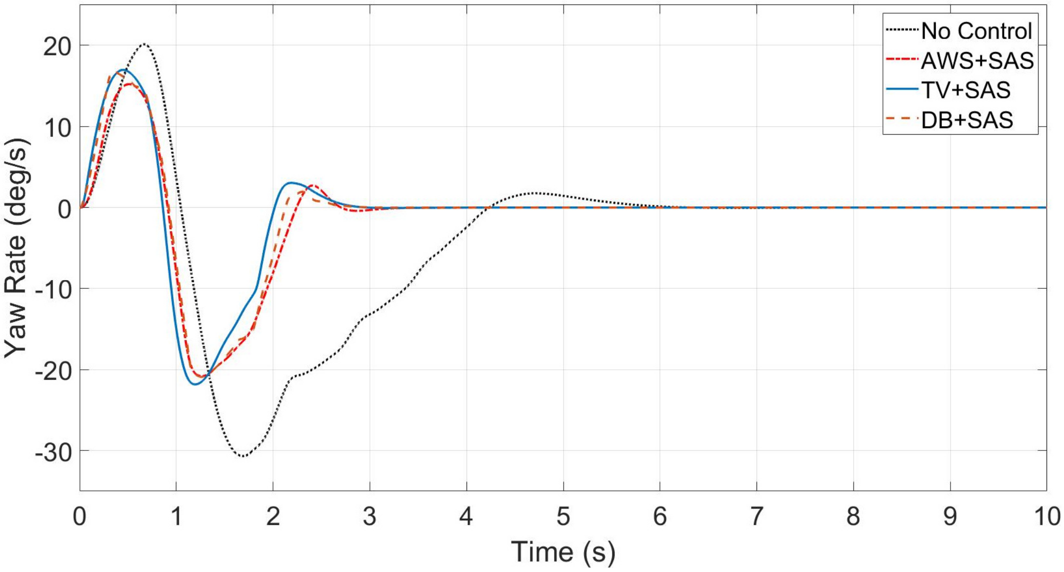

Figure 6-73 Yaw Rate during FMVSS 126 ESC at 100 Km/h (μ = 0.85)

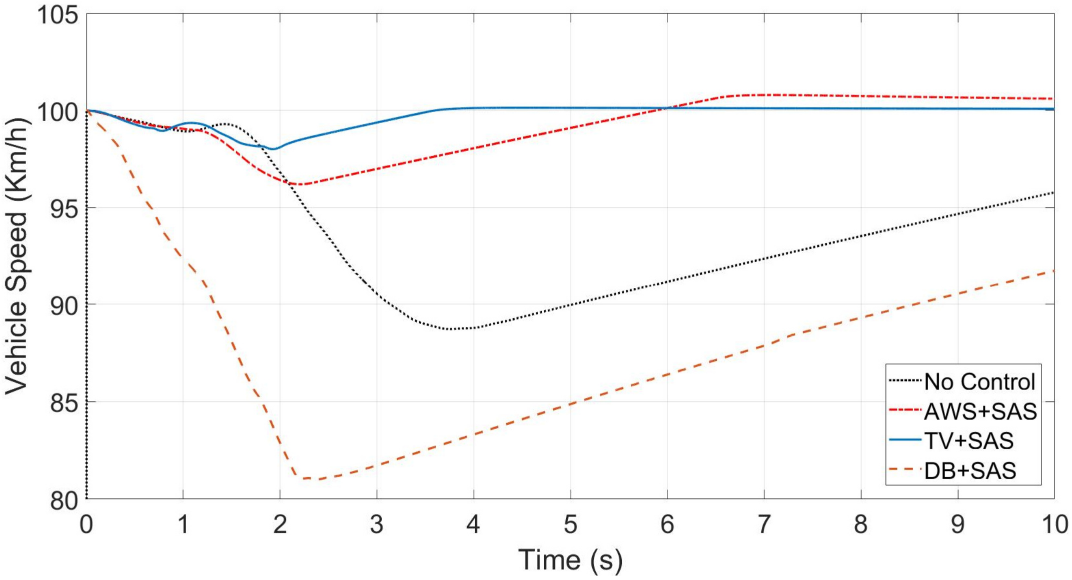

Figure 6-74 Vehicle Speed during FMVSS 126 ESC at 100 Km/h (μ = 0.85)

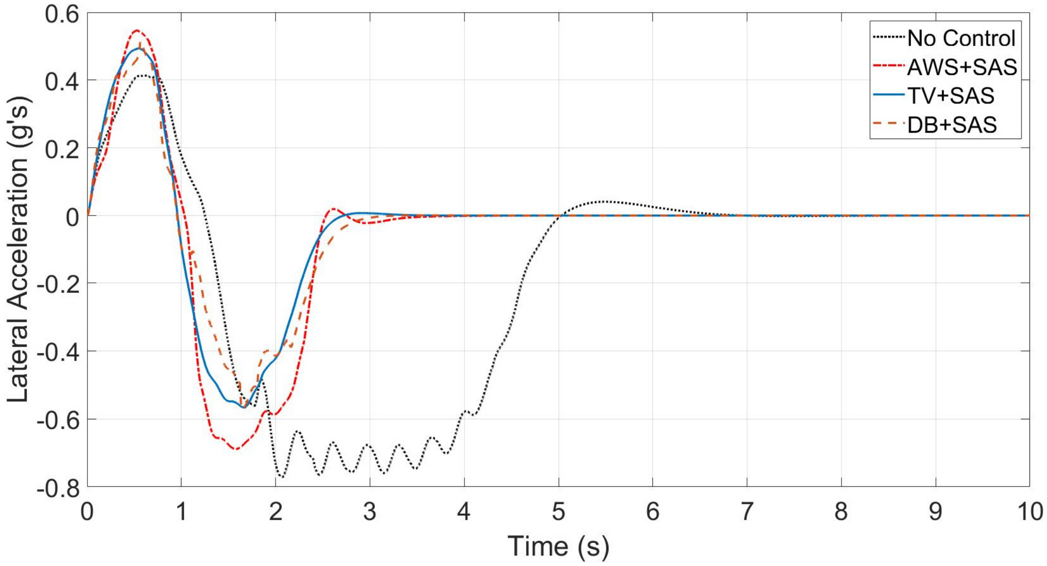

Figure 6-75 Lateral Acceleration during FMVSS 126 ESC at 100 Km/h (μ = 0.85)

Figure 6-76, Figure 6-77 and Figure 6-78 present the vehicle's sprung mass displacement, pitch, and roll angle, respectively. It is notable that AWS+SAS, TV+SAS and DB+SAS have significantly minimized the vertical displacement at the CG of the sprung mass compared to vehicle with no control. Furthermore, all the proposed control strategies have substantially reduced the pitch and roll angle due to longitudinal and lateral load transfer compared to vehicle with no control. However, DB+SAS has slightly obtained largest value for pitch angle, while AWS+SAS has slightly attained largest value for roll angle compared to TV+SAS.

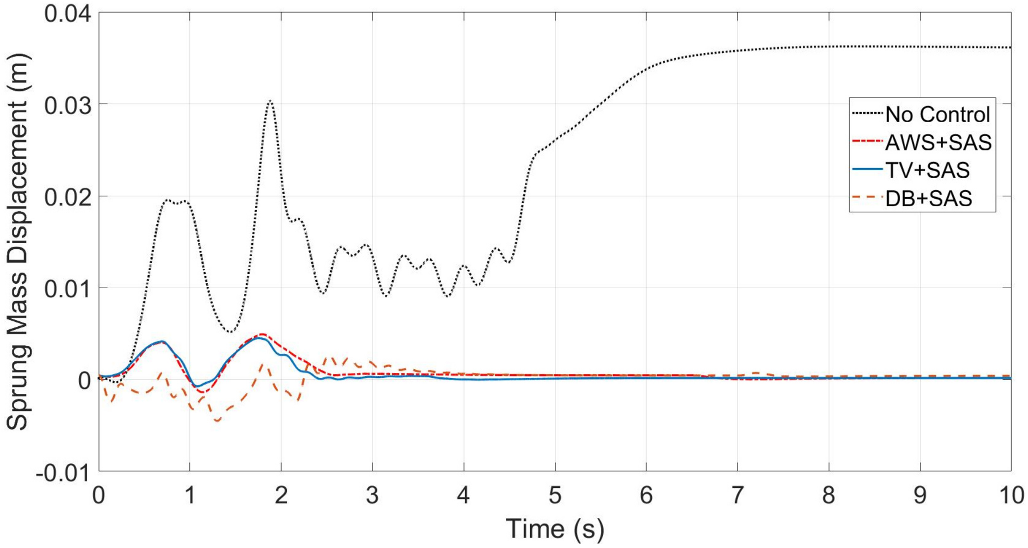

Figure 6-76 Sprung Mass Displacement during FMVSS 126 ESC at 100 Km/h (μ = 0.85)

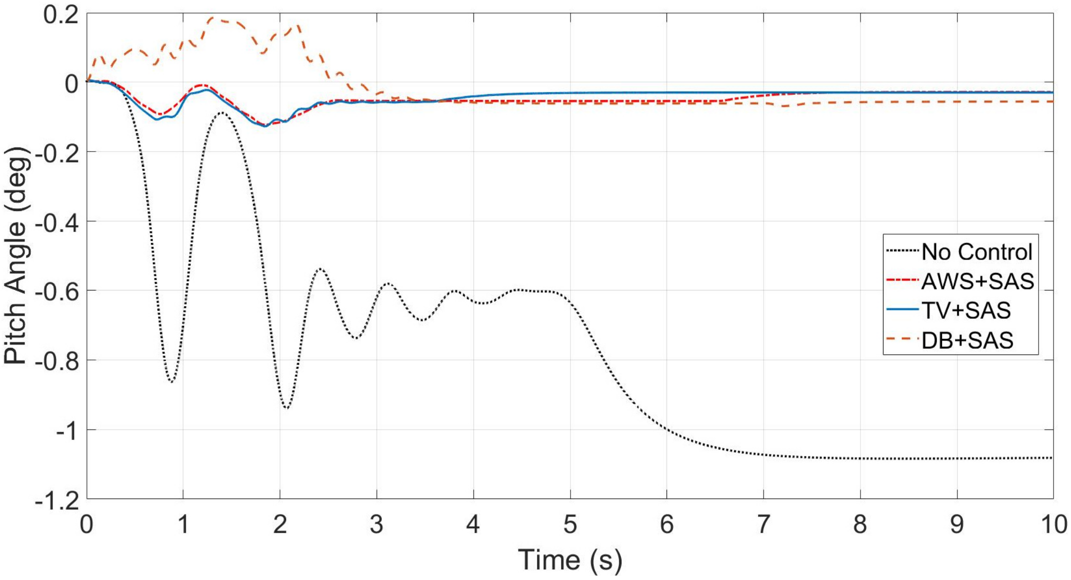

Figure 6-77 Pitch Angle during FMVSS 126 ESC at 100 Km/h (μ = 0.85)

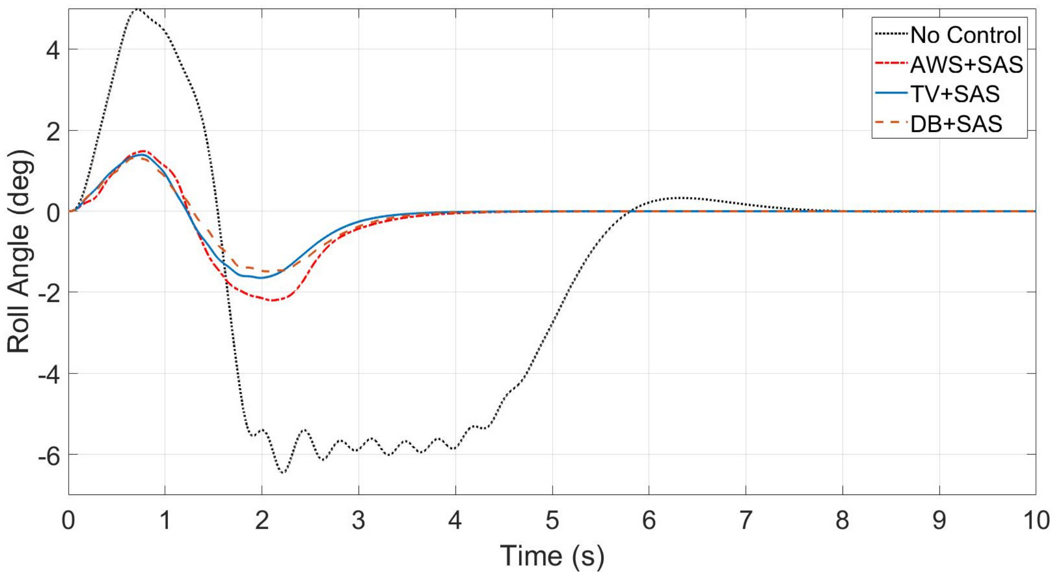

Figure 6-78 Roll Angle during FMVSS 126 ESC at 100 Km/h (μ = 0.85)

Figure 6-79 and Figure 6-80 show the front and rear road steer angles in (a) and (b) for vehicle with no control and AWS+SAS, respectively. The front steering angles are observed taking 2.4 seconds to be dampened for AWS+SAS, while the maximum achieved rear steering angle is 13.6 degrees. It should be noted that the rear steer angles for AWS+SAS are performing parallel steering (steering in the same direction as the front steering angles).

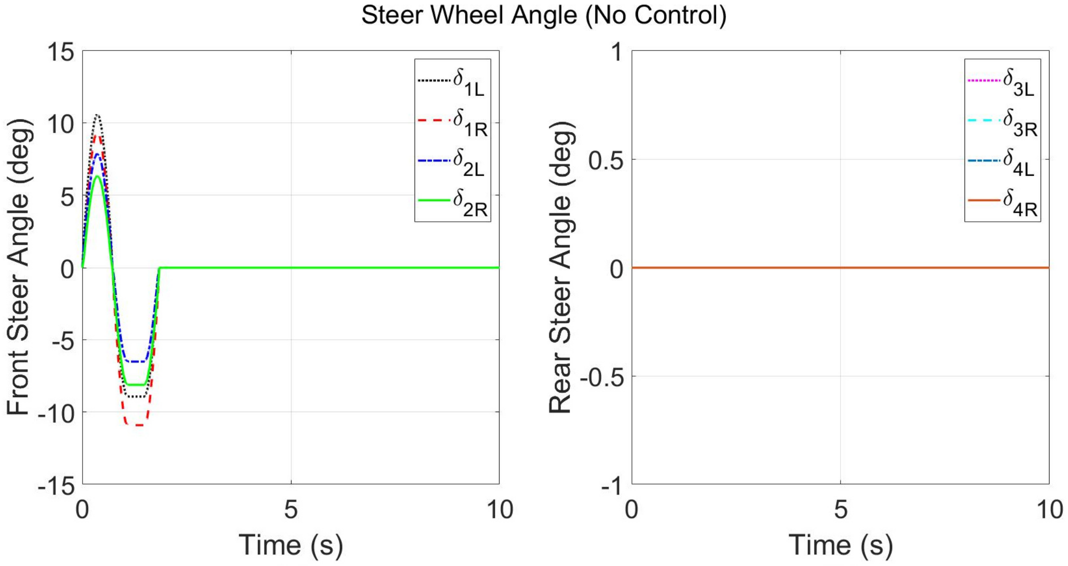

(a) (b)

Figure 6-79 (a) Front Steer Angle and (b) Rear Steer Angle for Vehicle (No Control) during FMVSS 126 ESC at 100 Km/h (μ = 0.85)

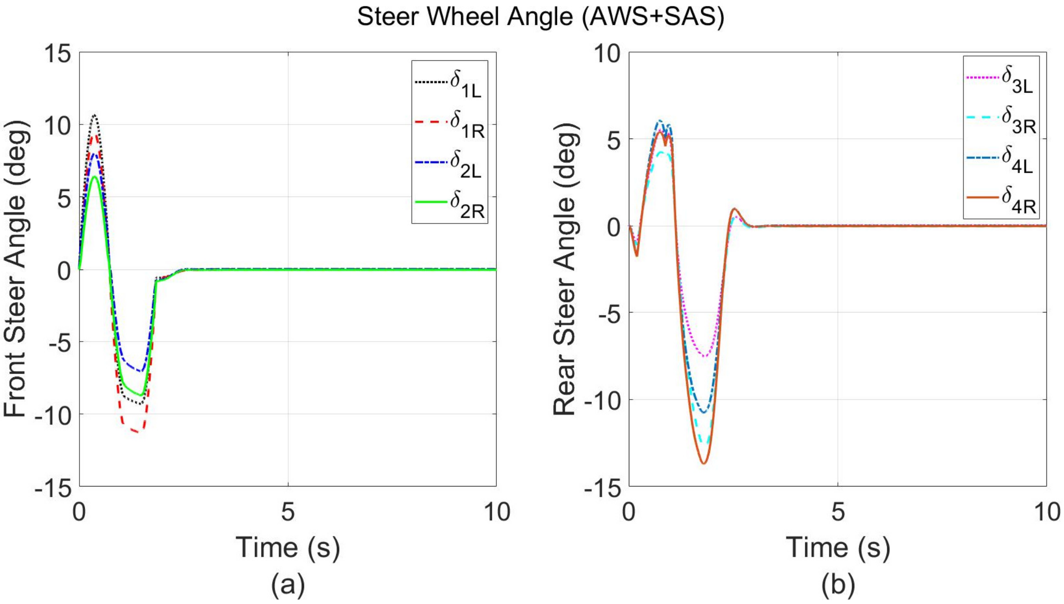

Figure 6-80 (a) Front Steer Angle and (b) Rear Steer Angle for AWS+SAS during FMVSS 126 ESC at 100 Km/h (μ = 0.85)

Figure 6-81 and Figure 6-82 express the left and right sides' vehicle wheels driving torque in (a) and (b) for vehicle with no control and TV+SAS, respectively. The maximum achieved driving wheel torque in the left and right side for TV+SAS is 5546.0 Nm and 5556.3 Nm, respectively. While 644.5 Nm in both sides for vehicle with no control.

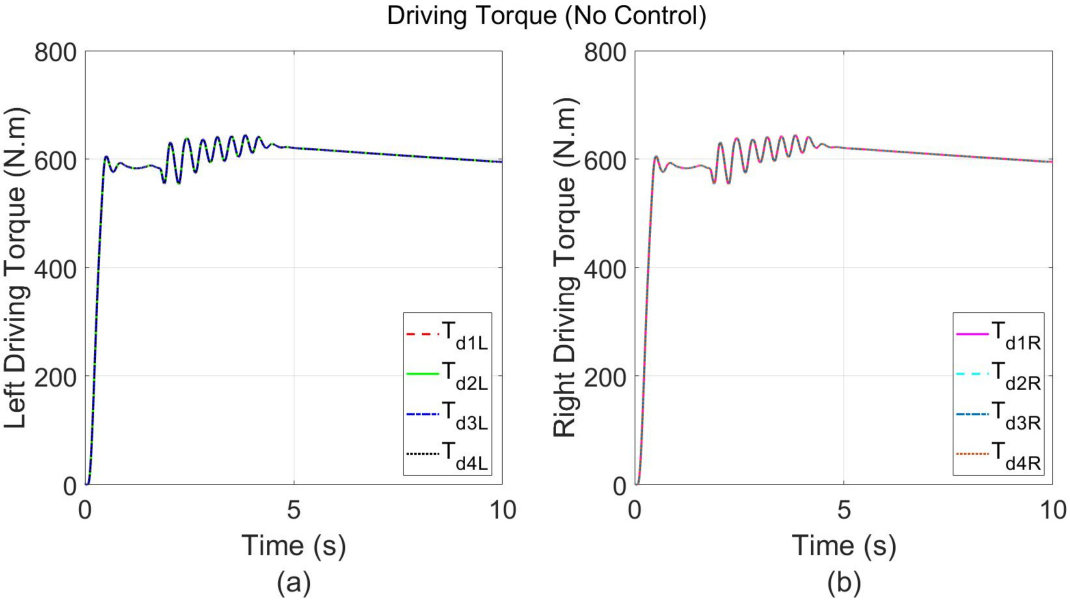

Figure 6-81 (a) Left Wheels Driving Torque and (b) Right Wheels Driving Torque for Vehicle (No Control) during FMVSS 126 ESC at 100 Km/h (μ = 0.85)

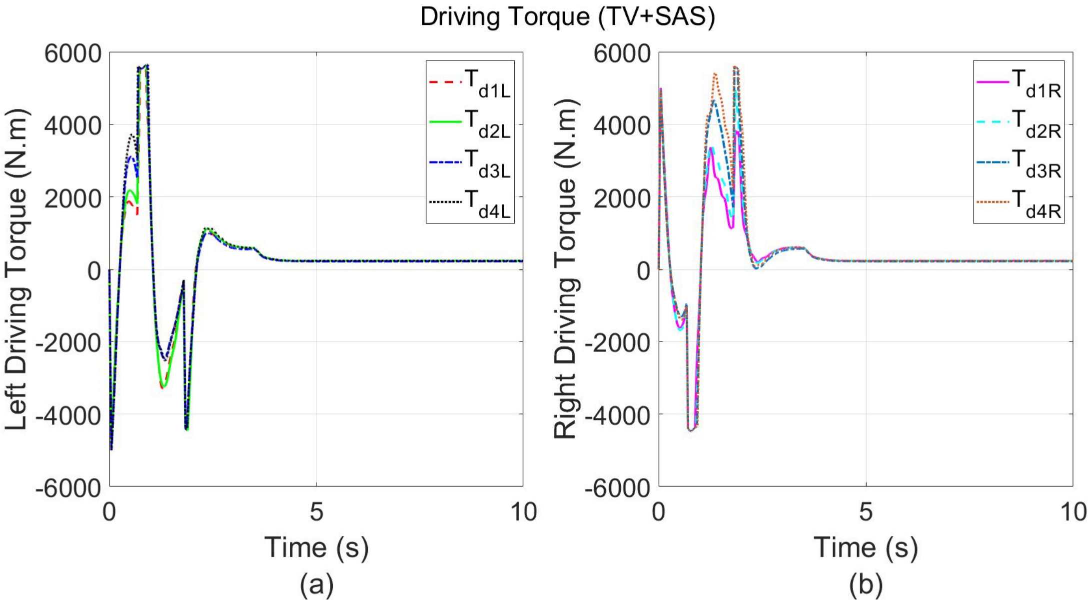

Figure 6-82 (a) Left Wheels Driving Torque and (b) Right Wheels Driving Torque for TV+SAS during FMVSS 126 ESC at 100 Km/h (μ = 0.85)

Figure 6-83 shows the left and right sides' wheels braking torque in (a) and (b) for DB+SAS. The maximum achieved braking wheels torque in the left and right side is -17033.0 Nm for both, respectively.

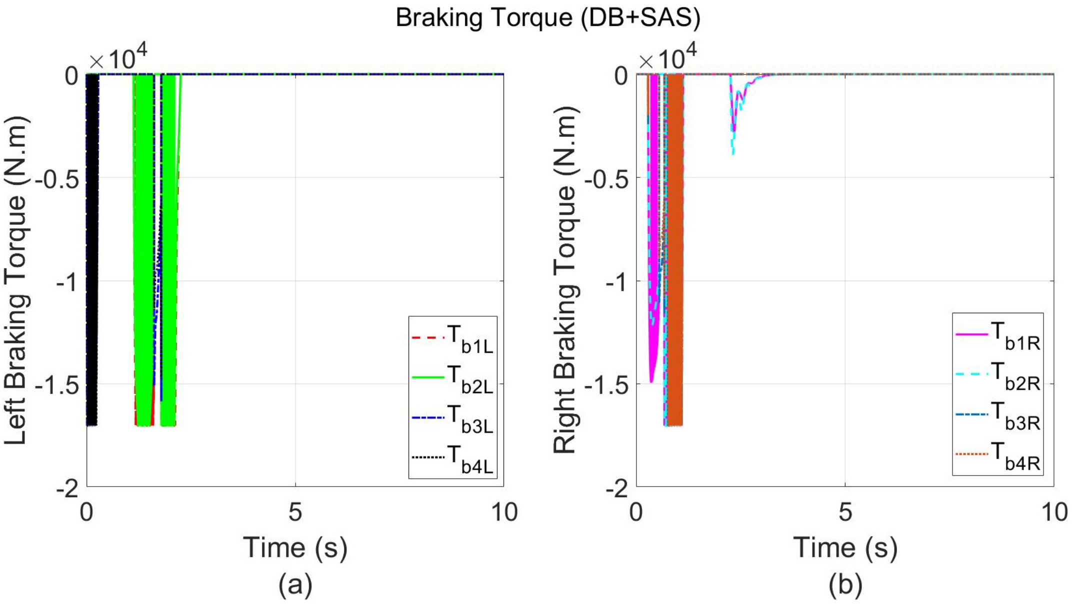

Figure 6-83 (a) Left Wheels Braking Torque and (b) Right Wheels Braking Torque for DB+SAS during FMVSS 126 ESC at 100 Km/h (μ = 0.85)

Figure 6-84, Figure 6-85, Figure 6-86 and Figure 6-87 show the left and right sides' vehicle damper forces in (a) and (b) for vehicle with no control, AWS+SAS, TV+SAS and DB+SAS respectively. It is remarkable that all proposed control strategies have obtained largest dampers' forces varying with time compared to vehicle with no control. However, DB+SAS have induced the largest dampers' forces followed by AWS+SAS compared to TV+SAS.

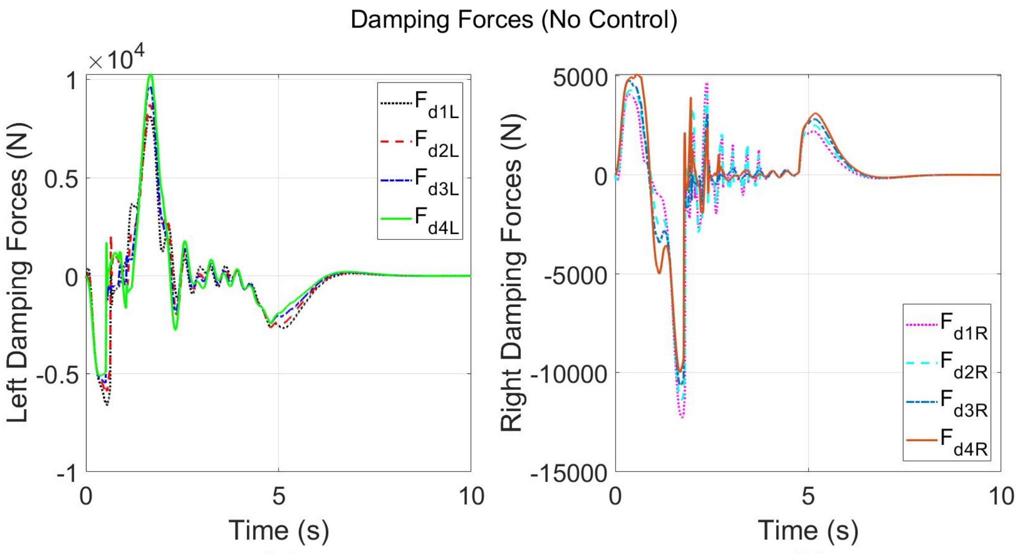

(a) (b)

Figure 6-84 (a) Left Damping Forces and (b) Right Damping Forces for Vehicle (No Control) during FMVSS 126 ESC at 100 Km/h ($\mu = 0.85$)

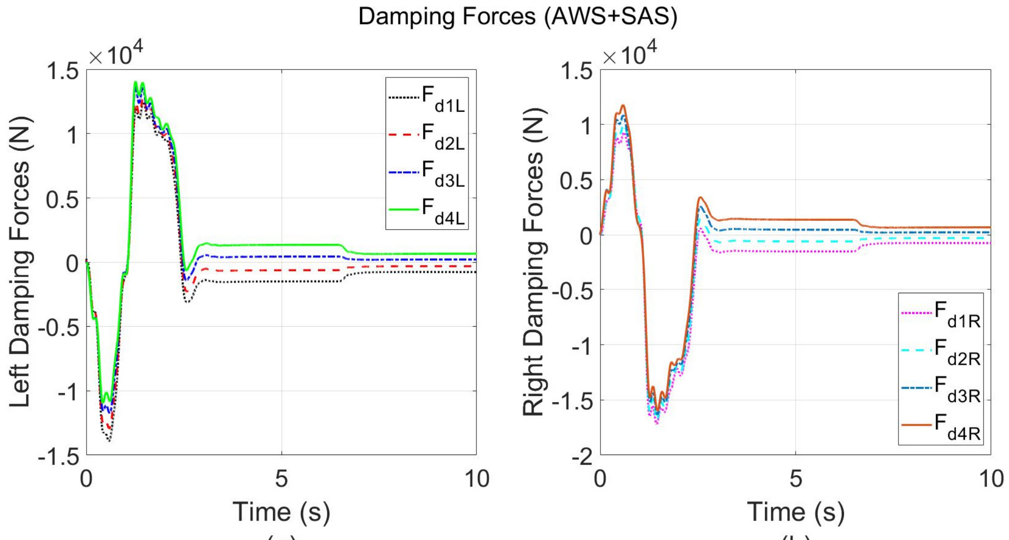

(a) (b)

Figure 6-85 (a) Left Damping Forces and (b) Right Damping Forces for AWS+SAS during FMVSS 126 ESC at 100 Km/h ($\mu = 0.85$)

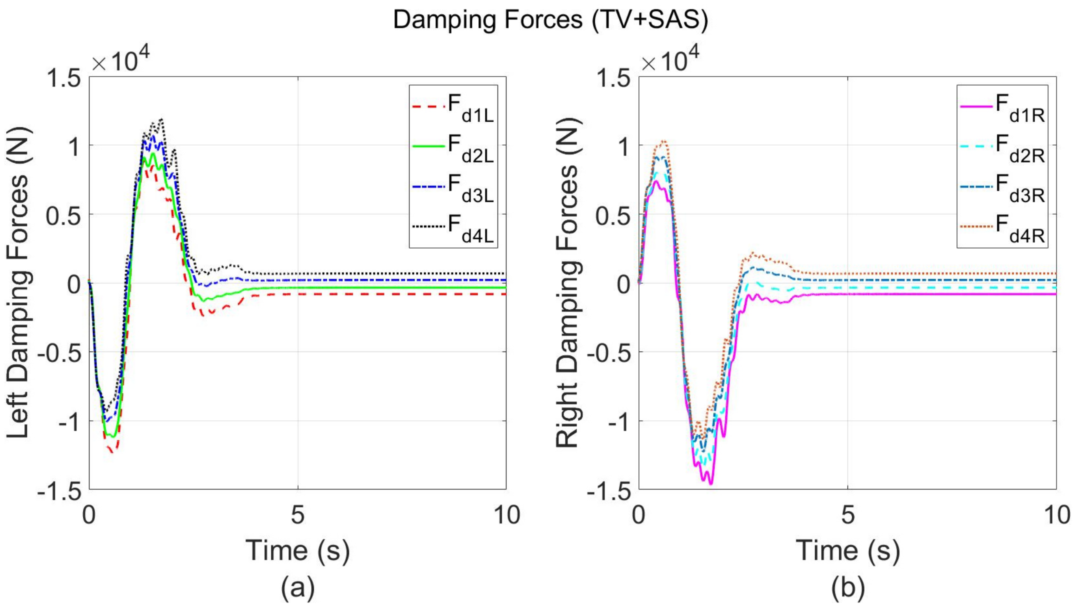

Figure 6-86 (a) Left Damping Forces and (b) Right Damping Forces for TV+SAS during FMVSS 126 ESC at 100 Km/h ($\mu = 0.85$)

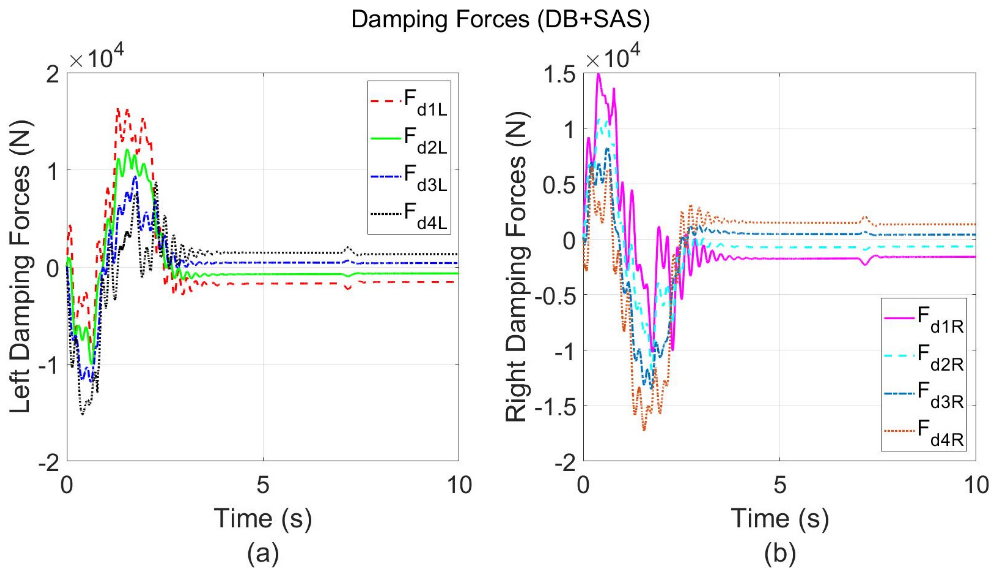

Figure 6-87 (a) Left Damping Forces and (b) Right Damping Forces for DB+SAS during FMVSS 126 ESC at 100 Km/h ($\mu = 0.85$)

6.2.3.2 Results and Discussion of Evaluation Method at Low coefficient of friction – FMVSS 126 ESC ($80\ \text{km/h}\ ;\ \mu = 0.35$)

The vehicle trajectory performed by each control strategy AWS, TV, DB, and vehicle with no control are shown in Figure 6-88. It can be remarked that TV and DB have achieved the smallest lateral displacement compared to AWS, while the vehicle with no control attained the largest value.

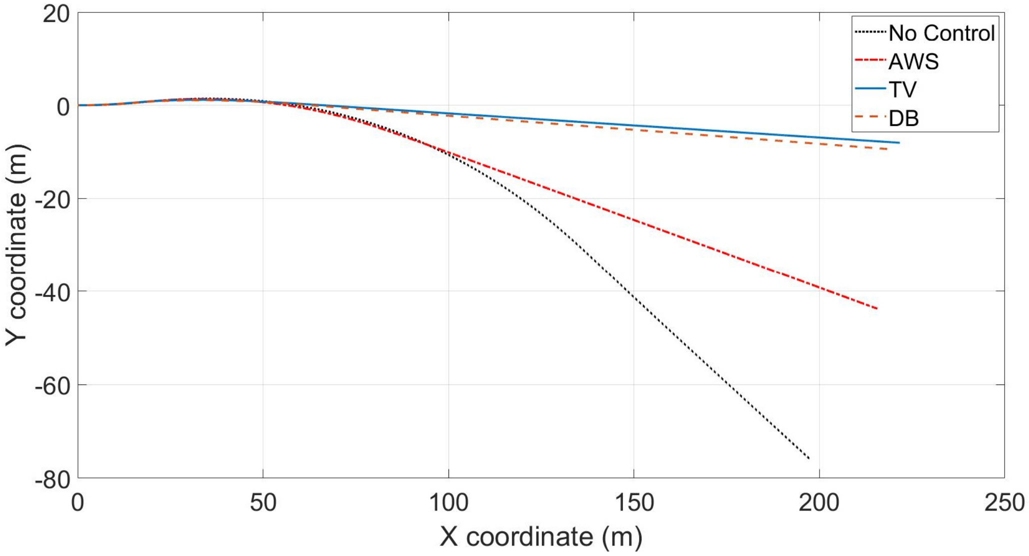

Figure 6-88 Vehicle trajectory during FMVSS 126 ESC at 80 Km/h ($\mu = 0.35$)

Figure 6-89, Figure 6-90, Figure 6-91 and Figure 6-92 illustrate the vehicle sideslip, yaw rate, longitudinal speed, and lateral acceleration respectively for AWS, TV, DB, and vehicle with no control. Its notable that TV and DB have significantly minimized the sideslip angle to the smallest possible value at very low friction road surface compared to AWS and vehicle with no control. The maximum attained sideslip angle for TV was 2 degrees, 2.4 degrees for DB and 4.2 degrees for AWS, while vehicle with no control obtained 15 degrees. Accordingly, TV has showed supremacy over the other control strategies in enhancing the vehicle's stability and stabilizing the vehicle faster at very low friction road surface. The vehicle's yaw rate is observed to be stabilized at 2.6 seconds by TV and DB and 4.8 seconds by AWS, while 8.1 seconds by vehicle with no control, respectively. Furthermore, TV has performed the least drop in longitudinal speed compared to the other control strategies followed by AWS. Moreover, TV and DB have attained the smallest peak value for lateral acceleration compared to AWS and vehicle with no control.

However, it should be noted that TV has stabilized the vehicle faster than the other control strategies based on the settling time.

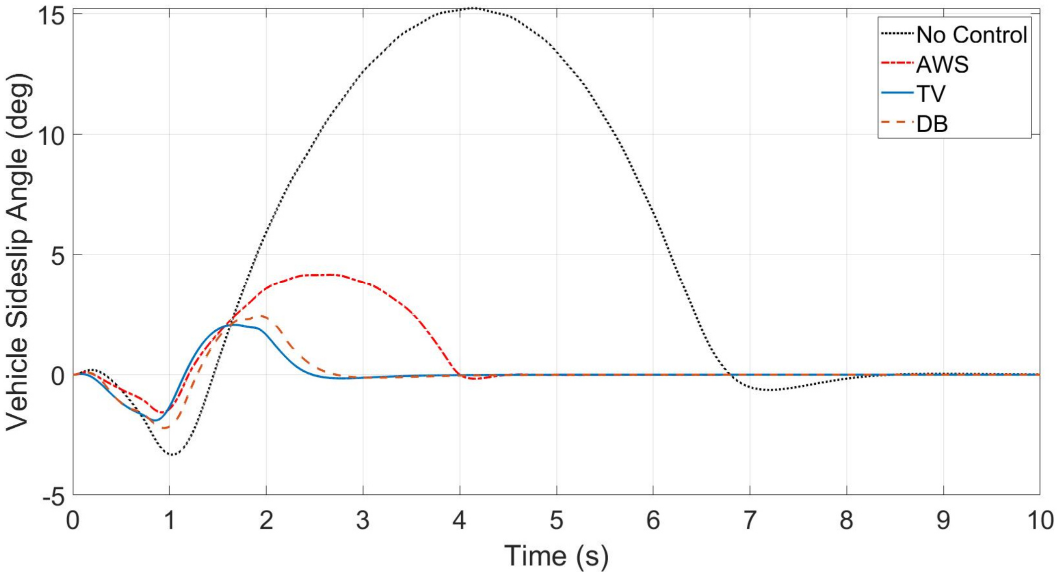

Figure 6-89 Vehicle Sideslip Angle during FMVSS 126 ESC at 80 Km/h (μ = 0.35)

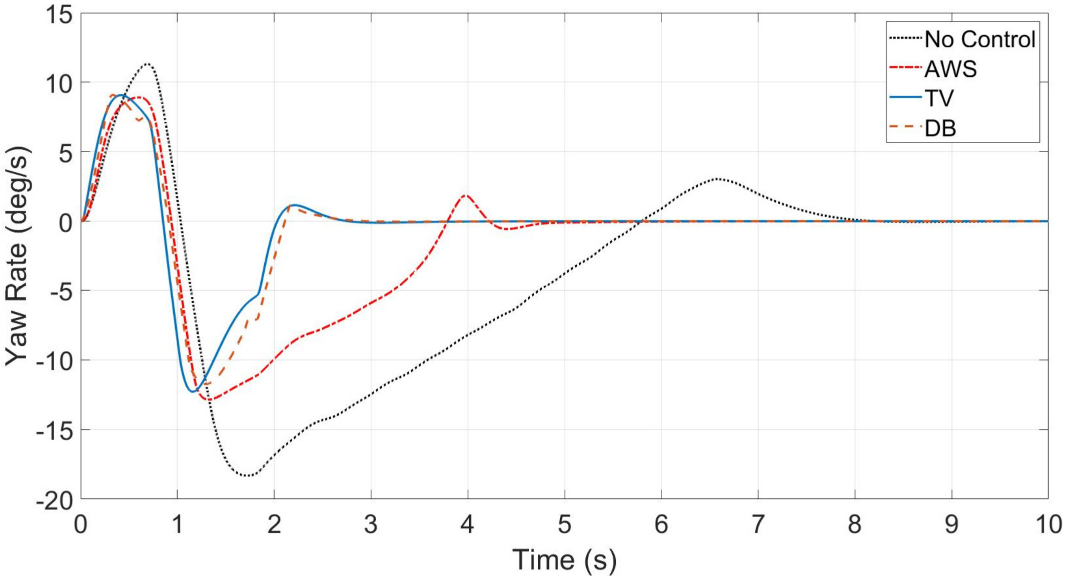

Figure 6-90 Yaw Rate during FMVSS 126 ESC at 80 Km/h (μ = 0.35)

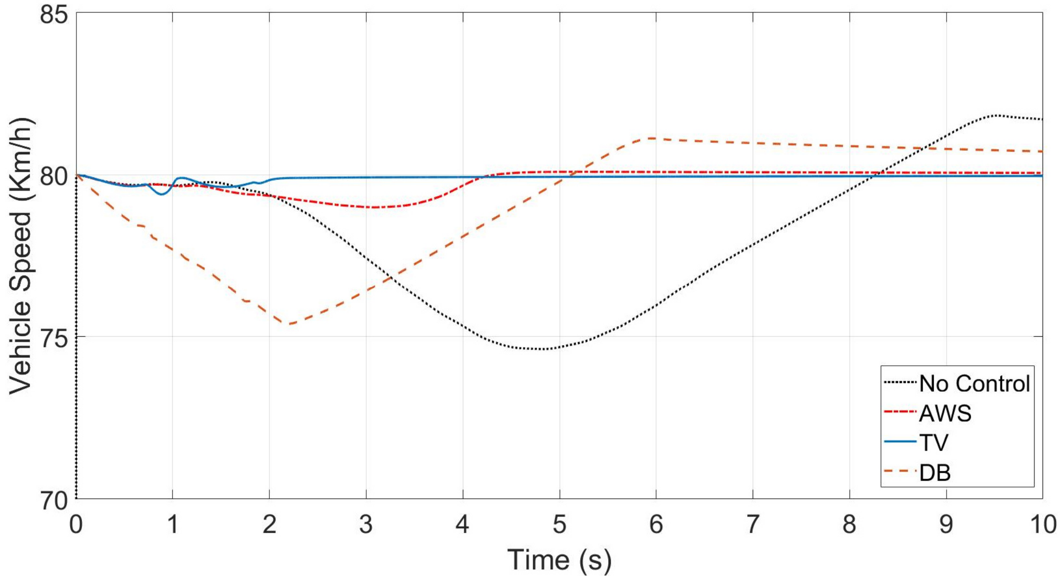

Figure 6-91 Vehicle Speed during FMVSS 126 ESC at 80 Km/h (μ = 0.35)

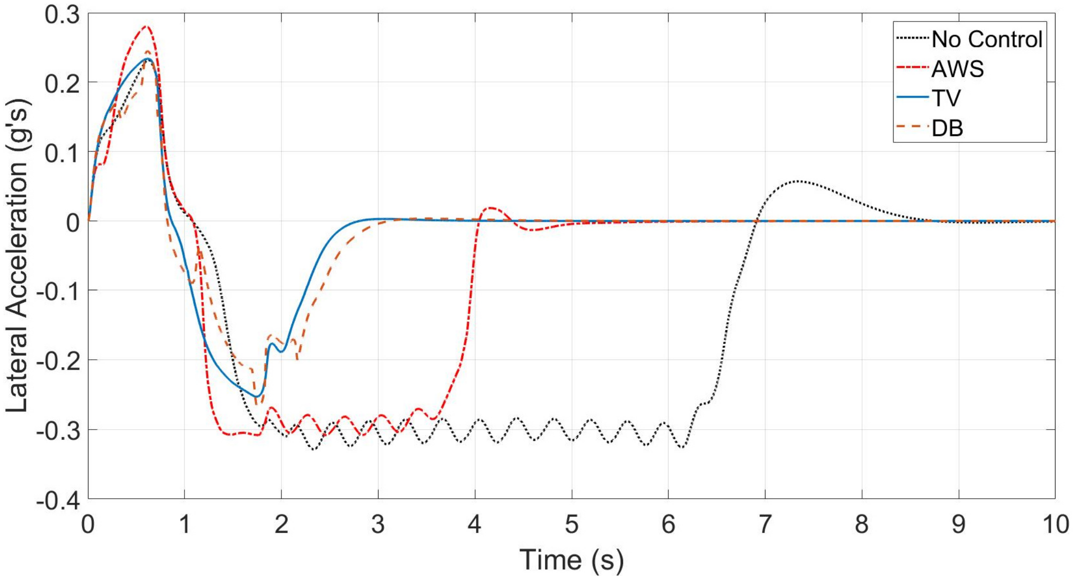

Figure 6-92 Lateral Acceleration during FMVSS 126 ESC at 80 Km/h (μ = 0.35)

Figure 6-93 and Figure 6-94 depict show the front and rear road steer angle in (a) and (b) for vehicle with no control and AWS, respectively. The front steering angles are observed taking 4 seconds to be dampened for AWS, while the maximum achieved rear steering angle is 15 degrees. It should be noted that the rear steer angles for AWS are performing parallel steering (steering in the same direction as the front steering angles).

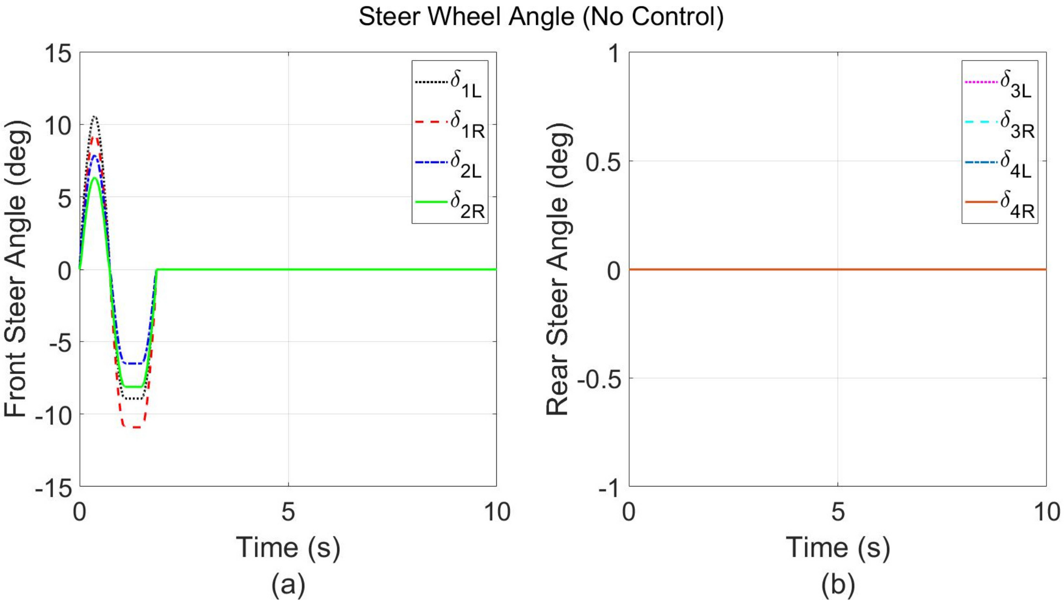

Figure 6-93 (a) Front Steer Angle and (b) Rear Steer Angle for Vehicle (No Control) during FMVSS 126 ESC at 80 Km/h ($\mu = 0.35$)

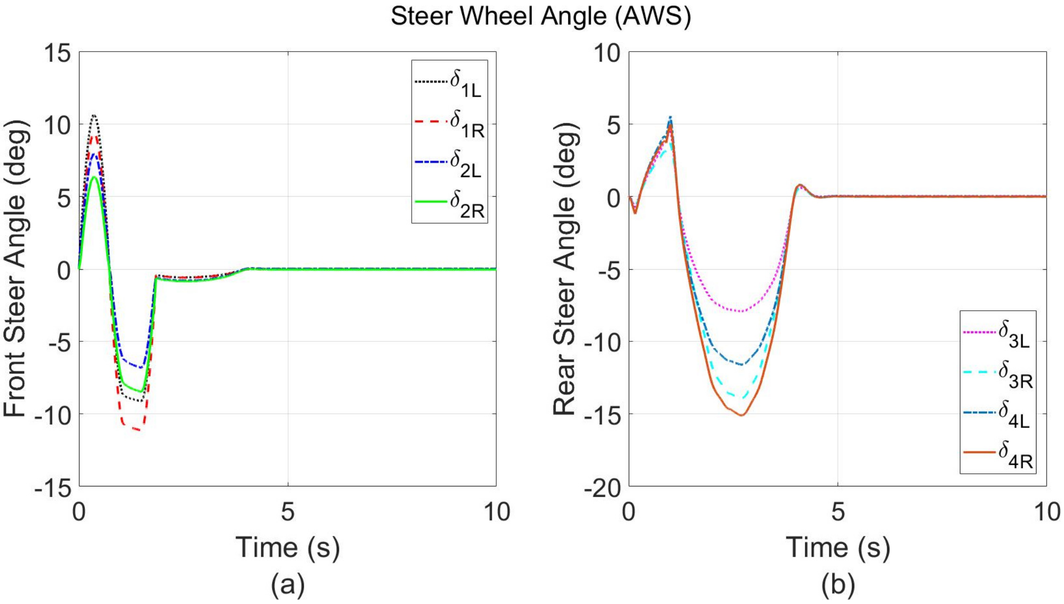

Figure 6-94 (a) Front Steer Angle and (b) Rear Steer Angle for AWS during FMVSS 126 ESC at 80 Km/h ($\mu = 0.35$)

Figure 6-95 and Figure 6-96 demonstrate the left and right sides' vehicle wheels driving torque in (a) and (b) for vehicle with no control and TV, respectively. The maximum achieved driving wheel torque in the left and right side for TV is 5372.2 Nm and -4643.4 Nm, respectively. While 785.0 Nm in both sides for vehicle with no control.

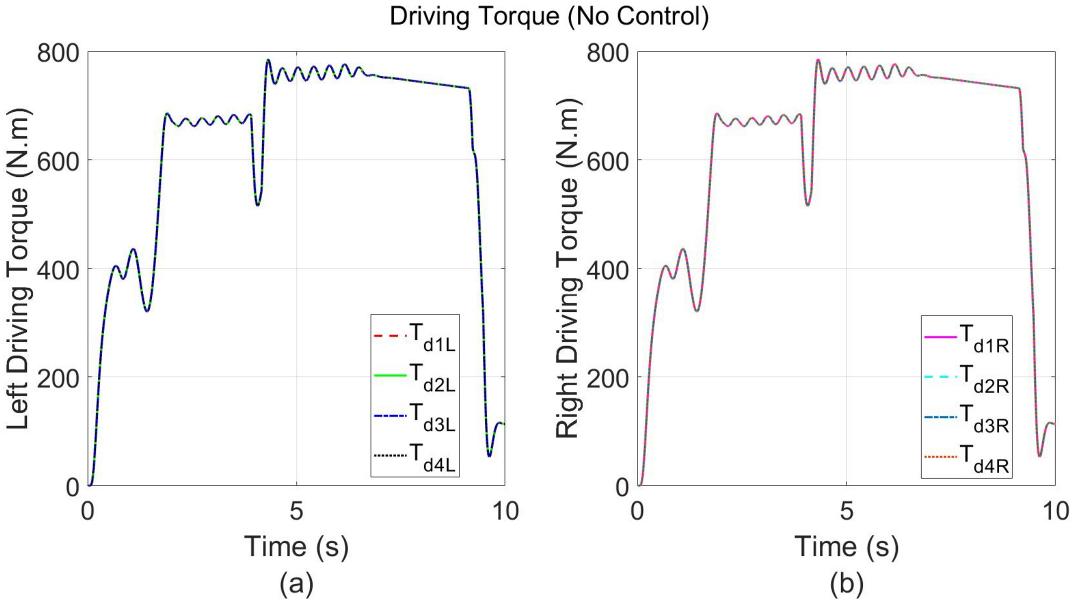

Figure 6-95 (a) Left Wheels Driving Torque and (b) Right Wheels Driving Torque for Vehicle (No Control) during FMVSS 126 ESC at 80 Km/h ($\mu = 0.35$)

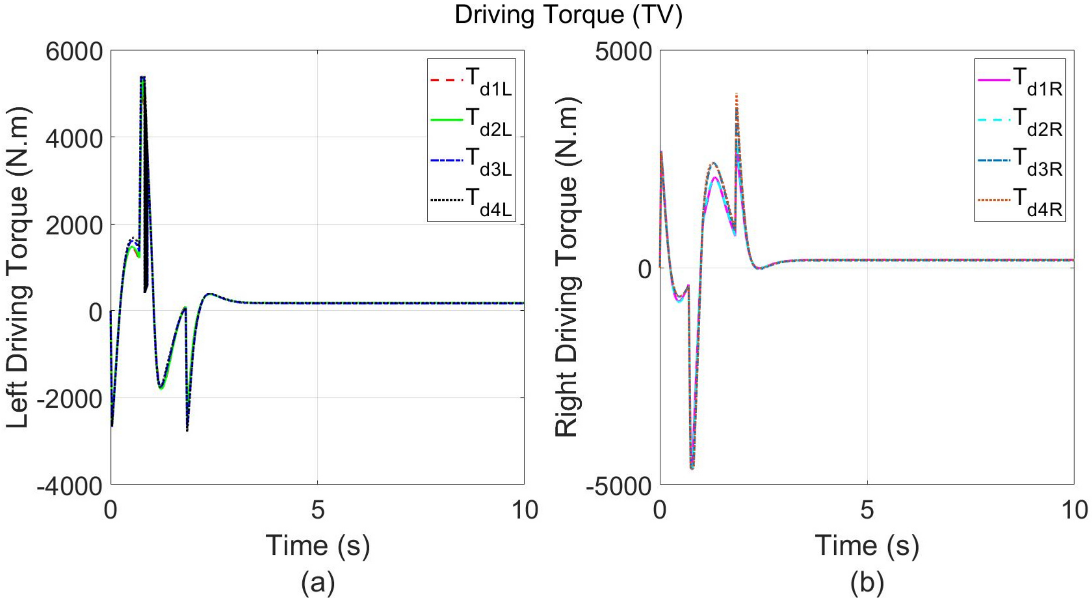

Figure 6-96 (a) Left Wheels Driving Torque and (b) Right Wheels Driving Torque for TV during FMVSS 126 ESC at 80 Km/h ($\mu = 0.35$)

Figure 6-97 shows the left and right sides' wheels braking torque in (a) and (b) for DB. The maximum achieved braking wheels torque in the left and right side is -17033.0 Nm for both, respectively.

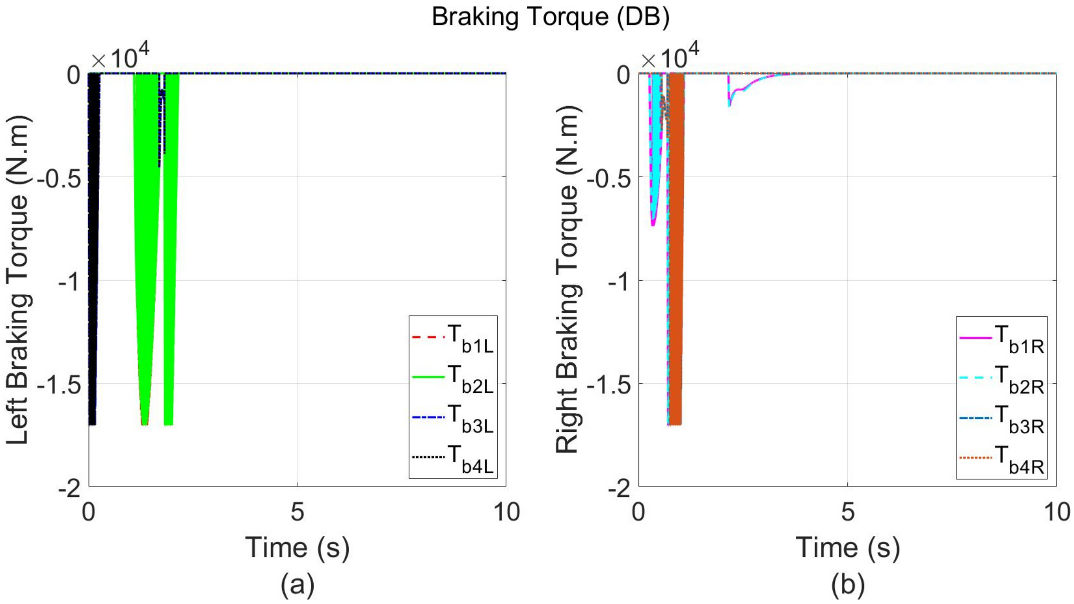

Figure 6-97 (a) Left Wheels Braking Torque and (b) Right Wheels Braking Torque for DB during FMVSS 126 ESC at 80 Km/h (μ = 0.35)

6.2.4 Modified J-Turn

The Modified J-Turn test serves as an open-loop maneuver course, where no target path to be follow. This test is utilized to assess the vehicle's performance in terms of maneuverability and stability at a given steering wheel input. The intended maneuver incorporates a gradual increasing in steering wheel angle up to a peak of 367.2 degrees followed by return prior to a fixed steering wheel angle of 26.96 degrees as shown in Figure 6-98.

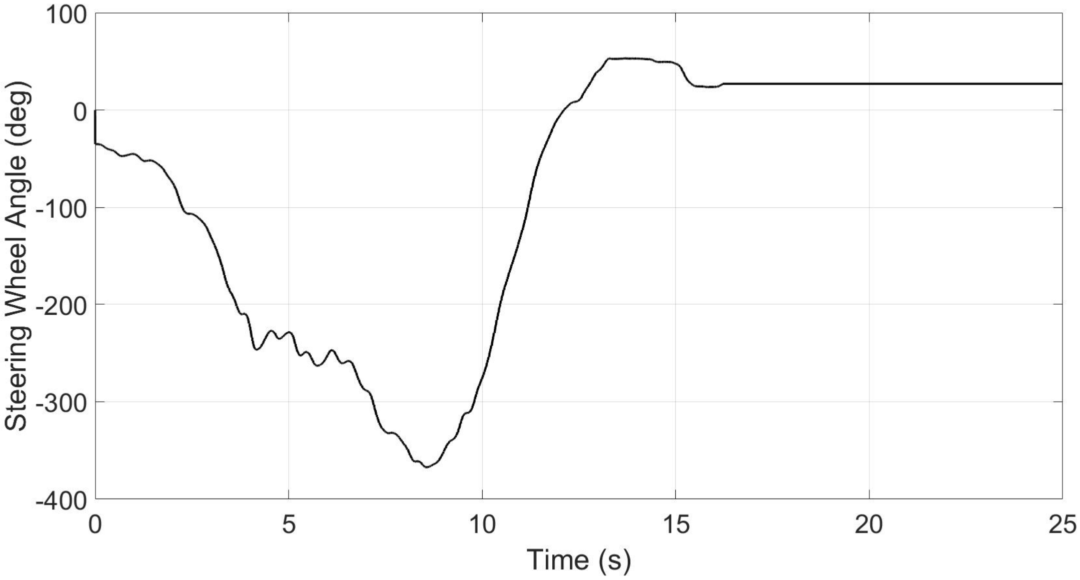

Figure 6-98 Steering Wheel Angle Input For Modified J-Turn Test Course

6.2.4.1 Results and Discussion of Evaluation Method at high coefficient of friction – Modified J-Turn ($100\ \mathrm{km/h}\ ;\ \mu = 0.85$)

The vehicle trajectory performed by each control strategy AWS+SAS, TV+SAS, DB+SAS, and vehicle with no control are shown in Figure 6-99. Its notable that AWS+SAS has achieved the largest turning radius among the other control strategies and vehicle with no control, while the smallest turning radius is obtained by DB+SAS. Consequently, DB+SAS has improved the vehicle's maneuverability by operating at small turning radius.

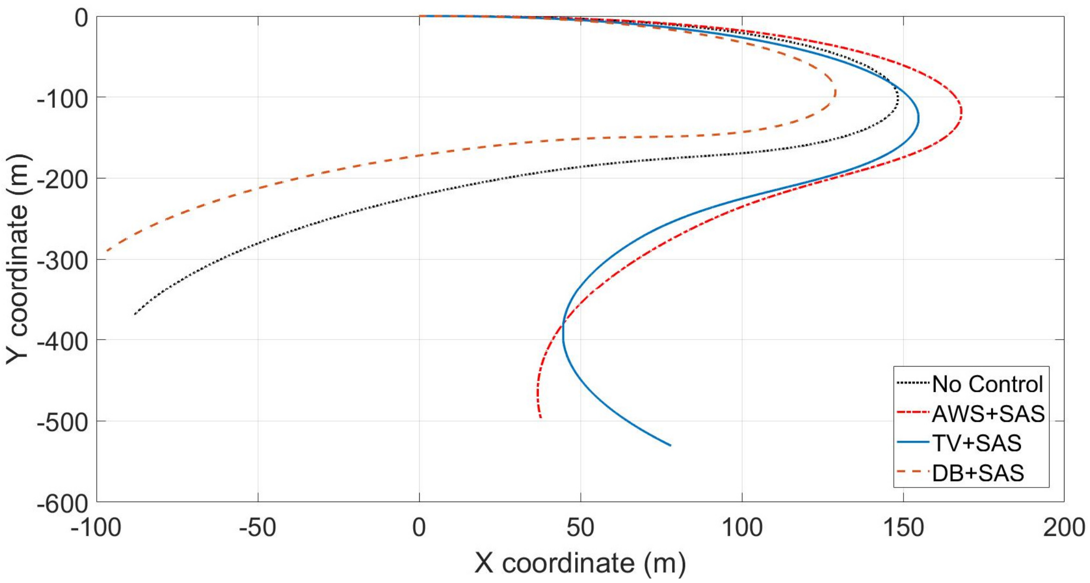

Figure 6-99 Vehicle Trajectory during Modified J-Turn at 100 Km/h (μ = 0.85)

Figure 6-100, Figure 6-101, Figure 6-102 and Figure 6-103 show the vehicle sideslip, yaw rate, longitudinal speed and lateral acceleration respectively for vehicle with no control, AWS+SAS, TV+SAS and DB+SAS. It can be observed that AWS+SAS has tremendously minimized the sideslip angle compared to the other control strategies, while vehicle with no control has obtained the largest value. Which considered as merit for AWS+SAS in enhancing vehicle's stability at high friction road surface. DB+SAS has attained the largest yaw rate response amplitude among the proposed control strategies and vehicle with now control. Accordingly, DB+SAS has greatly improved vehicle's maneuverability than other control strategies. Furthermore, TV+SAS and AWS+SAS have achieved less drop in longitudinal speed than DB+SAS and vehicle with no control, makes them close to maintain the desired speed. In addition, there is no significant observation about lateral acceleration except TV+SAS has obtained the lowest peak value than the other control strategies and vehicle with no control.

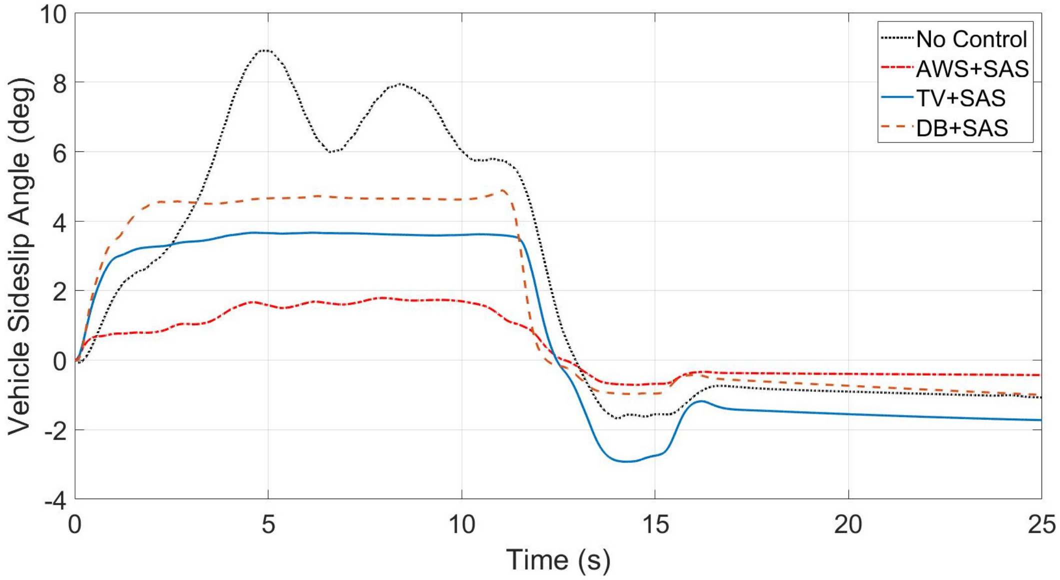

Figure 6-100 Vehicle Sideslip Angle during Modified J-Turn at 100 Km/h (μ = 0.85)

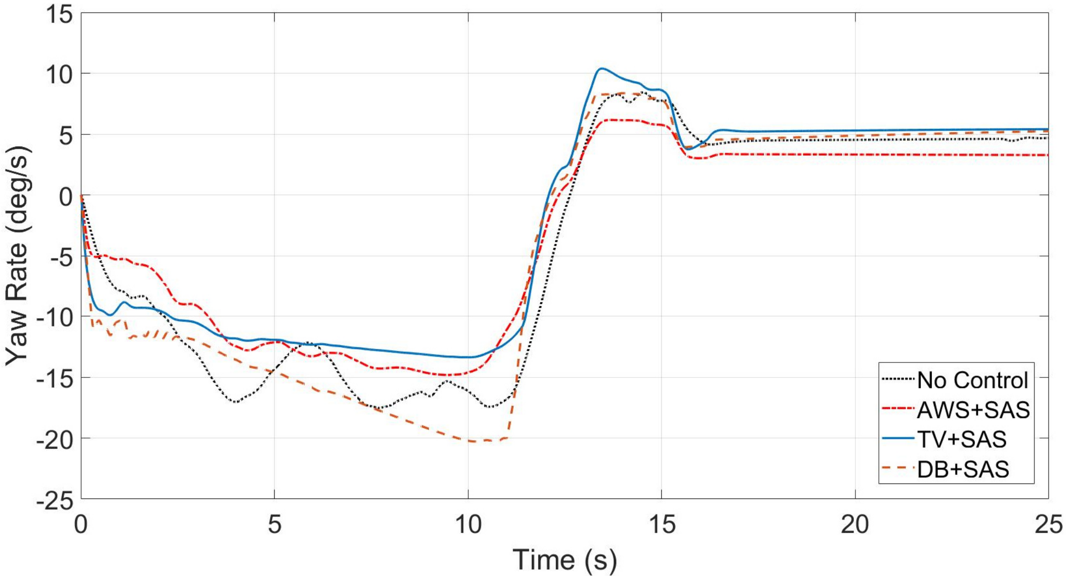

Figure 6-101 Yaw Rate during Modified J-Turn at 100 Km/h (μ = 0.85)

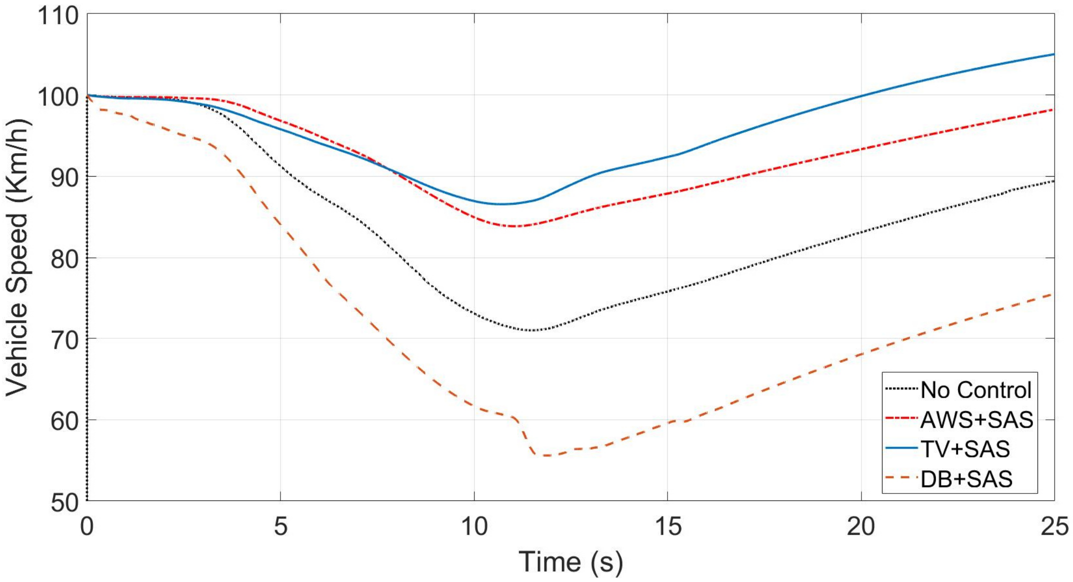

Figure 6-102 Vehicle Speed during Modified J-Turn at 100 Km/h (μ = 0.85)

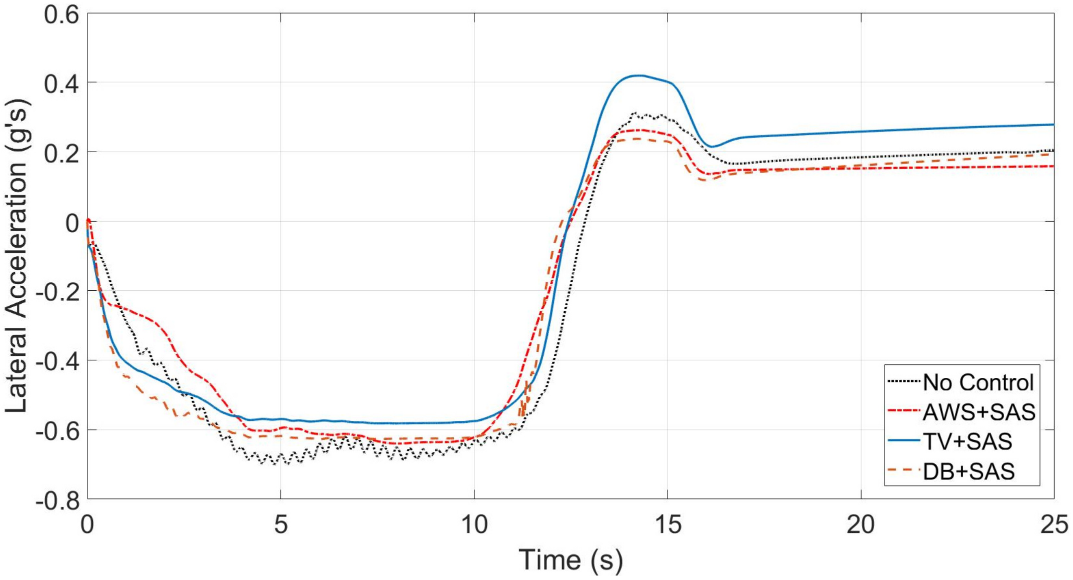

Figure 6-103 Lateral Acceleration during Modified J-Turn at 100 Km/h (μ = 0.85)

Figure 6-104, Figure 6-105 and Figure 6-106 present the vehicle's sprung mass displacement, pitch, and roll angle, respectively. It is notable that AWS+SAS, TV+SAS and DB+SAS have significantly minimized the vertical displacement at the CG of the sprung mass compared to vehicle with no control. Furthermore, all the proposed control strategies have significantly reduced the pitch and roll angle due to longitudinal and lateral load transfer compared to vehicle with no control. However, TV+SAS has slightly attained largest value for roll angle compared to AWS+SAS and DB+SAS.

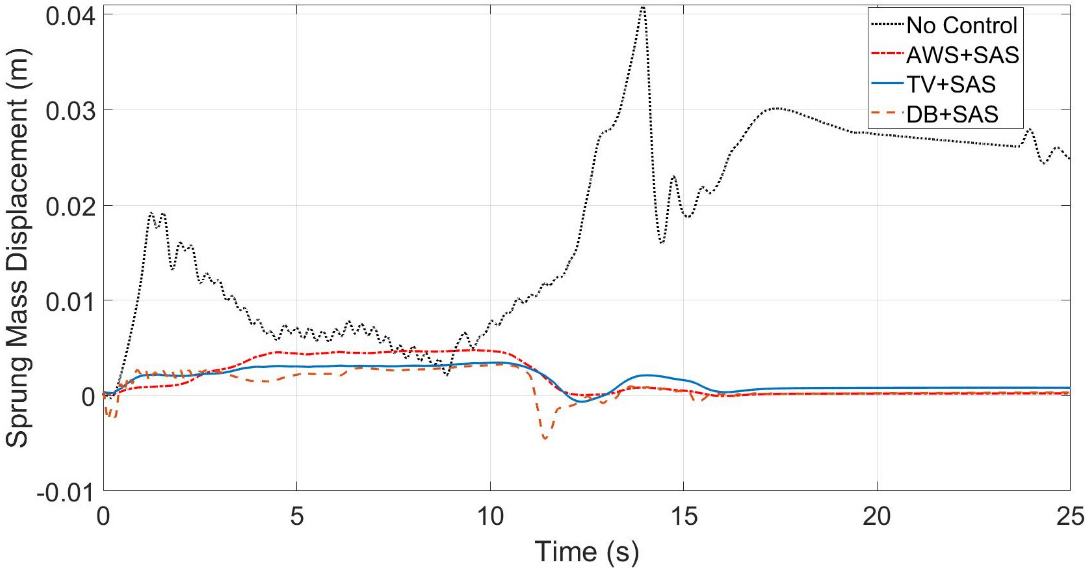

Figure 6-104 Sprung Mass Displacement during Modified J-Turn at 100 Km/h (μ = 0.85)

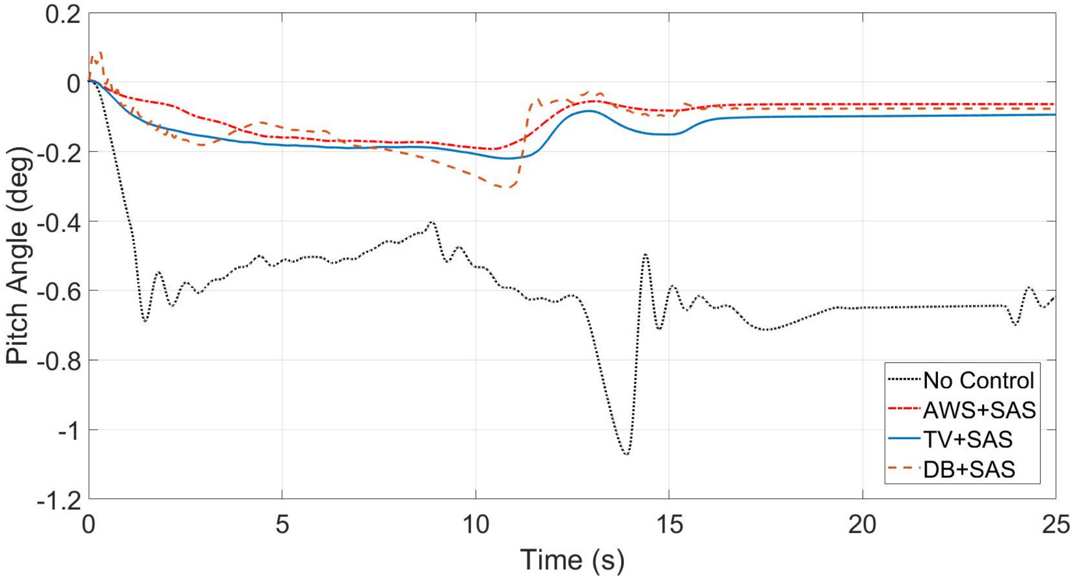

Figure 6-105 Pitch Angle during Modified J-Turn at 100 Km/h (μ = 0.85)

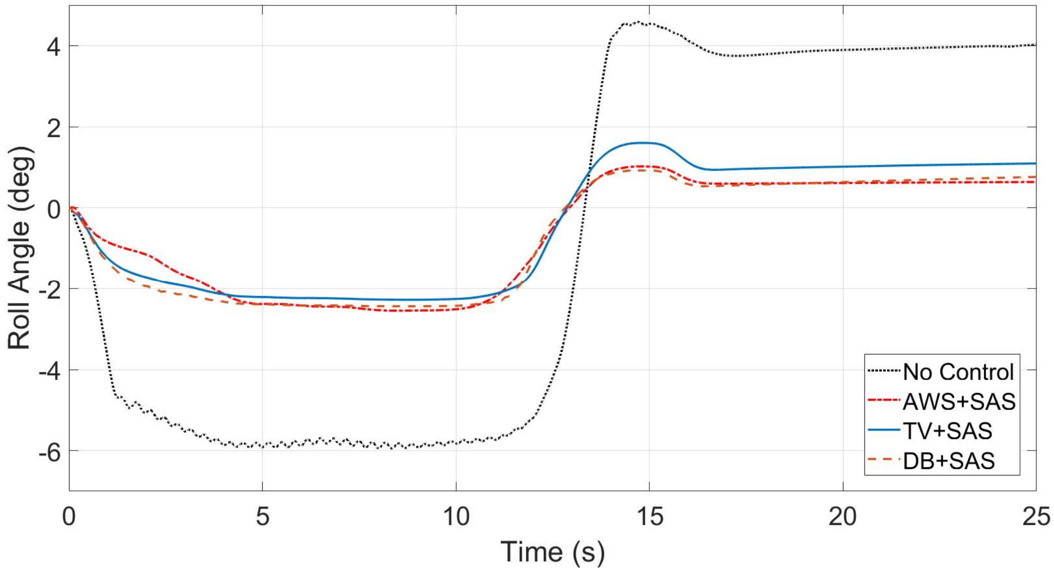

Figure 6-106 Roll Angle during Modified J-Turn at 100 Km/h (μ = 0.85)

Figure 6-107 and Figure 6-108 show the front and rear road steer angle in (a) and (b) for vehicle with no control and AWS+SAS, respectively. The AWS+SAS has achieved maximum front steering angles of 17.1 degrees, while 5.5 degrees for rear steering angles. It should be noted that the rear steer angles for AWS+SAS are performing parallel steering (steering in the same direction as the front steering angles).

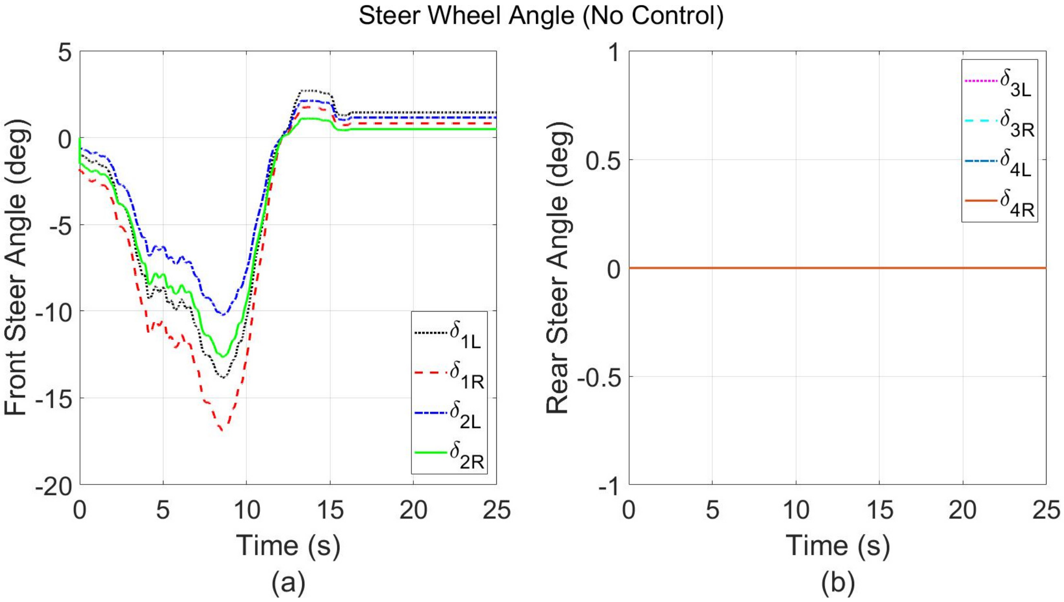

(a)

(b)

Figure 6-107 (a) Front Steer Angle and (b) Rear Steer Angle for Vehicle (No Control) during Modified J-Turn at 100 Km/h (μ = 0.85)

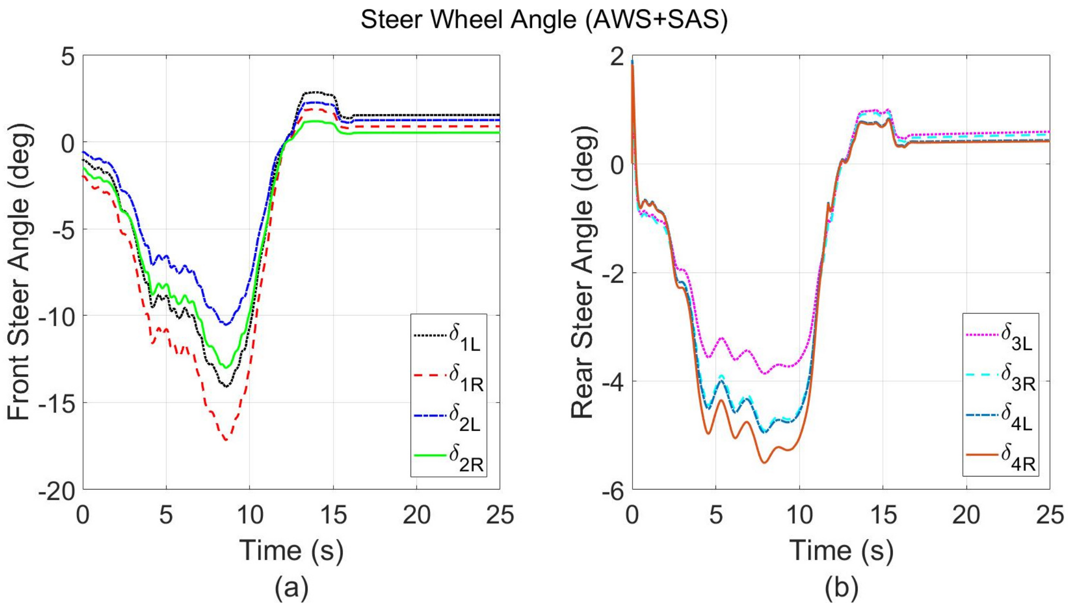

(a) (b)

Figure 6-108 (a) Front Steer Angle and (b) Rear Steer Angle for AWS+SAS during Modified J-Turn at 100 Km/h (μ = 0.85)

Figure 6-109 and Figure 6-110 demonstrate the left and right sides' vehicle wheels driving torque in (a) and (b) for vehicle with no control and TV+SAS, respectively. The maximum achieved driving wheel torque in the left and right side for TV+SAS is 3828.9 Nm and 3460.8 Nm, respectively. While 906.0 Nm in both sides for vehicle with no control.

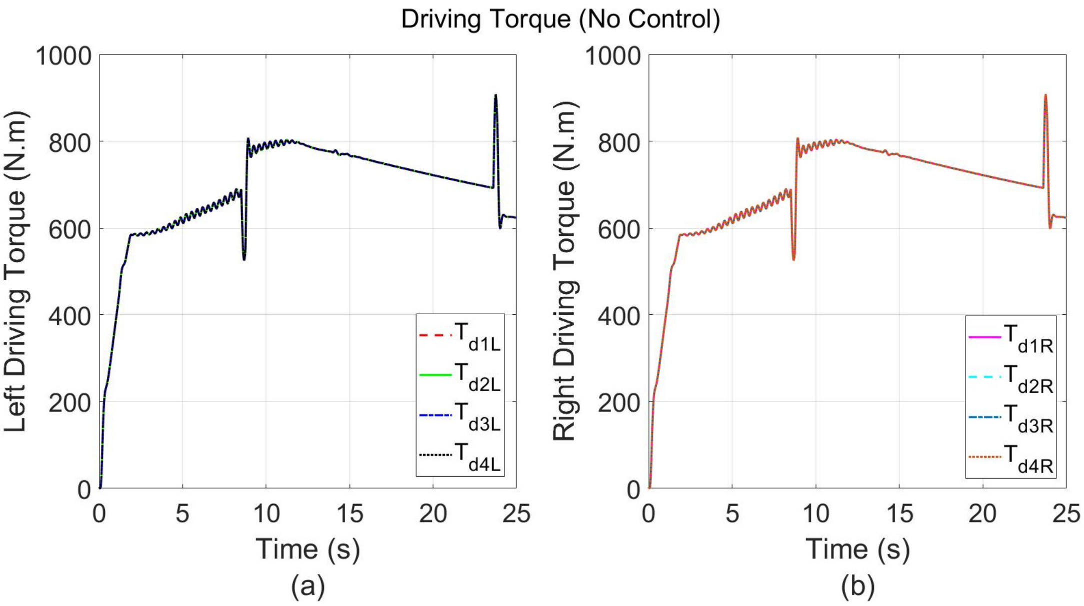

(a) (b)

Figure 6-109 (a) Left Wheels Driving Torque and (b) Right Wheels Driving Torque for Vehicle (No Control) during Modified J-Turn at 100 Km/h (μ = 0.85)

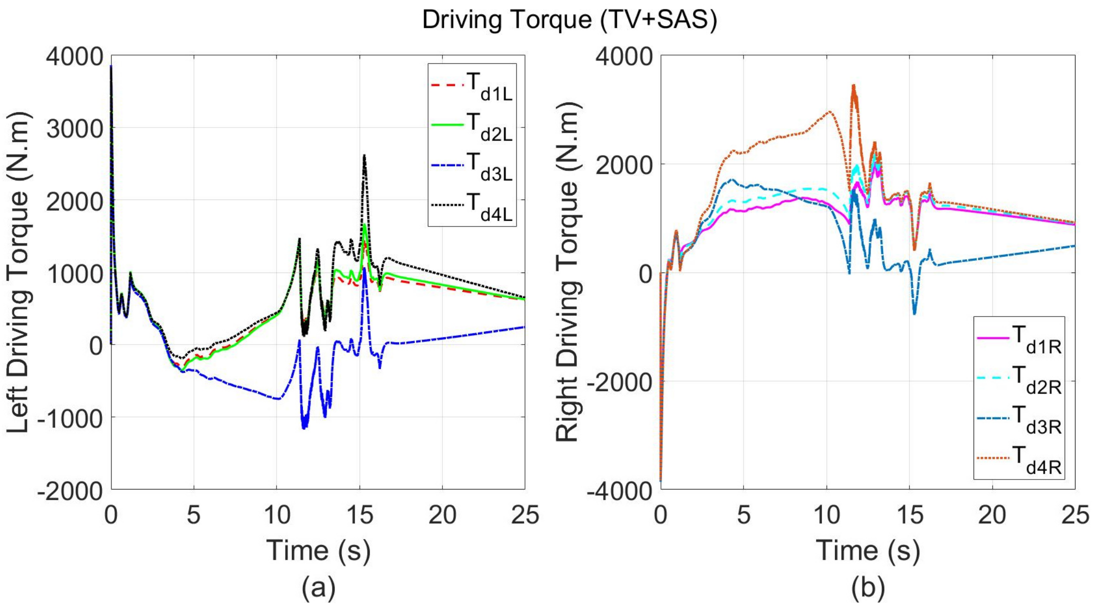

Figure 6-110 (a) Left Wheels Driving Torque and (b) Right Wheels Driving Torque for TV+SAS during Modified J-Turn at 100 Km/h ($\mu = 0.85$)

Figure 6-111 shows the left and right sides' wheels braking torque in (a) and (b) for DB+SAS. The maximum achieved braking wheels torque in the left and right side is -17033.0 Nm for both, respectively. From inspecting the wheels' braking torque on both sides, it should be noted that the vehicle exhibits drifting out (Understeer).

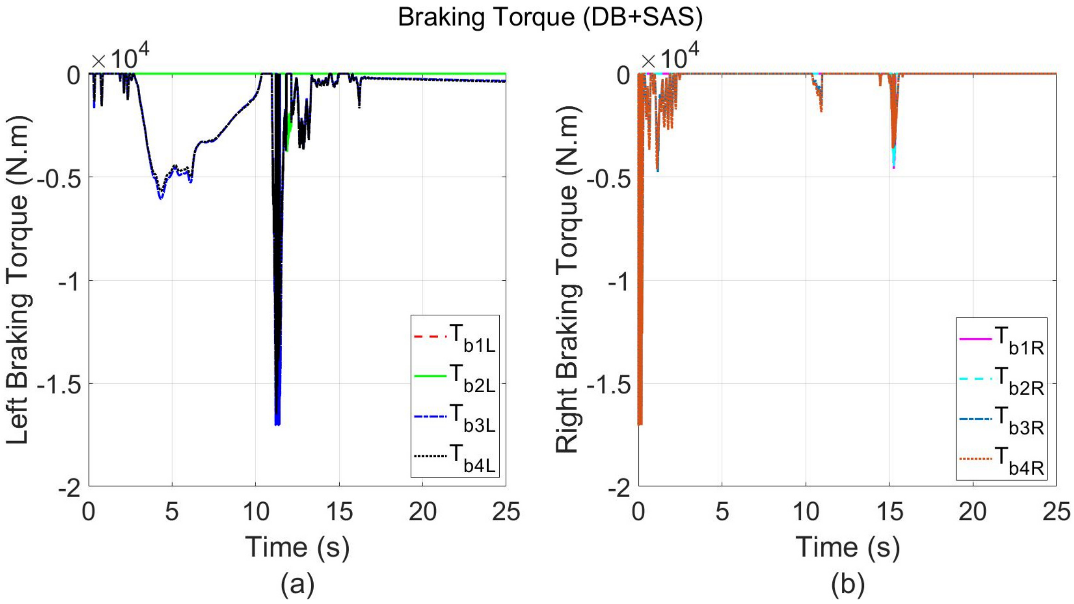

Figure 6-111 (a) Left Wheels Braking Torque and (b) Right Wheels Braking Torque for DB+SAS during Modified J-Turn at 100 Km/h ($\mu = 0.85$)

Figure 6-112, Figure 6-113, Figure 6-114 and Figure 6-115 present the left and right sides' vehicle damper forces in (a) and (b) for vehicle with no control, AWS+SAS, TV+SAS and DB+SAS respectively. It can be noticed that all proposed control strategies have obtained largest dampers' forces varying with time compared to vehicle with no control. However, TV+SAS have induced the largest dampers' forces in left side, while DB+SAS has obtained largest dampers' forces in right side.

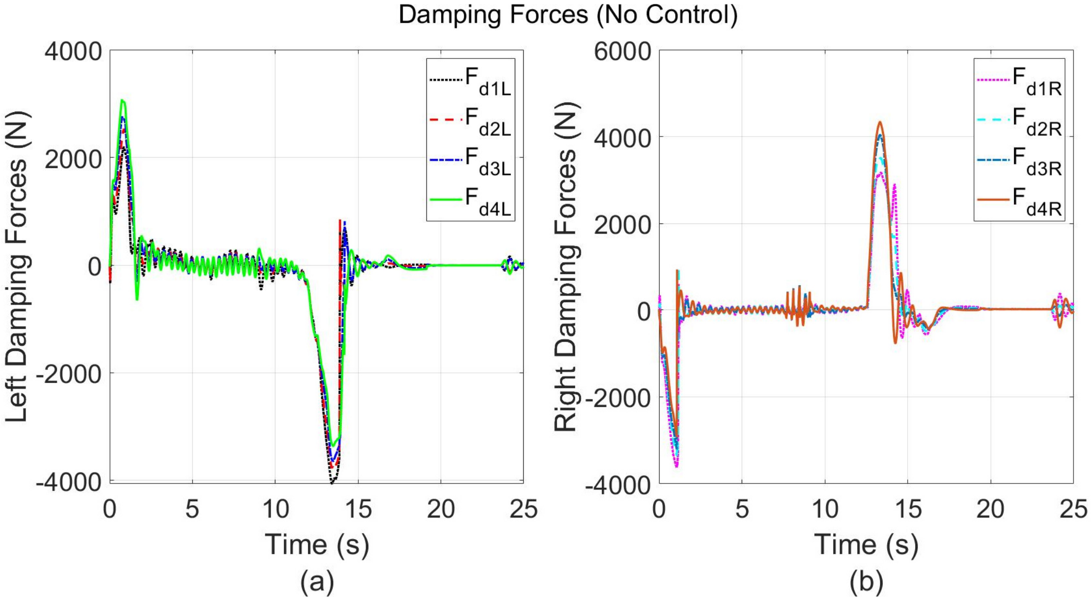

Figure 6-112 (a) Left Damping Forces and (b) Right Damping Forces for Vehicle (No Control) during Modified J-Turn at 100 Km/h ($\mu = 0.85$)

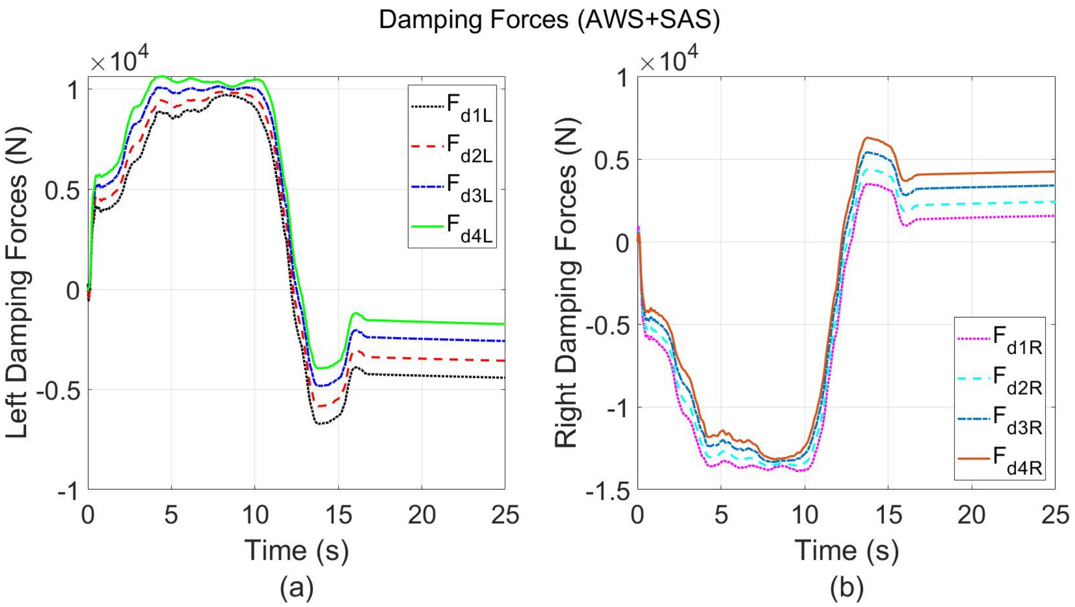

Figure 6-113 (a) Left Damping Forces and (b) Right Damping Forces for AWS+SAS during Modified J-Turn at 100 Km/h ($\mu = 0.85$)

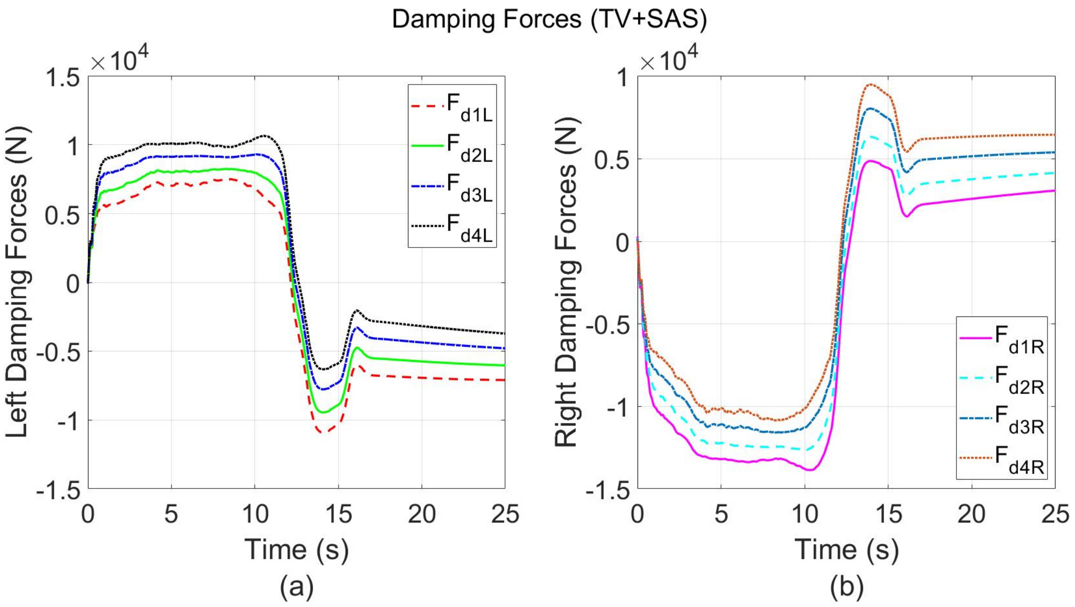

Figure 6-114 (a) Left Damping Forces and (b) Right Damping Forces for TV+SAS during Modified J-Turn at 100 Km/h ($\mu = 0.85$)

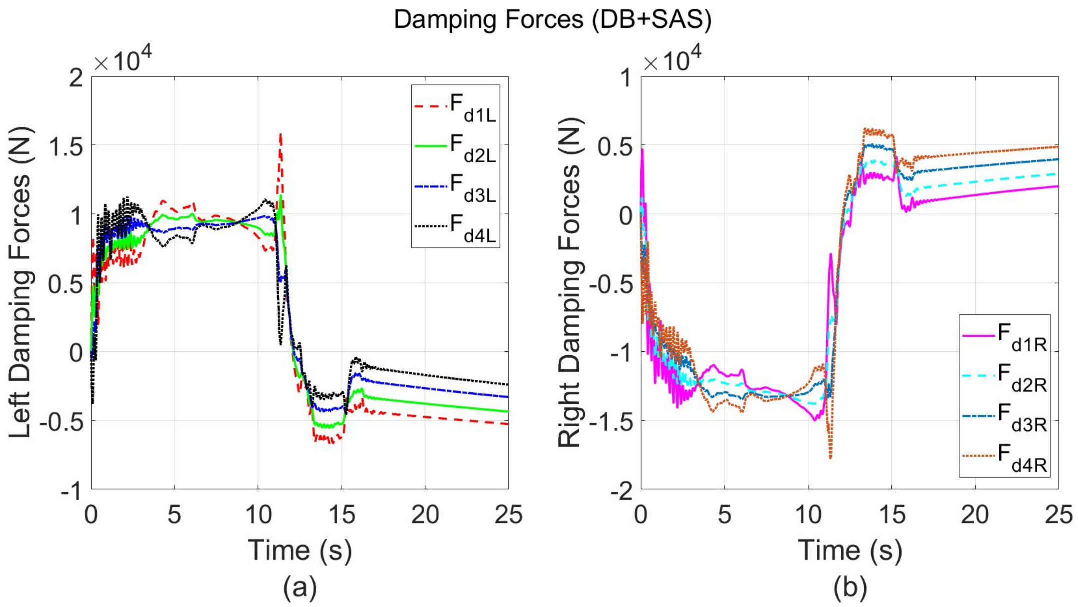

Figure 6-115 (a) Left Damping Forces and (b) Right Damping Forces for DB+SAS during Modified J-Turn at 100 Km/h ($\mu = 0.85$)

6.2.4.2 Results and Discussion of Evaluation Method at high coefficient of friction – Modified J-Turn ($80\ \mathrm{km/h}\ ;\ \mu = 0.35$)

The vehicle trajectory performed by each control strategy AWS, TV, DB, and vehicle with no control are illustrated in Figure 6-116. On low friction road surface all control strategies have relatively obtained same turning radius. However, it can be observed that DB and vehicle with no control have achieved the lowest value.

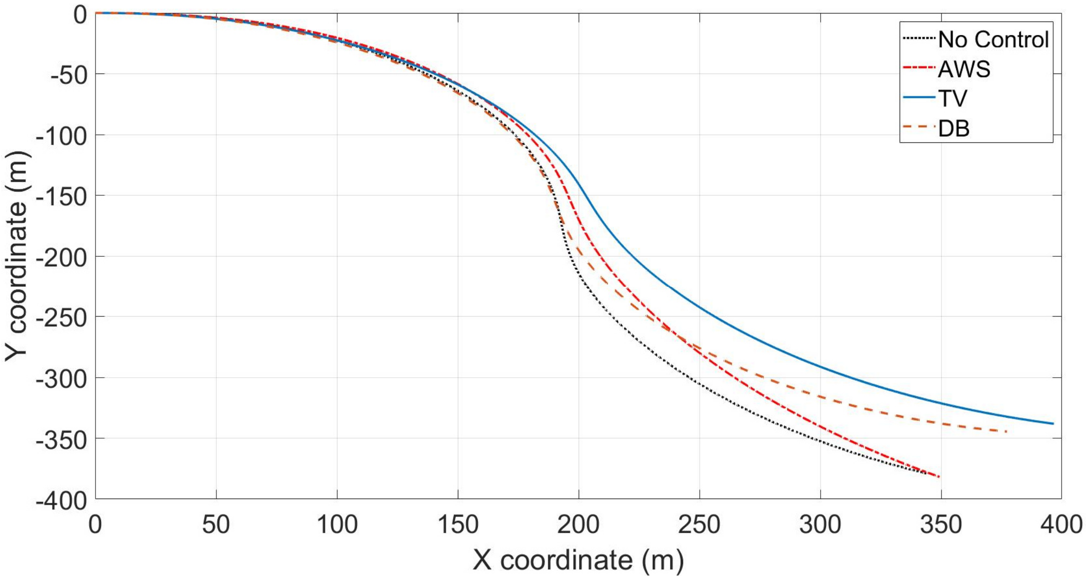

Figure 6-116 Vehicle Trajectory during Modified J-Turn at 80 Km/h ($\mu = 0.35$)

Figure 6-117, Figure 6-118, Figure 6-119 and Figure 6-120 demonstrate the vehicle sideslip, yaw rate, longitudinal speed and lateral acceleration respectively for vehicle with no control, AWS, TV and DB. It can be observed that AWS has significantly minimized the sideslip angle compared to the other control strategies, while vehicle with no control has obtained the largest value. Which considered as merit for AWS in enhancing vehicle's stability at low friction road surface. DB has attained the largest yaw rate response amplitude among the proposed control strategies and vehicle with now control. Accordingly, DB has greatly improved vehicle's maneuverability than other control strategies. Furthermore, TV and AWS have achieved less drop in longitudinal speed than DB, makes them close to maintain the desired speed. Moreover, there is no significant observation about lateral acceleration except TV has obtained the lowest peak value than the other control strategies and vehicle with no control.

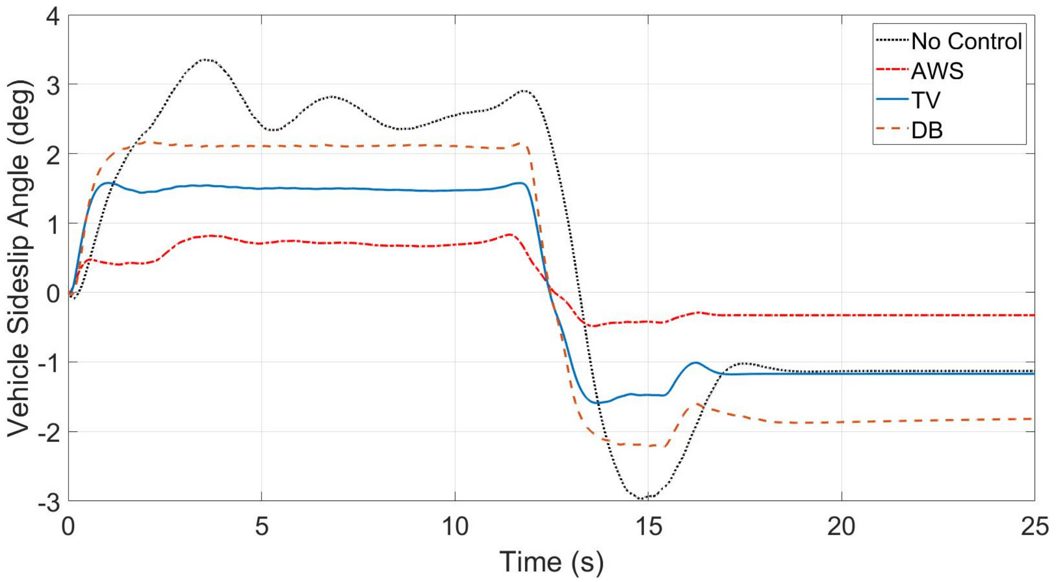

Figure 6-117 Vehicle Sideslip Angle during Modified J-Turn at 80 Km/h (μ = 0.35)

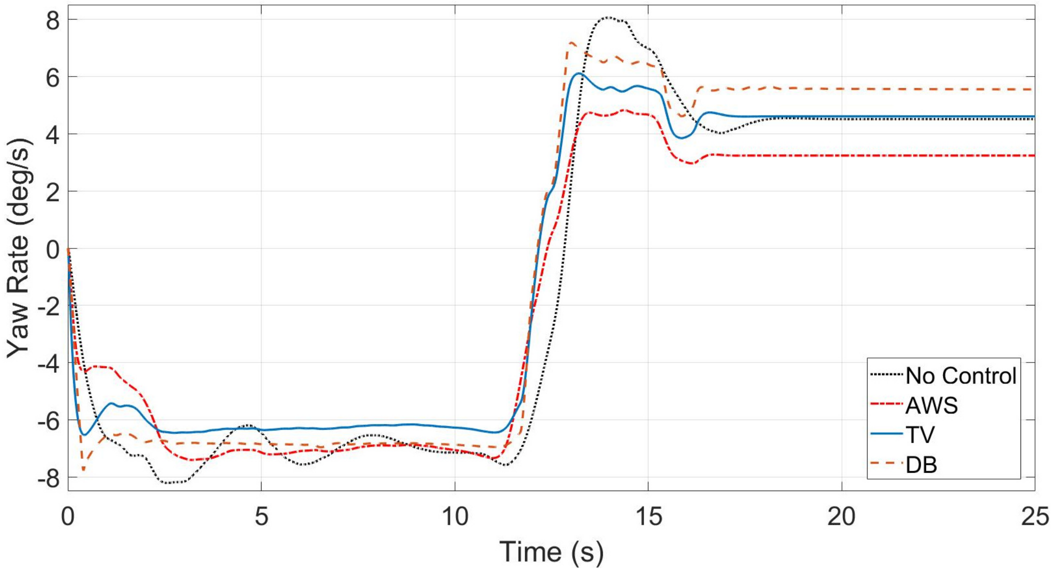

Figure 6-118 Yaw Rate during Modified J-Turn at 80 Km/h (μ = 0.35)

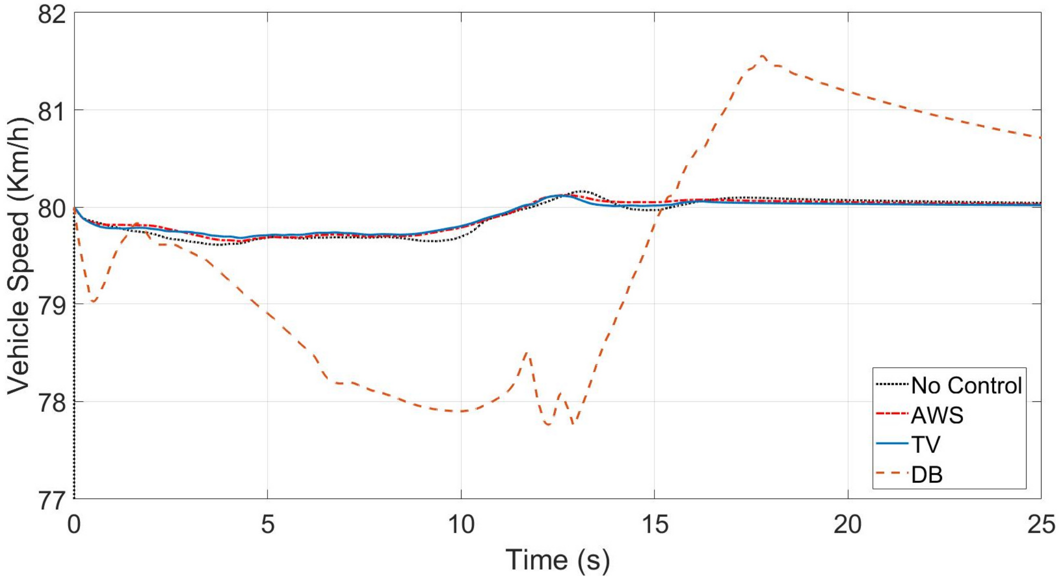

Figure 6-119 Vehicle Speed during Modified J-Turn at 80 Km/h (μ = 0.35)

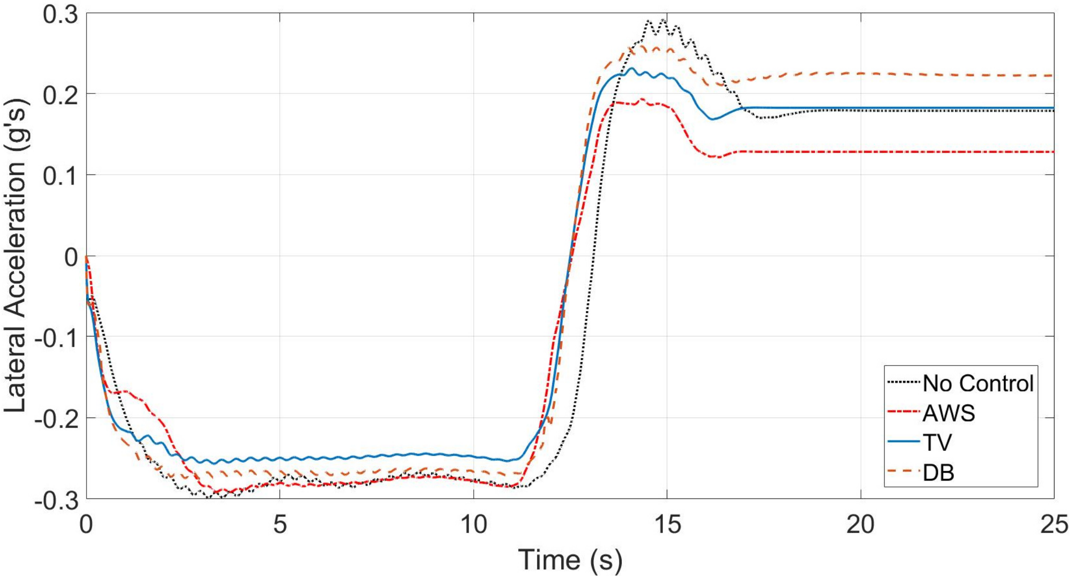

Figure 6-120 Lateral Acceleration during Modified J-Turn at 80 Km/h (μ = 0.35)

Figure 6-121 and Figure 6-122 (a) and (b) show the front and rear road steer angle in (a) and (b) for vehicle with no control and AWS, respectively. The AWS has achieved maximum front steering angles of 17.0 degrees, while 2.5 degrees for rear steering angles. It should be noted that the rear steer angles for AWS+SAS are performing parallel steering (steering in the same direction as the front steering angles).

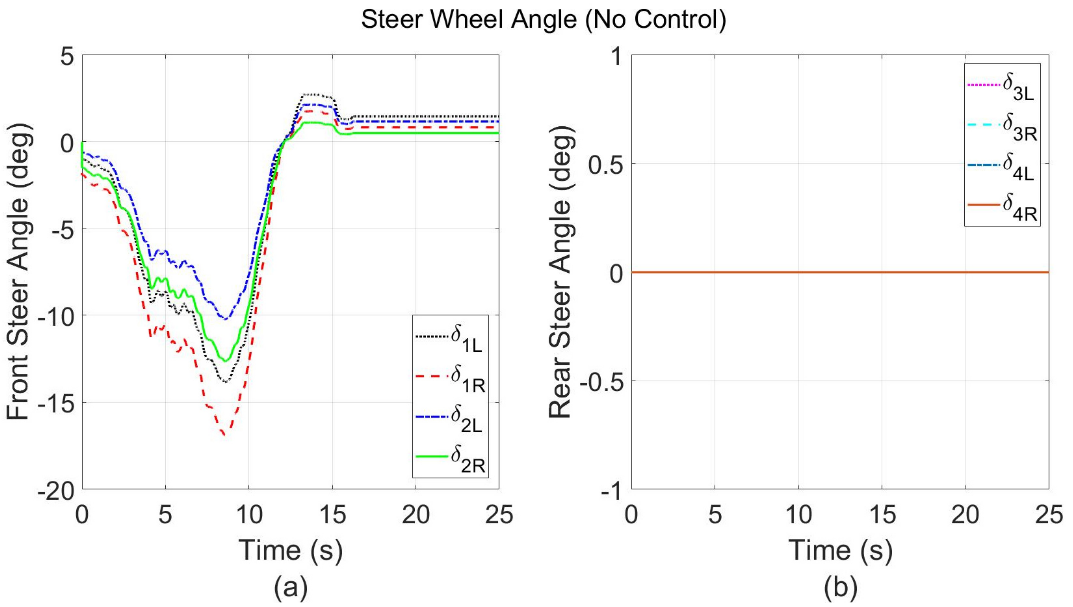

Figure 6-121 (a) Front Steer Angle and (b) Rear Steer Angle for Vehicle (No Control) during Modified J-Turn at 80 Km/h ($\mu = 0.35$)

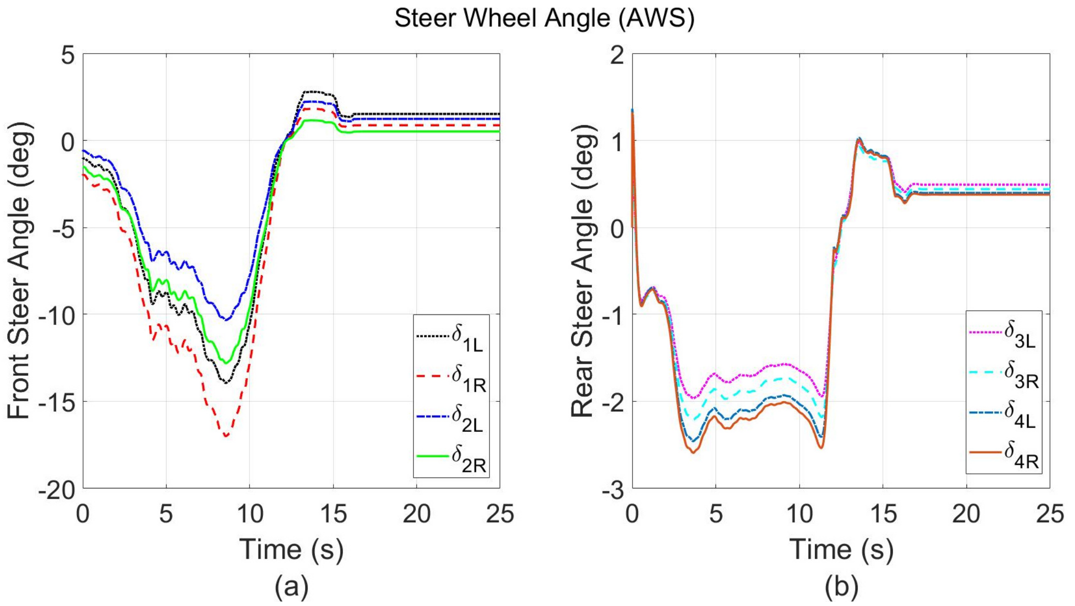

Figure 6-122 (a) Front Steer Angle and (b) Rear Steer Angle for AWS during Modified J-Turn at 80 Km/h ($\mu = 0.35$)

Figure 6-123 and Figure 6-124 depict the left and right sides' vehicle wheels driving torque in (a) and (b) for vehicle with no control and TV, respectively. The maximum achieved driving wheel torque in the left and right side for TV is -870.3 Nm and 1372.3 Nm, respectively. While 671.5 Nm in both sides for vehicle with no control.

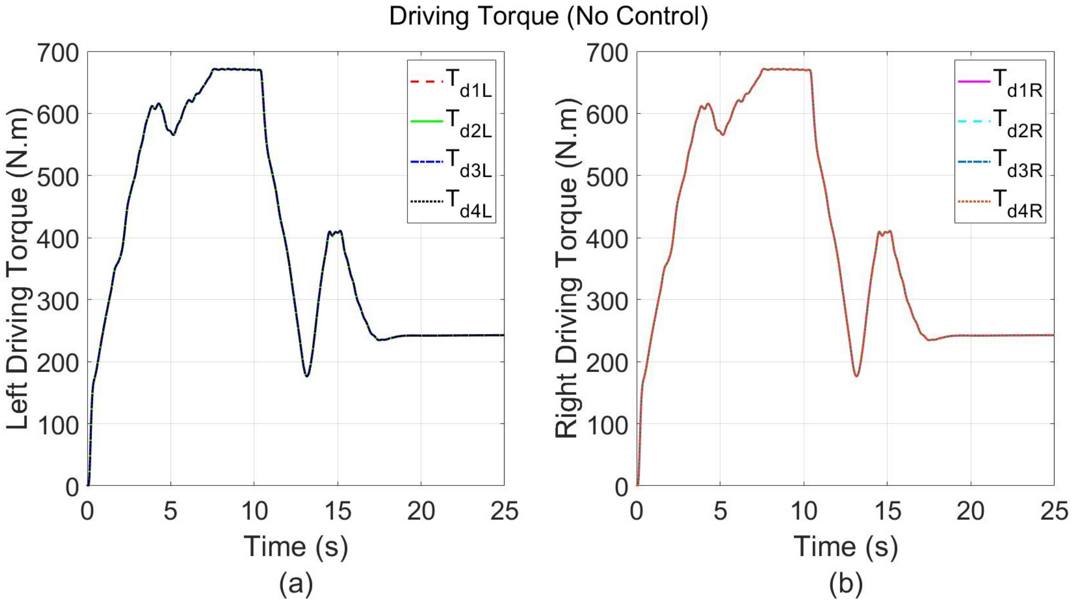

Figure 6-123 (a) Left Wheels Driving Torque and (b) Right Wheels Driving Torque for Vehicle (No Control) during Modified J-Turn at 80 Km/h (μ = 0.35)

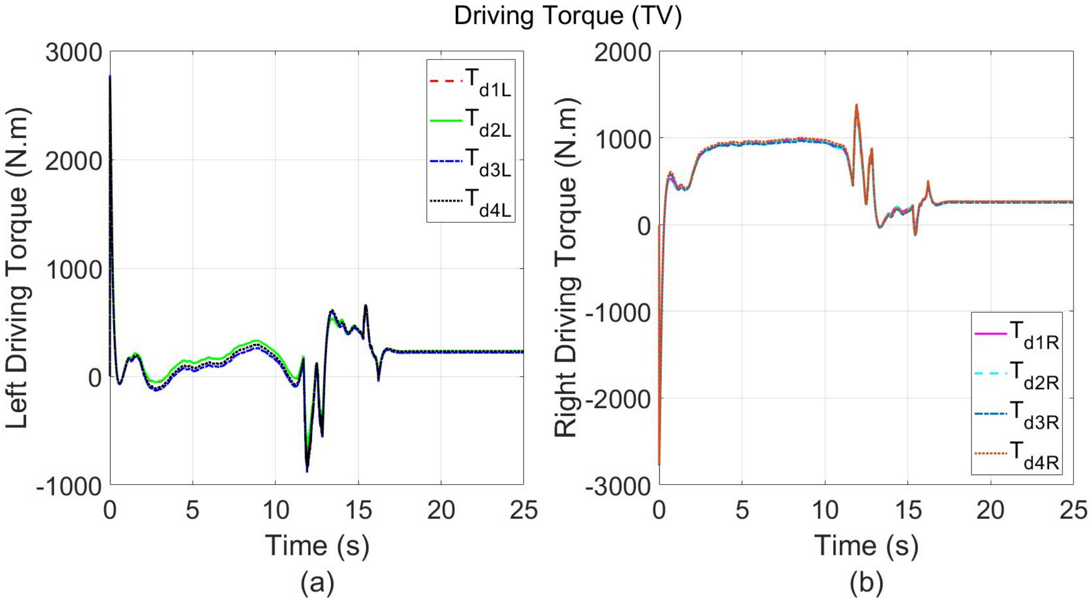

Figure 6-124 (a) Left Wheels Driving Torque and (b) Right Wheels Driving Torque for TV during Modified J-Turn at 80 Km/h (μ = 0.35)

Figure 6-125 express the left and right sides' wheels braking torque in (a) and (b) for DB. The maximum obtained braking wheels torque in the left and right side is -6780.0 Nm and -17033.0 Nm, respectively.

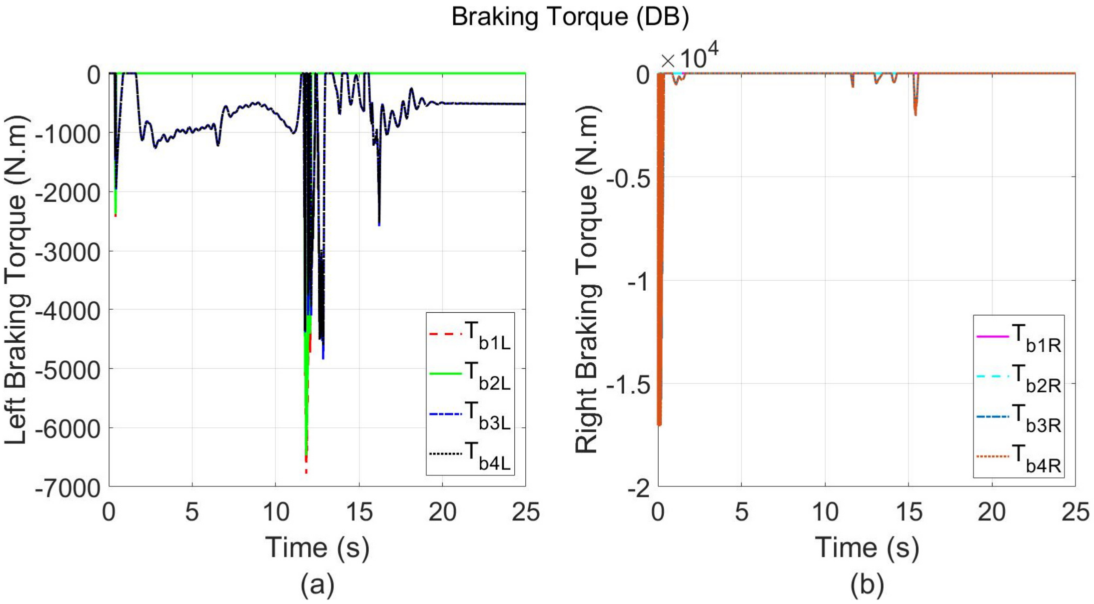

Figure 6-125 (a) Left Wheels Braking Torque and (b) Right Wheels Braking Torque for DB during Modified J-Turn at 80 Km/h ($\mu = 0.35$)

6.2.5 Open-Loop Step Slalom Test Event

This test is designed as an open-loop maneuver test, where no target path to be followed. A gradual increasing in steering wheel input is applied to the vehicle to investigate its performance against rollover scenario. The vehicle is intended to run at constant speed of 65 Km/h at high friction road surface of 1.0. Figure 6-126 illustrate the steering wheel input during this event.

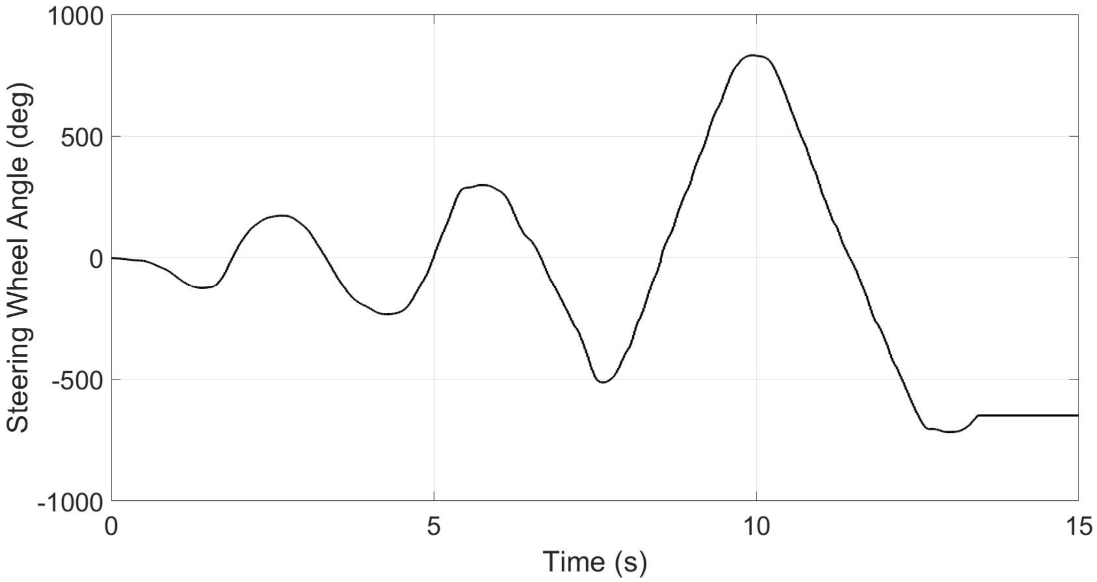

Figure 6-126 Steering Wheel Angle Input For Open-Loop Step Slalom Test Course

6.2.5.1 Results and Discussion of Evaluation Method at high coefficient of friction – Open-Loop Step Slalom Test (65 $\mathrm{km/h}$; $\mu = 1.0$)

The vehicle trajectory performed by each control strategy AWS+SAS, TV+SAS, DB+SAS, and vehicle with no control are demonstrated in Figure 6-127. Its notable that all the proposed control strategies have succeeded to maintain the maneuver, while the vehicle without control failed and tipped over.

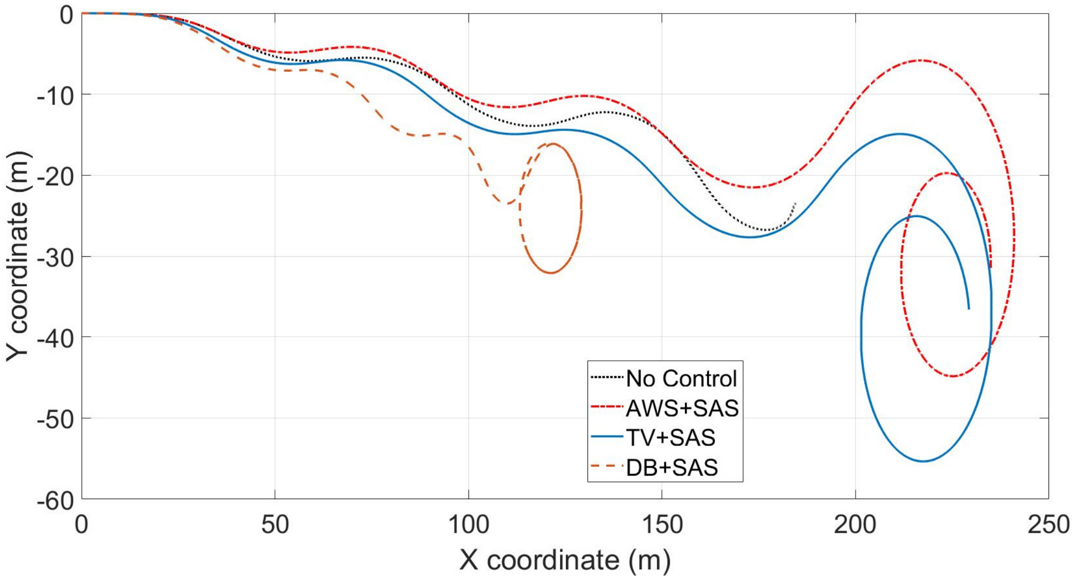

Figure 6-127 Vehicle Trajectory during Open-Loop Step Slalom Test at 65 Km/h ($\mu = 1.0$)

Figure 6-128, Figure 6-129, Figure 6-130 and Figure 6-131 depict the vehicle sideslip, yaw rate, longitudinal speed and lateral acceleration respectively for vehicle with no control, AWS+SAS, TV+SAS and DB+SAS. It can be observed that AWS+SAS has significantly minimized the sideslip angle compared to the other control strategies, while DB+SAS has obtained the largest value. Which considered as merit for AWS+SAS in enhancing vehicle's stability at high friction road surface. DB+SAS has attained the largest yaw rate response amplitude among the proposed control. Furthermore, each control strategy has encountered a significant drop in the vehicle's longitudinal speed. However, TV+SAS has obtained the least drop, 35 Km/h, followed by AWS+SAS, 30 Km/h while DB+SAS has attained the largest drop in speed, 15 Km/h. Nevertheless, it should be noted that DB+SAS has achieved the least peak value of lateral acceleration compared to the other control strategies and this is because of the reduction of speed occurred as a result of employing braking.

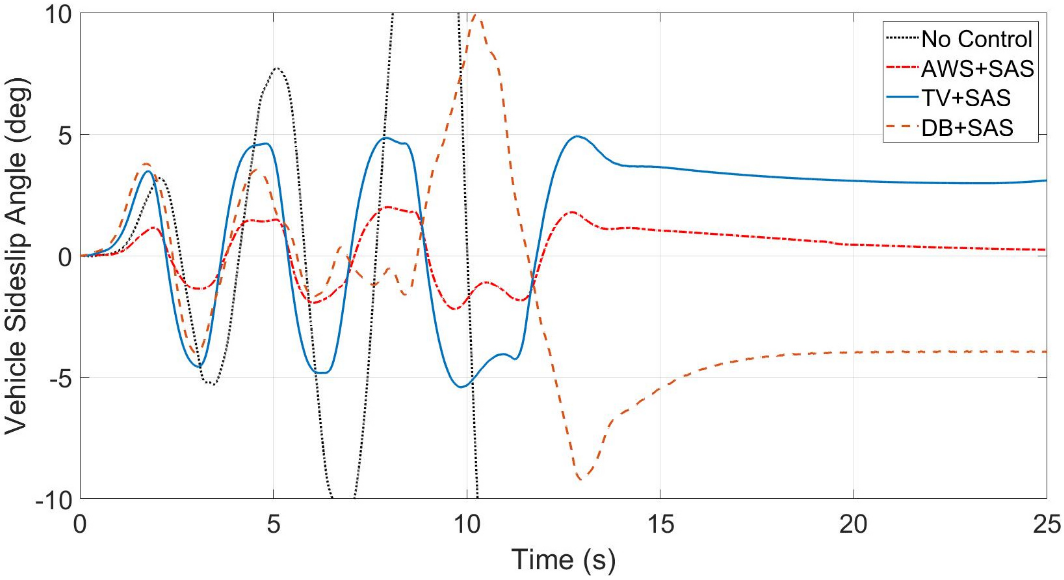

Figure 6-128 Vehicle Sideslip Angle during Open-Loop Step Slalom Test at 65 Km/h ($\mu = 1.0$)

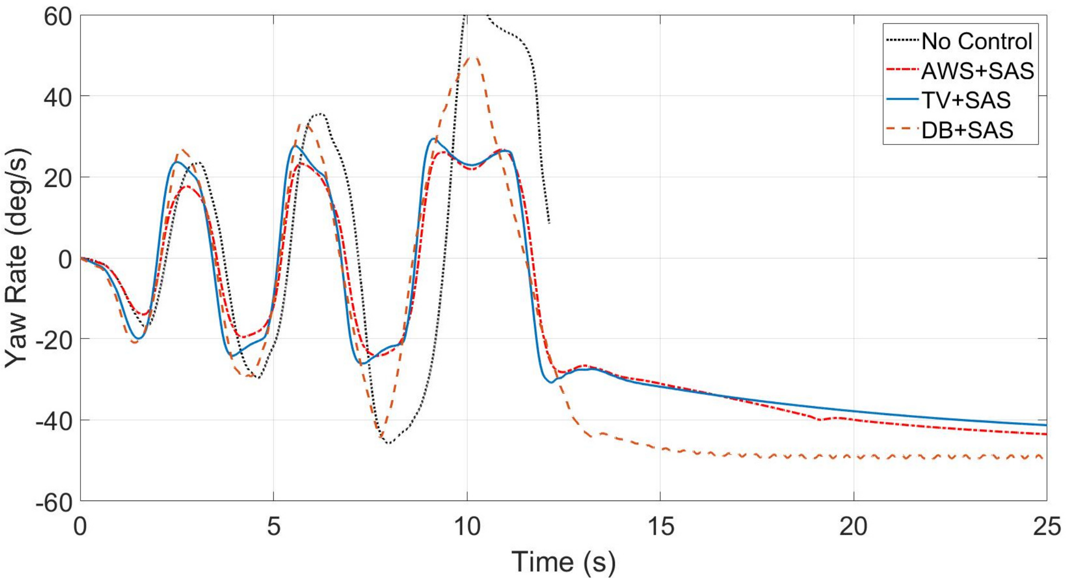

Figure 6-129 Yaw Rate during Open-Loop Step Slalom Test at 65 Km/h (μ = 1.0)

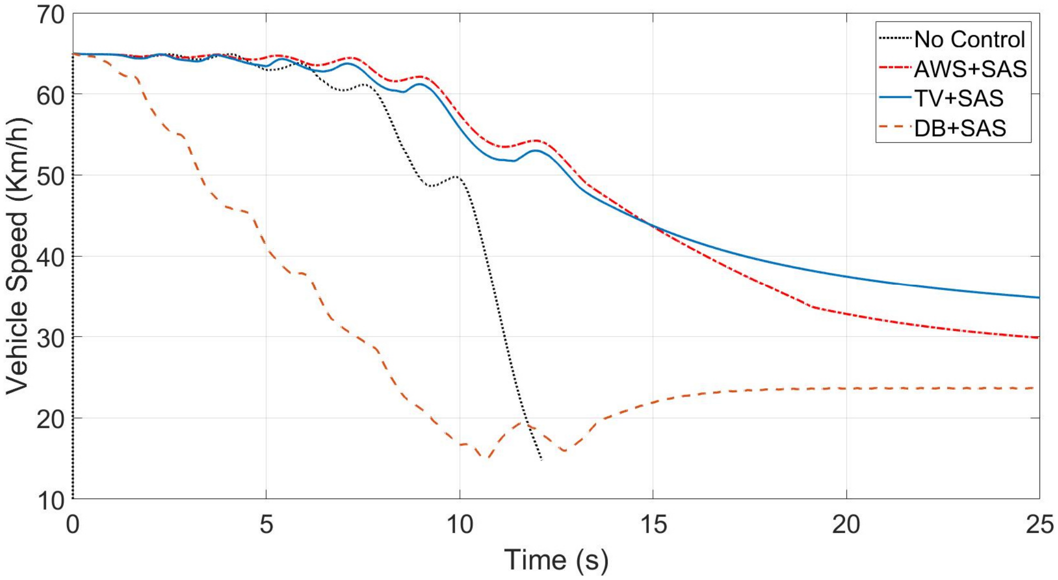

Figure 6-130 Vehicle Speed during Open-Loop Step Slalom Test at 65 Km/h (μ = 1.0)

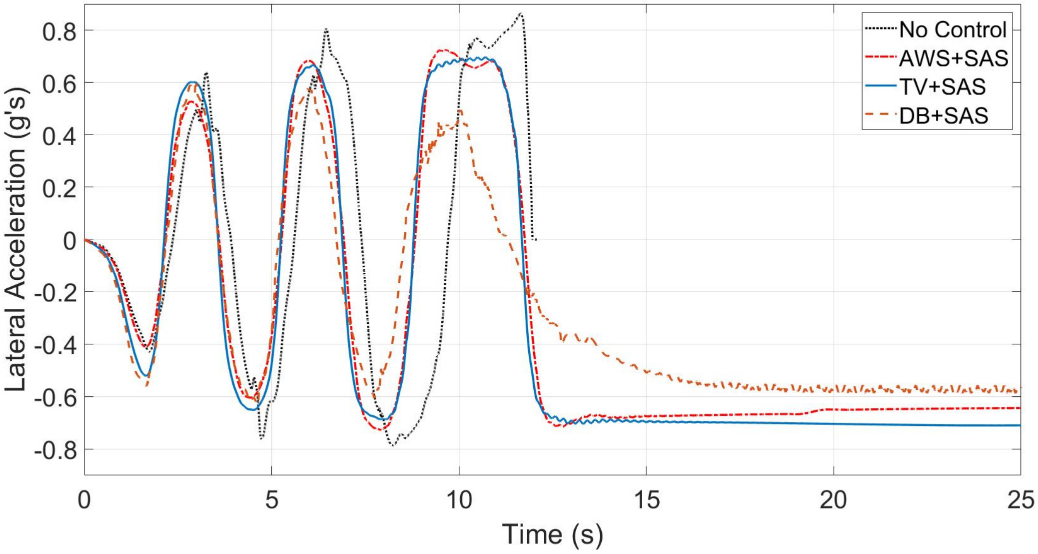

Figure 6-131 Lateral Acceleration during Open-Loop Step Slalom Test at 65 Km/h (μ = 1.0)

Figure 6-132, Figure 6-133 and Figure 6-134 present the vehicle's sprung mass displacement, pitch, and roll angle, respectively. It is notable that AWS+SAS, TV+SAS and DB+SAS have tremendously minimized the vertical displacement at the CG of the sprung mass. Furthermore, all the proposed control strategies have significantly reduced the pitch and roll angle due to longitudinal and lateral load transfer compared to vehicle with no control. However, TV+SAS has slightly attained largest value for pitch angle compared to the other control strategies, while DB+SAS has achieved the lowest value for roll angle, and this is because of reduction of speed induced by employing the braking.

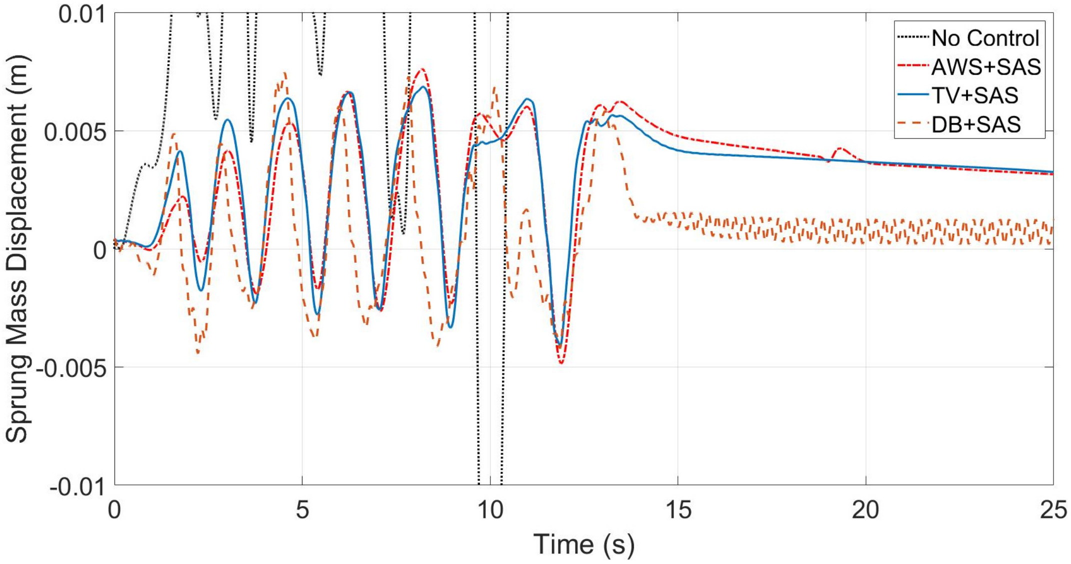

Figure 6-132 Sprung Mass Displacement during Open-Loop Step Slalom Test at 65 Km/h (μ = 1.0)

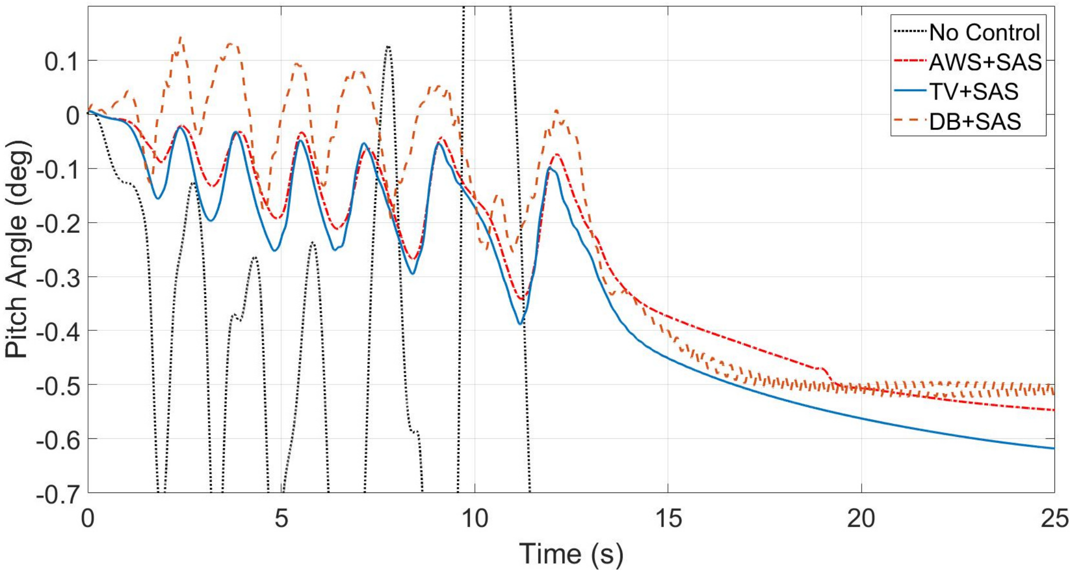

Figure 6-133 Pitch Angle during Open-Loop Step Slalom Test at 65 Km/h (μ = 1.0)

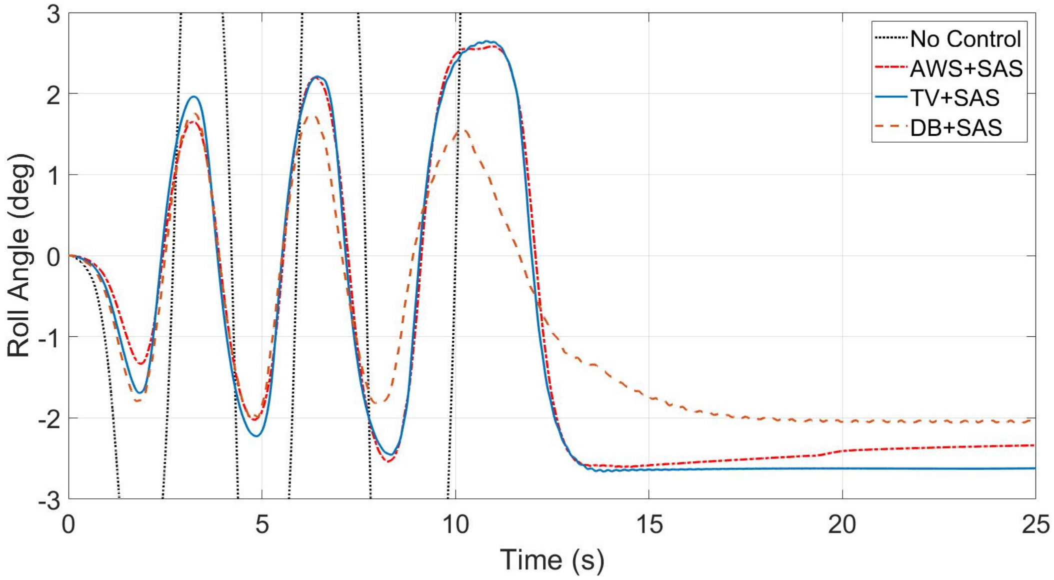

Figure 6-134 Roll Angle during Open-Loop Step Slalom Test at 65 Km/h (μ = 1.0)

Chapter 7 CONCLUSIONS AND FUTURE WORK

7.1 Conclusions

This thesis presents a comparison between various Active Chassis Control strategies to discover the merits of each to enhance the vehicle lateral dynamics in terms of vehicle stability and maneuverability at different road conditions. The proposed control strategies are Active All-Wheel Steering (AWS), Torque Vectoring (TV), Differential Braking (DB) and Semi-Active Suspension (SAS). Two degrees of freedom (DOF) vehicle mathematical model has been developed for Linear Quadratic Regulator controller (LQR) to control the vehicle yaw rate and sideslip angle. While an 11-DOF linear mathematical model is introduced to describe the multi-wheeled combat vehicle suspension for LQR control design purposes. The vehicle sprung mass has 3-DOF, heave, pitch, and roll motions, while the unsprung masses each have 1-DOF, vertical translational motion for a total 8-DOF. A validated TRUCKSIM vehicle model is utilized in co-simulation with the proposed control strategies in MATLAB SIMULINK to evaluate the performance of each proposed control strategy. All the proposed control strategies are designed in a hierarchical manner, comprised of upper and lower control levels. The upper control level is responsible to generate the gain needed based on the vehicle's parameters provided. Meanwhile, the lower control level is the actuator that intended to correct the vehicle deviation from the desired targets based on the error obtained between the reference model and actual vehicle behaviour during the test event.

An assessment of each control strategy was conducted through a comparison between each control strategy integrated and without integration of SAS to assess their performances during constant step slalom test event at limit handling speed and different road conditions. In the first test, the vehicle is running at 65 Km/h at 0.85 high road friction surface and the second test at 40 Km/h and 0.35 low friction surface. The main goal was to investigate the merits of integrating the SAS at high and low friction road surfaces. Based on this assessment it was found that the integration of SAS had a significant effect in improving the vehicle lateral dynamics at high road friction surface. While at low road friction surface no significant enhancements were observed in terms of vehicle stability and maneuverability. Accordingly, at a high coefficient of friction, the comparison was performed between each control strategy integrated with SAS. While at a low coefficient of friction the comparison was carried out between each control strategy without integration of SAS. The test events were expanded to include Slalom and NATO Double Lane Change (DLC) as a closed-loop test, where a target path is followed by the driver model. Also, Federal Motors Vehicle Safety Standard (FMVSS 126 ESC), Modified J-Turn and Open-Loop Step Slalom test maneuvers as an open-loop test, where no target path to be followed. Four road coefficients of friction were utilized, 1.0, 0.85, 0.35 and 0.2 at high cornering speed.

It can be concluded that.

At High Coefficient of Friction

TV+SAS and DB+SAS have shown superiority over AWS+SAS in maintaining the vehicle stable during severe maneuvers such as Slalom at 75 Km/h and coefficient of friction 1.0. At limit handling maneuvers Direct Yaw Moment controls are effective than All-Wheel Steering due to the saturation of the lateral forces of the tires.

AWS+SAS has exhibited in most test events the lowest value for vehicle's sideslip angle followed by DB+SAS compared to TV+SAS that attained the largest value. This indicates that AWS+SAS is the effective control method in enhancing vehicle stability compared to other control strategies.

It was found that TV+SAS has achieved better maneuverability in most test events, which yields a place to show supremacy over AWS+SAS and DB+SAS in improving vehicle maneuverability. However, in open-loop test event such as Modified J-Turn, DB+SAS has realized better maneuverability than TV+SAS and AWS+SAS.

TV+SAS has attained in all test events the least drop in speed followed by AWS+SAS compared to DB+SAS that performed a notable and huge drop in speed, which considers as a drawback for using braking as a control allocation.

All the proposed control strategies have succeeded to maintain the lateral acceleration at the lowest possible values and avoided rollover scenario compared to the un-controlled vehicle that tipped over, particularly during the open-loop Step Slalom test event. However, DB+SAS has achieved the lowest value, due to the reduction in speed caused by braking followed by TV+SAS compared to AWS+SAS which attained the largest value.

The integration of SAS with all control strategies has improved the vehicle's lateral dynamics at a high coefficient of friction and high-speed cornering maneuver, especially during severe maneuvers such as Constant step Slalom test event. The benefits of integrating SAS were observed in minimizing the pitch angle caused by longitudinal load transfer due to either speeding or braking. As well as reducing the roll angle at minimum possible value during high-speed cornering maneuver which prevents the drop of total lateral forces resulted from lateral load transfer. Furthermore, preventing the tires from losing contact with the ground and keep the normal loads at adequate values, to ensure transmitting all the forces and moments generated from the vehicle to the ground. Moreover, the integration of SAS has assisted in minimizing the oscillation of the sprung mass vertical displacement to the lowest values.

At Low Coefficient of Friction

In closed-loop test events, TV and DB have shown primacy over AWS and the un-controlled vehicle in maintaining the vehicle stable and completing the test event during severe maneuvers such as Slalom at 30 Km/h and coefficient of friction 0.2. while at 40 Km/h and the road friction surface of 0.35, AWS has achieved the least value followed by TV compared to DB and un-controlled vehicle. Furthermore, during the DLC test event, the performance of each control strategy was considerably close to each other in reducing the vehicle’s sideslip angle compared to the un-controlled vehicle that attained the largest value.

In open-loop tests, such as FMVSS 126 ESC, TV has maintained the least sideslip angle response peak value followed by DB compared to AWS, while the un-controlled vehicle has attained the largest value. Also, it was notable that AWS took much time to stabilize the vehicle based on the settling time compared to TV which was the fastest followed by DB. This is because of the first order delay of 0.3 seconds that set to the reference model to delay the action response of the steering of the wheels since the steering response is faster than the other actuators such as braking and differential. Whereas, during Modified J-Turn, AWS has shown superiority in minimizing the vehicle’s sideslip angle followed by TV compared to DB and un-controlled vehicle.

It was found in most test events either closed or open-loop that DB has achieved the highest yaw rate peak response compared to TV and AWS, which can be concluded that DB affords better maneuverability at low road friction surface. While AWS has achieved the highest peak value for lateral acceleration compared to TV and DB.

It was observed that DB exhibits a huge drop in longitudinal speed compared to TV and AWS. However, during Slalom and Modified J-Turn test events, the drop in speed was not that significant.

Finally, the AWS control allocation is efficient in enhancing the vehicle's stability and maintaining a small value for sideslip angle. However, it is very sensitive when it is associated with the steady-state yaw rate reference model and since the response of steering actuators is fast, thus it can make it more susceptible than TV and DB. Accordingly, a first order delay of 0.3 seconds was applied to the yaw rate reference model to eliminate such a problem. Nevertheless, it was observed that it did not work perfectly in some test events, particularly during FMVSS 126 ESC at low friction road surface 0.35 and speed 80 Km/h, which caused a notable delay in stabilizing the vehicle.

The TV and DB have proved in this comprehensive study that they are more effective and reliable than AWS control at limit handling speed and different coefficients of friction either high or low. However, the only drawback of DB the huge drop in speed, causing a delay in stabilizing the vehicle. Therefore, it can be concluded in all vehicle lateral dynamics aspects that TV is more effective than AWS and DB.

The integration of SAS has a tremendous effect in improving the vehicle lateral dynamics at high friction road surfaces where the vehicle experiences high lateral acceleration. However, at a low friction road surface, no significant effect was observed since the lateral acceleration exhibited at a lower value.

7.2 Future Work

- A nonlinear controller needs to be conducted to deal with the uncertainties such as the variation of road friction surfaces and tire cornering stiffness. All these factors can poorly affect the tracking of the desired yaw rate and sideslip angle.
- It is recommended to develop an active steering system with less dependency on yaw rate reference model.
- To avoid the huge drop in speed when employing braking torque, its recommended to design a differential braking considering an activation criteria.
- An integration of AWS, TV and SAS can enhance tremendously the vehicle lateral stability. However, incorporating SAS should be activated when lateral acceleration above 0.4 g's. Nevertheless, SAS has limited damper force compared to fully active suspension that has substantial range of damper forces.

7.3 Publications

Omar, M. and El-Gindy, M., "Direct Yaw Control Based on Optimal Longitudinal Tire Forces for 8×8 Combat Vehicle," SAE Technical Paper 2021-01-0261, 2021, https://doi.org/10.4271/2021-01-0261.

Ahmed, M., El-Gindy, M., Lang, H., and Omar, M., "Development of Active Rear Axles Steering Controller For 8X8 Combat Vehicle," SAE Technical Paper 2020-01-0174, 2020, https://doi.org/10.4271/2020-01-0174.

Omar, M., El-Gindy, M., "Vehicle Yaw Stability Control: Literature Review", *International Journal of Vehicle System Modelling and Testing (IJVSMT)*, 2020. (In press)

Ahmed, M., Omar, M., and El-Gindy, M., "Investigation of Various Passive Steering Modes for a multi-wheeled Combat Vehicle", *International Journal of Vehicle System Modelling and Testing (IJVSMT)*, 2021. (In press)

References

1. Army, C. *Light Armoured Vehicle (LAV) III Upgrade*. 2021 [cited 2021 February 10]; Available from: http://www.army-armee.forces.gc.ca/en/equipment/vehicles/light-armoured-vehicle-upgrade.page.
2. Logan, N. *CFB Wainwright accident: LAV III has a history of rollovers*. 2014 [cited 2014 May 22]; Available from: https://globalnews.ca/news/1347631/cfb-wainwright-accident-lav-iii-has-a-history-of-rollovers/.
3. Høye, A.J.A.A. and Prevention, *The effects of Electronic Stability Control (ESC) on crashes—An update.* 2011. **43**(3): p. 1148-1159.
4. Ismail, M., et al., *A Review of Active Yaw Control System for Vehicle Handling and Stability Enhancement.* 2014.
5. Wong, J.Y., *Theory of ground vehicles*. 2008: John Wiley & Sons.
6. Leegwater, M., *An active suspension system capable of economically leveling a car during cornering.* S010527 (TU/e), 2007.
7. Laoufi, M. and A. Eskandarian. *Fuzzy logic control for active suspension of a non-linear full-vehicle model*. in *2009 IEEE Intelligent Vehicles Symposium*. 2009. IEEE.
8. Krishnan, A., *A comparison between passive & semi active suspension systems.* International Journal of Innovative Research in Science, Engineering and Technology, 2013. **2**(6): p. 2412-2416.
9. Lacroix, B., Z.H. Liu, and P. Seers. *A comparison of two control methods for vehicle stability control by direct yaw moment*. in *Applied Mechanics and Materials*. 2012. Trans Tech Publ.
10. Zhou, H. and Z. Liu, *Vehicle yaw stability-control system design based on sliding mode and backstepping control approach.* IEEE Transactions on Vehicular Technology, 2010. **59**(7): p. 3674-3678.
11. Du, H., N. Zhang, and F. Naghdy, *Velocity-dependent robust control for improving vehicle lateral dynamics.* Transportation research part C: emerging technologies, 2011. **19**(3): p. 454-468.
12. Tamaddoni, S.H., S. Taheri, and M. Ahmadian, *Optimal preview game theory approach to vehicle stability controller design.* Vehicle system dynamics, 2011. **49**(12): p. 1967-1979.
13. Baslamisli, S.Ç., İ.E. Köse, and G.J.V.S.D. Anlaş, *Gain-scheduled integrated active steering and differential control for vehicle handling improvement.* 2009. **47**(1): p. 99-119.
14. Falcone, P., et al., *MPC-based yaw and lateral stabilisation via active front steering and braking.* Vehicle System Dynamics, 2008. **46**(S1): p. 611-628.
15. Cho, W., et al., *An investigation into unified chassis control scheme for optimised vehicle stability and manoeuvrability.* Vehicle System Dynamics, 2008. **46**(S1): p. 87-105.
16. Du, H., N. Zhang, and G. Dong, *Stabilizing vehicle lateral dynamics with considerations of parameter uncertainties and control saturation through robust yaw control.* IEEE Transactions on Vehicular Technology, 2010. **59**(5): p. 2593-2597.
17. Williams, D.E., *Generalised multi-axle vehicle handling.* Vehicle system dynamics, 2012. **50**(1): p. 149-166.

18. Başlamişli, S.Ç., İ.E. Köse, and G. Anlaç, *Handling stability improvement through robust active front steering and active differential control.* Vehicle System Dynamics, 2011. **49**(5): p. 657-683.
19. Wu, J., et al., *Studies on improving vehicle handling and lane keeping performance of closed-loop driver–vehicle system with integrated chassis control.* Mathematics and Computers in Simulation, 2010. **80**(12): p. 2297-2308.
20. Tekin, G. and Y. Samim Unlusoy, *Design and simulation of an integrated active yaw control system for road vehicles.* International journal of vehicle design, 2010. **52**(1-4): p. 5-19.
21. Boada, B., M. Boada, and V. Diaz, *Fuzzy-logic applied to yaw moment control for vehicle stability.* Vehicle System Dynamics, 2005. **43**(10): p. 753-770.
22. Yang, X., Z. Wang, and W. Peng, *Coordinated control of AFS and DYC for vehicle handling and stability based on optimal guaranteed cost theory.* Vehicle System Dynamics, 2009. **47**(1): p. 57-79.
23. Ikeda, Y. *Active steering control of vehicle by sliding mode control-switching function design using SDRE.* in *2010 IEEE International Conference on Control Applications*. 2010. IEEE.
24. Ding, N. and S. Taheri, *An adaptive integrated algorithm for active front steering and direct yaw moment control based on direct Lyapunov method.* Vehicle System Dynamics, 2010. **48**(10): p. 1193-1213.
25. Lu, S.-B., et al., *Integrated control on MR vehicle suspension system associated with braking and steering control.* Vehicle System Dynamics, 2011. **49**(1-2): p. 361-380.
26. Mammar, S. and D. Koenig, *Vehicle handling improvement by active steering.* Vehicle system dynamics, 2002. **38**(3): p. 211-242.
27. Zhao, C., W. Xiang, and P. Richardson. *Vehicle lateral control and yaw stability control through differential braking*. in *2006 IEEE international symposium on industrial electronics*. 2006. IEEE.
28. Mirzaei, M., *A new strategy for minimum usage of external yaw moment in vehicle dynamic control system.* Transportation Research Part C: Emerging Technologies, 2010. **18**(2): p. 213-224.
29. Cerone, V., M. Milanese, and D. Regruto, *Yaw stability control design through a mixed-sensitivity approach.* IEEE Transactions on Control Systems Technology, 2009. **17**(5): p. 1096-1104.
30. Zheng, S., et al., *Controller design for vehicle stability enhancement.* 2006. **14**(12): p. 1413-1421.
31. Esmailzadeh, E., A. Goodarzi, and G. Vossoughi, *Optimal yaw moment control law for improved vehicle handling.* Mechatronics, 2003. **13**(7): p. 659-675.
32. Canale, M. and L. Fagiano, *Comparing rear wheel steering and rear active differential approaches to vehicle yaw control.* Vehicle System Dynamics, 2010. **48**(5): p. 529-546.
33. Canale, M., et al., *Comparing internal model control and sliding-mode approaches for vehicle yaw control.* IEEE Transactions on Intelligent Transportation Systems, 2008. **10**(1): p. 31-41.
34. Moon, S., W. Cho, and K. Yi, *Intelligent vehicle safety control strategy in various driving situations.* Vehicle System Dynamics, 2010. **48**(S1): p. 537-554.

35. Yim, S., et al., *Optimum distribution of yaw moment for unified chassis control with limitations on the active front steering angle.* International Journal of Automotive Technology, 2010. **11**(5): p. 665-672.
36. Li, D., S. Du, and F. Yu, *Integrated vehicle chassis control based on direct yaw moment, active steering and active stabiliser.* Vehicle System Dynamics, 2008. **46**(S1): p. 341-351.
37. Hiraoka, T., O. Nishihara, and H. Kumamoto, *Automatic path-tracking controller of a four-wheel steering vehicle.* Vehicle System Dynamics, 2009. **47**(10): p. 1205-1227.
38. You, S.-H., et al., *Vehicle lateral stability management using gain-scheduled robust control.* Journal of mechanical science and technology, 2006. **20**(11): p. 1898.
39. Manning, W. and D. Crolla, *A review of yaw rate and sideslip controllers for passenger vehicles.* Transactions of the Institute of Measurement and Control, 2007. **29**(2): p. 117-135.
40. Ohara, H. and T. Murakami, *A stability control by active angle control of front-wheel in a vehicle system.* IEEE Transactions on Industrial Electronics, 2008. **55**(3): p. 1277-1285.
41. Kwak, B. and Y. Park, *Robust vehicle stability controller based on multiple sliding mode control.* SAE transactions, 2001: p. 514-520.
42. Rajamani, R., *Vehicle dynamics and control*. 2011: Springer Science & Business Media.
43. Baslamish, S.C., I.E. Kose, and G. Anlas. *Design of active steering and intelligent braking systems for road vehicle handling improvement: A robust control approach*. in *2006 IEEE Conference on Computer Aided Control System Design, 2006 IEEE International Conference on Control Applications, 2006 IEEE International Symposium on Intelligent Control*. 2006. IEEE.
44. Yih, P. and J.C. Gerdes, *Modification of vehicle handling characteristics via steer-by-wire.* IEEE transactions on control systems technology, 2005. **13**(6): p. 965-976.
45. Marino, R., S. Scalzi, and F. Cinili, *Nonlinear PI front and rear steering control in four wheel steering vehicles.* Vehicle System Dynamics, 2007. **45**(12): p. 1149-1168.
46. Falcone, P., et al., *Predictive active steering control for autonomous vehicle systems.* IEEE Transactions on control systems technology, 2007. **15**(3): p. 566-580.
47. Falcone, P., et al., *Linear time-varying model predictive control and its application to active steering systems: Stability analysis and experimental validation.* International Journal of Robust and Nonlinear Control: IFAC-Affiliated Journal, 2008. **18**(8): p. 862-875.
48. Borrelli, F., et al., *MPC-based approach to active steering for autonomous vehicle systems.* International journal of vehicle autonomous systems, 2005. **3**(2-4): p. 265-291.
49. Kawaguchi, Y., et al. *Passivity-based adaptive nonlinear control for active steering*. in *2007 IEEE International Conference on Control Applications*. 2007. IEEE.
50. Singh, S., *Design of front wheel active steering for improved vehicle handling and stability*. 2000, SAE Technical Paper.
51. Oraby, W., et al., *Improvement of vehicle lateral dynamics by active front steering control.* SAE transactions, 2004: p. 1101-1110.
52. Zhang, J.-Y., et al., *Development of an active front steering (AFS) system with QFT control.* International Journal of Automotive Technology, 2008. **9**(6): p. 695-702.
53. Zheng, B. and S. Anwar, *Yaw stability control of a steer-by-wire equipped vehicle via active front wheel steering.* Mechatronics, 2009. **19**(6): p. 799-804.

54. Yin, G.-D., et al., *A study on μ-synthesis control for four-wheel steering system to enhance vehicle lateral stability.* Journal of dynamic systems, measurement, and control, 2011. **133**(1).
55. Yu, F., D.-F. Li, and D. Crolla. *Integrated vehicle dynamics control—State-of-the art review*. in *2008 IEEE vehicle power and propulsion conference*. 2008. IEEE.
56. Mokhiamar, O. and M. Abe, *Active wheel steering and yaw moment control combination to maximize stability as well as vehicle responsiveness during quick lane change for active vehicle handling safety.* Proceedings of the Institution of Mechanical Engineers, Part D: Journal of Automobile Engineering, 2002. **216**(2): p. 115-124.
57. Raksincharoensak, P., T. Mizushima, and M. Nagai, *Direct yaw moment control system based on driver behaviour recognition.* Vehicle System Dynamics, 2008. **46**(S1): p. 911-921.
58. Canale, M., et al., *Robust vehicle yaw control using an active differential and IMC techniques.* Control Engineering Practice, 2007. **15**(8): p. 923-941.
59. Canale, M., et al., *Vehicle yaw control via second-order sliding-mode technique.* IEEE Transactions on Industrial Electronics, 2008. **55**(11): p. 3908-3916.
60. Lai, F. and Z. Deng. *Integrated control of automotive four wheel steering and active suspenion systems based on unifrom model*. in *2009 9th International Conference on Electronic Measurement & Instruments*. 2009. IEEE.
61. Zhou, S., L. Guo, and S. Zhang. *Vehicle yaw stability control and its integration with roll stability control*. in *2008 Chinese Control and Decision Conference*. 2008. IEEE.
62. Hu, A. and F. He. *Variable structure control for active front steering and direct yaw moment*. in *2011 2nd International Conference on Artificial Intelligence, Management Science and Electronic Commerce (AIMSEC)*. 2011. IEEE.
63. Hu, A. and B. Lv. *Study on mixed robust control for integrated active front steering and direct yaw moment*. in *2010 IEEE International Conference on Mechatronics and Automation*. 2010. IEEE.
64. He, Z. and X. Ji, *Nonlinear robust control of integrated vehicle dynamics.* Vehicle System Dynamics, 2012. **50**(2): p. 247-280.
65. Ahn, C., B. Kim, and M. Lee, *Modeling and control of an anti-lock brake and steering system for cooperative control on split-mu surfaces.* International Journal of Automotive Technology, 2012. **13**(4): p. 571-581.
66. Poussot-Vassal, C., et al., *Vehicle dynamic stability improvements through gain-scheduled steering and braking control.* Vehicle System Dynamics, 2011. **49**(10): p. 1597-1621.
67. Tjonnas, J. and T.A. Johansen, *Stabilization of automotive vehicles using active steering and adaptive brake control allocation.* IEEE Transactions on Control Systems Technology, 2009. **18**(3): p. 545-558.
68. Wei, J., Y. Zhuoping, and Z. Lijun. *Integrated chassis control system for improving vehicle stability*. in *2006 IEEE International Conference on Vehicular Electronics and Safety*. 2006. IEEE.
69. Shibahata, Y., et al., *The development of an experimental four-wheel-steering vehicle.* SAE Transactions, 1986: p. 862-869.
70. Ono, E., et al. *Robust stabilization of vehicle dynamics by active front wheel steering control*. in *Proceedings of 35th IEEE Conference on Decision and Control*. 1996. IEEE.

71. Feng, K.-T., H.-S. Tan, and M. Tomizuka. *Automatic steering control of vehicle lateral motion with the effect of roll dynamics*. in *Proceedings of the 1998 American Control Conference. ACC (IEEE Cat. No. 98CH36207)*. 1998. IEEE.
72. Zhao, W., et al., *Control strategy of a novel electric power steering system integrated with active front steering function.* Science China Technological Sciences, 2011. **54**(6): p. 1515.
73. Zhao, W., et al., *H∞/extension stability control of automotive active front steering system.* Mechanical Systems and Signal Processing, 2019. **115**: p. 621-636.
74. Sano, S., Y. Furukawa, and S. Shiraishi, *Four Wheel Steering System with Rear Wheel Steer Angle Controlled as a Function of Sterring Wheel Angle.* SAE Transactions, 1986: p. 880-893.
75. Hirano, Y. and K. Fukatani, *Development of robust active rear steering control for automobile.* JSME International Journal Series C Mechanical Systems, Machine Elements and Manufacturing, 1997. **40**(2): p. 231-238.
76. Fujita, K., et al., *Development of Active Rear Steer System Applying H∞-μ synthesis.* SAE transactions, 1998: p. 1694-1701.
77. Huh, K., J. Kim, and J. Hong, *Handling and driving characteristics for six-wheeled vehicles.* Proceedings of the Institution of Mechanical Engineers, Part D: Journal of Automobile Engineering, 2000. **214**(2): p. 159-170.
78. Russell, B., *Development and analysis of active rear axle steering for 8x8 combat vehicle*. 2018.
79. Ahmed, M., et al., *Development of Active Rear Axles Steering Controller For 8X8 Combat Vehicle*. 2020, SAE Technical Paper.
80. Shibahata, Y., K. Shimada, and T. Tomari, *Improvement of vehicle maneuverability by direct yaw moment control.* Vehicle System Dynamics, 1993. **22**(5-6): p. 465-481.
81. Ikushima, Y. and K. Sawase, *A study on the effects of the active yaw moment control.* SAE transactions, 1995: p. 425-433.
82. Osborn, R.P. and T.J.V.s.d. Shim, *Independent control of all-wheel-drive torque distribution.* 2006. **44**(7): p. 529-546.
83. Kim, H., S. Lee, and J.K.J.I.J.o.A.T. Hedrick, *Active yaw control for handling performance improvement by using traction force.* 2015. **16**(3): p. 457-464.
84. Abe, M., et al., *Improvement of vehicle handling safety with vehicle side-slip control by direct yaw moment.* Vehicle System Dynamics, 1999. **33**(sup1): p. 665-679.
85. Asiabar, A.N. and R. Kazemi, *A direct yaw moment controller for a four in-wheel motor drive electric vehicle using adaptive sliding mode control.* Proceedings of the Institution of Mechanical Engineers, Part K: Journal of Multi-body Dynamics, 2019. **233**(3): p. 549-567.
86. Koibuchi, K., et al., *Vehicle stability control in limit cornering by active brake*. 1996, SAE technical paper.
87. Park, J.H., *H∞ direct yaw-moment control with brakes for robust performance and stability of vehicles.* JSME International Journal Series C Mechanical Systems, Machine Elements and Manufacturing, 2001. **44**(2): p. 404-413.
88. Zhai, L., T. Sun, and J. Wang, *Electronic stability control based on motor driving and braking torque distribution for a four in-wheel motor drive electric vehicle.* IEEE Transactions on Vehicular Technology, 2016. **65**(6): p. 4726-4739.

89. Hancock, M., et al., *A comparison of braking and differential control of road vehicle yaw-sideslip dynamics.* 2005. **219**(3): p. 309-327.
90. Sawase, K. and Y.J.M.M.T.R. Ushiroda, *Improvement of vehicle dynamics by right-and-left torque vectoring system in various drivetrains.* 2008. **20**: p. 14.
91. Jalali, K., et al., *Development of an advanced torque vectoring control system for an electric vehicle with in-wheel motors using soft computing techniques.* 2013. **2**(2): p. 261-278.
92. Siampis, E., E. Velenis, and S. Longo. *Model Predictive torque vectoring control for electric vehicles near the limits of handling*. in *2015 European Control Conference (ECC)*. 2015. IEEE.
93. Oh, K., et al., *Yaw Stability Control of 4WD Vehicles Based on Model Predictive Torque Vectoring with Physical Constraints.* 2019. **20**(5): p. 923-932.
94. Siampis, E., E. Velenis, and S.J.V.S.D. Longo, *Rear wheel torque vectoring model predictive control with velocity regulation for electric vehicles.* 2015. **53**(11): p. 1555-1579.
95. Vasiljevic, G. and S. Bogdan. *Model predictive control based torque vectoring algorithm for electric car with independent drives*. in *2016 24th Mediterranean Conference on Control and Automation (MED)*. 2016. IEEE.
96. Kim, W., et al., *Drive control algorithm for an independent 8 in-wheel motor drive vehicle.* 2011. **25**(6): p. 1573.
97. Zhao, Y. and C. Zhang, *Electronic Stability Control for Improving Stability for an Eight In-Wheel Motor-Independent Drive Electric Vehicle.* Shock and Vibration, 2019. **2019**.
98. Ragheb, H., M. El-Gindy, and H. Kishawy. *Torque Distribution Control for Multi-Wheeled Combat Vehicle*. in *International Design Engineering Technical Conferences and Computers and Information in Engineering Conference*. 2014. American Society of Mechanical Engineers.
99. Ragheb, H. and M. El-Gindy, *Design of active yaw controller integrated with ABS and TCS for multi-wheeled vehicles.* International Journal of Vehicle Systems Modelling and Testing, 2019. **13**(4): p. 340-357.
100. Nagai, M., Y. Hirano, and S. Yamanaka, *Integrated control of active rear wheel steering and direct yaw moment control.* Vehicle System Dynamics, 1997. **27**(5-6): p. 357-370.
101. Gordon, T., M. Howell, and F. Brandao, *Integrated control methodologies for road vehicles.* Vehicle System Dynamics, 2003. **40**(1-3): p. 157-190.
102. Ono, E., et al., *Vehicle integrated control for steering and traction systems by μ-synthesis.* Automatica, 1994. **30**(11): p. 1639-1647.
103. Nagai, M., M. Shino, and F. Gao, *Study on integrated control of active front steer angle and direct yaw moment.* JSAE review, 2002. **23**(3): p. 309-315.
104. Boada, M., et al., *Integrated control of front-wheel steering and front braking forces on the basis of fuzzy logic.* Proceedings of the Institution of Mechanical Engineers, Part D: Journal of Automobile Engineering, 2006. **220**(3): p. 253-267.
105. Doumiati, M., et al., *Integrated vehicle dynamics control via coordination of active front steering and rear braking.* 2013. **19**(2): p. 121-143.
106. Choi, M. and S.B. Choi, *MPC for vehicle lateral stability via differential braking and active front steering considering practical aspects.* Proceedings of the Institution of Mechanical Engineers, Part D: Journal of Automobile Engineering, 2016. **230**(4): p. 459-469.

107. Rahimi, S. and M. Naraghi, *Design of an integrated control system to enhance vehicle roll and lateral dynamics.* Transactions of the Institute of Measurement and Control, 2018. **40**(5): p. 1435-1446.
108. Nah, J. and S. Yim, *Optimization of control allocation with ESC, AFS, ARS and TVD in integrated chassis control.* Journal of Mechanical Science and Technology, 2019. **33**(6): p. 2941-2948.
109. Mokhiamar, O., M.J.J.o.d.s. Abe, measurement,, and control, *Simultaneous optimal distribution of lateral and longitudinal tire forces for the model following control.* 2004. **126**(4): p. 753-763.
110. Li, D. and F. Yu, *A novel integrated vehicle chassis controller coordinating direct yaw moment control and active steering*. 2007, SAE Technical Paper.
111. Kim, W., K. Yi, and J. Kang, *Development of driving control system based on optimal distribution for a 6WD/6WS vehicle.* SAE International Journal of Passenger Cars-Mechanical Systems, 2010. **3**(2010-01-0091): p. 145-157.
112. D'Urso, P., *Development of H∞ control strategy for a multi-wheeled combat vehicle*. 2016.
113. Horiuchi, S., K. Okada, and S. Nohtomi, *Effects of integrated control of active four wheel steering and individual wheel torque on vehicle handling and stability-a comparison of alternative control strategies.* Vehicle System Dynamics, 1999. **33**(sup1): p. 680-691.
114. He, J., et al., *Coordination of active steering, driveline, and braking for integrated vehicle dynamics control.* Proceedings of the Institution of Mechanical Engineers, Part D: Journal of Automobile Engineering, 2006. **220**(10): p. 1401-1420.
115. Ahangarnejad, A.H., S. Melzi, and M. Ahmadian, *Integrated Vehicle Dynamics System through Coordinating Active Aerodynamics Control, Active Rear Steering, Torque Vectoring and Hydraulically Interconnected Suspension.* International Journal of Automotive Technology, 2019. **20**(5): p. 903-915.
116. Elmarakbi, A., et al., *New integrated chassis control systems for vehicle handling performance enhancement.* International Journal of Dynamics and Control, 2013. **1**(4): p. 360-384.
117. Hillegass, M.J., et al. *Validating the directional performance of multi-wheeled combat vehicle computer simulation models*. in *ASME International Mechanical Engineering Congress and Exposition*. 2004.
118. Hillegass, M.J., et al. *Validating the vertical dynamic performance of a multi-wheeled combat vehicle computer simulation model*. in *ASME International Mechanical Engineering Congress and Exposition*. 2005.
119. Ragheb, H., *Torque control strategy for off-road vehicle mobility*. 2014.
120. Odrigo, A., *Development of multi-wheel drivetrain control system for future electric combat vehicle*. 2017.
121. Ogata, K., *Modern control engineering.* Book Reviews, 1999. **35**(1181): p. 1184.
122. Murray, R.M., *Optimization-based control.* California Institute of Technology, CA, 2009: p. 111-128.
123. Jazar, R.N., *Vehicle dynamics: theory and application*. 2017: Springer.
124. Administration, N.H.T.S., *FMVSS No. 126: Electronic Stability Control Systems.* Office of Regulatory Analysis and Evaluation National Center for Statistics and Analysis, 2007.